AN XPS STUDY OF THE EFFECT OF ION BOMBARDMENT ON TRANSITION METAL OXIDES

Tanima Choudhury

Doctor of Philosophy

THE UNIVERSITY OF ASTON IN BIRMINGHAM

September 1991

AN XPS STUDY OF THE EFFECT OF ION BOMBARDMENT ON TRANSITION METAL OXIDES

Tanima Choudhury

A thesis submitted for the Degree of Doctor of Philosophy

1991

SUMMARY

The effect of ion bombardment on various transition metal oxides has been investigated by means of XPS. These oxides are commercially obtained powders of FeO, Fe_3O_4, Fe_2O_3, CoO, Co_3O_4, TiO_2, ZrO_2, Nb_2O_5, Ta_2O_5 and WO_3. In order to establish the beam induced effects, it is necessary to characterize the unbombarded oxide surface. For each oxide this has been carried out by determination of the binding energies associated with the core-electron levels of the metal and oxygen in various chemical states. In addition, the bulk-purity of the oxides were investigated using X-ray powder diffraction technique. Ion bombardment induced surface compositional changes of all oxides have been observed through a chemical reduction to the lower oxidation states and eventually to the metallic state. The results found have been quantified to yield the extent of the surface compositional change. This quantification is given in terms of the (metal to oxygen)-surface to bulk ratio, which enables comparisons to be made with predictions of the linear cascade theory of preferential sputtering.

Theoretical understanding of the ion bombardment induced compositional changes in oxides is currently insufficient, mainly due to a lack of quantified experimental evidence. The results found here thus provide an extensive basis of quantitative information. In addition to the effect of ion bombardment on the surface chemistry of the oxides, investigations involving the influence of the primary beam energy, current density , dose, mass and charge of the projectile on the extent of the chemical damage are also carried out. The results have been compared with recent theories of preferential removal of oxygen.

Keywords: Ion bombardment, preferential sputtering, transition metal oxides, X-ray Photoelectron Spectroscopy, surface compositional change.

Dedicated to my parents

ACKNOWLEDGEMENTS

I thank my supervisor at Aston University, Dr. J.L. Sullivan, for his support and guidance throughout the duration of this project. I am also grateful to Mr. A. Abott for his technical assistance during the experimental work.

I am greatly indebted to Dr. M.G. Dowsett (University of Warwick), whose support has been essential for the successful completion of this thesis.

Special thanks go to Dr. A. Brown (formerly VG Microtrace) for his support during my time at VG Microtrace, and for trying to make me see the light at the end of the endless tunnel which at times this thesis seemed to be.

Finally, my thanks go to Jim whose help has been generally indispensable.

CONTENTS

LIST OF FIGURES

LIST OF TABLES

CHAPTER 1: Introduction

1.1: Introduction to the thesis

In this chapter a brief review of ion bombardment of multicomponent targets will be presented, giving particular attention to the rare gas ion projectiles on transition metal oxides. Some of the experimental findings that have been reported so far and the current understanding to the problems initiated by the bombardment process will be presented. This is extended in to Chapter 2 which outlines the sputtering theory as proposed by Sigmund[1,2,3], for the cases of single and multicomponent targets. The analytical technique X-ray Photoelectron Spectroscopy (XPS) is discussed in chapter 3. This thus constitutes the background work for the thesis.

Chapter 4 gives the experimental details and chapter 5 summarises the results. In chapter 6, two current theories on ion bombardment induced surface chemical changes of metal oxides are discussed. Finally, chapters 7 and 8 incorporate the discussion of the results and the conclusions respectively.

1.2: An overview of ion bombardment induced compositional changes

Ion bombardment of solid surface is a technique which is now widely used for various purposes. These uses are primarily sputter cleaning prior to surface sensitive techniques such as XPS [4] and Auger Electron Spectroscopy (AES) [5], depth profiling [6,7], surface texturing [8], pattern fabrication [9] and ion implantation [10]. There are also analytical techniques that rely on ion bombardment to provide the primary excitation mechanism. These include 'Secondary Ion Mass Spectroscopy (SIMS) [11], Ion Scattering Spectroscopy (ISS) [12] and Rutherford Backscattering Spectroscopy (RBS) [13].

When a beam of ions is projected at a target it can lead, under suitable conditions, to a reversal of the incident momentum carried by the ions so that target atoms are ejected from the surface. This process of atomic ejection during bombardment is called

sputtering. The generally accepted theory for the sputtering mechanism is that proposed by Sigmund [1,2]. The elementary event is an 'atomic collision cascade' where the incident ion knocks target atoms off their equilibrium sites. These atoms can then move through the material and undergo further collisions and eventually cause the ejection of atoms through the target surface.

Ion bombardment of a solid surface, for the purposes of sputter etching, has the advantage of being able to micro-section all solid materials in a clean, controllable and relatively uniform way. It also has the advantage of being compatible with ultra-high vacuum environment which is required by various analytical methods such as those listed above. However the process of ion-bombardment itself will often influence the nature of the sample in such a way as to introduce ambiguities in the interpretation of the analytical data. In particular those data concerned with elemental composition as a function of depth from the surface. The major effects concern the non-stoichiometric removal of surface atoms leading to changes in surface composition. Thus it is essential that the changes caused by ion bombardment are known before absolute compositional analysis can be made.

1.3: Definitions associated with sputtering

In Sigmund's theory [1] of sputtering, three regimes of sputtering are defined based on qualitative considerations. Considering the atomic cascade inside the target set up by elastic collisions, the sputtering events are classified by the following three regimes:

i. The linear cascade regime: for medium and heavy mass ions with an incident energy of up to a few keV;

ii. The spike regime: for very heavy ions and energies above tens of keV;

iii. The single knock-on regime: for very low energies (hundreds of eV) and/or for light ions (H, He etc).

In the single knock-on regime, the recoil atoms from the ion-target collision receive

sufficient energy to get sputtered but not enough to generate recoil cascades. In the two other cases, recoil atoms are energetic enough to generate secondary and higher order recoils. The linear cascade regime differs from the spike regime by the spatial density of moving atoms which is small in the former and large in the latter. These three regimes are shown in figure (1.1).

Sputtering is quantified by the term known as sputtering yield. For single-element targets the total sputtering yield, Y, is defined as the average number of sputtered atoms per incident ion. For multicomponent targets there are different types of sputtering yield associated with it, which for clarification purposes need to be defined. A partial sputtering yield, Y_i, of the component 'i' in a multicomponent sample is defined as the average number of sputtered atoms of i per incident ion. Then the total sputtering yield is given by:

$$Y = \sum_i Y_i \qquad \text{.... (1.1)}$$

Also, a component sputtering yield, Y_i^c, is defined as the partial sputtering yield Y_i divided by the equilibrium surface concentration, c_i^S of i, i.e:

$$Y_i^c = (Y_i / c_i^S) \qquad \text{.... (1.2)}$$

Both the partial and component sputtering yields generally alter during ion bombardment if the surface concentration changes. As the ion bombardment proceeds, an equilibrium condition is eventually reached where the target loses material in its bulk composition. For such a steady state condition, a relation has been derived for the component sputtering yields and the bulk and surface concentrations (Patterson and Shirn [14], Shimizu and Saeki [15]). This derivation for a binary target containing 'a' and 'b' elements is as follows:

Let n_i be the number of sputtered atoms and c_i^B be the bulk concentration of component i. Then at the steady state, the ratio (n_a / n_b) must equal (c_a^B / c_b^B). From the definition of sputtering yield it follows that the ratio of the partial sputtering yield,

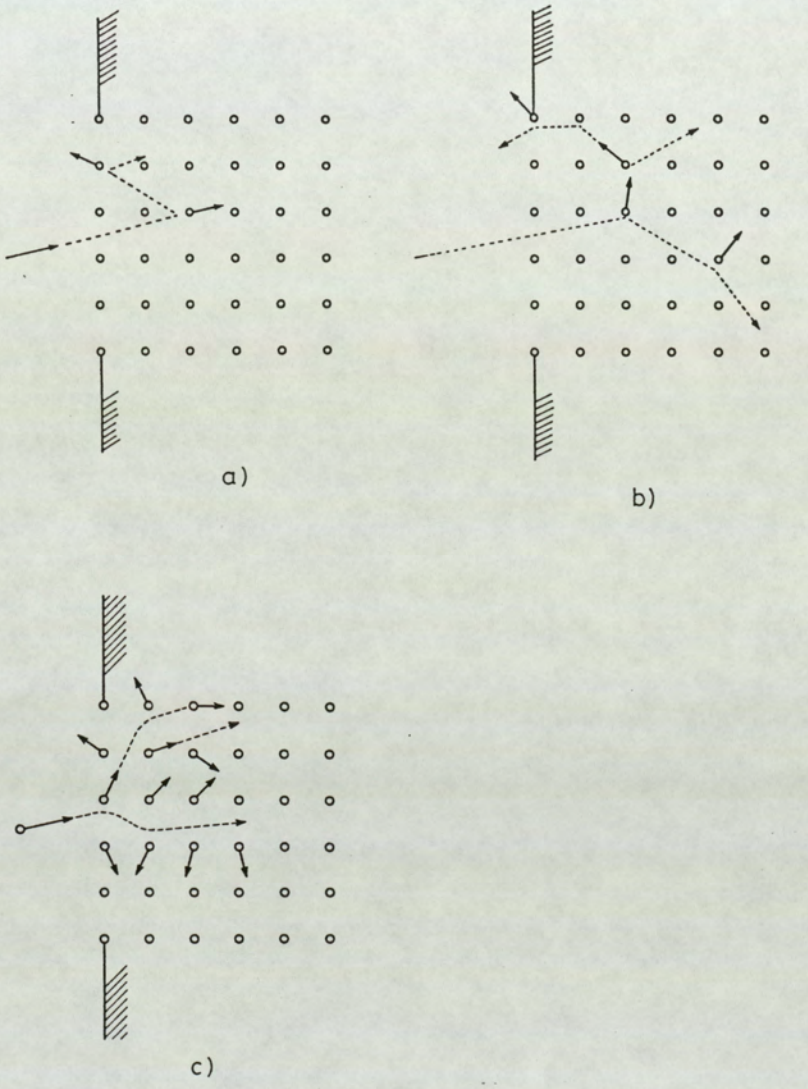

Figure1.1.

The three regimes of sputtering as defined by Sigmund [1].
a) the single knock-on regime
b) the linear cascade regime
c) the spike regime

Y_a/Y_b, is also equal to the component sputtered atom ratio n_a/n_b. Thus:

$$(Y_a^c/Y_b^c) = (c_a^B/c_b^B) / (c_a^S/c_b^S) \quad \text{.... (1.3)}$$

With this equation, it is possible to experimentally determine the component yields from a knowledge of the bulk concentration and the changes in the surface composition under ion bombardment. However one need to be aware that there is a problem associated with such measurements since strictly speaking the surface concentration, c_i^S, should refer to the weighed average composition of the layer from which sputtering takes place, i.e. the top two to three atomic layers. Depending on the probing depth of the surface analytical technique used to measure c_i^S, it is possible to find different values for the surface composition and thus different sputtering yields.

1.4: Preferential sputtering and the altered layer

For multicomponent systems, the change of surface chemical composition induced by the interaction of the ion beam with sample surface imposes some fundamental limitations on the use of ion beam bombardment. As a result of this interaction of the ion beam with the surface, random atomic mixing of the first few atomic layers is produced [16] with subsequent formation of new chemical bonds; this is accompanied by surface depletion of the preferentially sputtered elements.

The preferential removal of one component from the surface leads to the formation of an "altered layer" which is a near surface region with a stoichiometry different from that of the bulk. After sufficient bombardment time a steady state condition of the altered layer can be reached. In one group of solids, the transition metal oxides, this change in chemical composition is manifested by a reduction to lower oxidation states and in some cases eventually to the metallic state; this behavior has been attributed to be initiated by preferential sputtering. Betz and Whener [17] have compilled a summary of the surface chemical damage observed in various

multicomponent systems.

Preferential sputtering is the terminology given to the process during ion bombardment when there exist different ejection probabilities of the different sputtered atoms. In current literature the terms 'differential' or 'selective' sputtering are sometimes used to describe the preffered emission of one target constituent. Also, some authors [18,19] use the term 'preferential' with respect to the bulk composition of the solid. with this definition, preferential sputtering occurs only during the time until a steady state condition of the altered layer is reached, since afterwards material is removed according to its bulk composition. However, Andersen's [20] definition of preferential sputtering is now generally accepted. According to this definition the preferential sputtering is with respect to the composition of the target from which sputtered species originate; that is the outermost two or three atomic layers. Thus preferential sputtering also takes place during steady state as the composition of the material sputtered from the surface is generally not equal to the first few atomic layers of the surface. This latter definition will also be advocated here. The compositional changes in a surface layer with a thickness equivalent to the depth from which sputtered particles are ejected can then be contributed solely to preferential sputtering. However, experimental evidence shows (see for example Hoffman et al [21]) that the compositional changes occur to a much thicker depth; typically comparable to the range of the incident ions. Thus in addition to preferential sputterring other transport mechanisms must also exist. In current literature the general concensus is that some of these transport mechanisms that might be initiated during ion bombardment are as follows (their applicability to sputtering of oxides, in terms of exactly which mechanism is responsible, however, again has been a great source of controversy - no definite experimental evidence has been obtained so far to clarify if any of the mechanisms occur during metal oxide bombardment):

i. Radiation enhanced diffusion

ii. Recoil implantation

iii Bombardment induced Segregation

According to Betz and Wehner [17] and Sigmund [3] the radiation enhanced diffusion process can only counteract compositional changes produced by preferential sputtering, thus increasing the depth of the altered layer. The other transport mechanisms however, can produce compositional changes on their own and thus enforce or weaken compositional changes due to the preferred emission of one component. Some models have been proposed to describe the propagation of the changed surface composition deeper into the material due to radiation enhanced diffusion. These models, and also the applicability of the different transport mechanisms to oxide sputtering are briefly discussed here:

i. Radiation enhanced diffusion: During ion bombardment, many lattice atoms are displaced in the course of the collision cascade. This leads to the creation of vacancies, interstitials and finally larger defects, all of which enhance diffusion. Thus the altered layer components are in a highly mobile state and the diffusion coefficients can be much larger than for the undamaged material.

Pickering [22] in 1976 was the first to incorporate the effect of diffusion, in calculating the thickness and concentration profile of the altered layer at steady state. It is based on the idealised model of a binary alloy which consists of an easy-to-sputter and a difficult-to-sputter metal, although it is claimed that it may also be applied to metal oxides. The main assumption is that the component sputtering yields are different to a large degree, so that for steady state the surface concentration of the high-yield component tends to zero. He then used Fick's Second law to determine the diffusion fluxes of material towards the surface being sputtered. An effective thickness 'δ' of the depletion zone was obtained which is :

$$\delta = D/u \qquad \ldots. (1.4)$$

where D is the diffusion coefficient and u is the erosion rate given by the product of the molar volume of the alloy and the incident current density. This model has been

presented mainly in order to show how one may understand qualititatively the sputtering process.

In a model by Ho [23], the contribution of radiation enhanced diffusion is included to extend a previous model by Ho et al [24] which gives a kinetic analysis of preferential sputtering. Firstly considering the model by Ho et al [24], it describes the time dependent change of the average composition of the altered layer for an alloy target. The composition profile with depth is approximated by a step function. A mass balance equation is set up considering composition changes in the top monolayer and also in a layer of constant but altered composition. This model was later modified by Sanz and Hofmann [25] to apply to oxides such as Nb_2O_5 and Ta_2O_5 to account for the time dependent changes of the compositional profile which they had obtained using AES. In the extended version of the kinetic model by Ho [23], a mass balance is considered within the altered layer and on the surface, assuming that concentration gradients are the only driving forces for diffusion, and sputtering is the only effect that depletes the surface of a component. The solutions for the steady state shows that the composition of the altered layer varies in a exponential manner with the distance from the surface. The effective altered layer thickness is given by the diffusion coefficient divided by the velocity of the receding surface as was predicted by Pickering [22]. In the steady state the concentration $c(0,\infty)$, i.e., the atomic fraction of A atoms for an alloy AB is given by:

$$c(0,\infty) = c_0\sigma_B/\sigma_A[(1-c_0) + \sigma_B c_0] \qquad \ldots. (1.5)$$

where σ_i is the ratio of the sputtering yield for the element 'i' to its atomic density and c_0 is the stoichiometric concentration of A.

ii. Recoil implantation: This mechanism causes an enrichment of the heavy species near the surface, while the lighter species accumulate in a deeper layer [26]. No

experimental evidence exists so far of the altered layer formation that can be clearly contributed to recoil implantation. However some authors suggest [27,28] the possibility that the spreading of the altered layer may partly be due to this mechanism.

iii. Bombardment induced segregation: Ion bombardment induced point defects (i.e., interstitials and vacancies) and vacancy clusters can exist in an approximately random distribution throughout most of the ion range. The defects move to 'sink's (i.e., regions with low or zero defect concentrations) thus causing a redistribution of the constituents at the near-surface inaddition to preferential sputtering.

This mechanism is briefly mentioned here solely for the purpose of completeness since in the current literature no experimental evidence exists for the case of sputtering of oxides to justify definite contribution due to bombardment induced segregation.

1.5: Review of compositional changes: experimental results and the models predicted

The majority of sputtering investigations were confined to single element targets until the late 1960's, when surface sensitive analytical methods started to become available. These enabled detailed studies of the top few atomic layer composition to be made and investigations on the ion bombarded induced artefacts to the multicomponent surface started to gain renewed interest. However, even in the earlier sputtering investigations on multicomponent targets (mainly alloys), a change in the near surface composition as well as in the total sputtering yield was observed as a consequence of ion bombardment. In 1929 Asada and Quasebarth [29] found for Hg^+ ion bombardment of copper, which contained small amounts of Au, an increase of Au sputtering yield relative to the bulk composition. This observation was explained in terms of the formation of a Au enriched layer at the target surface which was continuously replenished by diffusion from the bulk.

The first reported case of the observation of a change in the near-surface composition due to ion bombardment was given by Gillam in 1959 [30]. He studied the near-surface composition changes due to bombardment with noble gas ions with energies up to 5 keV for Cu_3Au and Ag-Pd alloys using transmission electron diffraction. For Cu_3Au an altered layer, enriched with Au, with a thickness of up to 40 Å was found. This was the very first measurement of an altered layer thickness and probably the only one for the next ten years. For the Ag-pd alloys with the high Pd content again a layer enriched with Ag was formed and this enrichment increased with increasing bulk pd content of the alloy. However, the main difficulty in these early measurements was that no reliable method was known for accurate compositionsal analysis of such thin films.

Patterson and Shirn [14], in 1967, studied sputtering of Ni-Cr alloys and found an enrichment of Cr on the surface. As mentioned earlier, they presented a simple analytical model based on different sputtering yields of the components for explaining the observed compositional changes under ion bombardment. With various modifications, this method has been used since then to analyse measured experimental data.

No general predictions on the changes in the surface composition or the total sputtering yields could be made from these early measurements. However, one conclusion that could be made was that during the initial bombardment period a composition change in the target surface and of the sputtered atoms occured, and only at high bombarding fluences the composition of the sputtered deposit became identical to that of the original alloy [14, 31, 32].

Much progress in the investigation of multicomponent sputtering has since been made and there exist numerous publications on the surface chemical modification of alloys as a result of ion bombardment [33-36]. For the case of metal oxides, there have been some studies carried out using various techniques [37-46]. The general result that arises is that metal oxide surfaces lose oxygen as a result of ion bombardment. However most of these reports are only qualitative; in most cases the conclusions were

restricted to yes/no comments (i.e., yes/no to whether surface compositional changes have occured) and some of the results are often contradictory. As a result, the few models that have been proposed [47-50] to account for the ion induced compositional changes to metal oxides are in fierce diagreement with each other and with the experimental findings. Thus there is a need for accurate quantitative data which can lead to a better understanding of the processes initiated by ion bombardment.

At the energies generally used for ion bombardment, which range from several 100 eV to several keV, the depth to which the inert gas ions penetrate the solid is of the order of 10-100 Å [51]. The greater part of the transferred energy is thus absorbed near the primary ion impact (i.e, within a circumference of less than 100 Å). The energy received by the lattice atoms at the inside and surface of the target may exceed by several orders of magnitude the binding energies in molecules. It is thus sufficient to break chemical bonds, as shown by the occurence of high intensity fragment ions in secondary ion mass spectra, and to form new ones. New compounds are most likely to arise through the formation and reorganisation of fragment molecules, but they may also be formed through reaction of the fragments with one another and with neighbouring molecules. The existence of such ion induced reactions is undisputed [41,52,53] especially where high primary currents are used, as is found in ion microprobe [54]. To investigate such ion induced surface compositional changes, XPS is regarded as an ideal surface analysis technique [52,55-58]. Since a surface analysis method is required which, without ion bombardment, provides information that is sufficiently accurate and specific to the bonds. XPS provides binding energy measurement of core electrons in atoms and molecules [59] (due to the so-called chemical shift effect, discussed in detail in chapter 3). It permits non-destructive in-depth analysis and because of its chemical shift effect it is particularly suitable for detecting new compounds, as they are formed during ion bombardment. With XPS the measured intensities are hardly influenced by matrix effects; so quantitative results can be obtained too.

Since sputtering of multicomponent targets is a vast topic, for the purpose of the thesis, this chapter will be restricted to mostly the XPS investigations of binary metal oxides. One of the first XPS measurements on compact oxides consisting of oxide powder or thick oxide layers on metals were presented by Kim et al [60]. They concluded that the chemical specivity of XPS makes it an excellent technique for analysis of ion bombardment induced artefacts. They reported qualitative results for a series of pure metal-oxides after bombardment with 400 eV Ar^+ ions; these data are shown in Table 1.1. They proposed "the free energy of formation" model based on the bulk thermodynamic free energy, $-\Delta G_f^0$, to explain these results. According to this model there exists a correlation between the reactivity of the oxide and its room temperature $-\Delta G_f^0$ value. That is, all oxides with $-\Delta G_f^0$ below 60 kcal/mol were reduced by exposure to Ar^+ ions while those with $-\Delta G_f^0$ above 118 kcal/mol were stable to this exposure. In the case where higher oxides are found to be reduced, the reaction proceeds to a stable oxide with a large negative free energy. For example, with tungsten system, although WO_3 has a $-\Delta G_f^0$ value of -182 kcal/mol, production of WO_2 is favourable through the following scheme:

$$WO_3 \rightarrow WO_2 + 1/2\ O_2 \qquad -\Delta G_f^0 = -64 \text{ kcal/mol}$$

while WO_2 can be reduced to the metal through:

$$WO_2 \rightarrow W + O_2 \qquad -\Delta G_f^0 = -118 \text{ kcal/mol.}$$

Other systems such as PbO_2, MoO_3 and Fe_2O_3 behaves similarly. Systems such as Ta_2O_5, Al_2O_3 and SiO_2 have no stable intermediate form and hence are stable to ion bombardment.

The above model is based on the view that, for the 1 keV argon ion bombardment, a local thermal quasi-equilibrium is present and that the energy needed to reduce the oxide is related to the energy difference between the initial and final state of the system, i.e., when the oxide is at room temperature before and after ion bombardment. The significance of the cut-off energy (60 -120 kcal) is not clear. Kim et al [60] assume that it must be closely associated with the fraction of energy required

Table 1.1.

The standard free energy of formation of oxides and their reduction due to Ar^+ ion bombardment [60].

Sample	$-\Delta^\circ_f$ (kcal/mole)	Reduction observed?
Au_2O_3	-39	Yes
Ag_2O	2.6	Yes
Ag_2O_2	6.4[a]	Yes
PdO	20[a]	Yes
CuO	30	Yes
Cu_2O	35	Yes
IrO_2	40[a]	Yes
PbO	45	Yes
NiO	52	Yes
PbO_2	52	Yes
CdO	54	Yes
FeO	58	Yes
RuO_2	60	Yes
ZnO	76	No
$Ni(OH)_2$	108	No
WO_2	118	Yes
MoO_2	119	No
SnO_2	124	No
MoO_3	162	Yes
Fe_2O_3	177	Yes
WO_3	182	Yes
SiO_2	192	No
Cr_2O_3	250	No
Ti_2O_3	346	No
Al_2O_3	377	No
Ta_2O_5	471	No

a. $-\Delta^\circ_f$

to generate the quasi-equilibrium state and the fraction lost to sputtered surface atoms and to argon species leaving the surface with non-zero kinetic energy.

Other important observations have also been reported in this work by Kim et al [60]. In addition to monitoring the ion-bombardment induced compositional changes they also carried out investigations to observe the dependence of the the thickness of the reduced state with the energy of the incident ion. A layer of several micron thickness of PdO was grown thermally. When subjected to argon ion bombardment, surface enrichment of Pd was observed. The thickness of the Pd layer was then estimated using the intensities obtained by XPS; the results are shown in figure (1.2). At 200 eV, the limiting value for reduction is thought to be near 10 Å (it can be argued that, since the curve does not reach a steady state, whether the value of 10 Å is correct). At 600 eV the layer is nearly 20 Å thick and at 1 keV, the layer is found to be thicker than can be measured with XPS. Kim et al [60] conclude that since the penetration depth of argon ions into a solid at 1 keV is 20 Å, the altered layer thickness is approximately comparable to the penetration depth. They then suggest that these results indicate that the formation of the localised quasi-equilibrium state is mainly due to collisional energy transfer to the oxide lattice. It is also concluded that the role of the bombarding gas is largely to provide a mechanism for equilibration of surface components and only when formation of the oxide is strongly favoured by thermodynamic considerations will chemical reaction with the incident ion take place. This view was proposed since oxides such as IrO_2 and Au_2O_3 showed reduction to metal by O_2^+ ion bombardment.

However, some of the compounds that are thought to be non-reducible according to this theory such as $Ni(OH)_2$ and Ta_2O_5 have since been observed to reduce under ion bombardment (for example McIntyre and Zetaruk [61], Oechsner et al [62]).

Returning to the experimental evidence reported by other investigators, it is found that Ta_2O_5 is perhaps the most frequently studied oxide with respect to ion induced reduction. Nevertheless, the results reported are contradictory. In accordence with the

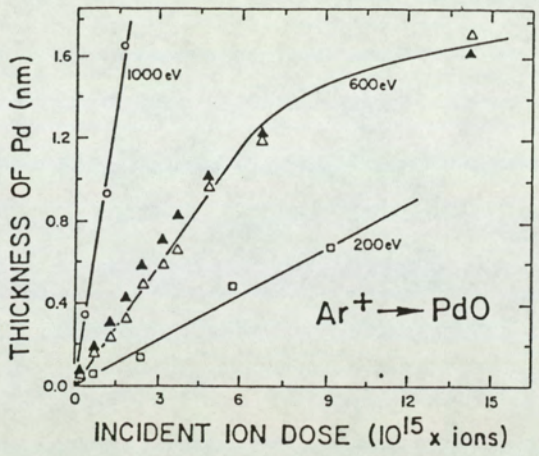

Figure 1.2.

Thickness of Pd overlay on PdO substrate as a function of dose and Ar^+ ion energy. the open and closed triangles show two different methods of converting the XPS signal to thickness [60].

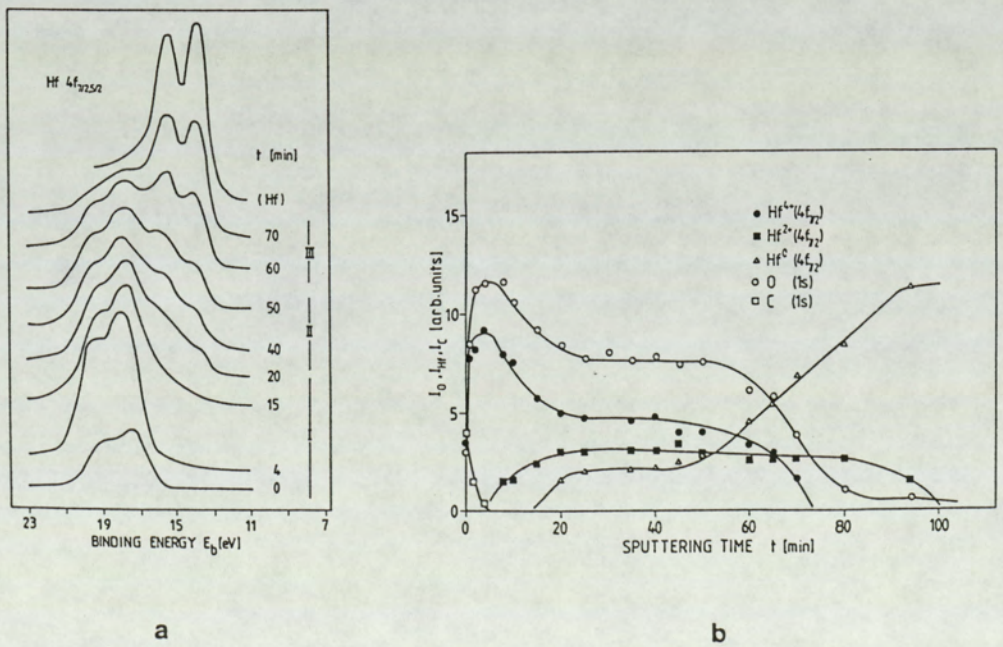

Figure1.3.

a) Hf 4f spectra after different bombardment times (3 keV Ar^+ ions) [66]
b) depth profile with intensity obtained from (a) above

results presented by Kim et al [60], Bispinck et al [63] observed no reduction under 3 keV Ar^+ ion bombardment. XPS measurements of Holm and Storp [52] however showed a reduction of Ta_2O_5 when bombarded with 5 keV Ar^+ ions. This was confirmed by Holloway and Nelson [64]. Measurements by Mathiew and Landolt [37], Taglauer and Heilander [65], and Hofmann and co workers [38,50,66] again agree in Ta_2O_5 decomposition under similar conditions. With higher energy (i.e., 35 keV) ion bombardment , oxygen depletion is also reported using RBS by Murti et al [67].

In spite of the many sputtering experiments for Ta_2O_5 cited above, only those due to Hofmann and Sanz [66] report on the generation of the three different oxidation states: TaO_2, TaO and Ta.

McIntyre and Zetaruk [68] investigated the effect of 3 keV Ar^+ ion bombardment of the oxides α-Fe_2O_3, $NiFe_2O_4$, Fe_3O_4 and FeO respectively using XPS. An ion beam flux of 20 mA/m^2 was incident on the target for ten minutes. They reported for the first three oxides, a reduction to the FeO state. No effect of ion bombardment on FeO was found. Mitchell et al [69] reported for α-Fe_2O_3 sputtered with 2 keV Xe^+ ions additional presence of metallic Fe in the XPS spectra. Brundle et al [70], however, observed that starting with bulk α-Fe_2O_3, they had to sputter for only 50 seconds before detecting a significant FeO (Fe^{II} state) concentration produced by reduction from α-Fe_2O_3 (Fe^{III} state) by Ar^+ beam. A further 370 seconds of sputtering resulted in the depletion of Fe^{III} from the escape depth (i.e., the depth from which photoelectrons can escape) leaving a mixture of Fe^{III}, Fe^{II} and metallic Fe. These results are in agreement with those due to Mills and Sullivan [53] and others [71,72]. This type of reduction behavior is also reported for Co_3O_4 by Chung et al [71], which is found to reduce to CoO and eventually to Co such that at the steady state all three states are present.

Investigations carried out by Holm and Storp [52] on the oxides MoO_3, WO_3, Nb_2O_5, Ta_2O_5, TiO_2, ZrO_2, SiO_2 and Bi_2O_3 showed a reduction due to 5 keV Ar+ ion bombardment. The samples were oxide layers on the corresponding metal substrate.

These results are only qualitative and information on which suboxides exist in the steady state was not given.

For the oxide Nb_2O_5, Murti and Kelly [73] observed a reduction to NbO with 35 keV kr^+ bombardment, and measurements by Karulker [74] showed that in fact all niobium oxides (i.e., Nb_2O_5, NbO_2 and NbO) were reduced by Ar+ bombardment, which is in agreement with work due to Hofmann and Sanz [66] and Brown et al [75].

A depletion of oxygen on the ion bombarded surface of TiO_2 was reported by Thomas [76] using AES. In a reflected electron diffraction investigation undertaken by Parker and Kelly [39], reduction to Ti_2O_3 was reported after 30 keV Kr+ bombardment. They suggested that the stoichiometry change to Ti_2O_3 was in part collisional and in part thermally activated and occured to a depth which is similar to the mean ion range. Contrary to the latter results, Hofmann and Sanz [66] reported that Ti_2O_3 was the first reduction product which was followed by TiO.

In accordence with the results of Holm and Storp [52], other workers [77] also reported weak reduction of SiO_2 due to ion bombardment. A direct reduction was not spectrally detected by Hofmann's group [78,79], although small increases (~1 eV) in the XPS linewidths of the Si 2p and the O Is peaks were observed. This peak broadening was qualitatively attributed to the breaking and rearrangement of SiO bonds in the glass network. It was speculated that the basic silicon environment was not changed within the ability to detect an elemental Si peak.

The experimental reports in the current literature so far (except those due to Hofmann and Sanz [66] and the published work from this thesis [80,81]) are only qualitative. Since, previous to this thesis, the only semi-quatitative work on the compositional change measurements of transition metal oxides are due to reference [66], its results are summarised here to enable comparisons to be made with this work. In addition to the Ta_2O_5, Nb_2O_5 and TiO_2 Hofmann and Sanz [66] also carried out investigations on ZrO_2, HfO_2 and Al_2O_3. They obtained XPS depth profiles by sputtering with 3 keV Ar^+ ion beam. With the exception of Al_2O_3, all oxides showed a

gradual build-up of an ion induced oxygen depletion layer. They calculated the thickness of the depletion layer using the measured values of the XPS intensities at the steady state. As an example of the typical measured depth profiles, the HfO_2 depth profile is shown in figure (1.3a, 1.3b). Three distinct regions were defined, characterised by a transition (I) to the stationary state (II) and the to the interface region (III). The overall results are summarised in Table (1.2). These results however can not account for other investigating parameters that are essential for full quantification of the reduction behaviour, such as a threshold current density for compositional change, a dependence on the bombarding ion energy, a dependence on the charge of the incident beam etc.

From the above, it is seen that even with all the contradictions concerning particular oxides, the general trend for the effect of ion bombardment is that preferential sputtering of oxygen takes place, leading to an oxygen depleted layer which has a composition different to the bulk composition at steady state. The questions that arises next is that "what causes this oxygen depletion and the changed surface chemical composition?" , also "why do some oxides show compositional change and others do not?". The general concensus now in the current literature is that the effects which can be responsible for the compositional changes are the mass effect and the bonding effect. The models which are proposed to account for these effects will be described below:

1.5.1: Models predicting surface composition changes

a) The mass effect

The collision cascade set up in a multicomponent target initiated by ion bombardment will be composed of different mass atoms. The momentum and energy will thus be distributed differently to each component resulting in different ejection probabilities for each atom species. This can, in general, cause preferential sputtering of the lighter component and therefore surface enrichment of the heavier component.

Considering the linear cascade regime, the following equation has been derived

Table 1.2.

The results of Hoffmann and Sanz [67], showing ion bombardment induced composition changes for 3keV Ar^+ ions.

oxide	decomposition product	mean comp. (at.%)	oxygen loss (at.%)	d (nm)
Al_2O_3	-	- -	-	
TiO_2	$Ti_2O_3 + TiO$	$X_{Ti} = 43$	10	1.8±0.6
ZrO_2	$ZrO + Zr$	$X_{Zr} = 62$	24	1.3±0.5
HfO_2	$HfO + Hf$	$X_{Hf} = 62$	24	2.0±0.6
Nb_2O_5	$NbO_2 + NbO$	$X_{Nb} = 47$	18	2.2±0.7
Ta_2O_5	$TaO_2 + TaO + Ta$	$X_{Ta} = 50$	21	2.5±0.7

by Sigmund [1] (the derivation of this equation is given in chapter 2):

$$Y_A^c/Y_B^c = \{M_B / M_A\}^{2m} . \{U_B / U_A\}^{1-2m} \quad \ldots. (1.6)$$

for a binary alloy AB, where Y^c, M and U denote the component sputtering yield, mass and surface binding energies respectively of the components A and B. For the linear cascade regime the constant 'm' lies in the range 0 to 0.2. Thus, neglecting the surface binding energies, a dependency of the sputtering yield on mass of $\{M_B / M_A\}^{2m}$ is given.

In a different model by Haff [82], which assumes equipartition of energy between the components, an enrichenment in the heavier constituent was also predicted. Haff obtained a $\{M_B / M_A\}^{1/4}$ dependence of the component sputter yield ratio.

This mass effect has been suggested as an explanation for the oxygen depletion since oxygen is the lighter component in most oxides [83, 84, 85]. However, counter examples also exist which do not show metal enrichment, for example the results for PbO for Kr^+ and Xe^+ bombardment [60]. Also, BeO [86] which should show oxygen enrichment ($M_O > M_{Be}$), cannot be explained by the mass effects, especially when weak Be enrichment was observed. In a review by Kelly [49] on the subject of applicability of mass effect and chemical bonding, it is stated that the correlation with mass is very poor. This is based on his claim that systems such as CoO, FeO, NbO and TiO appear not to lose oxygen. The bonding effect is suggested to be the dominant effect which manifests as the surface binding energy. Kelly's [49] claim for the above oxides not to lose oxygen has since been proved to be incorrect [71,80].

b) Bonding effects

Chemical bonding, reflected explicitly as the surface binding energy ,U, has already been considered in Sigmund's equation (1.6) given above. Thus, in the linear collision regime an approximate (1/U) relationship has been predicted. The differences in surface binding energy of the constituents will then result in preferential emission of the component with the lower binding energy and enrichment of the component with

higher binding energy.

An identification of U with the heat of atomization, ΔH^a, has been made by Kelly [49,87] for the case of oxides. For example in the case of MgO, it relates to the stoichiometric removal of the neutral atoms such that:

$$MgO\ (solid) = Mg\ (gas) + O\ (gas)\ ,$$

then the energy change per atom being an indication of the binding energy:

$$U_{Mg} = U_O = \Delta H_{MgO}{}^a = 1/2\ [-\Delta H^f_{MgO} + \Delta H^a_{Mg} + \Delta H^a_O]\ .$$

Here ΔH^f_{MgO} is the heat of formation of the and ΔH^a_O is equivalent to ΔH^f_O. In the above definition, the effects due to surface vacancy formation has been neglected. Kelly [87] also identifies the total and partial heats of atomization. The total heat of atomization is given by the above equation and the partial heat of atomization relates to the final reduced species at the bombarded surface (this is fully discussed later in Chapter 6). The important conclusion Kelly [87] proposes is that an oxide will reduce if the partial heat of atomization is less than the total heat of atomization. The suboxide or component with the lowest partial heat of atomization will be accumulated at the bombarded surface.

In a recent review paper by Kelly [88], the importance of the surface binding energy effects to oxide sputtering, however, has been questioned. His view is that, as with the role of mass effects, the problem is the lack of universality (i.e., "why do Al_2O_3, SiO_2 and UO_2 not show extensive oxygen loss?").

1.5.2: Comparisons of experimental data with theoretical predictions

Assuming linear cascade regime of sputtering and restricting considerations to the mass effect, Hofmann and Sanz [50] compared their experimental to a 'crude approximation' of Sigmunds equation (1.6) given by:

$$(X_{Me}/X_O)_s \sim (X_{Me}/X_O)_b \cdot (M_{Me}/M_O)^{1/2} \qquad \ldots\ (1.7)$$

where X is the molar fraction of the i^{th} component; the suffix 's' stands for surface and 'b' for bulk (the 2m value in eqn (1.6) is taken to be 0.5). Their comparisons of the

calculated value of from the above equation with the experimental value is shown in figure (1.4). From this result, they argued that even though equation (1.7) is a very crude approximation, the correlation obtained between the experimental and calculated values indicates that the effect of surface binding energy is of secondary importance compared to the mass ratio factor.

In a more recent paper by Malherbe, Hofmann and Sanz [47], comparisons are made between the experimental data previously published [50,66,17] and calculated values for $[(X_{Me}/X_O)_s/(X_{Me}/X_O)_b]$ using Sigmund's equation (1.6) for the cases when:

i. $U_{Me} = U_O$, $2m = 0.25$;

ii. $M_{Me} = M_O$, $2m = 0$.

These are shown in figures (1.5) and (1.6) respectively. For case (ii), they define U_O in terms of the 'metal-oxygen' bond energy, the dissociation energy of the oxygen molecule and the electronegativity values of the metal and oxygen atoms. Also, U_M is defined in terms of the sublimation energy of the metal and the electronegativity values. These definitions are fully discussed Chapter 6 on theoretical considerations. From the two figures (1.5) and (1.6), they concluded that both mass and binding energy effects need to be considered in attempting to explain ion bombardment induced surface compositional changes. Next, they compared the experimental and calculated values of $[(X_{Me}/X_O)_s/(X_{Me}/X_O)_b]$ taking both the mass effect and surface binding energy into account and taking 2m to be equal to 0.33. This is shown in figure (1.7); a much better correlation between the experimental data and calculated values can be seen. Malherbe et al [47] concluded that a thorough test of their proposed model is precluded by the lack of reliable data on the oxygen loss.

These models, however, do not take into account of other parameters which can influence the extent of the surface chemical damage; the parameters include the effect of the bombarding dose, the mass of the projectile, charge of the projectile, temperature of the target during bombardment etc. Few investigations [25,75,89] have been carried

$$(X_{Me}/X_O)_s \cong (X_{Me}/X_O)_b \cdot (M_{Me}/M_O)^{1/2}$$

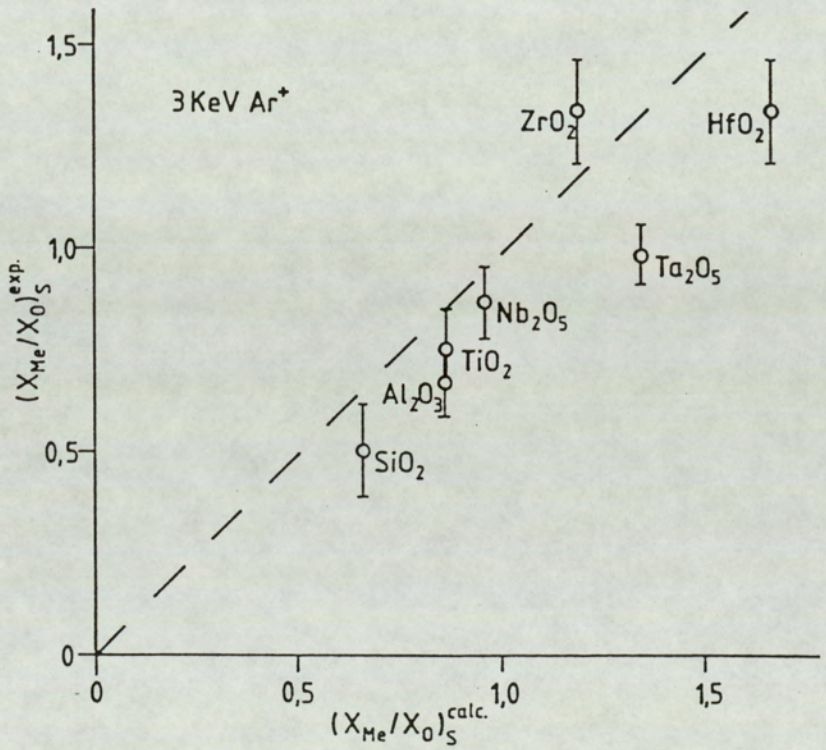

Figure 1.4.
Experimentally determined composition of the altered surface layer as a function of the calculated values given by equation 1.7, as above [50].

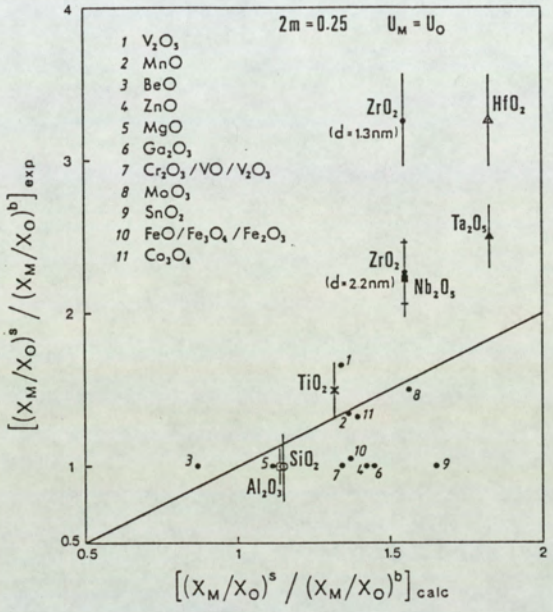

Figure 1.5.

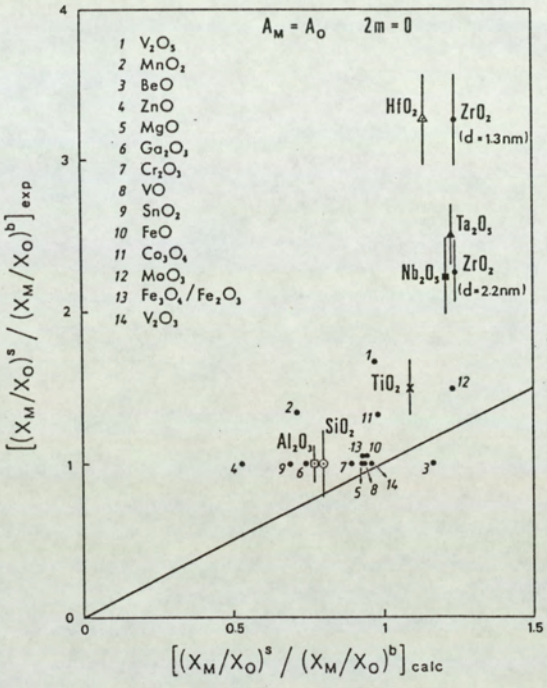

Figure 1.6.

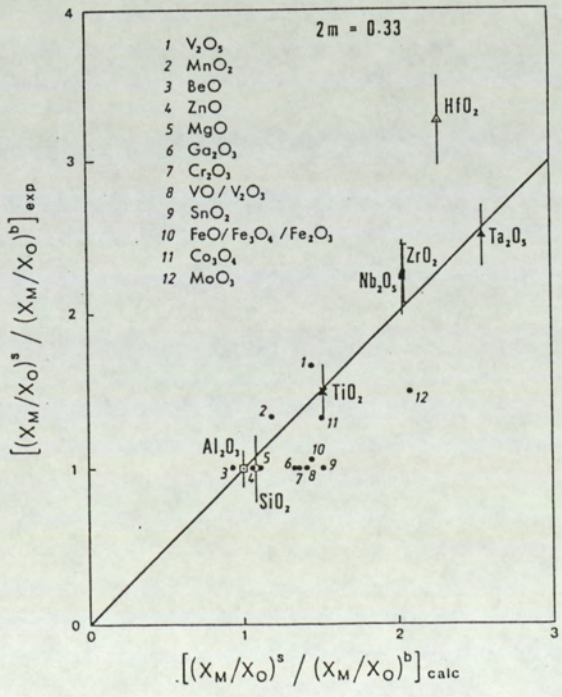

Figure 1.7.

Figures 1.5., 1.6 and 1.7.
The experimentally determined surface composition ratios as a function of the predicted ratio, [47].

out which indicate that some of these parameters attribute to the extent of the damage. These will be outlined in the next section.

1.5.3: Influence of incident beam parameters on the chemical damage

a) influence of the ion beam current density:

The time needed to reach steady state during bombardment has been observed to be dependent on the current density or the fluence[14, 17,89]. However, very few observations are reported for the current density dependency of the extent of surface chemical damage. Storp and Holm [89] reported that a net rate of reduction of bombarded MoO_3 depended on the current density. After the application of the same dose with a lower ion current density but a longer exposure time, the reduction effect was qualitatively claimed to be less marked. Thus a current density rather than dose dependency is claimed, although no quantification in terms of the surface compositional concentrations had been made.

In an investigation carried out by Langell [90] on the preferential sputtering of NiO and CoO single crystals, a dose dependency was observed for the oxygen to metal concentration ratio at the surface. In addition this study included the temperature measurements of the target. Langell's [90] results for NiO and CoO are shown in figures (1.8), (1.9) and (1.10).

b) Influence of ion beam energy

The only known reports so far for oxides of the surface compositional change variation with the beam energy are those due to Sanz and Hofmann [25] and Karulkar [74]. In the investigation by Sanz and Hofmann [25] on Ta_2O_5 and Nb_2O_5 using AES, the steady state surface molar concentration of the metal component is estimated for energies up to 5 keV. The results obtained showed that for energies above 2 keV, the surface concentration of the metal is independent of the energy, and a very small change in this concentration is observed between the primary energies of 1 and 2 keV (these results are shown in figure (1.11a,b)). It should be understood that these metal concentrations are only an estimation since AES does not give chemically specific data.

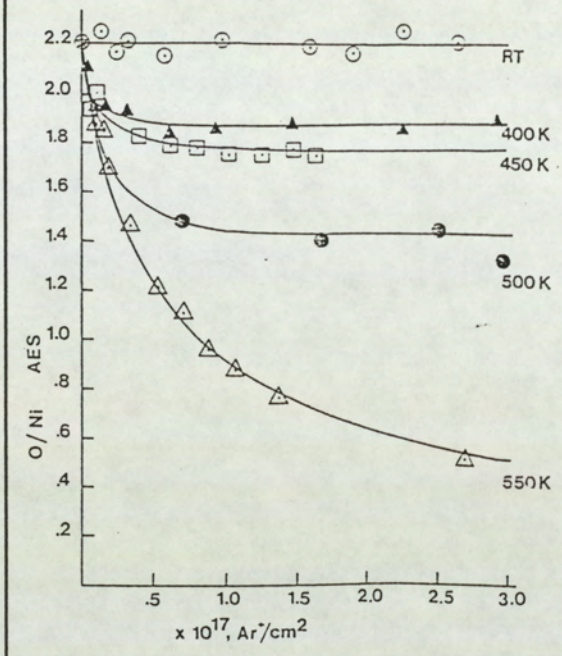

Figure 1.8.
NiO (100) surface oxygen concentration in terms of O/Ni AES as a function of ion fluence [90].

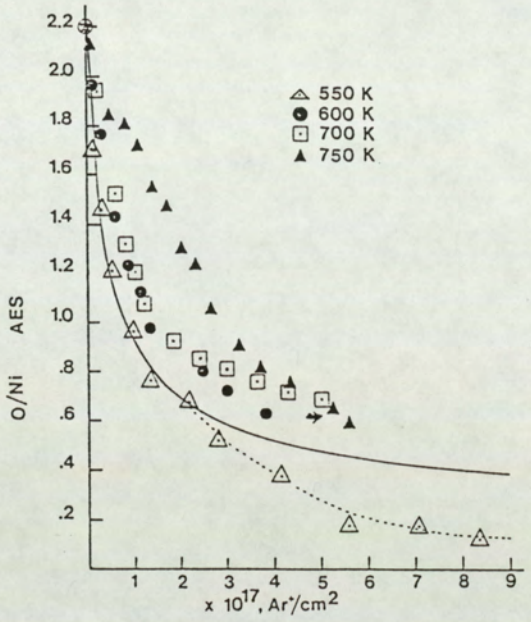

Figure 1.9.
As for figure 1.8, for higher temperature range [90].

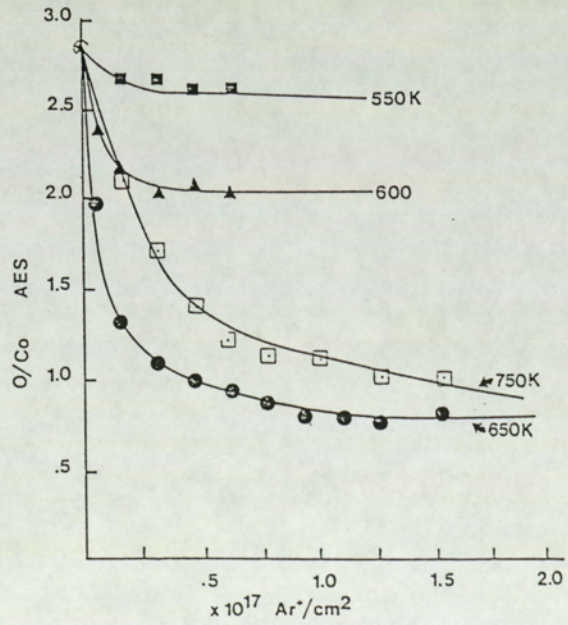

Figure 1.10.
CoO (100) surface oxygen concentration in terms of O/Co AES as a function of ion fluence [90].

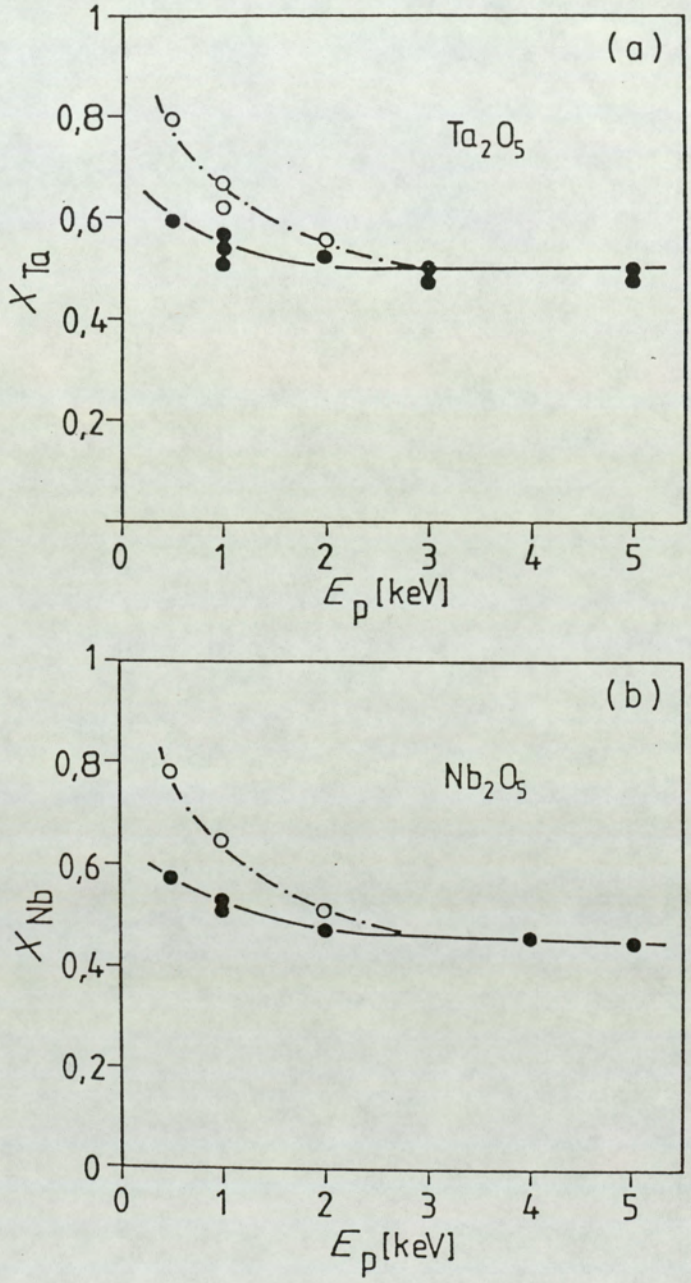

Figure 1.11.
Steady state surface composition in molar fractions of the metal, X_{Me}, as a function of the primary ion energy E_p [25].

This can only be carried out with a detailed XPS study.

Karulkar [74] also report an increase in Nb_2O_5 chemical reduction when the beam energy is decreased from 2 keV to 0.5 keV.

c) Influence of the charge of the projectile

The investigations by Brown et al [75] and the published work from this thesis [81] (details of the latter will be given in Chapter 5) report on the influence of the projectile charge. Brown et al [75] compared, using secondary ion mass spectroscopy, the surface damage caused on niobium pentoxide with equivalent ion and atom bombardment. Significantly less damage for the atom bombardment was found.

1.5.4: Sputtering yield measurements of oxides

The sputtering yield of an oxide, similar to an alloy or a metal, is defined as the number of emitted atoms per incident ions. Some yield measurements for oxides and its dependence on the ion energy has been carried out, however yield dependence measurements have not yet been performed. Betz and Wehner [17] have compiled a summary of the yield measurements by various investigators and concluded that the sputtering yields of oxides are in most cases similar to or even higher than those of the corresponding metals. As an example, the sputterring yield as a function of the ion energy is shown for the oxides Nb_2O_5 and WO_3 in figures (1.12) and (1.13). These figures are obtained from the compilations of Betz and Wehner [17].

1.6: Concluding remarks

There is disagreement in the few models that have been proposed to predict the bombardment induced surface compositional changes of oxides. This is mainly due to the reasoning that there exist very few quantitative experimental data for the surface chemical change and the qualitative studies of the compositional changes are also contradictory. It is felt that the contradictions in the qualitative studies have arisen to some extent due to the analysis techniques used. That is, the technique being not

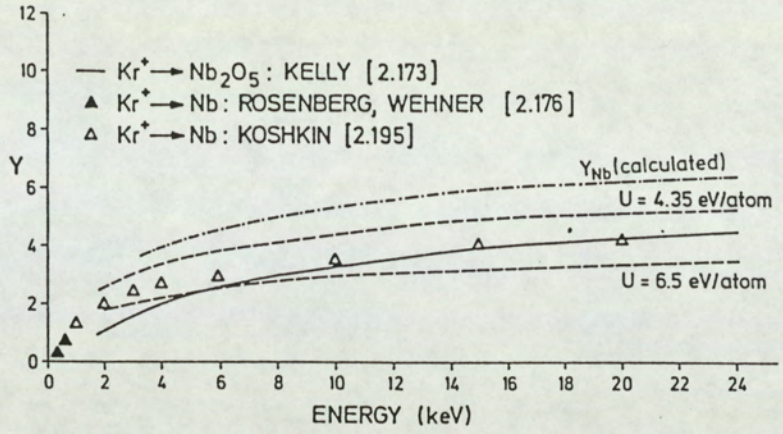

Figure 1.12.

Sputtering yield for Cr^+ bombardment of Nb_2O_5 thin film as a function of ion energy, determined by interference colour change measurements and by weight loss techniques. The dashed line shows calculated values due to Sigmund [1]. This figure is obtained from the compilation by Betz and Wehner [17].

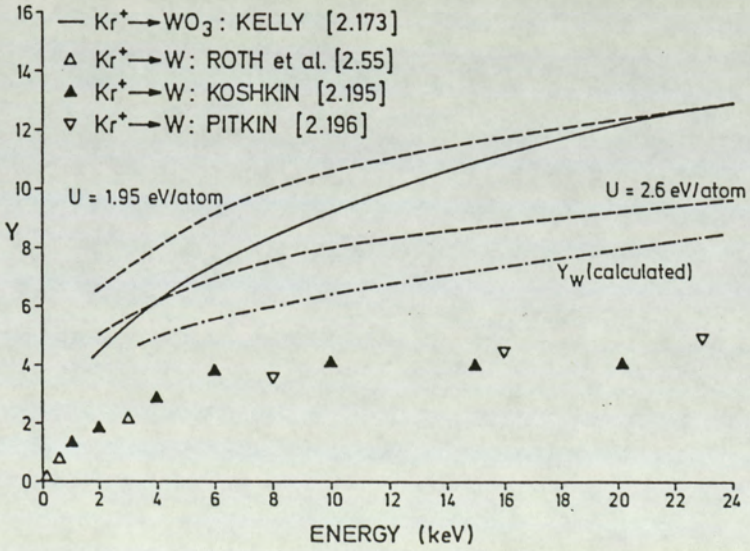

Figure 1.13.

As figure 1.12 for the case of WO_3.

particularly suitable for detecting the compositional changes in the top two or three atomic layers or not being chemically sensitive enough.

The work carried out in this thesis, accurately detemines the XPS binding energies associated with each chemical state using peak fitting methods. For a number of oxides the surface compositional changes have been quantified, in terms of all the reduced states, the bombardment time required to reach steady state and the exact extent of the chemical change after each bombardment time and at the steady state. The extent of the surface chemical change is also quantified as a function of beam parameters such as beam energy, current density, dose and charge. These results show that none of the existing models can explain the bombardment induced surface artefacts in oxides.

CHAPTER 2: Background to sputtering mechanism: Sigmund's theory

2.1: Introduction

Sputtering, which is the erosion of a solid surface by energetic particle bombardment, was first observed in gas discharges in the middle of the last century. However this phenomenon is now known universally. The majority of the sputtering investigations had been confined to the case for single element targets, while systematic research involving the sputtering of multicomponent targets has become important within the last twenty years. It is necessary here to be briefly familiarised with Sigmund's [1] theory of single element sputtering because mechanisms for multicomponent target sputtering, as given by Sigmund and others [1,47,49], are based on this.

Figure (2.1) shows results of Monte Carlo calculations [89] for 4 keV Ar^+ ions incident on a target of randomly distributed Cu atoms. It is clearly illustrated that the result of the incident ion hitting the surface is a "collision cascade" and sputtering occurs because the surface intersects this cascade. The sputtered particles generally have only small kinetic energies, with a distribution peaking at less than 10 eV. Because the sputtering effect is dominated by slow 'randomised' cascade of recoil atoms, it is possible to develope a semi-empirical analytical theory for this essentially statistical process. In the following, an account of some basic definitions and results incorporated in Sigmund's [1] linear cascade theory is given.

2.2: Sigmund's theory of sputtering for elemental targets

A primary quantity of interest in the cascade theory is the expected number of atoms perticipating in a cascade. Firstly, consider the cascade created in the target by the action of a single projectile. Let $n(E, E_0)$ describe the mean number of atoms set in motion with an initial energy greater than some value, say E_0, in a cascade. The cascade is initiated by a primary ion or recoil of energy E ($E>E_0$). Assuming elastic

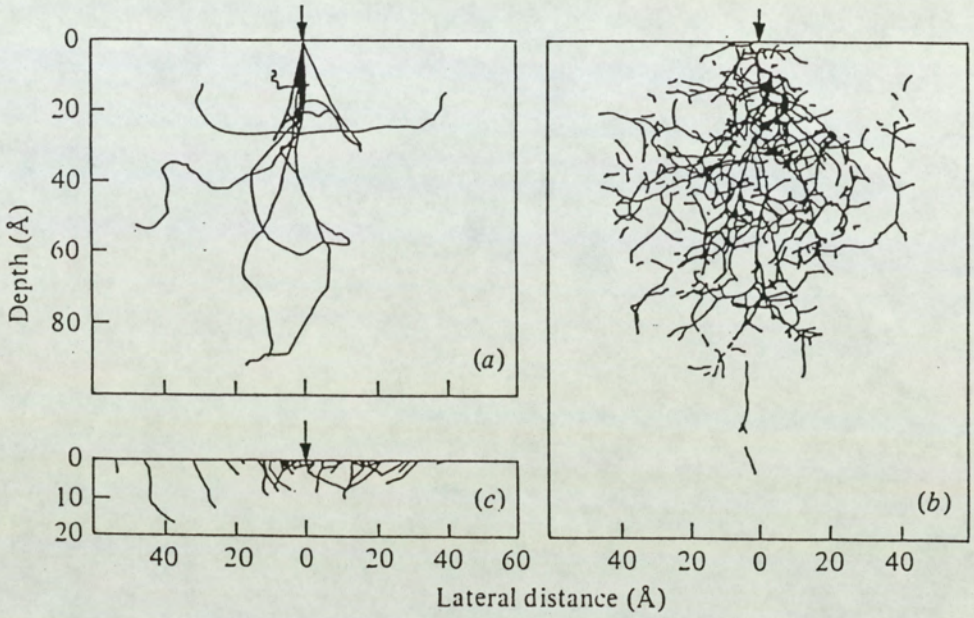

Figure 2.1.

Results of Monte Carlo calculations [89] for 4keV Ar^+ ions on a Cu target.
a) 10 incident particle trajectories
b) the resulting recoil distribution
c) the sputtering events resulting from 15 incident ions

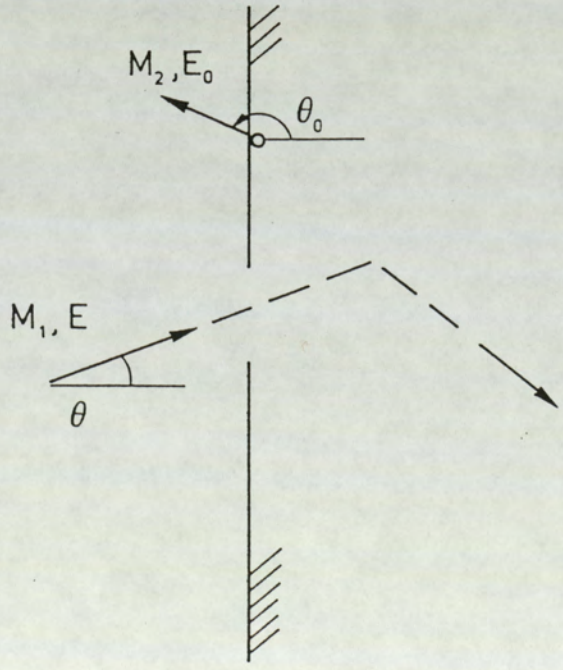

Figure 2.2.

Geometry for backscatter from a target with a plane surface [1].

collisions only and ignoring all binding forces between target atoms, Sigmund defines the following equation:

$$n(E, E_0) \sim \Gamma_m(E/E_0) \text{ for } \gamma E >> E_0. \quad \ldots. (2.1)$$

where γE is the maximum energy that can be transferred in a binary elastic collision; i.e,

$$\gamma = \{4M_1M_2 / (M_1+M_2)^2\} \quad [M_1 = \text{ion mass}; M_2 = \text{target atom mass}]$$

and Γ_m is a dimensionless function of m for power potentials; m characterises the scattering cross section. The values of m ranges between 1 (for high energies) and zero (for low energies).

Next, the effect of electronic stopping is taken into account such that the amount of energy available for creation of recoil is given by:

$$\nu(E) = E - \eta(E) \quad \ldots. (2.2)$$

$\eta(E)$ is the average energy taken up by electronic excitation during the whole slowing down process. Using the equations (2.1) and (2.2), the mean number of atoms recoiling, $F(E, E_0)dE_0$, into a given energy interval (E_0, dE_0) is given by differentiation; hence:

$$F(E, E_0) \sim \Gamma_m \nu(E) / E_0^2 \quad \text{for } E>>E_0 \quad \ldots. (2.3)$$

$F(E, E_0)$ is termed the "recoil density". Since it is thought that within the linear cascade the recoils of higher generations dominate, the initial direction of motion of the incident particle is immaterial and the distribution in the solid angle Ω_0 is isotropic. Thus:

$$F(E,E_0,\Omega_0)dE_0d^2\Omega_0 \sim \Gamma_m\{\nu(E)/E_0^2\}dE_0\{d^2\Omega_0/4\pi\} \quad \text{for } \gamma E>>E_0$$

$$\ldots. (2.4)$$

It is then necessary to know the distribution in space of the recoiling atoms. According to equations (2.1) and (2.4) the number of recoil atoms are proportional to the available energy. Hence, it is asserted that the spreading of the recoiling atoms in space scales according to the spreading of energy. Thus if the density of deposited energy, $F_D(E,\Omega,\mathbf{r})$, for an ion begining to slow down at $\mathbf{r}=0$ is defined such that:

$$\int d^3r\, F_D(E,\Omega,\mathbf{r}) = \nu(E) \quad \ldots. (2.5)$$

where Ω is the unit vector in the initial direction of motion, r equals the distance of colliding atoms and **r** is the vector distance of an ion in a solid from the entering point. Here energy is considered 'deposited' when being shared among the atoms down to the very end of linear energy dissipation (i.e, when spike regime rather than cascade regime characterises the state of motion). Next, it is assumed that the recoil atoms are generated according to the distribution:

$$F(E,\Omega,E_0,\Omega_0,\mathbf{r})dE_0d^2\Omega_0d^3r \sim \Gamma_m \{F_D(E,\Omega,\mathbf{r})/E_0^2\}dE_0[\{d^2\Omega_0/4\pi\}d^3r] \quad \ldots. (2.6)$$

The determination of $F_D(E,\Omega,\mathbf{r})$ is complex; however for comparisons purposes with experimental data (i.e, depth profiles), consideration of the deposited energy in the x-direction is adequate. The x-direction being the target surface normal to which the beam direction,Ω, makes an angle θ.; i.e,

$$F_D(E,\theta,x) \equiv \int_{-\infty}^{\infty} dy \int_{-\infty}^{\infty} dz\, F_D(E,\Omega,\mathbf{r}) \quad \ldots. (2.7)$$

Secondly, the flux of recoil atoms initiated by a number of projectiles is evaluated; (for convenience, the presence of the target surface is disregarded initially in the evaluation of the flux of recoil atoms and the target is considered to be an infinite medium). A source supplying φ projectiles per unit time of initial energy E is considered. Let $G(E,E_0)dE_0$ be the mean number of atoms moving at any time with energy (E_0,dE_0), then:

$$G(E,E_0)dE_0 = \varphi\, n(E,E_0)\, dt_0 \quad \ldots. (2.8)$$

where dt_0 is the mean time needed by a recoil atom to slow down from energy (E_0+dE_0) to E_0 and can be expressed as:

$$dt_0 = \{dE_0 / (|dE_0/dt_0|)\} = \{dE_0 / (v_0\, |dE_0/dx|)\} \quad \ldots. (2.9)$$

v_0 is the velocity of a target atom of energy E_0. Substituting equation (2.9) into (2.8):

$$G(E,E_0) = \{\varphi n(E,E_0) / v_0\, |dE_0/dx|\}$$

$$= \varphi\, E_0 / v_0\, |dE_0/dx| \,.\, F(E,E_0) \quad \ldots. (2.10)$$

since from equations (2.1) and (2.3), it is seen that $n(E,E_0) = E_0.F(E,E_0)$. Similar arguments leading from equation (2.3) to (2.6) also apply to equation (2.10), thus giving a mean number:

$$\varphi\Gamma_m \{F_D(E,\Omega,\mathbf{r}) / E_0 v_0 |dE_0/dx|\} dE_0 \{d^2\Omega_0/4\pi\} d^3r \quad .... (2.11)$$

of atoms with energy (E_0,dE_0) moving in the direction $(\Omega_0,d^2\Omega_0)$ in the volume $(\mathbf{r},d^3r)$ if there is a source at $\mathbf{r}=0$ supplying primaries per unit time with energy E and direction Ω. Multiplication of equation (2.11) with $v_0=v_0\Omega_0$ gives the current density of target atoms:

$$\varphi F_D(E,\Omega,\mathbf{r}) \{\Gamma_m dE_0 / E_0|dE_0/dx|\} \{\Omega_0 d^2\Omega_0/4\pi\} \quad .... (2.12)$$

which is differential in E_0 and Ω_0. This equation then serves as a starting point for evaluation of the sputtering yield.

Thirdly, the intention is to embed a target surface in the infinite medium and evaluate the flux through it, taking consideration of the surface binding forces. To achieve this, an ion of energy E impinging at an angle θ onto a plane surface is considered taking the x-direction along the inward surface normal (figure 2.2). Now, the lateral distribution of sputtered flux becomes of secondary interest; the parameter of importance is the outward current of target atoms through the surface plane at x equals zero. This outward backsputtered current is given by:

$$J(E_0,\Omega_0)dE_0d^2\Omega_0 = \varphi F_D(E,\theta,0) \, . \, \{\Gamma_m dE_0 / E_0|dE_0/dx|\} \, |\cos\theta_0| \, \{d^2\Omega/4\pi\} \quad .... (2.13)$$

θ_0 is the angle between Ω_0 and the surface normal. (Note that there is a typical artifact in the linear cascade theory which occurs at $E_0=0$ when equation (2.13) has a divergence. This cannot be real since the number of moving atoms cannot be infinite in a cascade of finite dimensions.)

Let $P(E_0,\theta_0)$ denote the probability for an atom to escape from the surface. The sputtering yield, Y, is then obtained by integrating over E_0 and θ_0 and dividing this sputtered current by the incident current, φ. Thus:

$$Y = \Lambda F_D(E,\theta,0) \quad .... (2.14)$$

where Λ, the material constant, is given by:

$$\Lambda = (\Gamma_m/2) \int (dE_0 / E_0 |dE_0/dx|) \int d(\cos\theta_0) |\cos\theta_0| P(E_0,\theta_0)$$

.... (2.15)

Equation (2.15) is simplified using the following:

i. Note that dE_0/dx is related to the nuclear stopping cross section, $S_n(E)$, such that:

$$dE/dx = N.S_n(E) \quad \text{.... (2.15a)}$$

where N is the density of atoms. S(E) is defined as:

$$S_n(E) = 1/(1-m)\, C_m \gamma^{1-m} E^{1-2m} \quad \text{.... (2.15b)}$$

C_m is the cross-section constant for power potentials and γ has already been defined in equation (2.1).

ii. Also, the simplest model for surface binding of a metal is based on a planar surface barrier, U_0, in which case:

$$P(E_0,\theta_0) = 1 \text{ when } (E_0 \cos^2\theta_0 > U_0).$$

$$= 0 \text{ when } (E_0 \cos^2\theta_0 < U_0). \quad \text{.... (2.15c)}$$

iii. Substituting equations (2.15a,b,c) into (2.15) and noting that knock-on collisions undergone by recoil atoms are equal mass events and hence $\gamma=1$, the following equation for the material constant is obtained:

$$\Lambda = \{\Gamma_m / 8(1-2m)\}. \{1 / NC_m U_0^{1-2m}\} \quad \text{.... (2.16)}$$

2.3: Sigmund's theory of sputtering for multicomponent targets

This theory is an extension to the theory of sputtering for elemental targets [1] and strictly speaking it accounts for alloys only. From a theoretical point of view, Sigmund argues that it is convenient to distinguish between 'primary' and 'secondary' effects. Primary effects comprise the physics of an individual sputtering event on a target with a given composition. Secondary effects include the changes in target composition caused by prolonged bombardment.

a) Primary effects

The primary sputtering events are assumed for the case of an homogeneous alloy.

Sigmund extended his theory for that of the single element targets to yield the following generalisation for the outward current, $J_i dE_o d^2\Omega_o$, of target atoms of type i (i=1,2):

$$J_i(E_o,\Omega_o = \{G_i/(G)_i\}\ \{\varphi F_D(E,\theta,0)\}\ \{\Gamma_{m_i}/E_o|(dE_o/dx)_i|\}\ \{|\cos\theta_o|/4\pi\} \quad \ldots. (2.17)$$

where, $F_D(E,\theta,0)$ is the energy deposited per unit depth at the alloy surface. $(dE_o/dx)_i$ is the stopping power of an i-atom in an elemental i-target. Also, m_i is the cross-section exponent m that is most appropriate to characterise the i^{th} atom at energy E_o. (G_i) represents the flux function (previously defined by equation (2.8)) for i-atoms in the elemental i-target, whereas G_i defines that for the i-atoms in the binary alloy. Following similar arguments as that given for the single element sputtering, Sigmund obtains the result for the partial sputtering yield, Y_i, of the i-th component in the alloy to be:

$$Y_i = c_i \Lambda_i' F_D(E,\theta,0) \quad i=1,2 \quad \ldots. (2.18a)$$

c_i represents the respective atomic concentrations and Λ_i' is given by:

$$\Lambda_i' = \{(U_0)_i/U_{0i}\}^{1-2m} \ .\ \{1/c_i\} \ .\ \{G_i/(G)_i\} \quad \ldots. (2.18b)$$

again, $(U_0)_i$ is the surface binding energy U_0 in the elemental i-target and U_{0i} is that for the i-atom in the alloy.

Next, a simple relationship for the yield ratio, Y_1/Y_2, is found by substituting equations (2.14, 2.16) into (2.18a, b) which leads to the following:

$$Y_1/Y_2 = \{G_1(E_0)\ (dE_0/dx)_1\ /\ G_2(E_0)\ (dE_0/dx)_2\}.\{U_{02}^{1-2m_1}\ /\ U_{01}^{1-2m_2}\} \quad \ldots. (2.19)$$

As defined before, E_0 is an arbitrary energy << E.

Sigmund states that equation (2.19) can also be written in the following form:

$$Y_1/Y_2 = \{c_1\ /\ c_2\}.\ \{S_{21}(U_{02})\ /\ S_{12}(U_{01})\} \quad \ldots. (2.20)$$

where S_{ij} is the stopping cross section for an i-th atom hitting j-th atom (defined similarly by eqn. (2.15b)). Taking $m_1=m_2$, and substituting equation for S_{ij} in equation (2.20) the following equation can be obtained:

$$Y_1/Y_2 = \{c_1\ /\ c_2\}\ .\ \{M_2\ /\ M_1\}^{2m}\ .\ \{U_{02}\ /\ U_{01}\}^{1-2m} \quad \ldots.(2.21)$$

Next, the "secondary effects" which include the changes in target composition caused by prolonged bombardment are considered.

b) Secondary effects

During ion bombardment, the composition profile changes near the target surface as a consequence of preferential sputtering. Thus, the contribution of the enriched component to the sputter yield is expected to increase after prolonged bombardment until the composition of the sputtered flux reflects that of the bulk target; which normally occurs after sputtering a layer a few times the depth from which the sputtered atoms emerge. The composition of the surface layer of thickness equivalent to the depth from which the sputtered atoms emerge should then be given by:

$$(c_1/c_2)_{surf} = (c_1/c_2)_{bulk} \cdot \{(Y_2/c_2) / (Y_1/c_1)\} \quad \ldots. (2.22)$$

the second factor on the right hand side of equation (2.22) is given by equation (2.21).

The above equations (2.22, 2.21) thus forms the basis for the mechanism of preferential sputtering of binary compounds as defined by the linear cascade theory.

CHAPTER 3: Background to X-ray Photoelectron Spectroscopy

3.1: Introduction

In this investigation, X-ray photoelectron spectroscopy (XPS) has been used to measure the differences in surface chemical states of the metal oxide samples before particle bombardment and after successive periods of bombardment. XPS provides an accurate and simple means of determining the binding energies of electrons in atoms and molecules.

XPS has its origins in the investigations of the photo-electric effect. The external photoelectric effect was first discovered by Hertz in 1887 and the principle of X-ray photoelectron spectroscopy was conceived as early as in 1914 by Robinson, who continued this work for approximately two decades [92]. However, the poor resolution of electron spectrometers at that time prevented the extraction of much of the information contained in the photoelectron spectra. It was not until high resolution electron spectrometers were available that the method could yield unique information of the energy distribution of electrons in matter; the first high resolution photoelectron spectra being published in 1957 [93]. The begining of XPS also corresponds to the development of ultra high vacuum systems. These developments in instrumentation together with an extensive survey of experimental observations and their theoretical interpretation were carried out by Siegbahn and his associates in Upsala, Sweden and are reviewed in two monographs [94,95]. More recent developments in electron spectroscopy for atoms, molecules and condensed matter have also been described by Siegbahn [96].

One aspect that was apparent very early in the development of XPS was its surface sensitivity. It was deduced from work on multi-layers of stearic acids [92] that the sampling depth was approximately 100 Å. The sensitivity was observed through examination of vitamin B12 molecules which have one cobalt atom amongst ~180 other atoms and a layer ~100 Å thick would contain very few cobalt atoms. The Co signal

however was easily detected in the XPS spectrum [94]. In 1972, work by Brundle and Roberts [97] carried out in ultra high vacuum showeded XPS to be a truly surface technique. In the same year, Seah [98] pointed out that the thickness of the surface layer characterised must be very similar to that in Auger electron spectroscopy (AES).

The other important aspect of XPS is its chemical specificity, by means of the existence of a "chemical shift" in the binding energy of a particular photoelectron, caused by differences in the chemical state and the chemical environment surrounding the atom (discussed fully in section 3.3.3). The first indisputable proof of the existence of the chemical shift effect was reported by Hagstrom et. al. [99] when the two sulphur atoms in $Na_2S_2O_3$ were shown to give two well-resolved K photoelectron lines, due to their different valence states 2^- and 6^+. This was followed in 1966 by the first attempts to explain the basis of the chemical shift [95,100]. As an example, figure (3.1) shows the the chemically shifted C 1s spectrum of ethyl trifluoroacetate (due to Gelius et. al. [101]).

The field of x-ray photoelectron spectroscopy, both in instrumentation and applications, has expanded tremendously and numerous books and reviews have been published [102-109]. An extensive review of the early history of XPS from 1900 to 1960 is given by Jenkin et. al. [110, 111]. Recent developments in the understanding of x-ray excited Auger and photoelectron spectra in the light of theoretical developments in atomic, molecular and solid state physics has been reviewed by Weightman [112].

3.2: X-ray Photoelectron Spectroscopy: the basic principles

The principle of X-ray photoelectron spectroscopy is to study the properties of electrons which are photo-emitted from a sample after being bombarded by monoenergetic X-ray photons. The incident photon with energy $h\upsilon$ (υ is the frequency of the incident photon and h is Planck's constant), ionises the sample atom or molecule, M, such that:

$$M + h\upsilon \rightarrow M^+ + e^- \qquad \ldots\ (3.1)$$

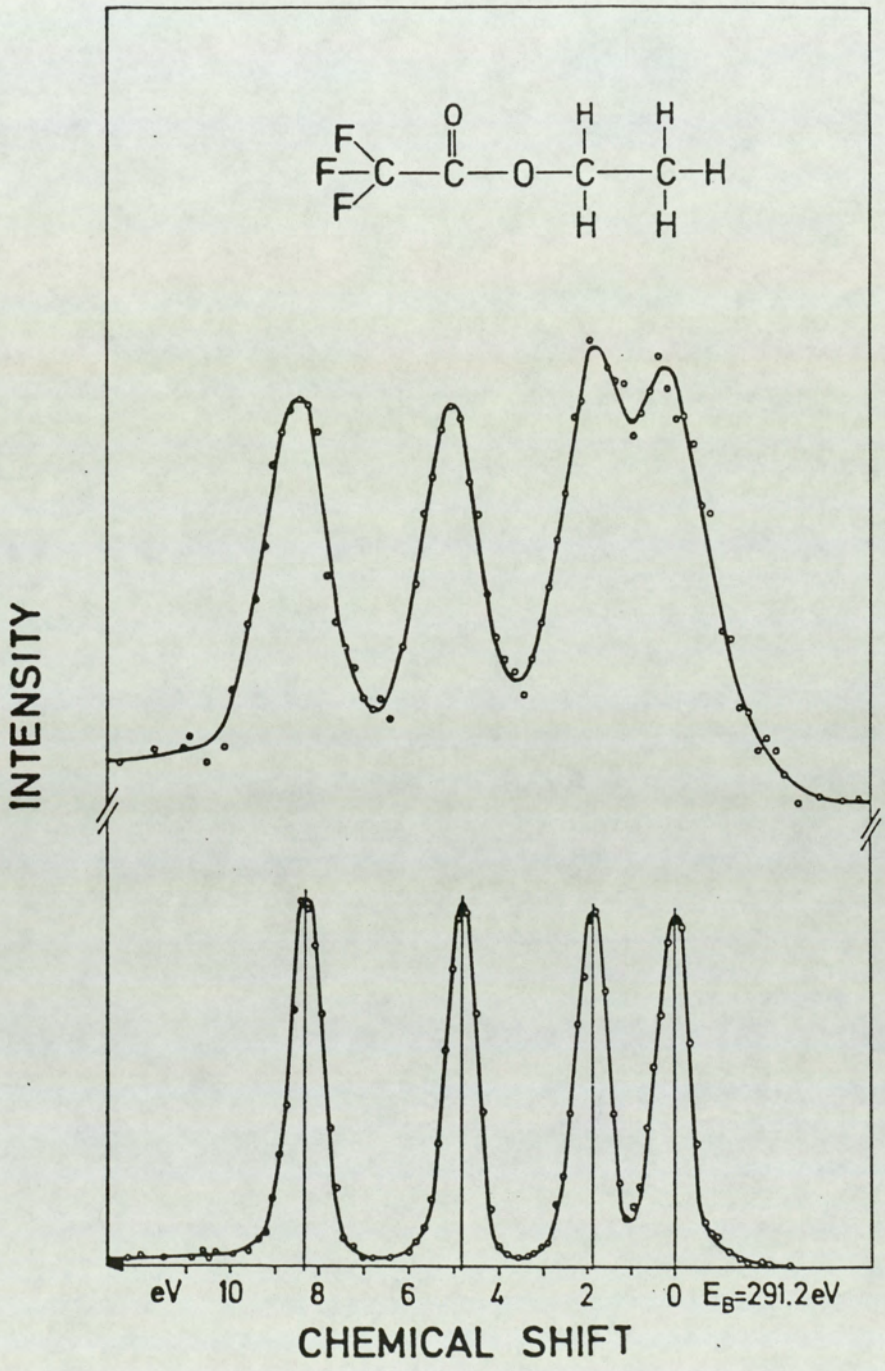

Figure 3.1.
XPS chemical shifts of the C 1s in ethyl trifluoroacetate. Upper spectrum without and lower with X-ray monochromatization [101].

M^+ is the resulting ion formed and e^- is the photoelectron. The basic photoionisation process is shown schematically in figure (3.2a). The ranges of some photon sources are shown in figure (3.3).

After a core electron is removed by photoionisation, the inner shell ionised atom has two possible methods of relaxation. The first is by the X-ray fluorescence effect in which an electron from an outer shell moves down to fill the vacancy and a quantum of x-ray energy is released to remove the excess energy. The alternative method of relaxation is via the radiationless emission of an electron, i.e., the Auger effect. For a particular situation, for example in the case of the inner K shell vacancy, it can be filled by an L_2 electron and the energy that could otherwise have been released as radiation is used in ejecting another electron whose ionisation potential is lower than the available energy from the electron relaxation process; this electron is termed the Auger electron. If the second ejected electron in the above example is released from the L_3 shell it is designated a KL_2L_3 Auger electron. Both X-ray fluorescence and Auger effects are two-step processes whereas the photoionisation is a one-step process. These two modes of relaxation of the photo-ion are shown schematically in figure (3.2b) and (c). The energy of the primary photoelectron is dependent on the energy of incident photon whilst the energy of the fluorescence X-ray or the Auger electron are not. In practice both the Auger mechanism and X-ray emission contribute to the decay of the core hole states, their relative probabilities being highly dependent on the atomic number of the element concerned (see figure (3.4)).

Auger electron spectroscopy (AES) [5,113] initiated by electron bombardment is another major surface analytical technique; Chang [114] reports the relative usefulness of the XPS and AES techniques. The potential of Auger chemical shifts in X-ray induced Auger electron spectroscopy (XAES) [115] is also considered to yield valuable chemical information.

In XPS there are three basic measurable properties which characterise the emitted photoelectron:

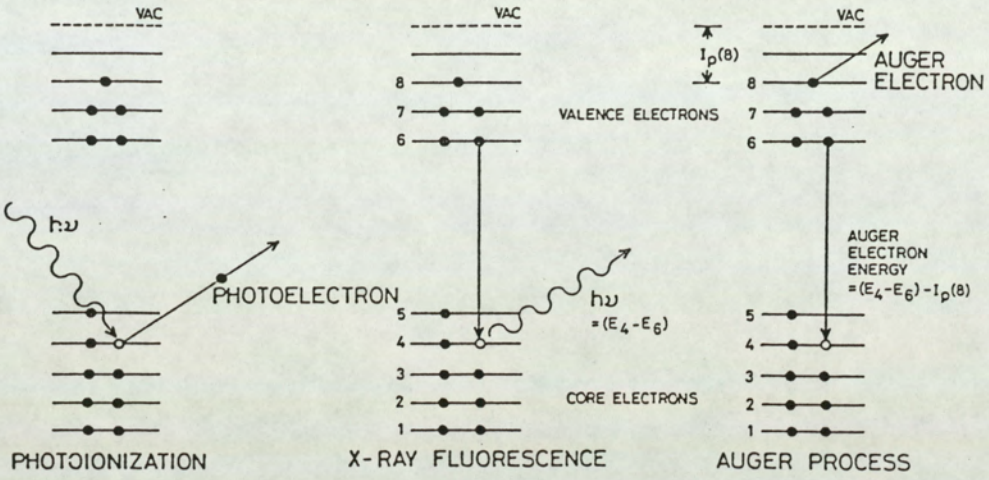

Figure 3.2.
X-ray fluorescence and Auger processes: photo-ionization, X-ray fluorescence, Auger process.

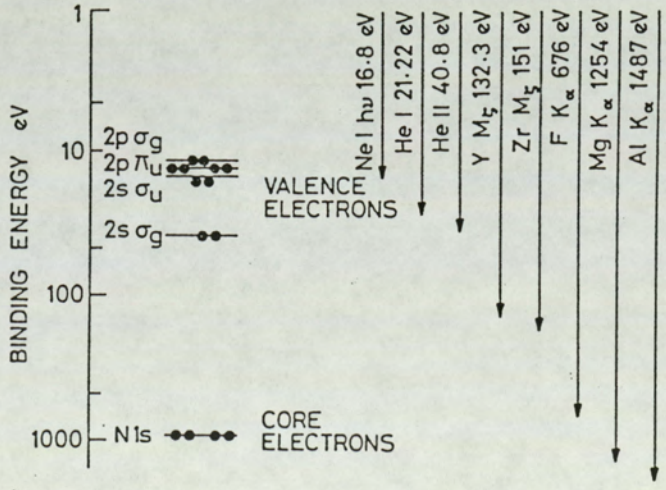

Figure 3.3.
Energy ranges of some radiation sources [105].

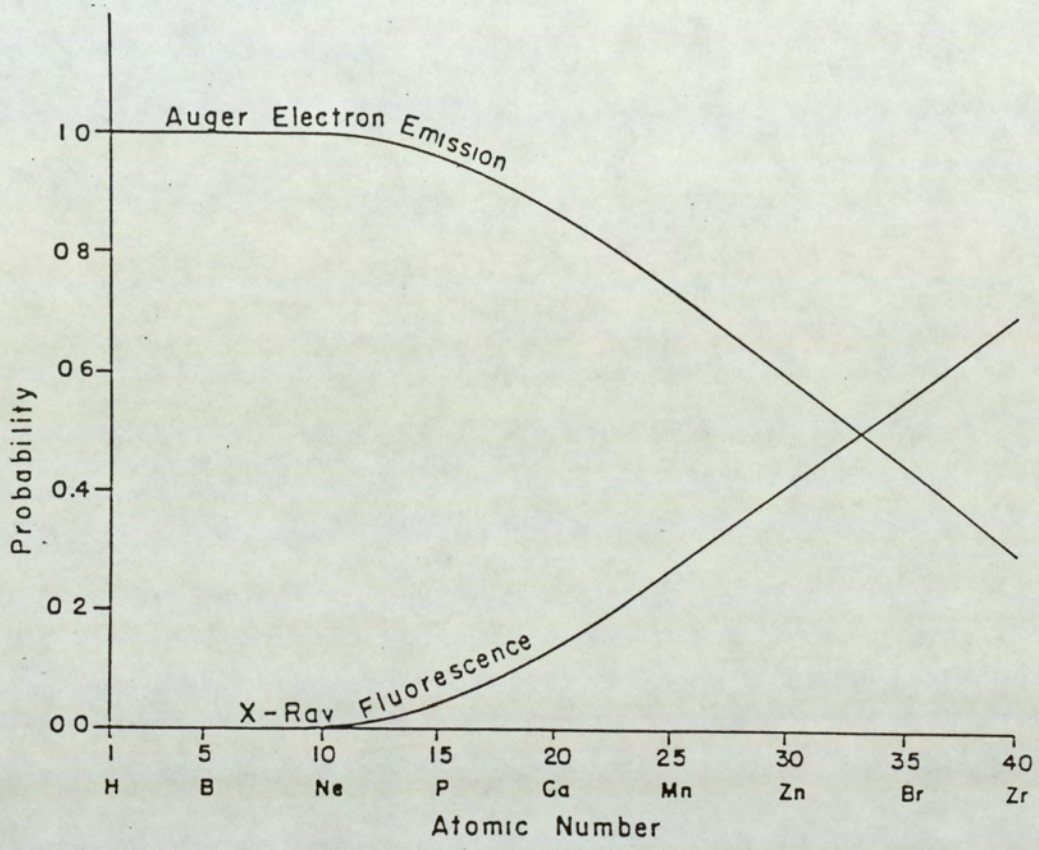

Figure 3.4.
Relative probabilities of relaxation by Auger electron emission and X-ray photon emission following the creation of a core hole.

1) The number distribution of the photoelectrons with kinetic energy - gives the photoelectron spectrum which is usually measured at fixed angles of electron emission relative to the photon source and the sample;

2) The distribution of photoelectron intensity with angle of emission (with respect to the photon propagation direction and to axes fixed with respect to the specimen) [116];

3) The spin distribution of the photoelectrons. This measurement is concerned with a sample that is first magnetically polarized, usually with the aid of an external field and then the relative numbers of spin-up and spin-down photoelectrons are measured.

The XPS studies carried out in this thesis measure the kinetic energy distribution with a fixed geometry of the photon source, specimen and the spectrometer. The fundamental equation for the energy balance in the photoelectric process is based on the energy conservation principle:

$$h\upsilon = E_{kin}(S) + E_b(k)^V + E_r \qquad \ldots. (3.2)$$

where: $h\upsilon$ is the energy of the incident photon;

$E_{kin}(S)$ is the kinetic energy of the k^{th} photoelectron ejected from the sample;

$E_b(k)^V$ is the ionisation potential or the binding energy of the k^{th} electron as referred to the vacuum level of the sample ;

E_r is the recoil energy.

By applying the law of conservation of momentum for the case when recoil is in the direction of the incoming photon, and assuming non-relativistic calculations, Siegbahn et. al. [94] obtained an upper limit for the recoil energy of the photoelectric ejection of a valence electron. They found that their calculated value of E_r, for most cases, was less less than one electron volt in magnitude and that with appropriate choice of X-radiation the recoil energy became negligible. The term E_r in equation (3.2), thereafter, was neglected and the basic equation thus can be written as:

$$h\upsilon = E_{kin}(S) + E_b(k)^V \qquad \ldots. (3.3)$$

For solid samples, the measurement of the binding energy E_b with respect to the Fermi level is usually more convenient than measuring the binding energy with respect to the vacuum level because the latter requires knowledge of the sample work

function. In general, there exists a small electric field in the space between the source and the entrance slit to the spectrometer even if both are grounded. When the sample and the spectrometer are in electrical contact (assuming that the sample is metallic), electrons in the material with the larger Fermi energy can move to the unoccupied lower energy states in the other material. This transfer of electrons causes the materials to acquire opposite charges. The charge difference causes the potential wells of the materials to shift until the Fermi surfaces align, so that there is no cause for further electron transfer. The shifts of the Fermi surfaces are brought about primarily by the charge difference of a few electrons [94] and so the work functions of the sample and the spectrometer material respectively remain unchanged. Any difference in work function of the sample material and the spectrometer material thus causes a potential difference between the two materials. The kinetic energy, $E_{kin}(A)$, of the electron when it enters the electron analyser is then slightly different from the energy, $E_{kin}(S)$, which it has from emerging from the sample and this is shown schematically in figure (3.5). It is the kinetic energy $E_{kin}(A)$ that is measured in the spectrometer, where:

$$E_{kin}(A) = E_{kin}(S) + (\Phi_S - \Phi_A) \qquad \ldots. (3.4)$$

The term $(\Phi_S - \Phi_A)$ is known as the contact potential [116] (Φ_S and Φ_A are the sample and the analyser material work functions respectively). Thus the electron in leaving the sample and entering the analyser is subjected to an accelerating or retarding potential equal to this contact potential. Choosing the Fermi level as the reference level for the electron binding energies, that is, taking binding energy to be equal to zero at the Fermi level, conservation of energy requires that:

$$h\upsilon = E_b(k)^F + E_{kin}(A) + \Phi_A \qquad \ldots. (3.5)$$

Electrically insulating samples can also be studied by XPS since an adequate number of free charge carriers are formed during X-ray irradiation and it is thought that the Fermi level can adjust to the required equilibrium state [94,118].

The definition of E_b relative to the Fermi level is a convenient one for solid samples as it bypasses the need for the work function of the sample material. There are

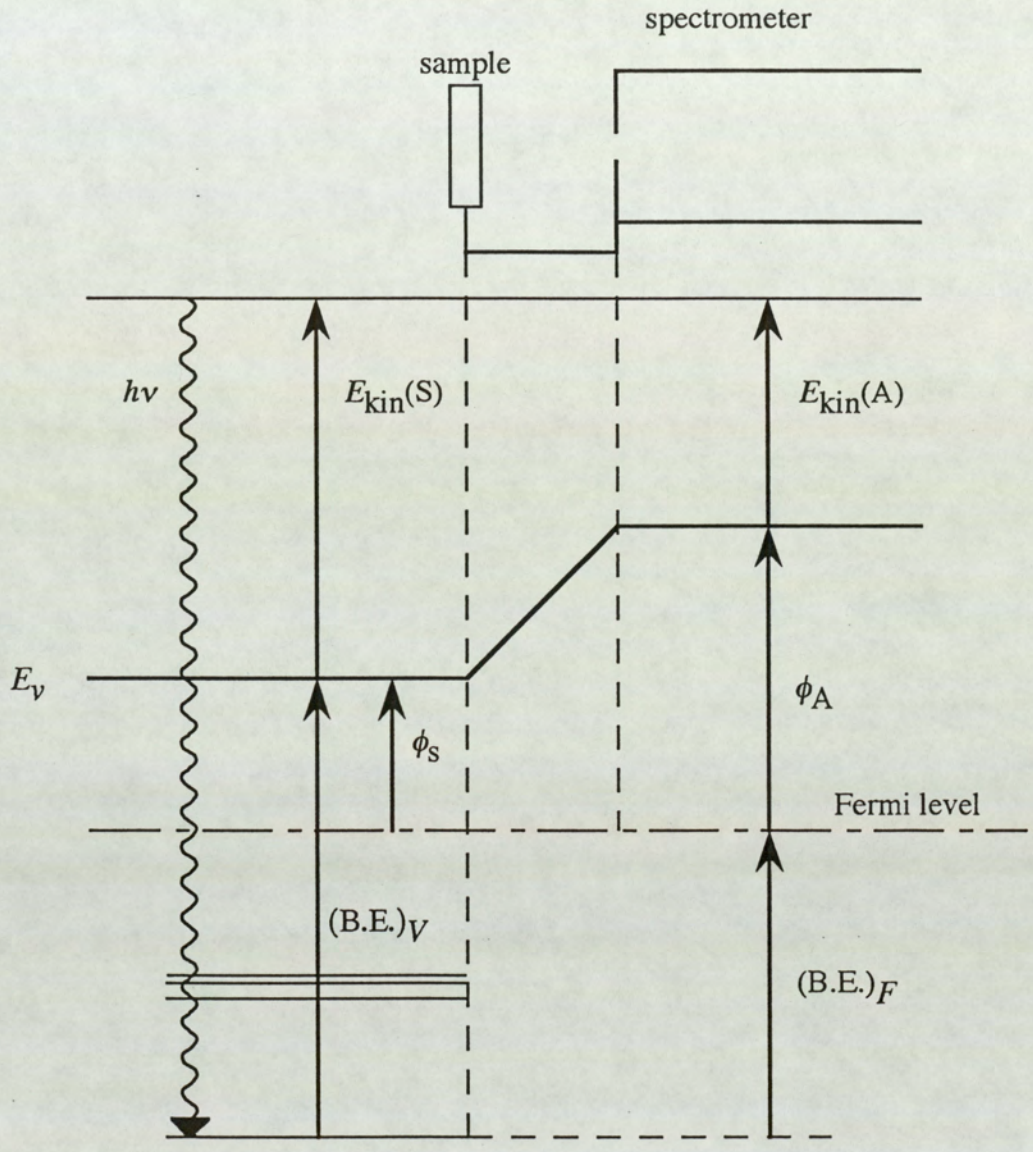

Figure 3.5.

Schematics showing the effect of the contact potential between a metalic sample and electron energy analyser.

however some difficulties associated with this definition. First, theoretically calculated binding energies are usually referred to with the electron at infinity; thus the work function of the sample material is required if comparisons to the theory are to be made. For metals the Fermi level is well defined and the work functions are known but, however, the Fermi levels of insulators and semiconductors are difficult to measure and the work functions are generally not known. Also it is difficult to establish whether for non-metallic samples the equilibrium between the Fermi levels of the sample and the spectrometer material is reached when brought in electrical contact. Finally, at the surface of the sample the work function and the position of the Fermi level relative to the electronic energy levels can be altered by surface effects such as adsorption, but, such changes in energy levels are considered to be of minor concern in XPS spectra. Thus even when only comparisons of binding energies of the same element in different chemical environments are required, the uncertainties in the position of the Fermi levels will introduce some errors in the results. Albridge [117] considers that this error can perhaps be as much as 1 eV.

As mentioned before, from a purely theoretical point of view, the binding energy of an electron within a molecule is defined as the energy required to move the electron from its orbital to a position of rest an infinite distance from the molecule. Since the electron in its final state has no kinetic or potential energy, the binding energy is equal to the difference in energies of the initial and final states of the molecule. Thus for any orbital , the binding energy is:

$$(E_b) = \{\text{total energy of neutral molecule}\} - \{\text{total energy of molecular ion}\} \quad \ldots. (3.6)$$

(E_b) will be equal in magnitude to the eigenvalue calculated in the one electron model, if one assumes that the electrons outside the orbital from which the electron was ejected have the same energy in the molecular ion as in the neutral molecule. This assumption is known as Koopmans' [119] theorem, and it gives orbital energies that are consistently two to ten percent too large because reorganisation or relaxation energy has

been ignored. Relaxation energy arises from the contraction of the electrons in the molecular ion leading to a gain in the total energy of the molecular ion thus equation (3.6) gives a lower value of (E_b). The Koopmans' theorem for core orbitals gives values for chemical shifts that are difficult to compare when there are large differences in relaxation energies for the molecules in different compounds. But, in general it can be stated that within the applicability of Koopmans' approximation a direct comparison can be made between the binding energy measured by means of X-ray photoelectron spectroscopy and the one electron eigenvalues calculated by theory.

3.3: The X-ray Photoelectron Spectrum

In any given photoelectron spectrum obtained using a non-monochromatised X-ray source, a series of peaks are observed on a background which generally increases on the high binding energy side. Sometimes step-like increases on the high binding energy side of a particular peak are also observed. Equation (3.5) assumes that the photoemission process is elastic and thus each characteristic X-ray will generate a series of photoelectron peaks which reflect the discrete binding energies of the electrons present in the solid. These photoelectron peaks can be divided into three basic groups: peaks due to inner shell (or core level) photoemission, peaks due to emission of electrons from valence levels and peaks due to X-ray induced Auger electrons. The general background which is dominant in the high binding energy side is caused by photoemission initiated by the Bremsstrahlung radiation. The Bremsstrahlung radiation is present in the output of a non-monochromatised X-ray source as a broad continuous distribution upon which the characteristics of the anode material (e.g. Mg or Al) is superimposed. The step-like feature on the high binding energy side is due to inelastic photoemission, i.e. energy loss of the photoelectron within the solid.

In this thesis, only the peaks due to core level photoemission will be considered.

Normally one expects a single photoelectron peak associated with each atomic

or molecular orbital. However there can be more than one final state resulting from the removal of a core electron. This situation is quite common and the transitions to various excited states are represented in the photoelectric spectra as satellite lines or multi-component structures.

3.3.1: The core level widths

The observed peak width, ΔE, is expressed as the full width at half maximum (FWHM) and is made up of several contributions:

$$\Delta E = (\Delta E_n^2 + \Delta E_x^2 + \Delta E_A^2)^{1/2} \quad \text{.... (3.7)}$$

where: ΔE_n = the natural FWHM of the core level.

ΔE_x = the FWHM of the X-ray line.

ΔE_A = the analyser resolution (FWHM).

This relation assumes that all the components have Gaussian line shape. In an ionised inner electron shell the vacancy is filled by an outer electron within a time interval, τ, of the order of 10^{-16} seconds [94]. Briggs and Riviera [120] gives values for Ag core levels of the order of 10^{-15} seconds. This finite life-time for a level corresponds, according to the uncertainty principle, to a lack of definition in the energy of that level of the order of a few electron volts. This line width is given by:

$$\Delta E_n = (h / \tau) = (4.1 \times 10^{-15} / \tau) \text{ eV}$$

3.3.2: Spin-orbit Splitting

From observed XPS of core levels it can be concluded that the non-s levels are well-resolved doublets. The doublets arise as the core-holes produced in the orbitally degenerate (i.e. $\ell > 0$) subshells are very susceptible to the spin-orbit (j-j) interaction. Two possible states characterised by the quantum number j ($j = \ell + s$, where $s = \pm 1/2$) arise when $\ell > 0$. The difference in energy of the two states , ΔE_j, increases as Z (the atomic number) increases for a given subshell (constant n,ℓ) or to increase as ℓ decreases for a given n. The relative intensities of the doublet peaks are equal to the ratio of their respective degeneracies, i.e.:

$$I_{\ell+s} / I_{\ell-s} = \{2(\ell+s) + 1\} / \{2(\ell-s) + +1)\} \quad \text{.... (3.8)}$$

where $I_{\ell+s}$ is the intensity of photopeak corresponding to the state with quantum number j having the value (ℓ+s) and $I_{\ell-s}$ is the intensity of that when j equals (ℓ-s).

3.3.3: Chemical-shift effect

Interest in the core-electron photoelectron spectroscopy has been stimulated very much by the chemical shift effect. The core levels of an atom are effectively inert as far as chemical bonding is concerned. However they are still affected by the chemical environment of the atom and show small changes in binding energy as their environment is changed. These changes, termed the chemical shifts, are due to the electrostatic interaction between the valence and the core electrons. This chemical shift effect can thus be interpreted as resulting from changes in structure and oxidation states of compounds in surfaces [94, 55,121,122].

One of the methods for interpreting chemical shifts is to use equation (3.6) to calculate binding energies. Shirley [123] gives a critical review of the various different model calculations that can be made. In the following some of these models describing the chemical shift effect are discussed.

3.3.3.1: The charge potential model

This is a widely used model that explains how the chemical shift depends upon the charge on the atom concerned and upon the charge on the surrounding atoms. This model is developed by Siegbahn and his co workers [95,124,125]. In this model, it is assumed that the atoms in a molecule may be considered as hollow electrostatic spheres, and that the core electron binding energy depends on the potential felt at the core site due to the valence electrons of the same atom as well as electrons of the surrounding atom. Then for a particular atom i the potential inside the sphere is same at all points and is given by:

$$\text{Potential energy due to the valence electrons} = q_i/r_i \qquad \ldots. \ (3.9)$$

where q_i is the valence charge and r_i is the average valence orbital radius. If each of the

surrounding atoms are reduced to point charges of charge q_j and r_{ij} is the distance between them, then the potential they will cause at the original atom i will be:

$$\text{Potential energy due to atom } j = q_j/r_{ij} \qquad \ldots. (3.10)$$

The overall effect will be the sum of equations (3.9) and (3.10), where equation (3.10) is summed for all other atoms of the sample, thus:

$$\text{Potential energy} = q_i/r_i + \sum_{j \neq i} q_j/r_{ij} \qquad \ldots. (3.11)$$

Equation (3.11) can be modified to give the shift in binding energy E_b for a core electron of an atom i in a molecule M, with respect to the binding energy of the same core electron in a reference compound and can be written:

$$\Delta(E_b)_i = a\{(q_i/r_i)_M - (q_i/r_i)_{ref}\} + a\{(\sum_{j \neq i} q_j/r_{ij})_M - (\sum_{j \neq i} q_j/r_{ij})_{ref}\}$$

$$\Rightarrow \quad \Delta(E_b)_i = \{k_i'\Delta q_i\} + \{a(\sum_{j \neq i} q_j/r_{ij})_M\} + \{-a(\sum_{j \neq i} q_j/r_{ij})_{ref}\}$$

$$\Rightarrow \quad \Delta(E_b)_i = \{k_i'\Delta q_i\} + \{V_i\} + \{l'\} \qquad \ldots. (3.12)$$

where, a is a conversion factor. $\Delta q_i = \{(q_i/r_i)_M - (q_i/r_i)_{ref}\}$, i. e. the charge difference on the atom i between the molecule it is in and the reference system. k_i' represents an average interaction between a core electron and a valence electron belonging to atom i (assuming an average radius of valence shells of atom i). The term V_i represents an effective interatomic potential and l' is a constant dependent only on the reference compound.

By separating the contributions of the reference compound from the first term and combining with l', it is possible to express the shifts in terms of q_i:

$$\Delta(E_b)_i = \{a(q_i/r_i)_M\} + \{a(\sum_{i \neq j} q_j/r_{ij})_M\} + \{-a(q_i/r_i)_{ref} - a(\sum_{i \neq j} q_j/r_{ij})_{ref}\}$$

$$= \{k_i q_i\} + \{V_i\} + \{l\} \qquad \ldots. (3.13)$$

Where k and l for a particular core ionisation can be determined independently if for a set of compounds the charges are known and the chemical shift data are also available. Thus as long as the valence electrons do not penetrate into the atomic core, this model predicts the same shift for the electrons in a given core.

According to this charge potential model the shift per degree of oxidation should increase as the state of oxidation increases, because for higher degree of oxidation, i.e. when more electrons are removed from the valence shell, the valence shell should contract (decreasing r). Using this model, good agreement with experimental shifts and calculated charges may be obtained [95,126]. The charges may be calculated by simple methods based on electronegativities.

3.3.3.2: The valence potential model

This model, as with the previous charge potential model neglects relaxation. The shifts in the binding energies of the core electrons are expressed in terms of the valence potential, ϕ_{val}. ϕ_{val} is defined as the potential experienced by a core electron of an atom i due to the valence electron density of the molecule and the cores of other atoms; it is related to the binding energy of a core electron of atom i by:

$$(E_b)_i = e\,(\phi^i_{val}) + \text{constant} \qquad \ldots. (3.14)$$

Comparing this binding energy with that of a corresponding core electron in a reference compound gives:

$$\Delta(E_b)_i = e\,(\Delta\phi^i_{val}) \qquad \ldots. (3.15)$$

The quantum mechanical average value of the potential is given by (Ghosh [105]):

$$\phi^i_{val} = -2\sum\langle \Phi_n | 1/R_n | \Phi_n \rangle + \sum(q_k^* / r_{ik}) \qquad \ldots. (3.16)$$

where R_n is the distance of the n^{th} valence electron from the nucleus of atom i, Φ_n is the wave function of the valence electron, q_k^* is the nuclear charge on atom k and r_{ik} is the internuclear distance. In the above equation (3.16) the first term is the electronic contribution and the second term is the nuclear potential due to the surrounding atoms.

3.3.3.3: The equivalent cores approximation

This method has been put forward by Jolly [121] and it correlates measured shifts in binding energies with thermodynamic data of heats of formation. The central assumption of this model is that the atomic cores that have the same charge are chemically equivalent. An element with an inner-shell vacancy is thus equivalent to the neutral element one step below in the periodic table.

3.3.4: Shake-up and Shake-off satellites

The valence electrons of an atom appear to experience an effect similar to an increase in the nuclear charge when a core vacancy is created by photoemission. This causes substantial reorganisation of the valence electrons (referred to as relaxation) which may involve excitation of one of the valence electrons to a higher unfilled level. Thus the energy required for this valence electron transition is not available to the primary photoelectron, instead there appears a discrete structure on the low kinetic energy side of the photoelectron peak. This is known as the shake-up satellite.

There are various reports of shake-up satellites in the transition metal compounds (Rosencwaig et al [127], Frost et al [128], Yin et al [129], Carlson et al [130], Briggs et al [131]). Strong satellites are observed in certain transition metal compounds which have unpaired electrons in the 3d or 4f shells. The sake-up satellites have important diagnostic value. There is a definite correlation between the presence of shake-up satellites in the transition metal complexes and paramagnetism [128,129]. The presence of these satellites can be used to distinguish cobalt (III) from cobalt (II); cobalt (III) is diamagnetic and thus shows no satellites whereas cobalt (II) gives more intense satellites in the high spin state than in the low spin state [56,131].

An extreme situation of the shake-up process is the complete loss of a valence electron by ionisation, and this is called the "shake-off" process. Such a loss, concurrent with the ejection of a photoelectron, generates a doubly charged ion and because the excess energy is distributed between two electrons, shake-off processes do

not contribute any discrete structures to photoelectron spectra.

3.3.5: Multiplet lines

Multiplet splitting of the core levels can occur when the atom or molecule under study has unpaired electrons in the valence shell, as in the transition metals (with incomplete d shells) or rare earth atoms (incomplete f shells). Thus interaction may take place between an unpaired electron formed by photoelectron ejection and any unpaired electron already existing in the incomplete valence shell resulting in more than one final state; this is also known as exchange or electrostatic splitting. The simplest case is that of a s core orbital. This type of multiplet splitting has been reported for the 3s levels of the Fe^{3+} and the Mn^{2+} ions by Fadley and Shirley et. al [132] and Fadley and Shirley [133]. As an example, photoemission of a 3s electron is considered for the Mn^{2+} free ion. This ion in its ground state has five 3d electrons (denoted in the Russell-Saunders coupling as ^6S) which are all unpaired and with parallel spins. After ejection of a 3s electron, the spin of the resulting unpaired electron can couple parallel with the spins of the 3d electrons (denoted ^7S) or antiparallel (denoted ^5S) corresponding to the two final states; the energy of the ^7S state being lower than that of the ^5S state. The separation in energy, ΔE, between the two peaks (due to the two final states) is given by:

$$\Delta E = (2S + 1)\, K_{3s\text{-}3d} \qquad \ldots. (3.17)$$

where S is the total spin of the unpaired valence electrons (5/2 in this example). $K_{3s\text{-}3d}$ is the 3s-3d exchange integral. The intensity of the two photoelectron lines, corresponding to the two states, will be proportional to the multiplicity of the states $\{2(S \pm 1/2) + 1\}$.

When core orbitals other than s orbitals are studied, the situation becomes more complex due of the additional involvement of spin and orbital angular momentum coupling, resulting in more than two final states. Theoretical calculations of multiplet structures of core p- vacancies have been made (Gupta and Sen [134]). Thus multiplet

splitting of non-s levels can cause peak broadening and assymmetries which can easily be confused with the chemical shift effect.

3.3.6: Discrete energy loss processes

Photoelectrons ejected from core levels may interact with other atoms and molecules (rather than with the valence electrons of their own atom). Such inelastic processes lead to energy loss of the electrons. These electrons usually do not give rise to a single peak in the photoelectron spectrum but contribute to the spectrum background. However if the interaction causes transitions of specific energy in the other atom or molecule, then the photoelectron will lose a discrete quantity of energy , and a single peak in the photoelectron spectrum will result.

The transition of a specific amount of energy will depend upon the possible transitions of the system which will depend upon the physical state of the system. In a gas, for example, valence electron excitation in other atoms may occur; the intensity of the peak is pressure dependent and becomes more intense than the shake-up peaks as the pressure is raised. In a solid, plasmon excitations of the conduction electrons of conductors and semiconductors may occur. A plasma oscillation in a metal is a collective longitudinal excitation of the conduction electron gas [135]. A plasmon is a quantum of a plasma oscillation. Any electron of sufficient energy passing through the solid can excite one or other modes of collective oscillations of these conduction electrons. These oscillations have a frequency, ω, given by $(4\pi ne^2/m)^{1/2}$ where n is the density of the free electrons, m is the electronic mass and e is the electronic charge. Plasmon excitation thus gives rise to discrete loss ($h\omega$) peaks. There may be surface plasmons ($h\omega_s$) as well as bulk plasmons ($h\omega_b$) and the frequency of the surface plasmon is $(1/\sqrt{2})$ times its frequency in the bulk [136]. Electrons which have suffered a plasmon loss can suffer further similar losses in a sequential manner. The spectrum then shows a series of loss peaks, all equally spaced by $h\omega$ but of decreasing intensity. Figure (3.6) shows such a series of plasmon loss features in spectrum of $Al+Al_2O_3$.

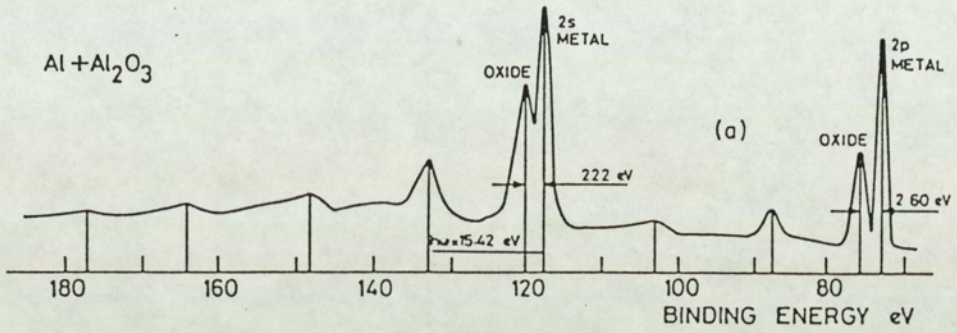

Figure 3.6.
A series of volume plasmon peaks in the Al + Al_2O_3 spectrum [105].

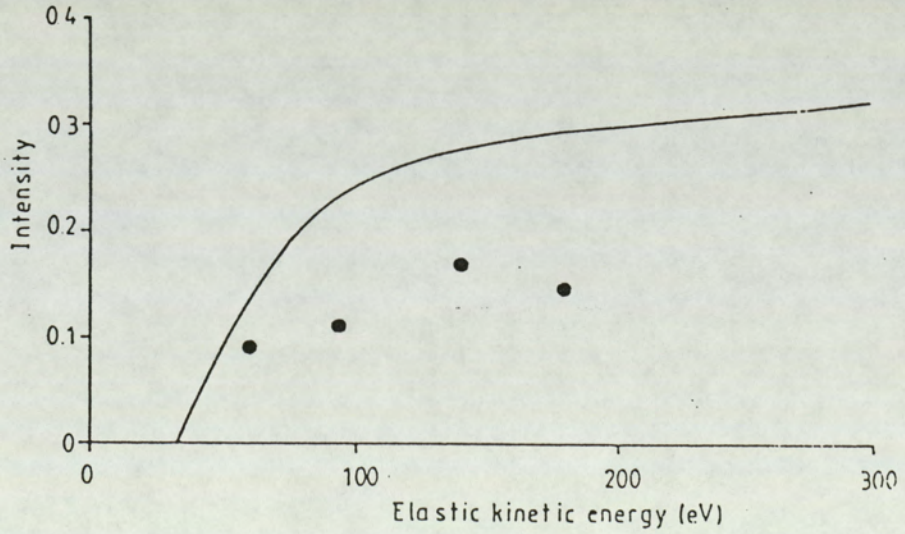

Figure 3.7.
Intensity of the plasmon satellites as a function of the kinetic energy of the no-loss photo electrons. The solid line shows the intensity of the bulk plasmon satellites, the circles shows the intensity due to the surface plasmon satellites [137].

However, Inglesfield [137] states that the plasmon satellites in X-ray photoemission from core levels in solids are weak until the photoemitted electron has an energy much greater than the bulk plasmon energy; in the case of Al which has a bulk plasmon energy of 15 eV, neither bulk nor surface plasmon satellites are observed until the electron has a kinetic energy of 40 eV and the intensity only becomes appreciable at an energy of about 100 eV. Figure (3.7) shows this variation of the relative intensity of the bulk plasmon satellite intensity with the kinetic energy of the no-loss photoelectron.

3.3.7: Ghost satellites due to the exciting radiation

Additional satellites due to the exciting radiation may also be present in the photoelectron spectrum and these may arise in various ways. When the radiation is obtained from a source not fitted with a monochromator (as is the case with most standard sources), there may be spurious lines due to the photoelectrons excited by the secondary X-rays (i.e. X-rays other than the principle $K\alpha_{1,2}$). Also, there may be satellites due to the excitations arising from impurity elements in the X-ray source. The most common ghost is that due to Al $K\alpha_{1,2}$ when the Mg anode is operational. This arises from the secondary electrons produced inside the source hitting the aluminium window and hence weak ghost peaks at 233 eV above the main photopeak generated by the Mg $K\alpha_{1,2}$ is observed. Old or damaged anodes can give rise to ghost peaks due to the Cu $L\alpha$ radiation (the main line from the exposed copper base) which appear at 323.9 eV below the peak energy due to Mg $K\alpha_{1,2}$. In dual anode X-ray sources, misalignment of the anode assembly with respect to the filaments may lead to one filament being able to "see" both the anodes and this is a further source of ghost peaks.

3.4: Surface sensitivity

This is a feature peculiar to solid state photoelectron spectroscopy. Electrons travelling through a material have a relatively high probability of experiencing inelastic collisions with locally bound electrons and thus suffer a loss in energy. The "inelastic

mean free path" (IMFP), λ, is a measure of the mean distance travelled by the electron without energy loss and thus also contains information regarding the depth that can effectively be sampled by XPS and hence gives rise to its surface sensitivity. λ is also known as the mean escape depth of an electron of energy E_e within the material concerned and it represents the depth from which (1/e) of the photoelectrons produced there can escape. λ is given by:

$$I_d = I_\infty (1 - e^{-d/\lambda}) \quad \text{.... (3.18)}$$

where, I_d is the intensity of photoelectrons obtained from a layer of materials of thickness d and I_∞ is the photoelectron intensity from an infinitely thick layer. By successively substituting $d = \lambda$, $d = 2\lambda$ and $d = 3\lambda$, in the above equation (3.18), it can be seen that 63% of the total signal intensity is due to electrons originating from a layer of thickness λ, 87% from 2λ and 95% from 3λ. Thus it can reasonably be assumed that most of the photoelectrons originate within a surface thickness of about 3λ; this thickness is also known as the sampling depth.

Experimental IMFP data have been compiled by Seah and Dench [138] for electrons in the energy range $0<E_e<10$ keV above the Fermi level. Data have been obtained from published measurements and matched for the groups: I) elements, II) inorganic compounds, III) organic compounds and IV) adsorbed gases. Figure (3.8) shows the universal curve for the dependence of λ on E_e [138]; the path lengths are very high at low energies, decrease to $0.1< \lambda < 0.8$ nm for energies $30< E_e <100$ eV and then rise again 'roughly as the square root of energy E_e' [138]. (Note that the general formula for the curve shown in figure (3.8) is of the form $\{\lambda=(A/E^2) + (BE^{1/2})\}$ where A and B are constants dependent on the sample).

3.4.1: Increase in surface sensitivity, take-off angle dependency

The usefulness of varying the angle of electron emission or "take-off" angle in XPS is an important consequence of the IMFP. A surface sensitivity (surface : bulk signal ratio) enhancement of roughly 10x could be achieved at low take-off angles. Table (3.1) shows the relationship between the take-off angle α and the sampling

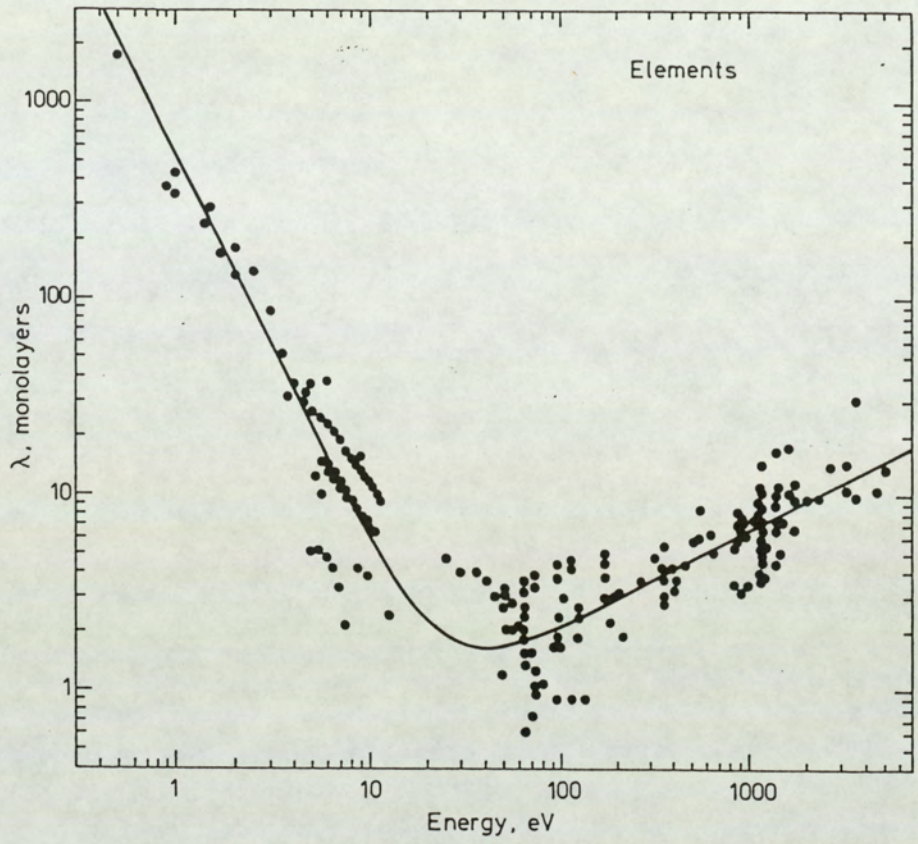

Figure 3.8.
The dependence of IMFP, λ, on electron energy [138].

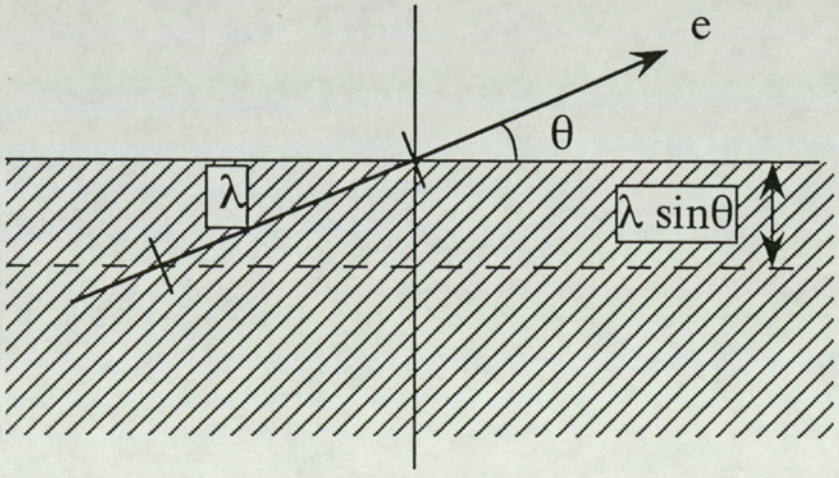

Figure 3.9.
Schematic showing the enhancement of surface sensitivity as a consequence of the take-off angle.

Table 3.1.
The sampling depth dependency on the take-off angle.

Take-off angle, Θ	relative effective sampling depth
90°	1.0
30°	0.5
11°32'	0.2
5°44'	0.1

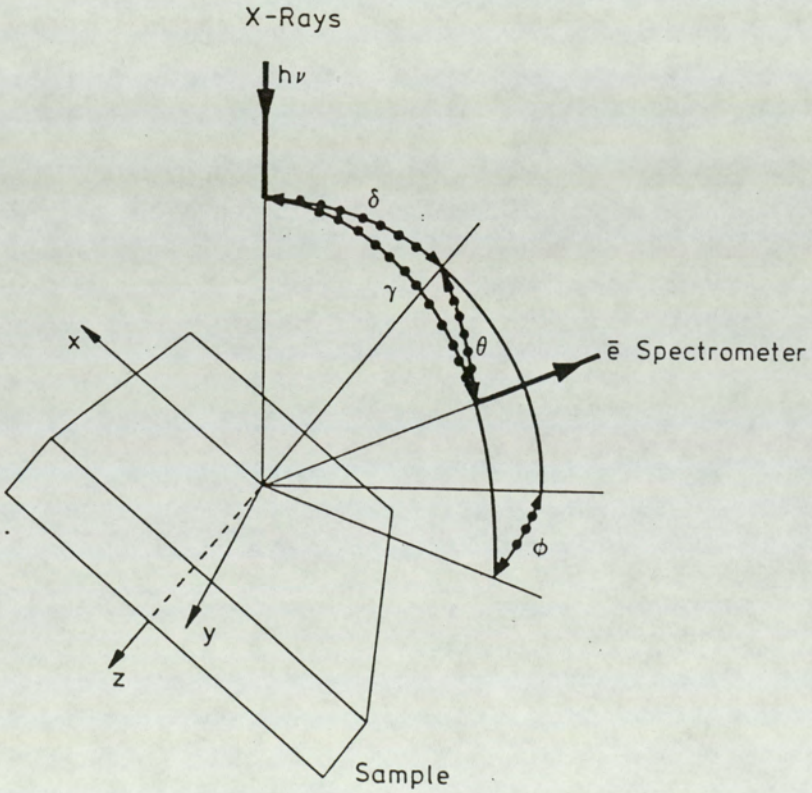

Figure 3.10.
Geometry of XPS analysis configuration [105].

depth. The reason for the enhancement of the surface sensitivity can be simply demonstrated by figure (3.9); it is seen that the vertical depth sampled is given by:

$$d = 3\lambda \sin\theta \qquad \text{.... (3.19)}$$

thus d is a maximum value when α is 90^0. Equation (3.18) would then need to be modified to:

$$I_d = I_\infty (1 - e^{-d/\lambda \sin\theta}) \qquad \text{.... (3.20)}$$

This aspect has lead to the development of techniques for depth profiling of very thin surface layers by using variable take-off angle XPS [139,140] without having to resort to ion etching.

However, one of the consequences of using low angles of emission is that the signal becomes very dependent on the nature of the surface, i.e. roughness. Surface roughness leads to an averaging of electron exit angles and also to shadowing effects (both of the incident X-rays and emerging electrons) such that in most cases the sensitivity enhancement cannot be observed.

3.5: Quantification

3.5.1: Basic consideration

In investigations carried out with XPS, it may be necessary to determine the relative concentrations of the various constituents of the sample. The simplest form of quantification can be expressed as follows:

The molar fractional content of element A, $X_A = I_A / I_A^\infty$

.... (3.21)

where I_A is the signal from element A in the solid and I_A^∞ is the signal from A in its pure form. In general, I_A^∞ may not be known but the ratio (I_A^∞/I_B^∞) may be, where B is another constituent of the solid; thus a more practical form of equation (3.21) is :

$$X = (I_A/I_A^\infty) \; / \left(\sum_{n=A,B} I_n/I_n^\infty\right) \qquad \text{.... (3.22)}$$

The denominator sums over all the constituents of the solid. Equation (3.22) represents the first basic step to quantification in XPS; it requires the evaluation and determination of the various I_n and I_n^{∞} terms. The procedures involved in the measurement of I_n and the measurement or calculation I_n^{∞} will be discussed in the following sections.

3.5.2: Quantification of homogeneous binary solids

The quantification method outlined here is due to Seah [104]. During analysis the incident X-rays penetrate the solid to a depth, Z, of many micrometers and ionise atoms over this depth. However, only electrons created in a zone characterised by a depth of ($\lambda \cos\theta$) escape from the solid to provide the line intensity in the spectrum. The emitted photoelectron is detected by an electron spectrometer with transmission efficiency, $T(xy\ \gamma\phi\ E_A)$, and an electron detector efficiency, $D(E_A)$; the subscript A denotes for the element A in the solid and the terms inside the bracket denote dependencies on various parameters. For any sample, the photoelectron intensity, I_A, of element A in matrix M can be given by:

$$I_A = \Big[\sigma(h\upsilon)\, D(E_A) \int_{\gamma=0}^{\pi} \int_{\phi=0}^{2\pi} L(\gamma) \int_{y=-\infty}^{\infty} \int_{x=-\infty}^{\infty} J_0(xy)\, T(xy\ \gamma\phi\ E_A) \int_{z=-\infty}^{\infty} N_A(xyz) \times \{\exp[-z/\lambda_M(E_A)\cos\theta]\}\, dz\, dx\, dy\, d\phi\, d\gamma\Big] \qquad \ldots.(3.23)$$

Where $\sigma(h\upsilon)$ is the photoelectric cross section for the atomic orbital of interest;

$N_A(xyz)$ is the number of atoms of the element concerned per cubic centimeter of the sample;

$L(\gamma)$ is the angular assymmetry parameter which describes the intensity distribution of the photoelectrons ejected by the unpolarised X-rays; it is dependent on the angle γ which is the angle between the incoming photon and the outgoing photoelectron;

$J_0(xy)$ is the flux intensity of the characteristic X-ray line; and the parameters x, y, z the depth, γ, ϕ are as shown in figure (3.10).

For a homogeneous sample, the integral over z in equation (3.23) reduces to $N_A\lambda_A(E_A)\cos\theta$. To solve this equation, data from reference samples are used which can be achieved by: i) using data for reference spectra of the pure element (I_A^{∞} etc.) measured on the same instrument; or

ii) using data for the the reference spectra measured from a different instrument. Considering this two cases separately:

i) **Case 1- reference data from same instrument**

Using equation (3.23), the following simplified equation can be obtained:

$$\frac{I_A / I_A^{\infty}}{I_B / I_B^{\infty}} = \frac{\lambda_{AB}(E_A)\,\lambda_B(E_B)}{\lambda_{AB}(E_B)\,\lambda_A(E_A)} \times \frac{R_B^{\infty}}{R_A^{\infty}} \times \frac{N_A N_B^{\infty}}{N_A^{\infty} N_B} \qquad \ldots. (3.24)$$

the terms σ, J_0 and the analyser parameters (i.e. D, T, L etc.) are absent because they cancel each other out as they are measured on the same instrument for both I_A and I_A^{∞}. λ_{AB} is the inelastic mean free path in the binary alloy; R_A^{∞} and R_B^{∞} are factors for the pure reference samples which define the intensity emitted from the surface as a function of its roughness. N_A^{∞} and N_B^{∞} are the atom densities in the pure reference samples. However, equation (3.24) can be further simplified by using the substitutions:

$$N_A = a_A^{-3} \quad \text{and} \quad N_A^{\infty} = a_{AB}^{-3} X_A \qquad \ldots. (3.25)$$

such that:

$$N_A N_B^{\infty} / N_B N_A^{\infty} = X_A / X_B \left(a_A / a_B \right)^3 \qquad \ldots. (3.26)$$

where X_A is the required molar fractional composition of the solid and a_A is the atomic size of A which can be derived from:

$$1000\, \rho_M N\, a_M^3 = \underline{A}_M \qquad \ldots. (3.27)$$

where, ρ_M is the density (in kilograms per cubic metre), N is Avagadro's number and

$\underline{A}_M$ is the mean atomic weight of the matrix atoms (if the matrix is element A then this is simply the atomic weight of A). Also, from the work of Seah and Dench [138] the mean free path can be approximated by:

$$\lambda_M = 0.41\ a_M^{1.5}\ E_M^{0.5} \qquad \ldots. (3.28)$$

Thus substituting equations (3.26) and (3.28) in equation (3.24), the following is obtained:

$$X_A/X_B = F_{AB}\,(I_A/I_A^{\infty}) / (I_B/I_B^{\infty}) \qquad \ldots. (3.29)$$

where $$F_{AB} = (R_A^{\infty} / R_B^{\infty})\,(a_B / a_A)^{1.5} \qquad \ldots. (3.30)$$

if F_{AB} is unity equation (3.29) reduces to the simple equation (3.22) but an analysis carried out by Seah [141] on 8000 element pairs showed that the values for F_{AB} scatter about unity with a standard deviation factor of 1.52.

Quantification using the above procedure, assuming that reference data can be recorded on the same instrument, can take considerable effort and is open to various errors. It is thus simpler to use the second case where use of published sets of data are employed.

ii) Case 2: analysis in instrument (1) and published reference data from instrument (2)

In this case equation (3.23) is first simplified by assuming that the electron spectrometer has a small entrance aperture and that the sample is uniformly illuminated, thus:

$$I_A = \left[\sigma(h\upsilon)\ D_1(E_A)\ L_A(\gamma_1)\ J_0(1)\ N_A\ \lambda_M(E)\ \cos\theta_1 \int_{y=-\infty}^{\infty} \int_{x=-\infty}^{\infty} T_1(xy\ E_A)\ dx\ dy\right] \qquad \ldots. (3.31)$$

The last term, which is the product of the area analysed and the analyser transmission, is known as the analyser etendue, $G_1(E_A)$, (Heddle [142]). Hence using the above equation (3.31), the following can be written:

$$\frac{I_A / I_A^{\infty}}{I_B / I_B^{\infty}} = \frac{L_A(\gamma_1)\, G_1(E_A)\, D_1(E_A)\; L_B(\gamma_2)\, G_2(E_B)\, D_2(E_B)}{L_B(\gamma_1)\, G_1(E_B)\, D_1(E_B)\; L_A(\gamma_2)\, G_2(E_A)\, D_2(E_A)} \times \frac{X_A}{F_{AB}\, X_B}$$

.... (3.32)

To facilitate evaluating this equation, determination of each of the parameters associated with the spectrometers is necessary. Considering the detector efficiency, $D(E_A)$, it is noted that in most XPS investigations the electron spectrometer is used in the constant ΔE mode (or, more precisely, the fixed retarding ratio mode, i.e. the constant $\Delta E/E$ mode). The electrons then strike the multiplier at the analyser pass energy, and the detector efficiency D(E) is constant through the spectrum and hence this term can be ignored [105].

The angular assymmetry parameter is given by [143]:

$$L(\gamma) = 1 + 1/2\, \beta\{(3/2 \sin^2 \gamma) - 1\} \qquad \text{.... (3.33)}$$

where β is a constant for a given subshell of a given atom and X-ray photon. Reilman et al [143] have tabulated calculated values of β for the important transitions of all elements using the commonly used X-ray sources such as Al kα and Mg Kα.

The calculated values for the cross-section σ has been tabulated by Schofield [144] for the Kα lines of magnesium and aluminium; all subshell cross-sections are given for Z values up to 96.

Seah [105] gives the following relationships of analyser etendue for some of the commercial instruments for constant ΔE mode:

$$G(E_A) \propto E_A^{-1}$$

and, $$G(E_A) \propto E_A \qquad \text{for constant } \Delta E/E \qquad \text{.... (3.34)}$$

Thus all the spectrometer terms can be estimated. However, factors affecting the measurement of I_A and the types of reference data banks for I_A^{∞} should also be considered.

3.5.3: The measurement of intensity, I_A

In the XPS spectrum the peaks appear on a small background and I_A is obtained by simply calculating the area under the appropriate peak. To be able to calculate the peak area it is necessary first to define a precise position of the background over which the peaks are superimposed. This is necessary because contributions from secondary structures such as Shake -up/off satellites, ghost satellites due to the X-ray source and contributions due to multiplet splitting have to be taken into account.

Two popular methods of background data subtraction are currently in common use and most commercial data analysis systems have facilities for carrying out either method. The first method is the "linear background subtraction", in which two suitably chosen points R and T, on either side of the given spectrum, are defined and a straight line, as shown in figure (3.11a), drawn between these points represents the background. The linear line, however, can underestimate the background at the low kinetic energy side of the peak as it may not take into account the full contributions due to inelastic photoemission, i.e. energy loss of the photoelectron within the solid. The second method is the non-linear background subtraction due to Shirley [145] and this gives the curved background as shown in figure (3.11a). In this method the background at any point is assumed to arise solely from the scattering of electrons of higher kinetic energy. The background is thus assumed to be proportional to the integrated photoelectron intensity of all the electrons with higher kinetic energy than the channel comcerned such that if the signal at the i^{th} channel is S_i, which is a sum of the background contribution, B_i and the peak contribution, P_i, then:

$$B_i = k \sum_{j = 1+i, N} P_j \qquad \text{.... (3.35)}$$

Similar to the linear background method, the end points R and T must be chosen.

Modification of Shirley's method have also been suggested [146] to take into account that some of the tail at the low kinetic energy side can be due to shake-up and shake-off electrons. Bishop [146] also points out that symmetry problems may arise with the choice of the precise position of point R, which can be worse for linear

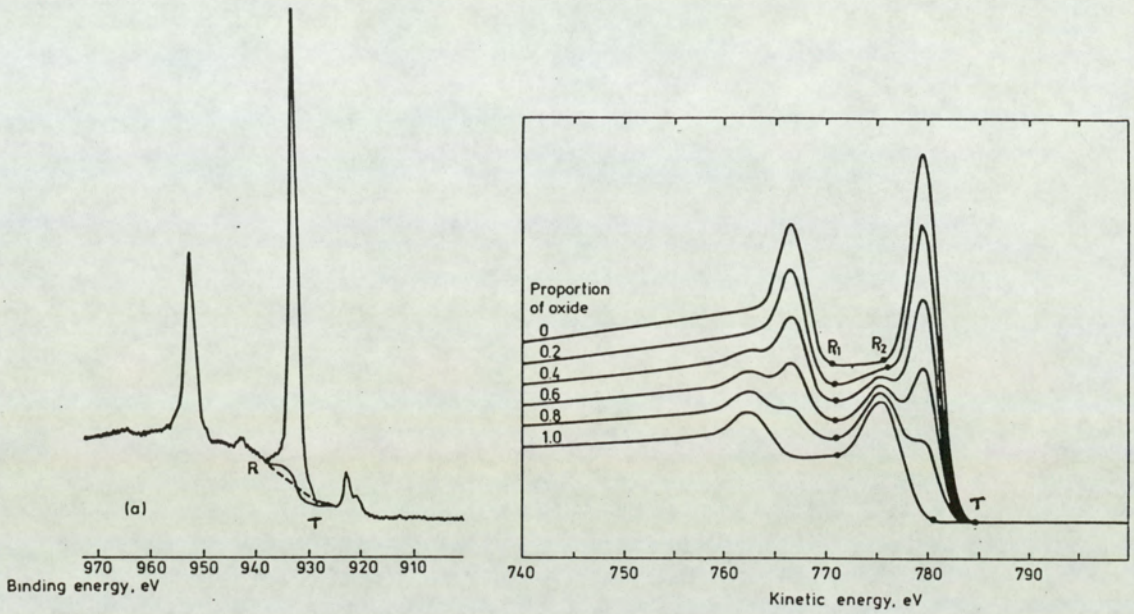

a b

Figure 3.11.
a) photoelectron peak from metallic copper showing background substraction methods [141].
b) simulated spectra for mixtures of Fe and Fe_2O_3 at various proportions, the two options for R are shown by R_1 and R_2 [146]

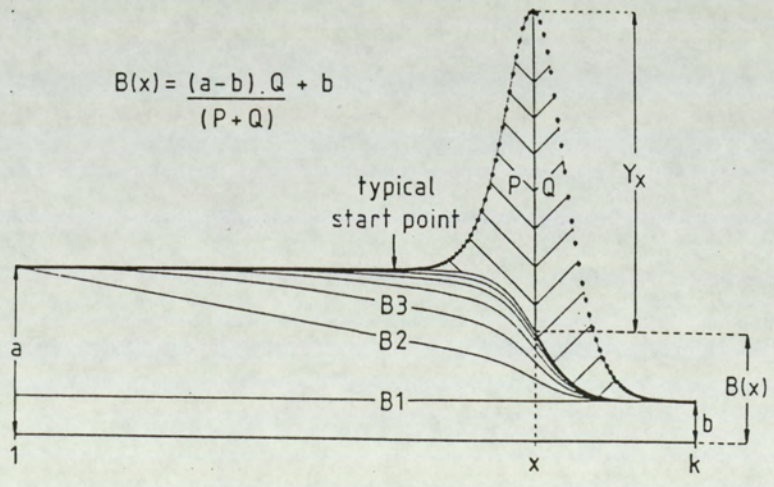

Figure 3.12.
Inelastic background determination. B(x) is the background at point x in the spectrum which contains k equally spaced points [147].

background subtraction as is shown in figure (3.11b) for the case of the oxide/metal signals of Fe_2O_3/ Fe. The points R_1 and R_2 can be chosen which will give either an overestimation or underestimation respectively of the area to within 30%.

Non-linear background subtraction may also be performed using the method suggested by Proctor and Sherwood [147], which is shown in figure (3.12). Here, the value of the background at a point x in a spectral array of k equally spaced points of separation h is given by:

$$B(x) = \{(a - b)Q / (P + Q)\} + b \qquad \ldots. (3.36)$$

where a and b are the average start and end points respectively, (P + Q) is the total background subtracted peak area and Q is the background subtracted area from point x to point k, which is found by using the trapezoidal rule to be:

$$Q = h\left[\left(\sum_{i=x,k} y_i\right) - 0.5\,(y_x + y_k)\right] \qquad \ldots. (3.37)$$

Initially, the background subtracted areas are calculated by choosing a linear constant background of magnitude b as shown by the line B_1, which is then used to calculate new background as shown by line B_2. The process is then repeated until the area A (where area A = P = Q) remains essentially unchanged on successive iterations. Typically the start point is chosen close to the peak under study to keep the number of required iterations to a minimum.

There are however drawbacks of using any type non-linear background subtraction. In general the non-linear background removal becomes more and more prone to error as the energy range over which the subtraction is carried out is increased. Also, the non -linear subtraction underestimates the background at the high kinetic side of the spectra. Thus, for cases where an element is present in various chemical states, the contributions due to the higher kinetic energy electrons (from the lower oxidation states) may seem to be more enhanced. Thus a recommended universal method of defining I_A (i.e. defining a background) does not exist. However, Seah [105]

suggests that the linear background subtraction works well for most insulators due to the fact that on the lower kinetic energy side there exists a clearly observed energy interval between the peak and the background rise; and for metallic samples any measurement of the area, consistently used, will give reasonable results between metallic systems.

Once the background line is chosen, measurement of the peak area is simple for well resolved and well defined single components. But often there may be more than one chemical state of the same element present which may have different binding energies and give rise to multiple peaks. These peaks are often not separated sufficiently to appear well resolved and thus in order to obtain accurate binding energies and areas it is necessary to resolve the multiplet envelope into its single component peaks. This operation is referred to as curve resolution or curve synthesis and is carried out using a computer. The first requirement to any form of curve synthesis is a knowledge of the line shape exhibited by a typical single peak. For most purposes a typical starting point may be the assumption of a 50% Gaussian and 50% Lorentzian shape for component peaks, which then can be successively changed to give the best line shape. The component peak heights, widths and positions are adjusted until the calculated envelope matches the experimental one.

In all curve synthesis excerises it is necessary to be aware of the fact that there are many possible solutions, depending on the number and widths of the components. A prior knowledge of the width and peak position (i.e. binding energy) of a standard sample is useful in evaluating the number of peaks that may be present. Also, a few restrictions have to be made depending on theoretical considerations. Some of these restrictions are listed as below:

1) the intensity ratios of the doublets are kept fixed (according to the area ratio given by the spin-orbit splitting);

2) the widths of the components should be semi-fixed as it should take into account that the widths of the $2p_{1/2}$ peaks are virtually always found to be broader than

the $2p_{2/3}$ companions (Briggs [108]);

3) The peak shapes of the components should be approximately the same.

Hence using the curve synthesis process, with some prior knowledge of the sample and a few restrictions, the areas due to the component peaks can be determined.

3.5.4: Reference data banks for I_A^∞

In current literature there are many sets of reference data available for I_A^∞ [148-150]; they were obtained using one of the following methods:

i) measurements from known reference compounds in powder form [149,150];

ii) measurements from elemental foils [150];

iii) calculation [148].

In this thesis, the calculated values due to Wagner et al [148] are used which are also referred to as "atomic sensitivity factors". The calculations are based on equation (3.23), which may be written for a spectrometer with uniform illumination of a homogeneous sample as:

$$I_A^\infty = \sigma_A(h\upsilon)\, L_A(\gamma)\, N_A^\infty\, \lambda_M(E_A)\, G(E_A) \qquad \ldots. (3.38)$$

But substituting for $G(E_A)$ as given by equation (3.34), the following is obtained:

$$\Rightarrow \qquad I_A^\infty = B\{\, \sigma_A(h\upsilon)\, L_A(\gamma)\, N_A^\infty\, \lambda_M(E_A)\,\} / E_A \qquad \ldots. (3.39)$$

where B is the proportionality constant, which may be eliminated by referring the I_A^∞ values to the intensity of one particular peak defined as unity. Wagner et al [1979] uses the intensity, I_F^∞, for F 1s to be unity in their calculations, thus their data bank is relative to the F 1s intensity. They have also used calculated values of $\sigma_A(h\upsilon)$ given by Schofield [144] and Penn' [151] calculated values for $\lambda_M(E_A)$. It should be noted here that Wagner's data bank [148] should only be used when the electron spectrometer used for measuring I_A has the same transmission characteristics as the double pass cylindrical mirror type analyser supplied by "Physical Electronics" (Perkin-Elmer). Investigations carried out by the Surface Science group at Aston University on the

measurements of sensitivity factors using the Kratos XSAM-800 system yielded the setsitivity factors to be approximately the same as those by Wagner et al [148].

The use of calculated reference banks in XPS measurements will normally yield quantitative results accurate to within 10-20%. However there are some drawbacks. In case of the transition metals, for example, the value of the sensitivity factors in one chemical state may not be valid for another chemical state.

3.6: Energy Calibration of the spectrum

One of the common methods of calibrating the electron spectra is to employ a relative calibration procedure (Johansson et al [152]) in which well known standard calibration lines such as the gold 4f line and the carbon 1s line are used. These lines are suitable for calibration for several reasons. The intensity is high and since the lines are narrow, the line positions can be accurately determined. These lines are usually incorporated with the sample spectra by either mixing gold or graphite in powder form with the unknown sample (which is also in powder form) or depositing the gold by evaporation. This method of relative energy calibration is advantageous as it is also employed for reducing surface charging effects (this is further discussed in section 3.7 in connection with sample charging effects). However the main disadvantage is the uncertainty caused by the spread of values in literature; for the C 1s line it ranges from 284.6 eV to 285.2 eV and for the Au 4f line the range is 84 eV ± 1 eV. Bird and Swift [153] carried out investigations to determine accurately the binding energy values of some of the common standard calibration lines; compilations of data from other workers are also given.

3.7: Charging effects in XPS

This is again a feature particular to XPS of solids. When the sample atoms lose electrons in the photo-emission process, the surface acquires a net positive charge. Conducting samples in electrical contact with the spectrometer probe are not influenced

by such charge buildup as the positive holes left by ejected photoelectrons are filled by electrons conducted from earth through the bulk interior of the surface. Thus the positive charge build up only affects insulating and semiconducting surfaces. The positive charges produce a retarding effect on the ejected photoelectron and the measured kinetic energies for electrons from such a sample is thus lowered. Any charging effects can be easily determined from the positions of two calibration lines at appreciable distance from each other [152].

In spectrometers where an achromatic X-ray source is used, this net positive charge is partly neutralised by a background of low energy electrons (< 5 eV) produced by the bremsstrahlung X-rays striking the inside of the source window and the internal parts of the apparatus. These low energy electrons are drawn to the positively charged sample such that an equilibrium charge results. There are three main procedures of reducing the effects of charging:

1) Use of standards; this procedure makes use of standard reference lines which can be obtained either from powder mixtures (i.e. both the unknown sample and the standard sample) or from a deposit on solid. The standards chosen should be unreactive with the sample and should closely follow the charge fluctuations in the sample. Problems can arise from if differential charging exists between the sample and the standard. Powdered graphite (C 1s line) is a commonly used reference material [153], whereas gold (Au 4f) can be used in the powder mixture form [154] or deposited [155]. The main limitation in using the mixture method is the experimental difficulty in obtaining homogeneous mixtures. The C 1s peak from contamination layers can also be used for the purpose of energy referencing [156]. This is not usually affected by differential charging with the sample.

2) Use of low energy electron flood gun; An electron floodgun can be used to bombard the samples with electrons to neutralise the positive charges. The best results can be obtained with an electron beam of low energy (<1 eV), with respect to the vacuum chamber at earth, from a source very close to the specimen (Hunt et al [157]).

This use of the low energy electron flood gun is advantageous in situations where investigations of insulating materials are carried out with an X- ray source fitted with a monochromator (flood gun compensates for the loss of Bremsstrahlung-excited electrons) and for situations where the static charge is inhomogeneous across the sample. However this technique has its own problem in that it can create a negatively charged sample.

3) X-ray induced Auger peaks; The X-ray induced Auger peaks can be used to reference shifts in the Photoelectron peaks.

3.8 RADIATION DAMAGE

The XPS technique has been used as the analytical tool for the investigations carried out in this thesis because of its chemical specificity and surface sensitivity and as well as for its relatively non-destructive nature (as far as induced changes in the surface chemistry is concerned) [158] compared with other techniques such as AES [159].

CHAPTER 4: Instrumentation and experimental details

4.1: Introduction

In this investigation XPS has been used to analyse the surface chemical damage induced by particle bombardment (ions electrons and atoms). This chapter describes the different sample types, the experimental conditions employed, the various types of analysis involved and the instrumentation constituting the photoelectron spectrometer and various radiation sources. The samples used were mostly transition metal oxides, but other metal oxides have also been used.

4.2: Materials and preparation

The materials used were all commercially obtained high purity (99.99%) metal oxides. These were: MgO, Al_2O_3, TiO_2, FeO, Fe_2O_3, Fe_3O_4, CoO, Co_3O_4, ZrO_2, Nb_2O_5, Ta_2O_5 and WO_3. All were obtained in powder form except the titanium dioxide, which was in the form of small chunks. These oxide chunks were finely ground to the powder form using a porceline mortar and pestle, thus minimizing contamination. Pure (99.99%) soft lead sheet was used to mount the powders for analysis in the spectrometer. Prior to the mounting procedure, the oxide powder was intimately mixed with gold powder in order to provide a reference binding energy, unless otherwise stated. Sample surfaces were prepared by first covering a sheet of lead of dimensions 4mm x 15 mm with the oxide powder. Another piece of lead sheet was placed over the powder and the lead/powder "sandwich" was then placed between two flat hardened steel blocks which were pressed gently using a hydraulic press thus embedding the powder into the surface of the soft metal. The two lead sheets were then separated to give two specimens for analysis. Any loose powder remaining on the surface was removed by gently tapping the specimen. The sample surface was then attached to a rectangular copper sample holder at the end of the fast insertion probe (FIB) by means of a strip of double-sided adhesive tape. A thin strip of aluminium foil

was wrapped around the double-sided tape before placing the specimen on to it. This provided the electrical contact between the specimen and the FIB.

High purity gold, silver and copper foils were used for the purpose of calibrating the energy scale of the spectrometer. The foils were cut into rectangular strips of approximate dimensions of 4mm x 15mm. The surfaces were cleaned using acetone and then followed by a thorough rinsing in IPA, before being attached to the FIB; this was carried out as described above for the case of powder oxide on lead sheet specimens.

4.3: Bulk characterization of powder samples: X-ray diffraction

Each of the metal oxide powders were first bulk characterised by employing X-ray diffraction by means of the Debye-Scherrer technique. The powder was placed in a fine glass capillary tube of 0.5 mm in diameter, which was then mounted in a conventional powder diffraction camera. The camera has an inside diameter of 180 mm such that 1 mm of the x-ray film corresponds to 1^{o} in the angle 2θ where θ is the Bragg angle. This enables direct measurements of the 2θ values. Cobalt kα radiation was used to irradiate the powder specimens of FeO, Fe_2O_3, Fe_3O_4, CoO and Co_3O_4 as these oxides have a relatively low mass absorption coefficient for this line. For the oxides MgO, Al_2O_3, TiO_2, Nb_2O_5, ZrO_2, WO_3 and Ta_2O_5, copper kα radiation was used. The x- ray tube was operated at 40 kV and 20 mA, with exposure times of around 1 hour being typical. The powder samples were then bulk characterised by comparison of the interplaner spacings obtained from the diffraction pattern with interplaner spacings listed in the x-ray powder data file of the American Society for Testing and Materials (ASTM) [160].

4.4: X-ray Photoelectron Spectroscopy and particle bombardment

4.4.1: General features of the electron spectrometer

The X-ray photoelectron spectrometer can be divided into several parts: the

X-ray source which is used to excite photoelectrons from the sample, the analysis chamber with its ancillary vacuum systems maintaining the sample at whatever conditions are desirable for the experiment, the electron analyser which selects the electrons emitted by the sample according to their kinetic energy and an electron detector.

The electron spectrometer used in this investigation was a XSAM 800 ESCA-AUGER instrument manufactured by KRATOS. It is based on an electrostatic hemispherical electron analyser which combines high resolution with high transmission (i.e. high sensitivity) in the same instrument. Figure (4.1) show the arrangement of the main components in the specimen analysis chamber and figure (4.2) shows a schematic diagram of the x-ray photoelectron facility.

4.4.2: The X-ray source

The XSAM 800 is fitted with a standard dual anode X-ray source, allowing the use of either magnesium or aluminium Kα radiation by simple external switching without the need to break the vacuum. A schematic diagram of the x-ray source can be seen in figure (4.3). The anode has a tapered end with two inclined faces on which films of magnesium and aluminium respectively are deposited. The base material is copper to allow for high heat conduction to the coolant (water). Typically ~10 μm in thickness of anode material is needed representing a compromise between being thick enough to exclude copper Lα radiation and thin enough to allow heat transfer. The anode assembly is surrounded by a cylindrical focussing shield at the same potential as the filament. The anodes are operated at a high positive potential with respect to the filament; there are two filaments, one corresponding to each anode. A thin aluminium window in front of the anode protects the sample from stray electrons, heating effects and from possible contamination originating inside the source. However, the main function of the window is to act as a X-ray filter to cut out all but the Kα radiation. The gun is pumped differentially by its own ion pump to reduce the chances of

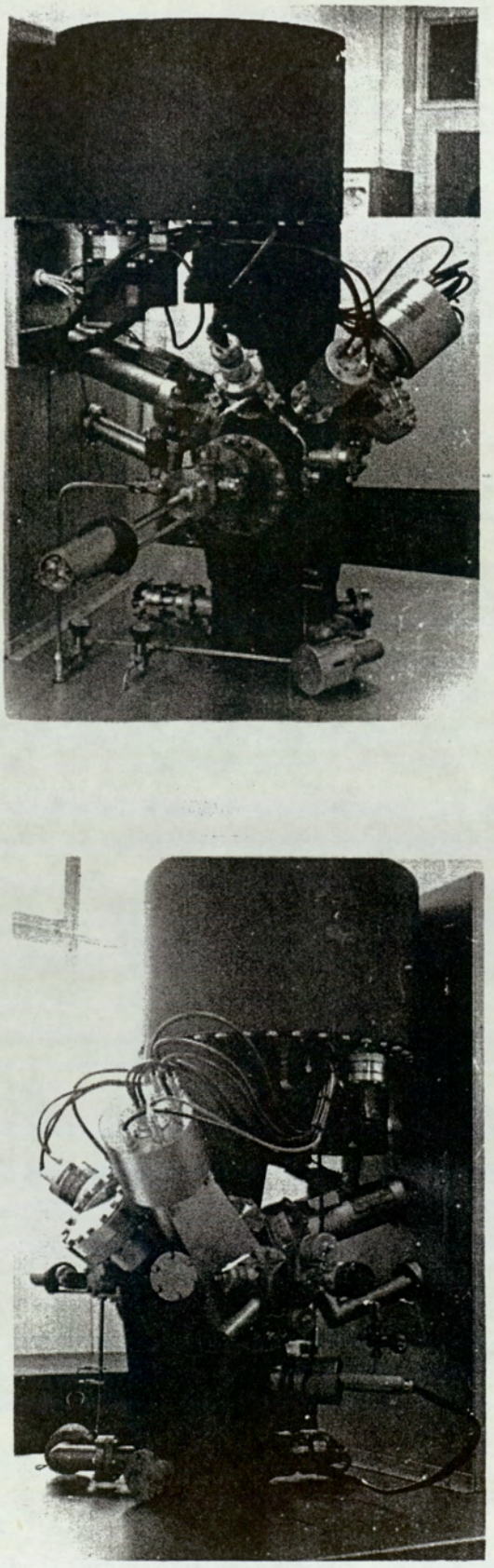

Figure 4.1.

Two views of the Kratos XSAM 800 system.

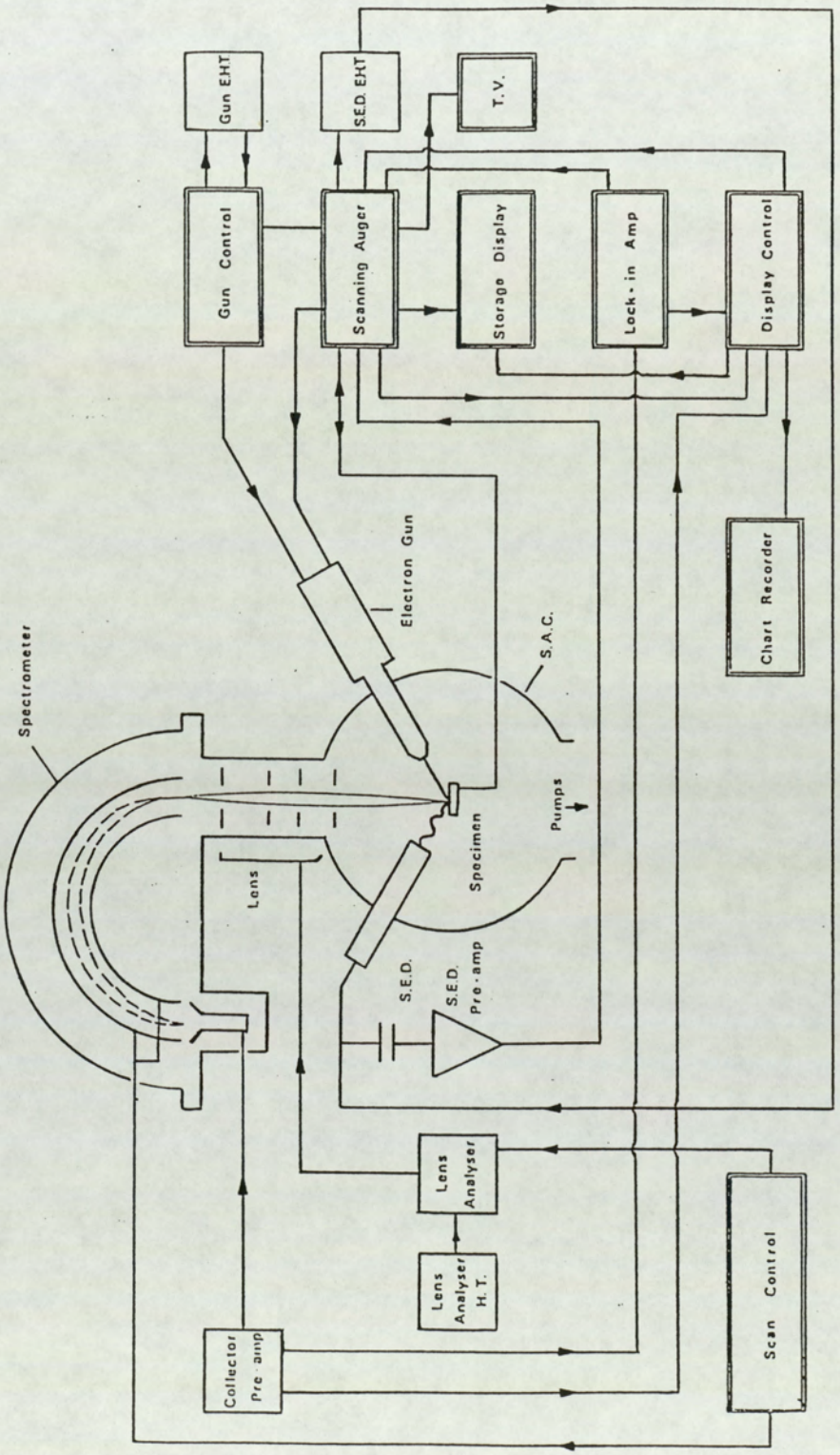

Figure 4.2.
Schematic diagram showing the XSAM-800 system.

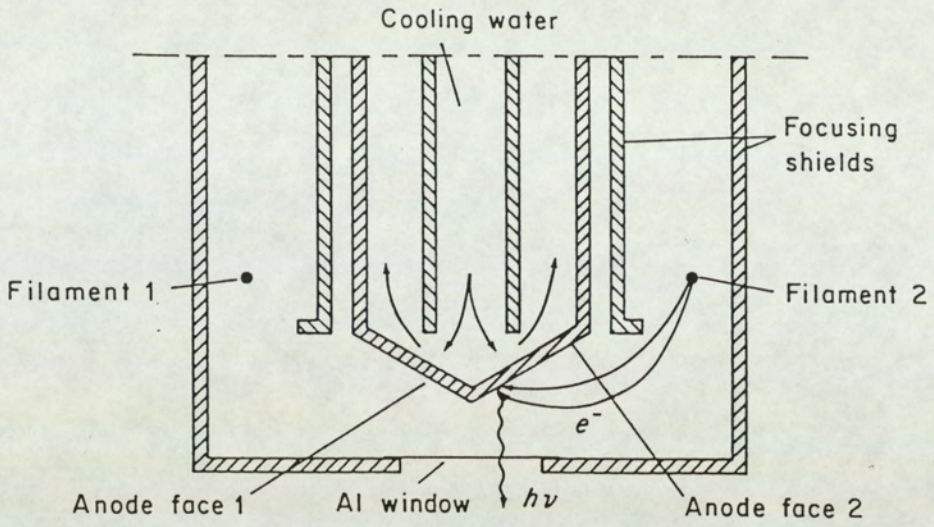

Figure 4.3.
Schematic diagram of the X-ray source.

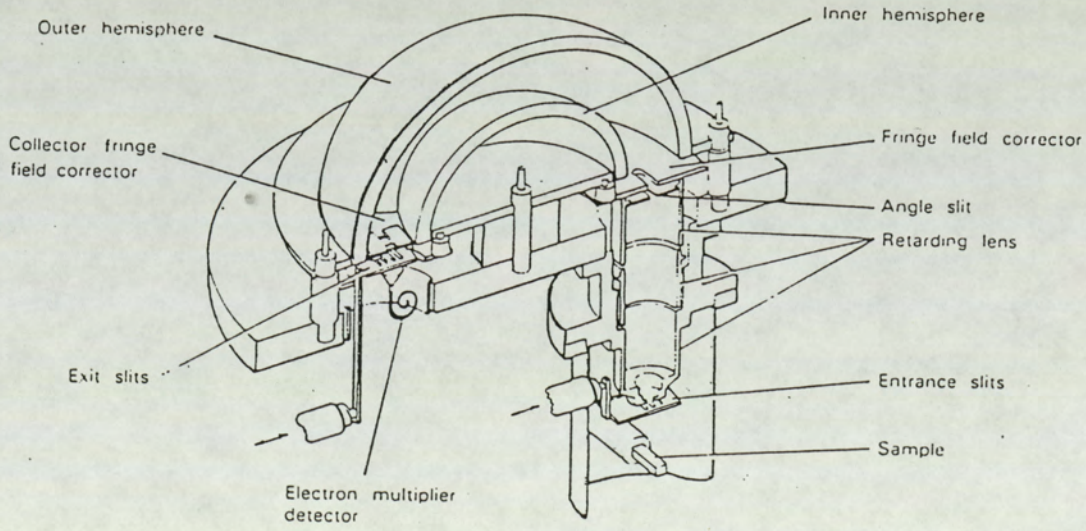

Figure 4.4.
Schematic diagram of the hemispherical sector analyser.

contamination of the anode itself.

The Mg Kα and Al Kα x-ray lines have associated energies at 1253.6 eV and 1486.6 eV with F.W.H.M. values of 0.75 eV and 0.85 eV respectively. There is an essential reason for the double anode facility; in any x-ray excited electron spectrum both photoelectron and Auger peaks appear and interferences can result. Since photoelectron energies are dependent on the excitation energy, whereas Auger electron energies are fixed, a second X-ray line with different energy can thus resolve the difference.

Although the characteristic line energies of the dual anode x-ray gun are in the region 1250 - 1500 eV, it is necessary to use exciting electron energies of about an order of magnitude higher for efficient production of X-rays [161]. The accelerating potential in the instrument used here can be varied in the range 0 - 15 kV, the maximum total power dissipation being 450 watts. The bombarding current used throughout the investigation was 15 mA, as a high bombarding current is desirable for purposes of optimising sensitivity at a given resolution since photon flux is directly proportional to the current.

4.4.3: The electron energy analyser

In X-ray photoelectron spectroscopy, two types of electrostatic analysers are in common use; these are the concentric hemispherical analyser [162] and the cylindrical mirror analyser [163]. Both are dispersive, i.e., the action of a deflecting electrostatic field disperses the electron energy in the range E to E + δE where E is the pass energy and δE is the energy window. In general the hemispherical analyser is capable of high resolution whilst the cylindrical mirror type gives a high transmission. The XSAM 800 is fitted with a hemispherical sector analyser (HSA) in which high resolution has been combined with high transmission by means of an aberration compensated input lens [164].

The HSA is shown schematically in figure (4.4). Two hemispherical surfaces of inner radius R_1 and outer radius R_2 are positioned concentrically with a potential

difference ΔV applied between them. This arrangement of a spherical deflector was first described by Purcell [165]. Electrons focussed at the entrance slit with a kinetic energy E pass between the hemispheres in circles and are then refocussed at the exit slit. The entrance and exit slits are each centred on a distance R_0 from the centre of curvature and lie on the same diameter; where $R_0 = (R_1 + R_2)/2$. The particles follow a circular orbit of main radius R_0 [164] when:

$$\Delta V = E\{(R_2/R_1) - (R_1/R_2)\} \quad \ldots. (4.1)$$

For equal entrance and exit slit widths W (as is the case in the XSAM 800) the resolution of the system, in its simplest form (neglecting the angular terms) is given by Kuyatt and Simpson [166] to be:

$$\Delta E = (E \times W)/2R_0 \quad \ldots. (4.2)$$

From the above equation, it can be seen that for a pass energy E of 1000 eV and a mean radius of 127 mm and a typical slit width of 3 mm, the resolution is ~11.8 eV which is inadequate for XPS analysis. The input lens overcomes this problem by retarding the electrons to a much lower transmission energy dependent on the mode of operation of the analyser (i.e. the FRR or the FAT modes which will be discussed below). For example, if the 1000 eV electrons are retarded to 100 eV then the resolution achieved would be 1.18 eV. This effect of a focussing retarding field at the input of a dispersive analyser was discussed by Heddle [142] and shown generally to increase the resolution.

The disadvantage of using the retarding input lens is that the collected photoelectron current is made smaller due to the acceptance angle of the input lens being smaller than that of the analyser. This is a direct consequence of the Helmholtz Lagruanges law which can be expressed as :

$$\text{Magnification, } M = \{(E_s)^{1/2} \sin \alpha_s\}/\{(E_a)^{1/2} \sin \alpha_a\} \quad \ldots. (4.3)$$

where E_s and E_a are the kinetic energy of the photoelectrons leaving the sample and that of the electrons leaving the lens (to enter the analyser) respectively. α_s is the angle that the electron path makes with the normal after leaving the sample and α_a is the

acceptance angle of the analyser. In general, the magnification is approximately unity. Equation (4.2) can also be written (again neglecting angular terms) as:

$$\Delta E = (E \times W)/2R_0\} \times (E_s/E_a)^{-1} \quad \ldots. (4.4)$$

where (E_s/E_a) is known as the retardation ratio of the analyser. Thus, for a given R_0, the resolution can be improved by either decreasing the slit width and/or increasing the retardation ratio.

Two settings of the spectrometer magnification are possible as a consequence of using the input lens. These are denoted by a high and low settings on the control console, and are schematically illustrated in figures (4.5a,b). In low magnification mode, the input lens accepts electrons only through a narrow angle although a large number of cones may be accepted resulting in a wide area of surface being analysed. This magnification setting is ideal for maximum signal intensity. In the high magnification mode, the input lens accepts electrons through a wide angle which have originated from a small "spot" on the surface. The high magnification setting was chosen for the production of spectra in this thesis. This enabled a small spot area of the surface to be analysed thus enhancing the chances of detection of reduced states of the oxides after ion bombardment.

In addition, two modes of analyser operation are available on the XSAM 800. These are the fixed analyser transmission (FAT) and the fixed retarding ratio (FRR) energy modes.

In the FAT mode, the transmission energy of the HSA is maintained constant such that the electrons entering the analyser have their energy retarded by a varying proportion, dependent upon the kinetic energy. Three fixed transmission energies of 38, 65 and 100 eV are possible and these correspond to the resolution settings of high, medium and low respectively. These transmission energies are independent of the possible modes of magnification. Thus, in the FAT mode the resolution is constant

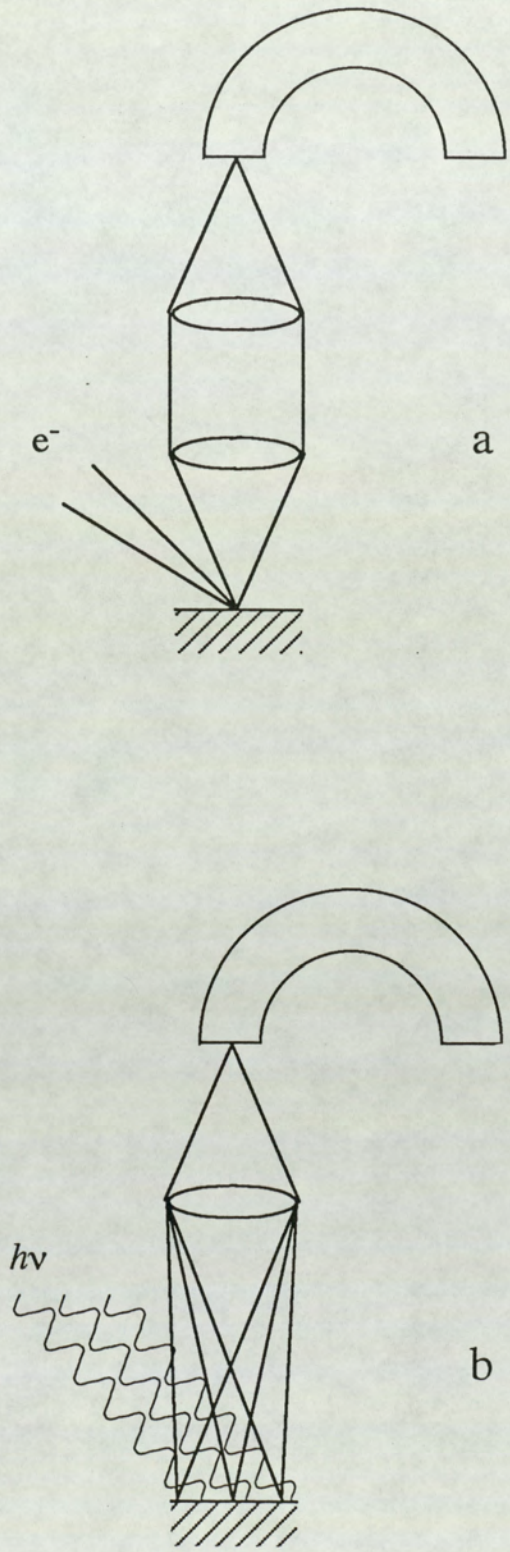

Figure 4.5.
Schematic diagram showing the two modes of analyser magnification.
a) high magnification
b) low magnification

throughout the whole kinetic energy scan range. However, the sensitivity is inversely proportional to the kinetic energy at the sample, E_s.

In the FRR mode, electrons entering the analyser have their energy retarded by a constant proportion of their initial energy. The transmission energy of the analyser is continuously varied throughout the energy scan range in order to maintain the constant retarding ratio. Four retarding ratios are possible and these are set by the magnification and resolution settings. Also, the resolution and sensitivity vary with the kinetic energy at the sample, E_s; in the entire scan range the sensitivity being directly proportional to E_s.

The analyser energy mode chosen during analysis depends upon the types of information required. The XPS data presented in this thesis were obtained with the analyser operated at the FRR mode. This mode was chosen for various reasons. Firstly, it is desirable that inter-spectrometer spectrum comparisons be made. This is difficult at low energies when operating in the FAT mode since under these conditions the transmission behavior is a very individual aspect of the analyser [164]. Secondly, in the FRR mode the area of the sample analysed remains constant throughout the whole energy range, whilst it may vary slightly with energy in the FAT mode. For accurate quantification of the ion bombardment induced damage, it is essential that the analysis area remains constant. Thirdly, the XPS spectra of interest obtained using FRR mode was of adequate intensity. In the FRR mode, the high magnification and medium resolution settings have been used throughout the whole investigation. This was found to provide sufficient resolution while maintaining a reasonable signal intensity.

An additional means of controlling the instrument resolution and sensitivity is provided by means of the adjustable entrance and exit slits of the analyser. A single control alters the width of both slits simultaneously, thus keeping the slit widths equal. Widths of 1, 2, 3 and 5 mm are available. The smallest slit width provides maximum resolution with minimum sensitivity. The spectra presented in this thesis were generated with the slit widths adjusted to the highest setting in order to obtain maximum

sensitivity.

The HSA and the SAC are surrounded by a mu-metal casing to provide shielding from stray external fields.

4.4.4: The electron detection system

The electrons which emerge from the electron analyser are detected by a channeltron continuous dynode type multiplier. The output of the multiplier is Pre-amplified then and fed to a bar-graph ratemeter and to a microcomputer. The pre-amplifier is capable of giving two modes of operation, namely the pulse mode and the current mode of detection.

The pulse mode gives a true count rate, on the ratemeter, of the electrons being detected by the multiplier. The disadvantage of this mode of operation is that the multiplier can be saturated by a very high count rate. The current rate of operation allows the multiplier to operate at a lower gain and thus overcoming the problem of detection at very high count rates. Most of the experimental work presented in this thesis has been carried out with the pre-amplifier at the current mode. However, the pulse mode of operation has also been used occasionally.

4.4.5: Recording the spectral information

The XSAM 800 is interfaced to an Apple Plus (48 k) microcomputer system with a 16 k Ram card, Increasing the random access memory to 64 k. This is adequate for complex data collection with graphics facility. Instrument control and data collection was achieved by means of the software written in UCSD Pascal by Sherwood [167]. The microcomputer has facilities for a maximum of seven expansion boards and five expansion cards were added. These were as listed below:

1) Expansion board no 0; this is the 16 k Ram card to give upto 64 k to be able to run the software written in UCSD Pascal.

2) Expansion board no 1; the printer card.

3) Expansion board no 3; 80 column card; this facilitates the display on the monitors as the Pascal software requires 80 column output (the Apple Plus has a 40 column output).

4) Expansion board no 4; Parallel I/O , can be used as either input or output but used here only as output. There are 32 lines and this is adequate for instrument control as the XSAM requires 32 output lines for setting instrument conditions such as : starting kinetic energy, energy window, analyser modes (i.e. FRR or FAT), resolution settings, magnification settings, number of scans and the operation of the X-ray gun power supply and the ion gun power supply.

5) Expansion board no 5; Counter card, this is the input card and counts the output pulses from the pre-amp and stores the data on to a floppy disk. The data is displayed as it is collected.

6) Expansion board no 6; Controls an extra disk drive.

A second microcomputer, an Apple IIe (64 k), can then be used to analyse the stored data. Facilities for data transfer from the Apple IIe to an IBM PC are also available; thus fast peak synthesis can be achieved using the curve-fitting procedure as outlined by Sherwood [167-170]. Each data file is first converted into a text file and then transferred to the IBM.

The spectra is presented in the conventional manner by recording the number of electrons, N(E), emitted from the surface as a function of the energy E. More correctly, however, EN(E) as a function of E is given by a hemispherical sector analyser in the FRR mode, and $E^{-1}N(E)$ as a function of E in the FAT mode except at lower energies [164].

4.4.6: The vacuum system

A schematic diagram of the spectrometer vacuum system is shown in figure (4.6). The vacuum system essentially consists of a diffusion pump and two rotary pumps for providing the backing pressure. A backing pressure of approximately 0.2

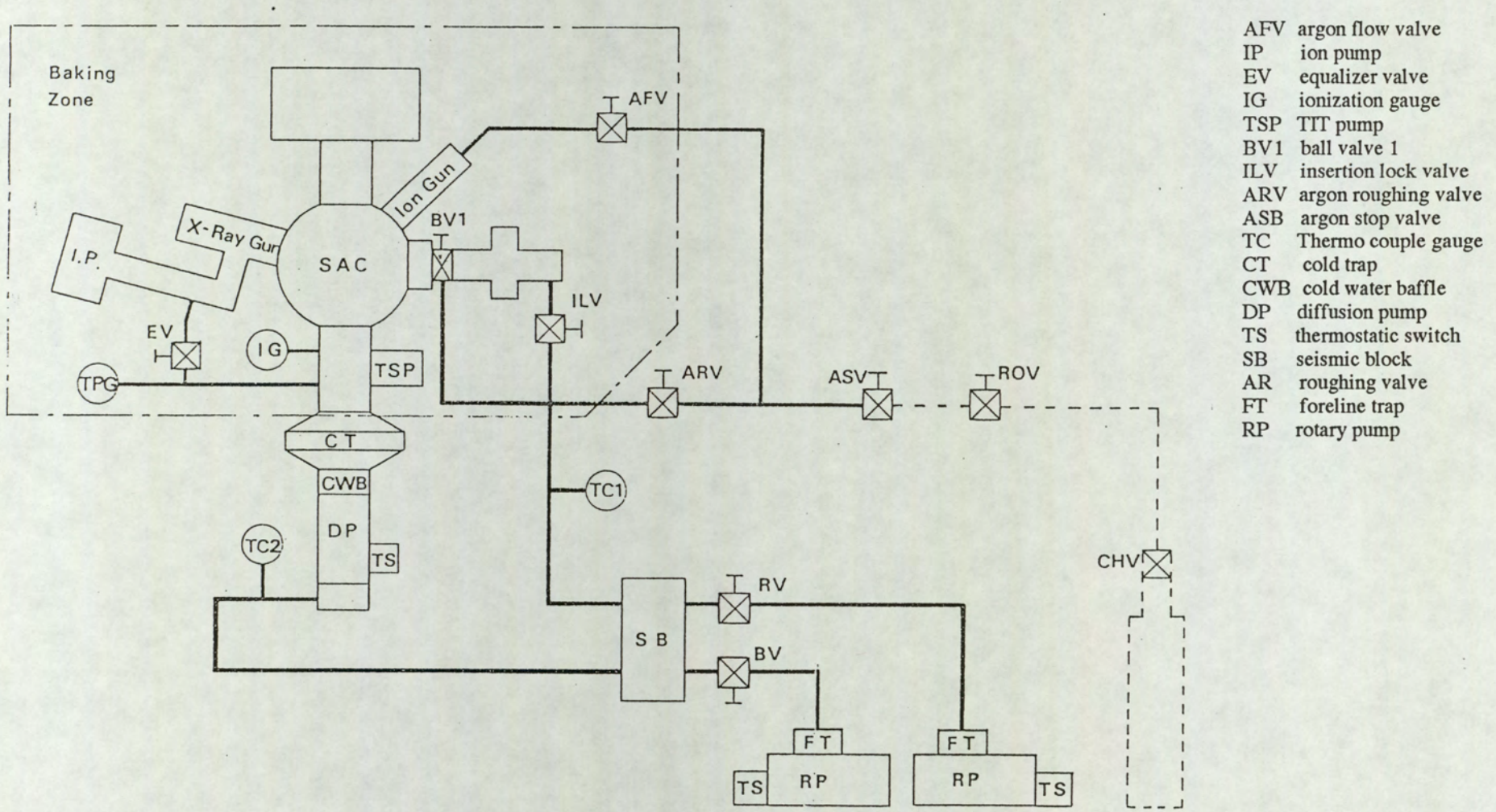

Figure 4.6. Schematic diagram of the vacuum system.

torr is required before the diffusion pump can be operated. A small water filled baffle followed by a larger liquid nitrogen filled baffle mounted above the top of the diffusion pump provides the cold trap to reduce the amount of pump fluid entering the system, while the rotary pumps are equipped with molecular sieve traps. The vacuum system also contains a titanium sublimation pump which operates by "gettering" i.e. by reaction of evaporating titanium with other molecules and can be used at pressures as high as 10^{-6} torr. It is excellent for pumping most atmospheric constituents including hydrocarbons but its main contribution is to achieve the last order of magnitude or so decrease in pressure necessary if an ultra high vacuum of 10^{-10} torr or below is required. However, owing to its reactive nature this pump was not operated while a sample was being investigated.

The twin anode x-ray gun is pumped independently by a 8 litre/sec ion pump and because of its evacuation procedure no intervening traps are required.

The UHV system is of all stainless steel construction, bakable at 150 °C; the system was backed regularly to expel adsorbed gases and water from the SAC walls. The UHV pressure maintained inside the SAC during analysis was always better than 10^{-9} torr. Pressure monitoring inside the SAC is achieved by the means of an ionization gauge and also a trigger-penning gauge for accurate measurement in the UHV range. Two thermocouple gauges are provided to monitor the backing and roughing pressures.

A direct fast insertion lock enables the sample to be inserted within a few minutes without degradation of the vacuum. This is achieved by first placing the insertion probe head containing the sample into a very small pre-chamber which is then evacuated from atmospheric pressure to ~5×10^{-3} torr with one of the trapped rotary pumps. A ball valve between the pre-chamber and the SAC is then opened slowly and the insertion probe is pushed into the required analysis position. Rotation of the insertion probe in any plane is possible such that the sample could be tilted or placed in a horizontal position as required. All the investigations in this theses were carried out

with the sample in a horizontal position at approximately 90^0 to the analyser input lens.

4.4.7: The ion source

Initial ion-bombardment of the transition metal oxide surfaces was achieved by the use of a KRATOS MACROBEAM ion gun. A simplified schematic diagram is shown in figure (4.7). A hot tungsten filament provides the electron emission into a positively biased grid, the electrons making several oscillations before being collected. Argon gas within the grid space is thus ionized and then extracted by an extractor plate. Electrostatic lens 1 focuses and adjusts the beam size and lens 2 provides the final focussing of the ion beam. Finally, the deflection plates which are located just inside the exit aperture position the beam onto the target. These plates also enable rastering of the beam.

The area of the sample rastered by the ion beam can be changed by varying the voltage, V_d, between the deflection plates. As the area of the sample rastered depends on the primary beam energy, E_0, and V_d by the equation [171]:

$$d = 0.79 \times (V_d/E_0) \times (D_g + 5.2) \qquad \ldots. (4.5)$$

Where d is the off-axis defletion and D_g is the distance between the sample to gun exit aperture; the value of D_g was kept constant at 5mm. Hence for the case of the set of investigations involving the beam energy variation at a given current density, the rastered area was kept constant by keeping the ratio (V_d/E_0) constant. The beam current was kept constant (at the different energies) by changing the pressure of argon inside the gun assembly.

For the set of investigations involving the variation of beam current density at a fixed beam energy the beam current was changed by again varying the argon pressure. Throughout the whole investigation of ion-bombardment using the MACROBEAM ion gun, the extraction current I_e and the ratio (V_d/E_0) were kept constant.

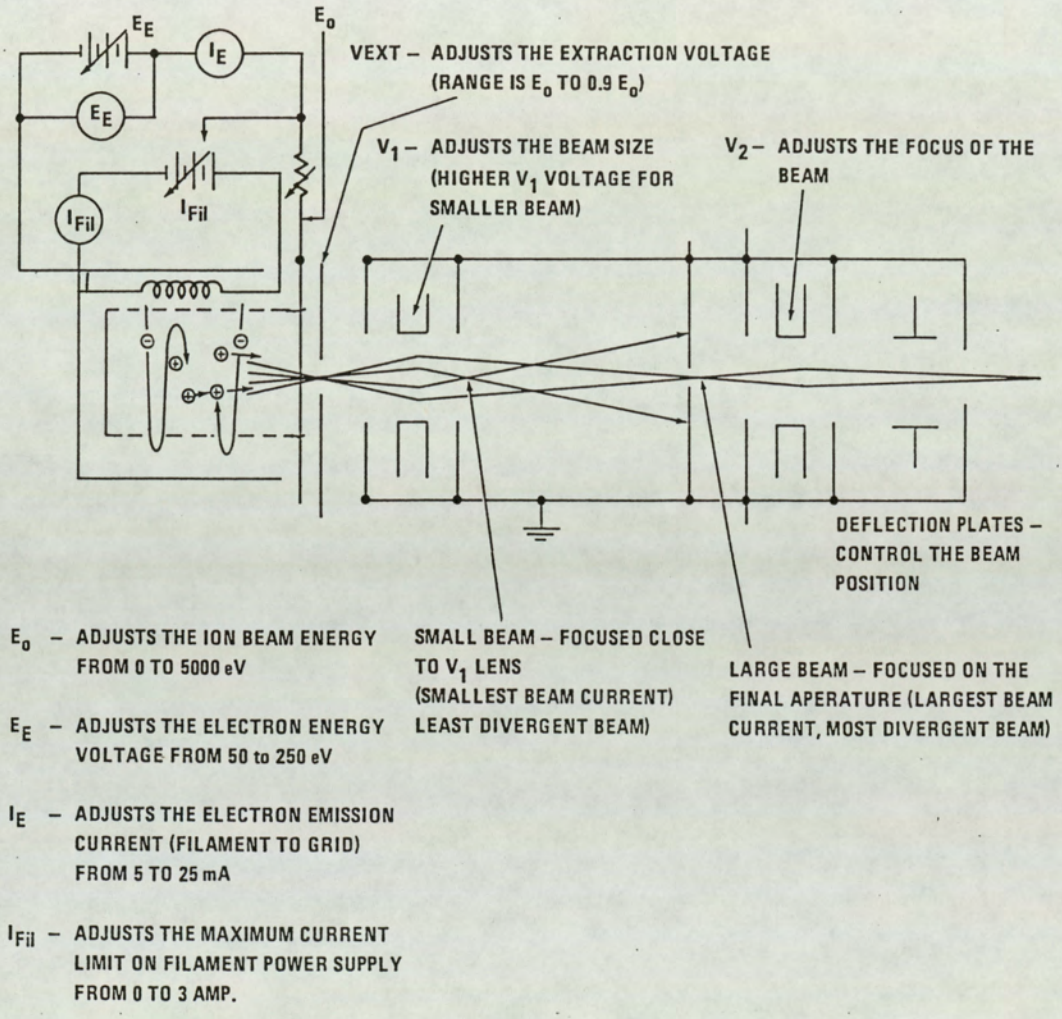

Figure 4.7.
Schematic diagram of the KRATOS Macro-beam ion gun.

4.4.8: The atom source

An Ion Tech FAB 11 saddle field source was used for the purpose of comparing the effect of fast atom and ion bombardment of some transition metal oxide surfaces under equivalent etching conditions. According to the manufacturer, the FAB 11 source provides a hundred percent neutral beam. However, characterization of the source carried out by Saied et al [172,173] showed the beam to be a mixture of neutrals and charged particles. This property was found to be advantageous for the purpose of this investigation as the same source can be used, with the aid of a positively biased deflection plate, for either atom or ion bombardment. This enables parameters such as beam energy and beam current density to be kept constant for comparisons of the effects of ion versus atom bombardment.

The FAB 11 source is shown schematically in figure (4.8). It is a modified version of the Ion Tech B11 saddle field ion source. The basic principle of this source has been described by Franks and Ghander [174]. The source is essentially a cold cathode device which operates without the aid of magnetic fields. The high voltage is applied to a pair of tungsten anodes. The inert gas is fed directly into the gun. A discharge is set up between the anodes and the cathode and the oscillating electrons are constricted to the "figure-of eight" paths as shown. Because of the long electron path lengths the probability of ionisation of a gas admitted inside the source is relatively high even at low pressures. The ions produced are then accelerated towards the cathodes and some of these ions are self-extracted into a small cylindrical chamber containing gas at the same pressure as that of the source interior. The exit aperture is at the end of this chamber. The production of the fast atom beam is achieved inside this chamber, the mechanism of which is not yet fully understood. It has been suggested by Fitch et al [175] that the fast atoms are produced by a charge exchange mechanism within this chamber, whereas Franks [176] proposes that this is due to electron capture of the secondary electrons produced at the exit aperture by ion collisions.

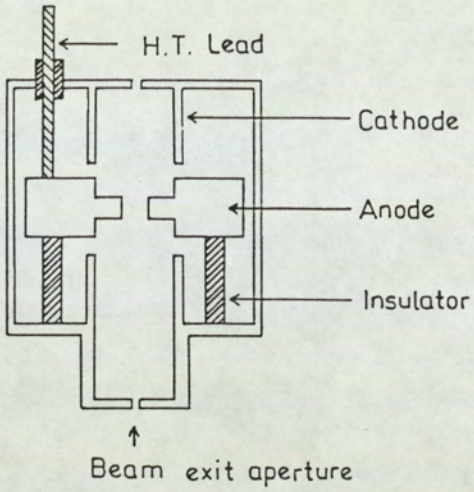

Figure 4.8.
Schematic diagram of the saddle field atom source, manufactured by Ion Tech Ltd.

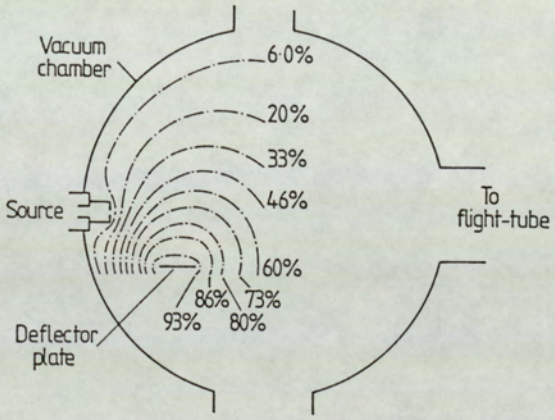

Figure 4.9.
Diagram showing equipotentials inside the chamber, due to a single deflection plate placed at 25mm from the source aperture.

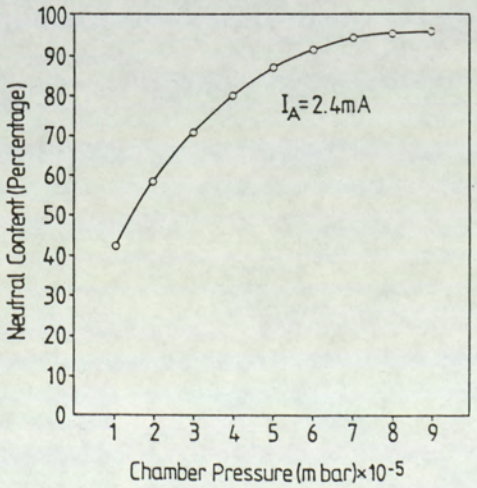

Figure 4,10.
Proportion of neutrals in the beam as a function of chamber pressure for a constant anode current of 2.4 mA.

During the operation of this source as a ion gun a gas pressure of approximately 10^{-5} torr was used which gave a low neutral content of about 30% and for use as a atom source a gas pressure of ~10^{-6} torr was used which corresponded to a neutral content of about 90% [173]. The deflector plate, as mentioned before, was used to deflect the ions such that in the mode of operation as a atom source, only neutrals would be incident on the oxide surface. The deflector plate was positively biased to 3 kV, although it was found that about 2.5 kV was adequate to deflect most of the ions. It is pointed out here that there has been suggestions that the introduction of an electrostatic field in close proximity to the source reduces the neutral content in the beam [176]. However, Saied et al [173] have measured the ratio of the target current produced by neutrals to the current produced by total beam for varying chamber pressures for three different distances of separation between the source and the deflection plate. The results were found to be independent of this separation. Their results of the equipotentials plotted on resistance paper (shown in figure (4.9)) clearly shows that the electrostatic field due to the deflector plate has little influnce in the region around the exit aperture. Figure (4.10) shows an important source characteristics which was used for operation of the gun as a ion source or as a atom source.

4.4.9: the electron source

A KRATOS electrostatic electron gun was used for the purpose of electron bombardment of the surfaces. Electron bombardment has only been carried out on the transition metal oxides TiO_2 and Nb_2O_5. The electron emitter is a "hairpin" type heated tungsten filament mounted in a triode configuration. The emitted electron beam passes through an electrostatic alignment stage, which compensates for any misalignment of the electron source with the electron optical axis of the system. The alignment stage is followed by two demagnifying lenses which reduce the apparent diameter of the source, and the final lens focuses the electron beam onto the specimen. An electrostatic stigmator located just before the final lens corrects any astigmatism (i.e.

focussing in the X and Y directions not coincident). Four electrostatic deflector plates mounted just after the final lens enables the beam to be scanned. The electron beam can be focussed down to a spot size of 1μm in diameter. The gun is evacuated through the final aperture.

4.4.10: Spectrometer operating conditions

In the following, details of the spectrometer operating conditions employed, for the analysis of surfaces and the production of the spectra presented in this thesis, are given:

a) X-Ray Photoelectron Spectroscopy

X-ray source E.H.T. : 15 kV

X-ray source filament current : 15 mA

Analyser energy mode : FRR

Analyser slit widths : 5 mm, unless otherwise specified

Analyser Resolution : medium

Magnification setting : high

Spectrum mode : N(E)

Pre-amplifier setting : both pulse mode (Δq) and current mode ($\int$) were used

SAC pressure during analysis : ~ $1x10^{-9}$ torr.

b) Kratos Macrobeam Argon ion gun

Three sets of experiments were carried out with the ion gun, these were:

i. To investigate the effect of ion bombardment on all the samples. For each sample the beam energy and the beam current density were kept constant at 5 keV and 56 mA/m^2.

ii. To investigate the effect of the ion current density variation for selected samples. These samples were TiO_2, Fe_2O_3, ZrO_2, Nb_2O_5 and WO_3. The beam energy was kept constant at 5 keV and the beam current density was varied between 8 to 139 mA/m^2.

iii. To investigate the effect of ion beam energy variation on the samples as for case (ii). The current density was kept constant at 28 mA/m^2 whilst the beam energy was

varied between 1 and 5 keV.

Ion gun emission current : was set at 25 mA.

Ion gun filament current : 2 A.

Gas used : research grade Argon, unless otherwise stated.

Argon pressure in SAC during etching : was varied between $1x10^{-7}$ and $2x10^{-6}$ torr depending on the beam current density required.

c) Ion Tech FAB 11 ion/atom gun

Investigations with the FAB 11 gun were carried out to compare the effect of ion beam bombardment of surfaces with atom beam bombardment. Two different gases were used to establish the effect of the incident particle mass on the bombardment induced changes.

Beam energy : ~ 5 keV

Beam current density : Various.

Inert gases used for bombardment : Research grade argon and helium.

d) Electron gun

Electron gun EHT : 5 kV

Electron gun filament current : 2.75 A

4.4.11: Calibration of the electron spectrometer energy scale

The energy scale calibration of the instrument was achieved by a procedure known as the single sample, dual anode x-ray source method. A thin gold foil sample was used for this purpose. It is important to realize the distinction between the measured kinetic energy of the photoelectron (i.e. as passed through the analyser) and the standard tabulated kinetic energy. The kinetic energy of the photoelectron as passed through the analyser is given by the equation 3.5, as stated in chapter 3 section 3.2, to be:

$$E_{kin}(A) = h\upsilon - E_{b\cdot} - \Phi_A$$

i.e. measured kinetic energy = (photon energy - binding energy - analyser work function). The tabulated kinetic energies do not take the analyser work function into account, such that : (kinetic energy = photon energy - binding energy).

Since the difference between the photon energies of Mg Kα and Al Kα radiation is assumed to be exactly 233.0 eV, it is expected from the above equation that the energy separation between a photoelectron peak produced by Mg Kα and the corresponding peak due to Al Kα would also be 233.0 eV for a correctly calibrated energy scale. This forms the basis for the method of spectrometer energy calibration.

The gold foil was mounted onto the sample holder at the end of the fast insertion probe, which was then placed inside the SAC in the correct analysis position and the sample was earthed by connecting the end of the FIP to the metallic spectrometer casing. The settings for kinetic energy and the magnesium anode is selected on the control console. The spectra was taken of the Au 4f peak and the kinetic energy at the peak centre recorded. The same procedure was repeated for the aluminium anode and then adjustments were made, on the coarse and fine potentiometers located on the analyser high voltage supply, for the energy at peak centre obtained with the Al Kα to be exactly 233.0 eV above that recorded for the Mg Kα photon. After this calibration had been carried out, the measured kinetic energy for the peak centre as read on the operating console digi-switch settings then differed from the tabulated kinetic energy by an amount equal to the work function of the analyser. The calibration of the energy scale and the value of the work function were checked regularly during the surface analysis work presented in this thesis.

Foils of silver and copper were also used to check that correct calibration had been achieved. Separation of the Ag 3d peaks and the Cu 2p peaks, produced by the Mg Kα and the Al Kα radiations were 233.0 eV, indicating a correctly calibrated, linear energy scale.

4.5: Curve analysis and synthesis procedure

The curve-fitting software by Sherwood [167,168] is written in two parts: curve analysis and curve synthesis. With the curve analysis program, techniques such as smoothing, differentiating, binding energy scale calibration etc. can be carried out, whereas the curve synthesis program is used solely for curve-fitting. For each experiment the spectra were first analysed prior to employing the curve synthesis procedure. Initially the binding energy scale was calibrated with the gold $4f_{7/2}$ peak centre to read 84.0 eV (for the cases where the gold powder was added) and this calibration was then compared with the binding energy for the C 1s line to check for any differential surface charging effect with the gold. For the cases where differential charging of the gold was observed and for the cases where gold powder were not used, the C 1s (centred at 284.6 eV) line was used for binding energy calibration. The calibration was checked for the spectra obtained at each etching period. Other data analysis techniques such as smoothing or differentiation was carried out on some of the complex spectra for purposes of locating a suitable peak position that can then be used in curve-fitting. However, it is pointed out that these methods can lead to errors and loss of real data points and so the curve fitting method was carried out on the original untreated data rather than on the data saved after pre-treatment with smoothing or non-linear background subtraction etc.

The curve synthesis procedure carried out was the Gauss-Newton non-linear least squares method (as outlined by Sherwood [168]). A spectrum can be synthesized to sum a series of functions representing individual peaks in order to produce a final function that closely represents the experimental spectrum. The peak function is a combination of the appropriate peak variables such as position, hight, width, function-type and peak tail characteristics. The curve synthesis was carried out using a microcomputer system such that the result of the fit could be displayed graphically together with the statistical information of the fit.

The function used was a mixed Goussian/Lorentzian functions which was

proposed by Ansell et al [177] to be the most effective in practice. It is as shown below:

$$f(x) = H \bullet g(x) = H / [1 + M(C-C_0)^2 / \beta^2] \exp\{(1-M)[\ln 2(C-C_0)^2] / \beta^2\} \quad \ldots.(4.6)$$

Where C_0 is the peak centre, H the peak height and M is the mixing ratio which is defined as unity for a pure Lorentzian peak and zero for a pure Gaussian peak. The parameter β is given as approximately 0.5 times the full width at half maximum [177].

The curve synthesis program allows each peak to be composed of seven parameters: 1) peak centre. 2) peak height. 3) peak width. 4) Gaussian / Lorentzian peak shape mixing ratio, M. 5) constant tail height ratio, CT. 6) exponential tail height, ET. 7) constant / exponential tail mixing ratio, TM. There are also two parameters for the linear background slope and the right hand side intercept. Thus for each peak a maximum of (7n + 2) parameters can be allowed to vary. However, during the curve-fitting procedure the parameters 3), 4), 5) and 7) were generally kept constant. In addition, for the doublet components, the spin-orbit splitting intensity ratio was kept constant at the expected theoretical value. The background line chosen was a linear approximation from the high to the low energy side of the peaks and the fitted curves with their resultant envelope were superimposed onto this line. In general, the tail function is required at the high binding energy side of the metal peaks to account for any assymmetry. The tail function (T) is governed by the tail parameters 6), 7) and 8) and is given by:

$$T = TM \times CT + (1 - TM) \exp\{(-D_x) \times ET\} \quad \ldots.(4.7)$$

where D_x is the separation from the peak centre in channels. The peak function to the right of the peak (i.e the lower binding energy side of the peak) is chosen to have no tail and can be represented as f(x) or {H x g(x)}. The peak function with the tail is then represented as:

$$Y = H\{g(x) + (1 - g(x))\, T\} \quad \ldots. (4.8)$$

The quality of the curve fit obtained is given by a number known as the χ^2 value, which is defined as:

$$\chi^2 = \sum W_r \{ y_r - f(x_r / q) \}^2 \qquad \ldots. (4.9)$$

where y_r is the observed count at $x = x_r$, $f(x / q)$ is the fitted peak envelope, n is the total number of points in the spectrum and W_r is a weighting function, chosen to be equal to $(y_r)^{-1}$ [168]. In the Gauss-Newton non-linear curve fitting method the requirement is to minimize χ^2, i.e. $(\delta\chi^2 / \delta q_i)$ must be equal to zero.

4.6: Experimental procedure and types of experiments

After sample insertion into the sample analysis chamber, the chamber pressure was allowed to settle to approximately 10^{-9} torr before any data collection was performed. The sample was positioned horizontally approximately 90^0 to the axis of the x-ray source. For each experiment, the pre-amplifier high voltage was checked such that an adequate signal to noise ratio was obtained. The microcomputer was then set up for instrument control and data acquisition with the pre-amplifier high voltage set at the value found previously. It was ensured that the instrumental parameters which are not computer driven, were set at the appropriate operational mode. In addition to the pre-amp high voltage and the pre-amp operation mode, these parameters were the x-ray tube bombarding current and the accelerating voltage, also the analyser slit width. The KRATOS MACROBEAM ion source was also computer controlled such that, for bombardment, the high voltage to the ion gun could be switched on, and at the end of a defined period the high voltage power supply was switched off and returned to the data acquisition mode. However, the FAB 11 saddle field source and the electron gun (when used for the purposes of electron bombardment) had to be manually operated. It was made sure that the inert gas used was only allowed to enter the chamber during the ion or atom bombardment and the gas inlet valve was turned off at the end of each

bombardment period.

Prior to particle bombardment of the oxide surface, the x-ray photoelectron spectra were recorded for the most intense metal core-level lines together with the oxygen 1s, the carbon 1s and the gold 4f lines (for the cases where the gold powder was added for reference purposes). The oxide surface was then bombarded for periods of known durations (either the set 2, 10, 30, 60 and 120 minutes or the set 10, 30, 60, 90 and 120 minutes were used). Spectra were recorded after each period of particle bombardment. Each experiment was performed several times to ensure reproducibility of the results.

The spectra were analysed to measure the correct binding energies of the core levels; this was performed for the unbombarded surface first since the peaks associated with the unbombarded surface could be visually analysed to obtain approximate peak positions and other peak parameters. For the cases where gold powder was used, the binding energy scale was calibrated for the Au $4f_{7/2}$ peak centre to read 84.0 eV. However if sample charging was observed then the binding energy scale was recalibrated with the carbon 1s peak centre to read 284.6 eV. The latter binding energy calibration was also adopted for the cases where gold powder was not used. A more accurate peak parameter location and calculation of the area under the curve were carried out, for the unbombarded surface and for the peaks obtained after etching, using the curve synthesis program. A careful measurement of the energies associated with the core level lines in the different chemical states were thus made. For each sample used the binding energies associated with each state were then recorded.

Four different types of investigations were carried out and these were as follows:

4.6.1: The effect of ion bombardment on various transition metal oxide surfaces and AL_2O_3 and MgO surfaces

Investigations were carried out on the transition metal oxides TiO_2, FeO, Fe_2O_3, Fe_3O_4, CoO, Co_3O_4, ZrO_2, Nb_2O_5, Ta_2O_5 and WO_3. For each oxide the ion

beam was kept constant at 5 keV and the beam current density used was 56 mA/m^2. The metal core levels investigated were:

1) for the iron oxides - the 2p and the 3p lines,

2) for the cobalt oxides - the 2p and the 3p lines,

3) for the titanium oxide - the 2p and the 3p lines,

4) for the zirconium oxide - the 3d line,

5) for the niobium oxide - the 3d and the 3p lines,

6) for the Ta oxide - the 3d line,

7) for the tungsten oxide - the 4f and 4d lines

These spectral peaks (as well as the C 1s and the O 1s lines) were analysed and the curve fitting procedure employed after each bombardment period to observe the chemical effect of the ion beam on the sample surface constituent. The intensity of each component was recorded. On each sample up to 120 minutes of ion bombardment were carried out.

4.6.2: The effect of ion beam energy variation on the surface chemical damage

The next step of the investigation was to vary the ion beam energy for a constant current density. The beam energy was varied between 1 to 5 keV whilst the current density was kept constant at 28 mA/m^2. The oxides investigated were TiO_2, Fe_2O_3, ZrO_2, Nb_2O_5, and WO_3. Thus for each oxide a total of five experiments were carried out (i.e. at 1, 2, 3, 4 and 5 keV) and a different sample was prepared for each experiment.

4.6.3: The effect of the ion beam current density variation on the surface chemical damage

The same oxides as in section 4.6.2 were again investigated for the current density variation at a constant beam energy of 5 keV. For the oxides TiO_2, Fe_2O_3,

Nb_2O_5, and WO_3, the current density was varied between 8 to 139 mA/m^2. Thus 6 experiments were carried out, on each oxide, at current densities of 8, 28, 56, 83, 111 and 139 mA/m^2. The actual experimental settings corresponding to these current densities were beam currents of 0.3, 1, 2, 3, 4 and 5 μA over a rastered area of 4 mm x 9 mm. However for the zirconium oxide, beam current density variation upto 111 mA/m^2 was carried out. Thus a total of twenty nine experiments were carried out and again a new sample was prepared for each.

This investigation of current density variation was then repeated for a lower constant beam energy of 2 keV. With each of the oxides, four more experiments were carried up to the current density of 83 mA/m^2. However, the maximum current density possible for the zirconium oxide at the beam energy of 2 keV was 56 mA/m^2.

4.6.4: Comparison of fast atom beam bombardment with ion bombardment

This was carried out on the TiO_2 surface to investigate the comparison with two different incident gas species. These inert gases used were helium and argon (which have a large mass difference) with the intenstion that charge and mass effects of the incident particles may be separated.

4.6.5: The effect of electron bombardment

For this investigation the oxides Nb_2O_5 and TiO_2 were chosen. The electron beam energy employed was 5 keV and the electron current used was approximately 5 μA. Each oxide surface was subjected to 120 minutes of electron bombardment.

CHAPTER 5: Results

5.1: Introduction

The results obtained from the various investigations carried out here are presented in this chapter. Section 5.2 gives the results for the bulk characteristics of the metal oxide powders obtained by means of x-ray powder diffraction. The results showing the effect of ion bombardment of the surfaces are presented in section 5.5. These results show spectra of TiO_2, ZrO_2, Nb_2O_5, WO_3 and Ta_2O_5 for which curve-fitting procedure were carried out assuming a linear background line. A linear background line rather than a Shirley non-linear background subtraction was chosen in these cases (where the lineshape is not too assymmetric) due to the reasoning that a non linear line subtraction may lead to errors in the curve-fitting results for the peaks where the background slope is substantially high. This is clearly demonstrated in section 5.5.11, where comparisons are made of results obtained when curve-fitting was carried out taking a linear background line and those with curve-fitting after a non-linear background subtraction. These comparisons are made for the case of the niobium oxide (i.e. Nb 3d peak) which has a relatively low background slope for the main photopeak at a binding energy of approximately 207 eV and for the case of the titanium oxide (i.e. Ti 2p peak) with the main photopeak at about 458 eV, the background slope of which is high. However, for the oxides of iron (i.e, α-Fe_2O_3, Fe_3O_4 and FeO) and the oxides of cobalt (Co_3O_4 and CoO) it was found necessary to carry out a non-linear background subtraction on the 2p peaks. The 2p line-shapes of these oxides were found to show extreme assymmetry causing inaccuracies in the the curve-fitting results after a linear background subtraction. These findings are described fully in section 5.5.11. The effects of ion bombardment of the two non-transition metal oxides are described in section 5.5.12.

The variations in ion beam current density and beam energy results are shown in section 5.6 and 5.7 respectively. The effect of atom bombardment and a quantitative

comparison with an equivalent (i.e. beam energy and current density) atom-beam bombardment are demonstrated in section 5.8. Lastly, section 5.9 gives a brief account of the effect of electron bombardment of TiO_2 and Nb_2O_5 surfaces.

5.2: X-ray powder diffraction results

In this section, a number of microdensitometry traces of powder diffraction photographs are presented. X-ray powder diffraction technique was applied to establish the bulk purity of commercially available powders. For each sample the identities of the diffraction lines obtained on the photographs are tabulated, along with a comparison of experimentally obtained d-spacings and relative diffracted intensities with standard values quoted in the ASTM index.

All oxides were confirmed to be pure within the detectibility of the X-ray diffraction technique, apart from FeO. The microdensitometer traces of FeO diffraction photograph showed the presence of small amounts of metallic iron and Fe_2O_3. As an example of the typical microdensitometry traces obtained, the results for the FeO powder is shown in figure (5.1) especially since FeO was found to be the only sample with traces of impurity. The identities of the diffraction lines obtained are given in table (5.1) along with comparisons of the experimentally measured d-spacings with standard values quoted in the ASTM index.

5.3: Results for the spectrometer energy scale calibration

Figures (5.2a, b and c) show the respective Au $4f_{7/2}$, Ag $3d_{5/2}$ and the Cu $2p_{3/2}$ photoelectron peaks obtained once the energy scale of the electron spectrometer had been correctly calibrated. Measured kinetic energy values now differed from tabulated energy values by an ammount equal to the spectrometer work function. In order to calculate the work function from equation (3.5) it was first necessary to assign a value to the binding energy of the Au $4f_{7/2}$ line produced from the primary gold standard. A value of 84.0 eV was chosen for this binding energy in accordance with

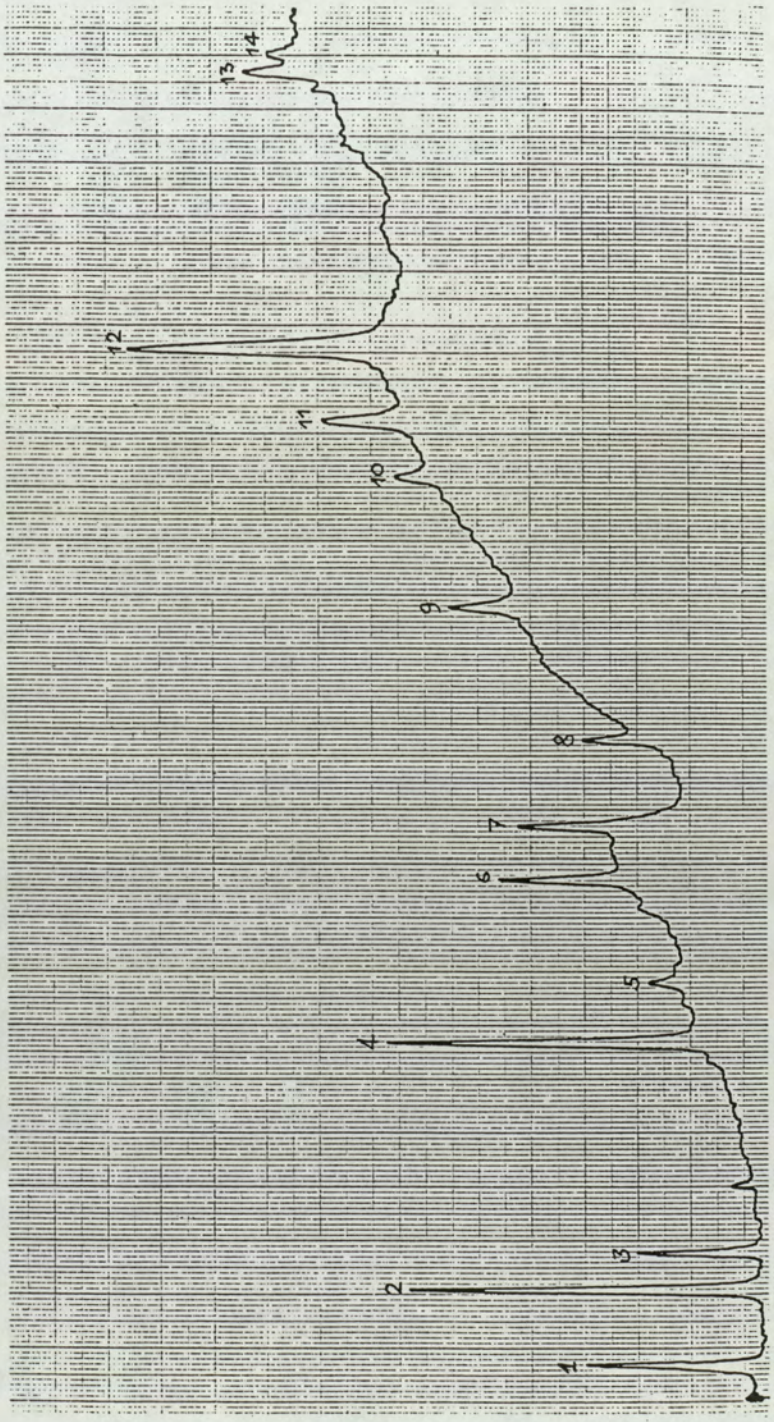

Figure 5.1.

Microdensitometer trace of bulk FeO powder taken from X-ray diffraction photograph. The identification of the lines are given in Table 5.1.

Table 5.1.

X-ray diffraction results for FeO. Lines 3,10, 13 and 14 correspond to metallic Fe contamination.

line	estimated intensity	2Θ/deg.	d_{hkl}/Å	identity from ASTM	
				FeO	α–Fe_2O_3
1	S	42.4	2.4762	2.49 (80)	
2	VS	49.3	2.1470	2.153 (100)	
3	M	52.8	2.0157		
4	VS	72.0	1.5234	1.523 (60)	
5	F	77.5	1.4306		1.425 (35)
6	M	87.2	1.2985	1.299 (25)	
7	M	92.0	1.2448	1.243 (15)	
8	M	100.0	1.1689		1.162 (10)
9	MB	112.3	1.0782	1.077 (15)	
10	MB	124.3	1.0128		
11	MB	129.8	0.9889	0.988 (10)	
12	SB	136.4	0.9644	0.9631 (15)	
13	M	161.5	0.9060		
14	FB	163.5	0.9060		

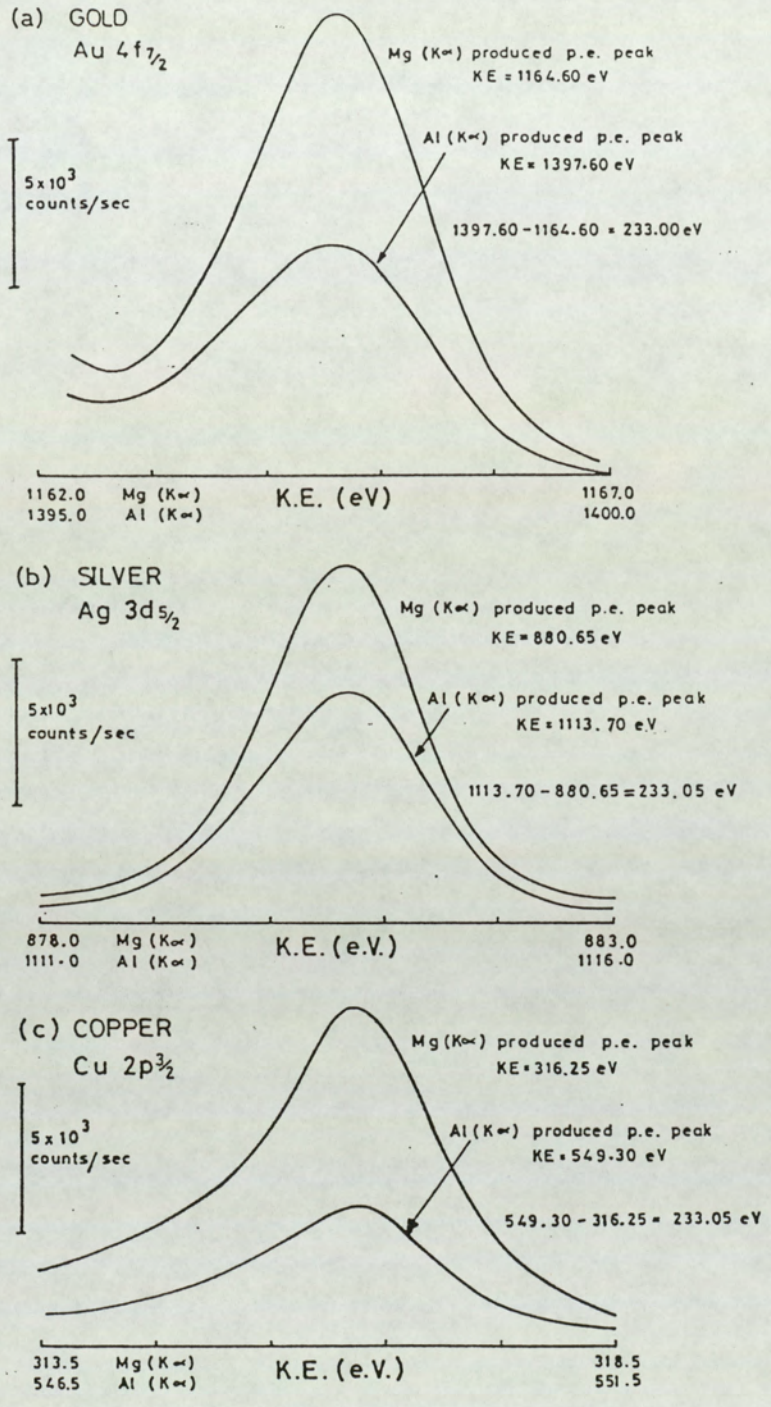

FIGURE 5.5 Photoelectron Peaks of Metal Standards

Figure 5.2.

Photoelectron peaks of the metal standards, to show the energy scale calibration of the electron spectrometer.

the work of Powell et al [178] and Asami [179]. It was found that:

spectrometer work function, $\phi_{sp} = 5.0$ eV

5.4: Resolution versus intensity for different slit widths

Usually in any XPS spectrum, there is a trade-off between resolution and transmission, improvement of one degrades the other. Since, for the work described in this thesis, it would be ideal to have a high transmission (such that even the smallest trace of the reduced state could be detected) combined with a very high resolution (such that the reduced states could be resolved separately), it was decided to optimise the transmission and resolution of the spectrometer. An experiment was then carried out on the powder oxide Nb_2O_5 for which the $3d_{(3/2,\ 5/2)}$ doublet was recorded for the spectrometer slit widths (entrance and exit) 5 mm, 3mm, 2mm and 1mm. Figure (5.3) shows the spectra obtained for the different slit widths. Curve-fitting carried out on these spectra yields the 3d line widths (FWHM) to be 1.9 eV, 1.8 eV, 1.7 eV and 1.6 eV for the slit widths 5, 3, 2 and 1 mm respectively. Thus only an improvement in resolution of 0.1 eV per mm decrease in slit width was observed. This slight improvement (~5%) in spectrum resolution was not considered to be worth taken into account, especially since the decrease in transmission observed was approximately 2 to 4 times per mm decrease in slit width. Figures (5.4a and b) show the change in the 3d doublet after ion bombardment but recorded with respective slit widths of 1 mm and 2 mm giving corresponding maximum counts to be 1528 and 4920. In this figure (5.4) the decrease in transmission with slit width is clearly visible, whereas the resolution of the reduced states has not improved; the whole spectral envelope being just slightly narrower.

From the above results, the spectrometer slit width of 5 mm was thus chosen to be used for whole of the investigation such that high transmission could be attained.

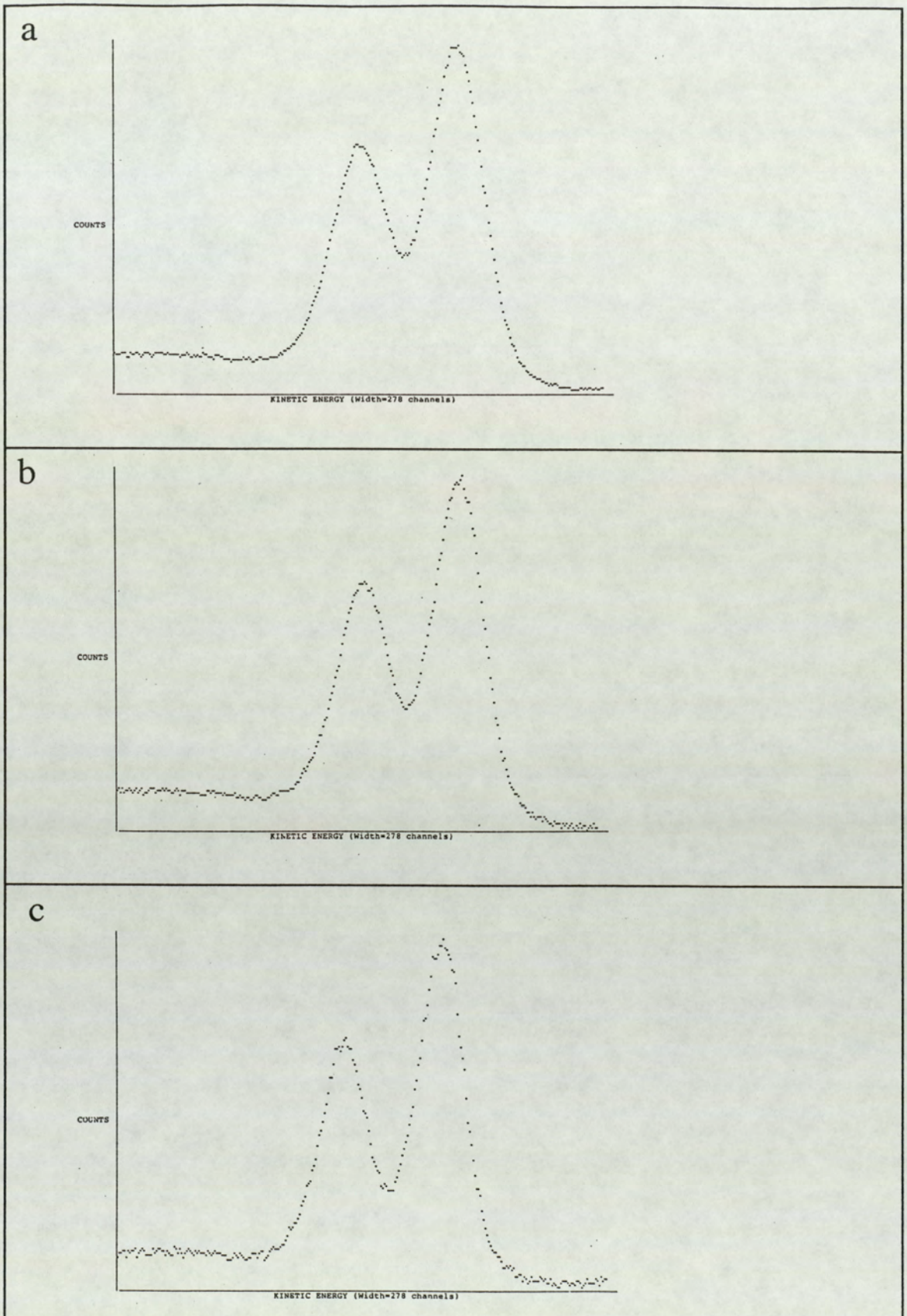

Figure 5.3.

Nb 3d spectra from unbombarded Nb_2O_5 surface, measured with different slit widths of the spectrometer.

a) slit width = 3mm, maximum count is 10634, FWHM = 1.8 eV
a) slit width = 2mm, maximum count is 5713, FWHM = 1.7 eV
a) slit width = 1mm, maximum count is 1786, FWHM = 1.6 eV

a

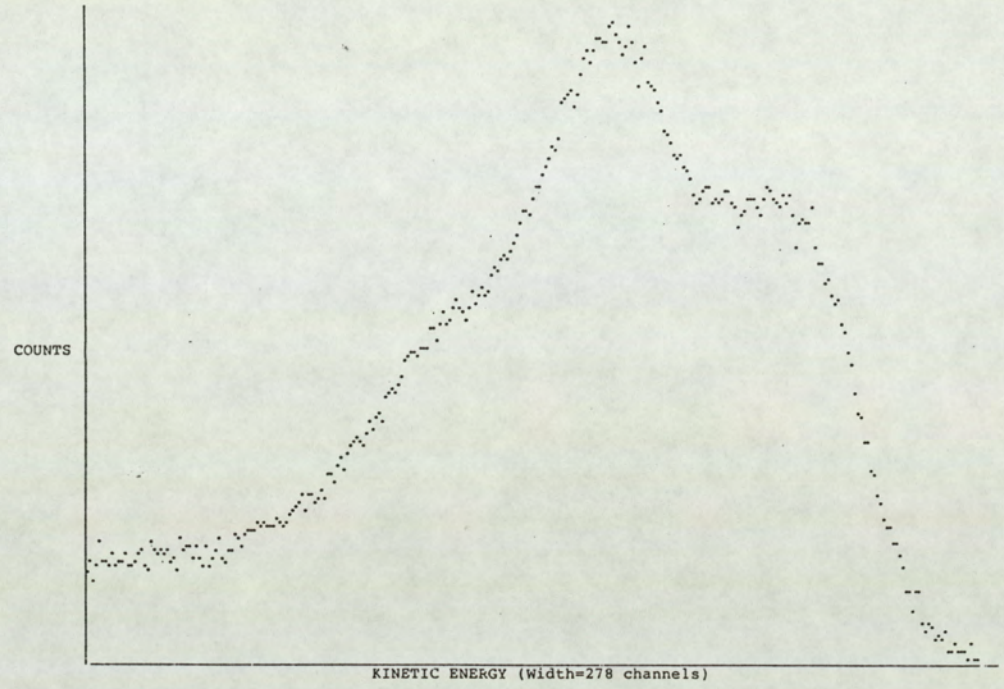

b

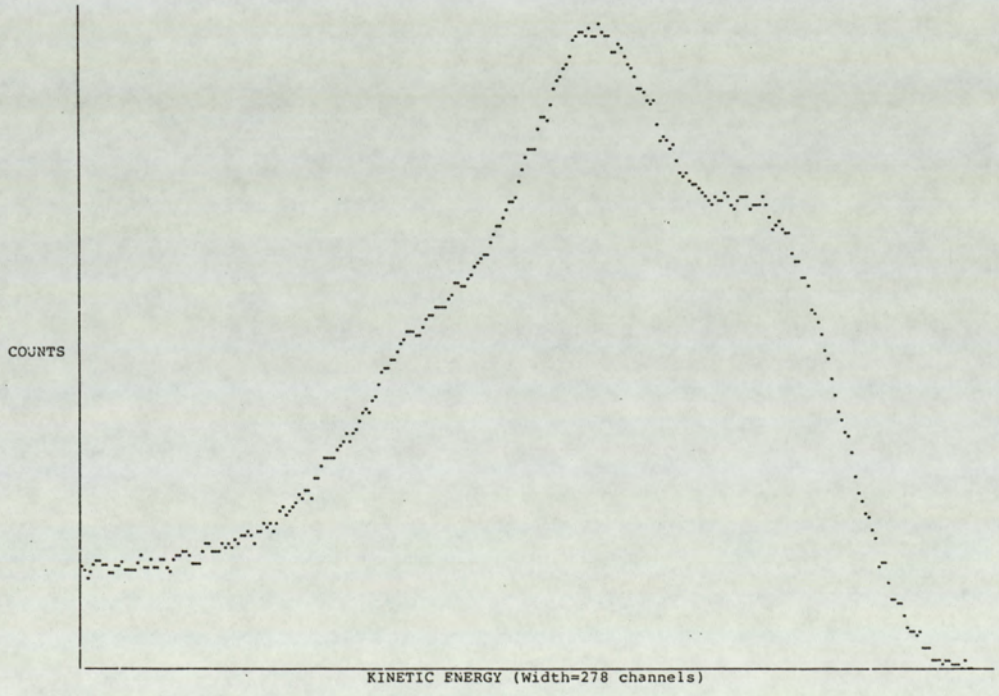

Figure 5.4.

Nb 3d spectra from Nb_2O_5 surface after ion bombardment, measured with different slit widths of the spectrometer.

a) slit width = 1mm, maximum count is 1528, FWHM = 1.6 eV
a) slit width = 2mm, maximum count is 4920, FWHM = 1.6 eV

5.5: Results showing the effect of ion bombardment.

The results showing the effect of ion bombardment on the metal oxides considered are described below:

5.5.1: FeO

The XPS spectral lines of Fe $2p_{1/2}$, $2p_{3/2}$, the oxygen 1s, the carbon 1s and the gold 4f were recorded for the unbombarded air-exposed FeO powder surface and for the surface after argon ion bombardment for durations of 10, 30, 60, 90 and 120 minutes. For the air exposed unetched surface the curve-fitting procedure on the Fe $2p_{3/2}$ peak reveales two components, one at binding energy 711.8 eV and the other at 710.8 eV, both with a FWHM of 3.3 eV. These values are assigned in current literature (discussed fully in Chapter 6 on Discussion) to be due to the Fe^{III} ions in FeOOH and α-Fe_2O_3 states respectively. The broadness of these peaks is expected to be due to multiplet splitting. It thus appears that the surface of the FeO powder has oxidised to form α-Fe_2O_3 which has further reacted with atmospheric water vapour to form FeOOH. Figure (5.5a and b) show the Fe $2p_{3/2}$ and the $2p_{1/2}$ spectra for the unetched surface; curve-fitting carried out on the Fe $2p_{1/2}$ also shows the existence of the two peaks due to FeOOH and α-Fe_2O_3 at binding energies of 725.5 and 724.5 eV respectively. For both these chemical states the ratio of $2p_{3/2}$ to $2p_{1/2}$ is found to be about 2.2, showing a good fit to the curves within allowed experimental errors.

The oxygen 1s spectrum for the unetched surface confirms the above view. Two major peaks can be observed in this spectrum, figure (5.6a), at binding energies of 530.4 eV and 531.9 eV with a third, less intense, peak centred at 533.4 eV. All three peaks have a FWHM of 1.8 eV. Thus the O 1s peak profile provides a good indication of the chemical state of the surface. The peak at 530.4 eV is due to the metal-oxygen bond and the second major peak at 531.9 eV is due to the hydroxyde bond (OH). The small peak centred at 533.4 eV is expected to be due to a multiplicity of chemicaly or physically bonded water on or within the surface.

The carbon 1s spectral profile (figure (5.6b)) for the unbombarded surface shows the presence of two peaks, both with a FWHM of 2.0 eV. The major peak appears at the lower binding energy of 284.6 eV (sometimes used for reference purposes), expected to be due to surface borne hydrocarbons. The minor peak at 1.5 eV above the main carbon peak is expected to be due to the surface bound carbon in a carbon-single oxygen bond-oxygen molecule. Upon progressive periods of ion bombardment, both carbon peaks gradually diminish, the higher binding energy being removed first.

Within 10 minutes of argon ion bombardment, considerable broadening of the iron spectra is observed together with a marked shift towards the lower binding energy. Curve-fitting carried out on the Fe $2p_{3/2}$ spectra, figure (5.7a), shows an intensity reduction of the two peaks, previously observed at the unetched surface, due to the Fe^{III} ions in FeOOH and α-Fe_2O_3. Additional appearence of a third peak of binding energy 709.2 eV (FWHM=3.3 eV) with its associated satellite at 715.2 eV can also be observed. The peak at 709.2 eV is the most intense peak and is due to Fe^{II} ions in FeO. The Fe^{II} ionic state is a high spin state and the associated satellite is expected to be due to a shake-up process. Thus, the appearence of the 709.2 eV peak and the diminution of the hydroxyl component in the oxygen spectra (figure (5.7b)) indicates the sputter removal of the surface contaminants to expose the underlying FeO surface. It is thought that part of the Fe^{II} species arises from "ion induced reduction" of surface FeOOH and α-Fe_2O_3.

Figures (5.8a and b) show the Fe $2p_{3/2}$ and the O 1s lines after 30 minutes of ion bombardment. In the Fe $2p_{3/2}$ profile, further reduction of the contaminants, i.e. FeOOH and α-Fe_2O_3, is observed with the FeO state becoming dominant. However, the most important feature is the appearence in the Fe $2p_{3/2}$ spectra of a much narrower peak at binding energy 707.0 eV (FWHM=1.9 eV) which is due to metallic Fe^0. This finding is indicative of the occurance of partial reduction of the oxide caused by ion bombardment.

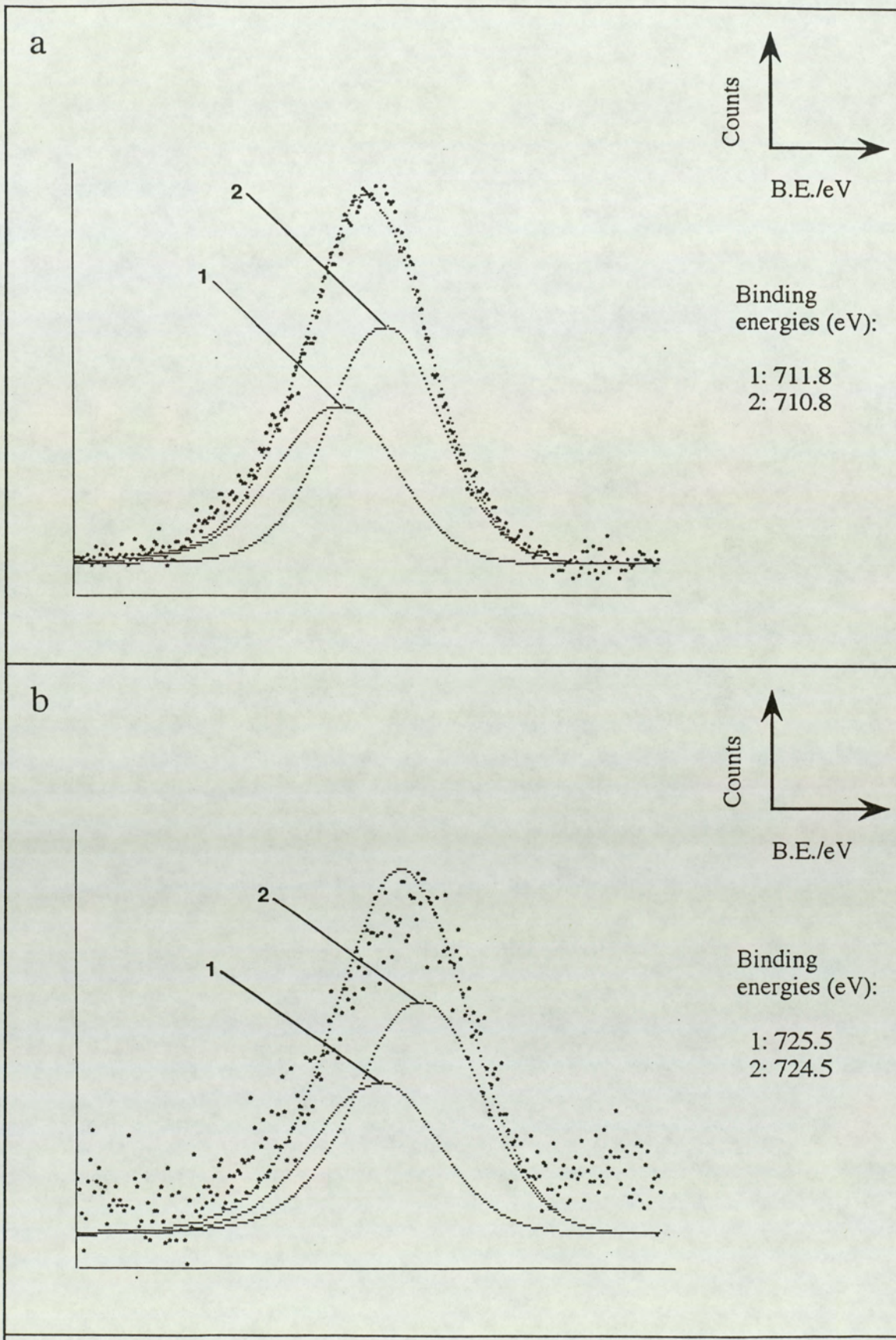

Figure 5.5.

Unbombarded FeO surface.

a) Fe $2p_{3/2}$

b) Fe $2p_{1/2}$

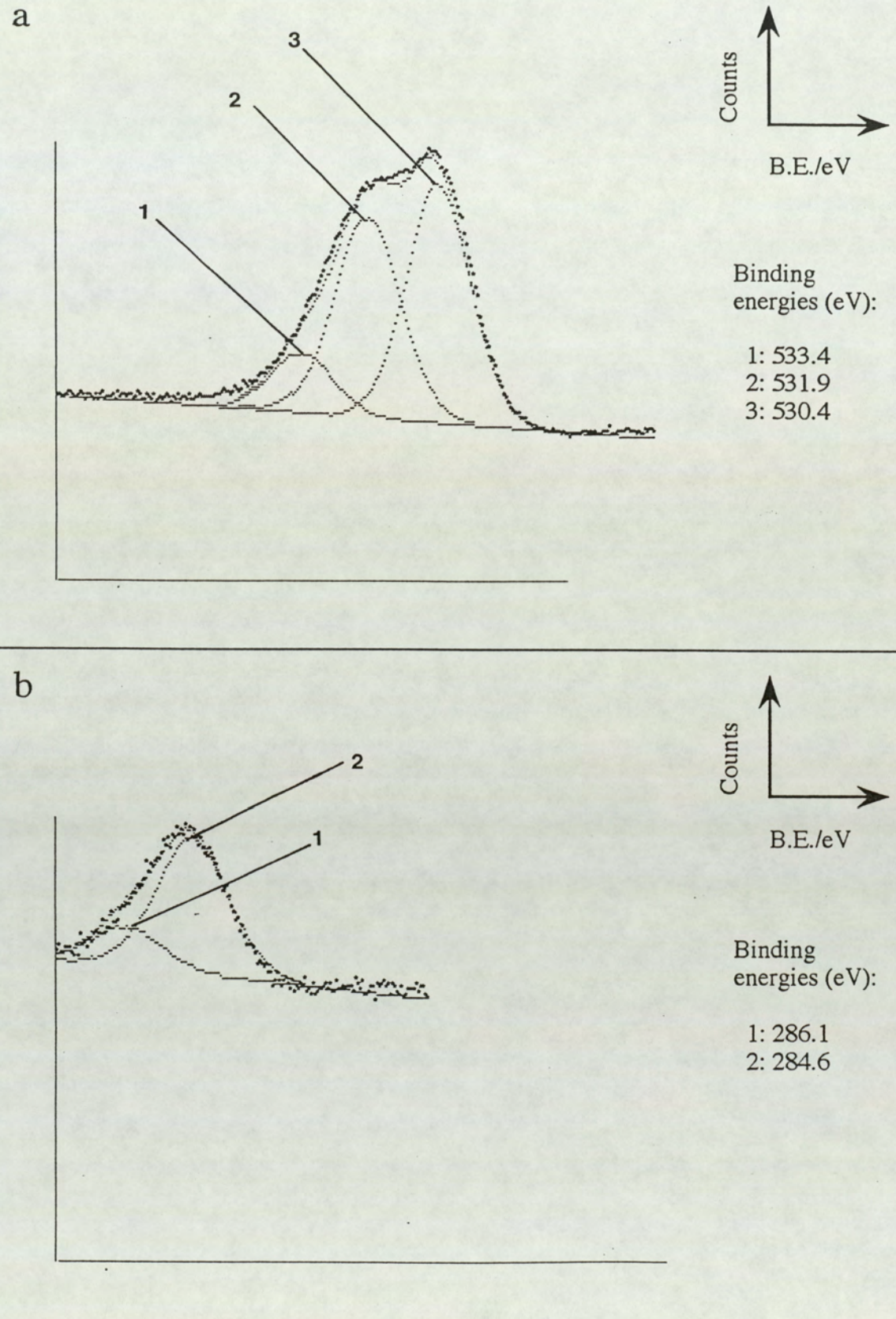

Figure 5.6.

Unbombarded FeO surface.
a) O 1s
b) C 1s

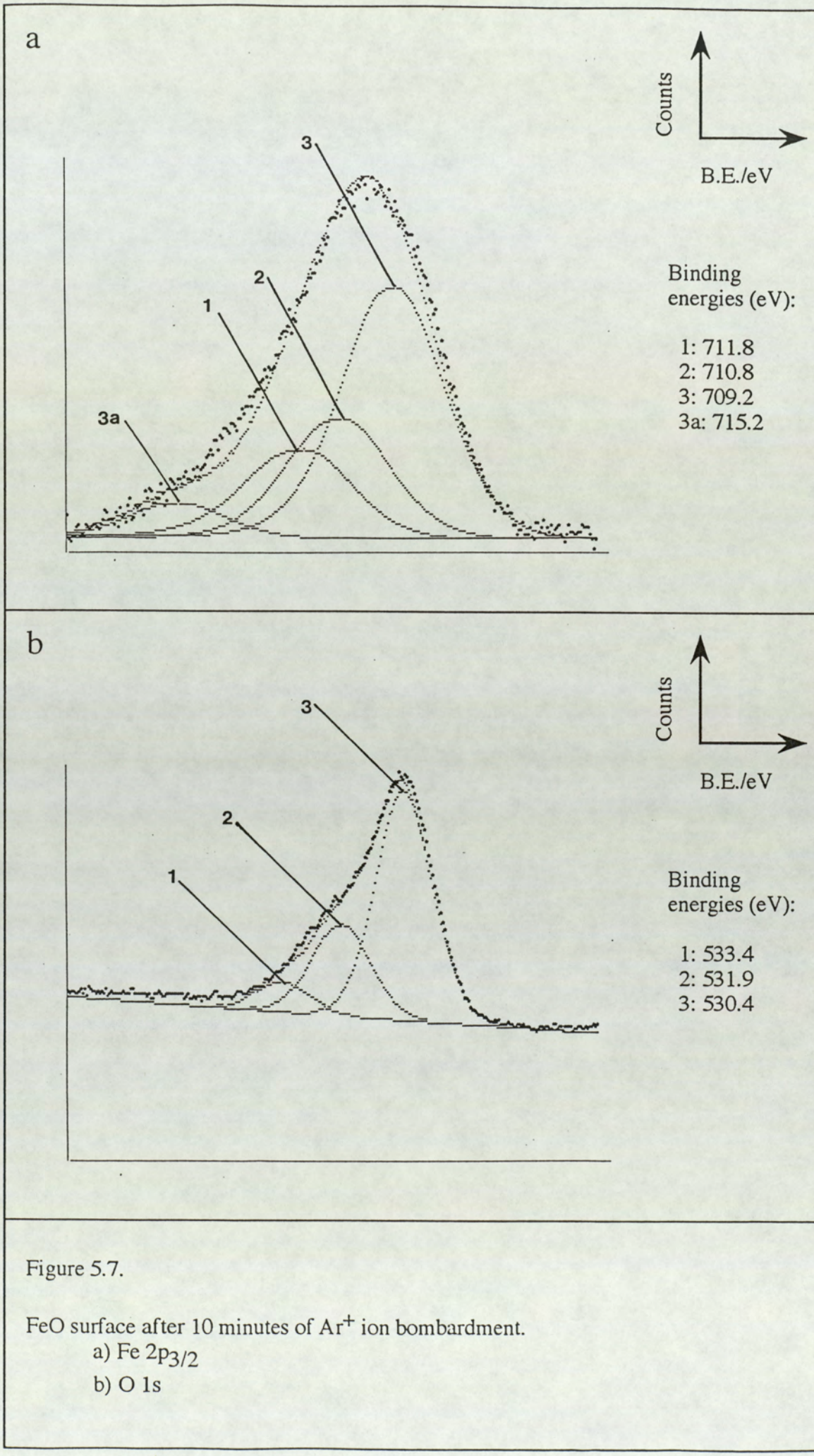

Figure 5.7.

FeO surface after 10 minutes of Ar^+ ion bombardment.

a) Fe $2p_{3/2}$

b) O 1s

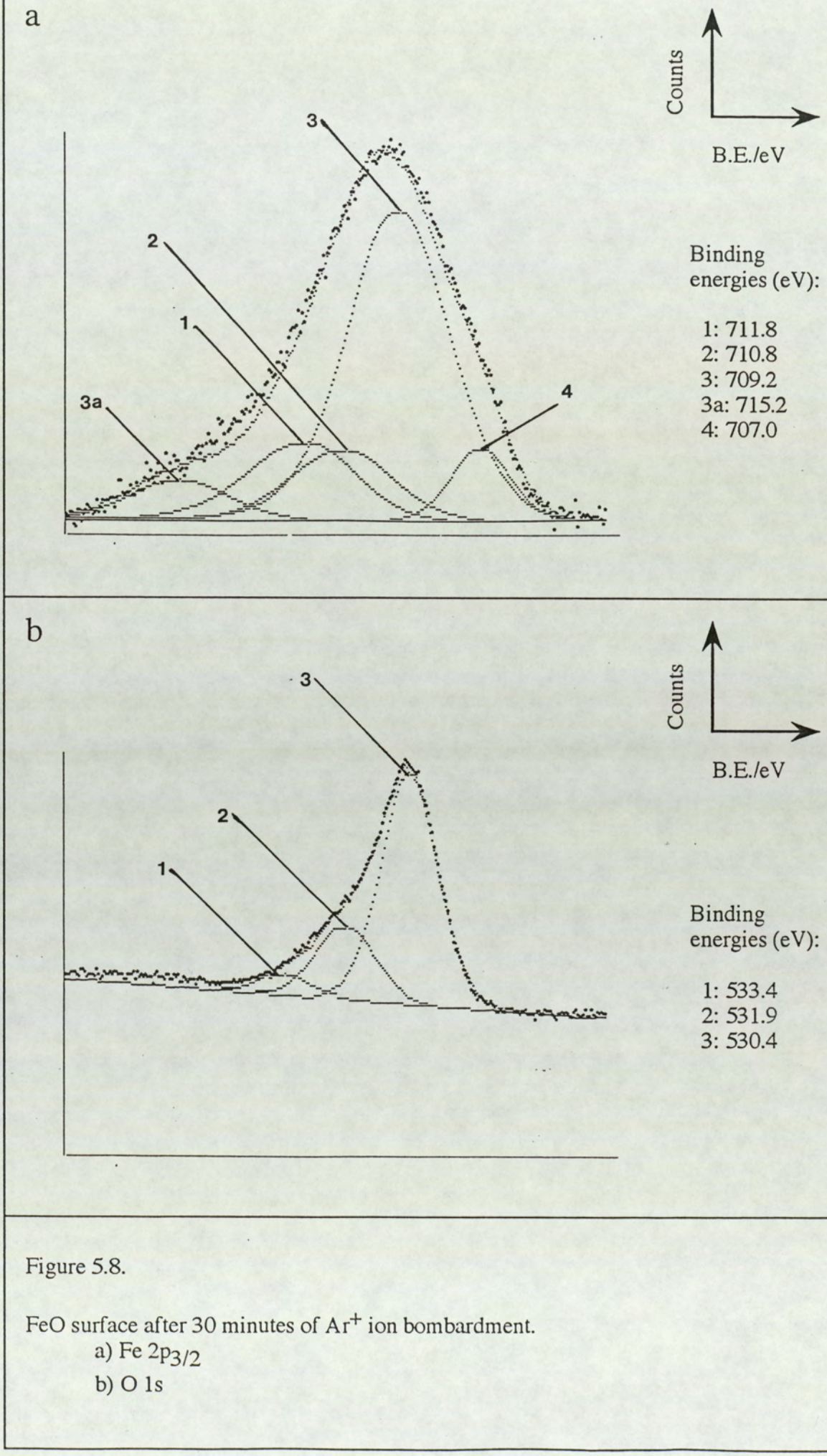

Figure 5.8.

FeO surface after 30 minutes of Ar^+ ion bombardment.

a) Fe $2p_{3/2}$

b) O 1s

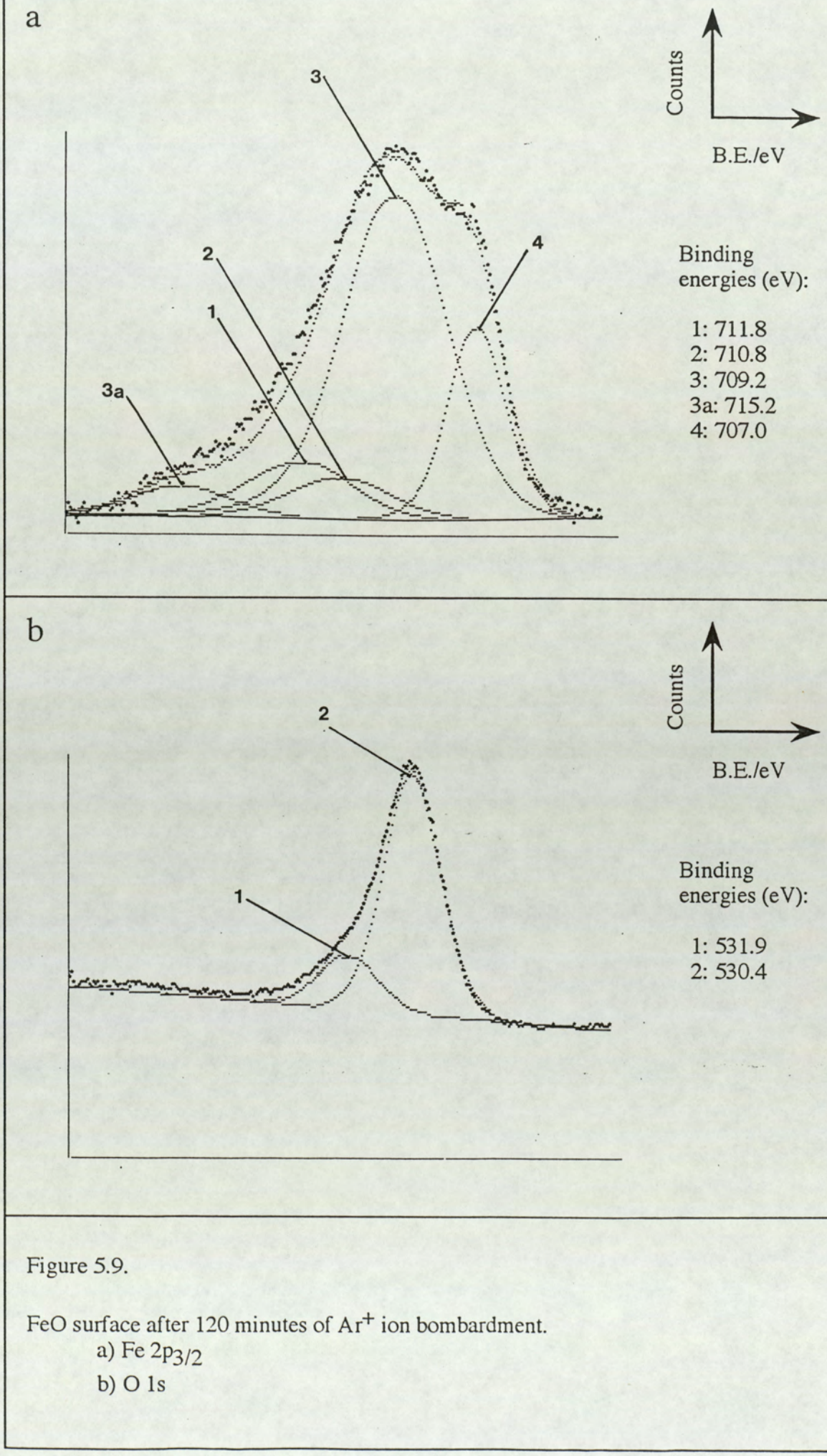

Figure 5.9.

FeO surface after 120 minutes of Ar^+ ion bombardment.

a) Fe $2p_{3/2}$

b) O 1s

Table 5.2

Measured binding energy values (±0.2eV) and corresponding FWHM values (±0.2eV) for iron and its oxides. Calibration is with respect to the Au $4f_{7/2}$ peak at 84.0 eV.

identity		core level	binding energy (eV)	FWHM (eV)
Fe_2O_3	Fe^{III}	$2p_{3/2}$	710.4	3.3
		$2p_{1/2}$	724.5	3.3
	satellite Fe^{III}	$2p_{3/2}$	719.1	3.3
Fe_3O_4	Fe^{III}	$2p_{3/2}$	710.8	3.3
		$2p_{1/2}$	724.5	3.3
	Fe^{II}	$2p_{3/2}$	709.2	3.3
		$2p_{1/2}$	723.0	3.3
FeOOH	Fe^{III}	$2p_{3/2}$	711.8	3.3
		$2p_{1/2}$	725.5	3.3
FeO	Fe^{II}	$2p_{3/2}$	709.2	3.3
		$2p_{1/2}$	723.0	3.3
	satellite Fe^{II}	$2p_{3/2}$	715.2	3.3
Fe-metal	Fe^0	$2p_{3/2}$	707.0	1.9
		$2p_{1/2}$	720.8	1.9
Oxygen	metal-oxygen bond	1s	530.4	1.8
	hydroxide bond	1s	531.9	1.8
	surface bound oxygen	1s	532.5	1.8
	surface bound water	1s	533.4	1.8
Carbon	hydrocarbon bond	1s	284.6	2.0
	carbon-oxygen bond	1s	286.1	2.0

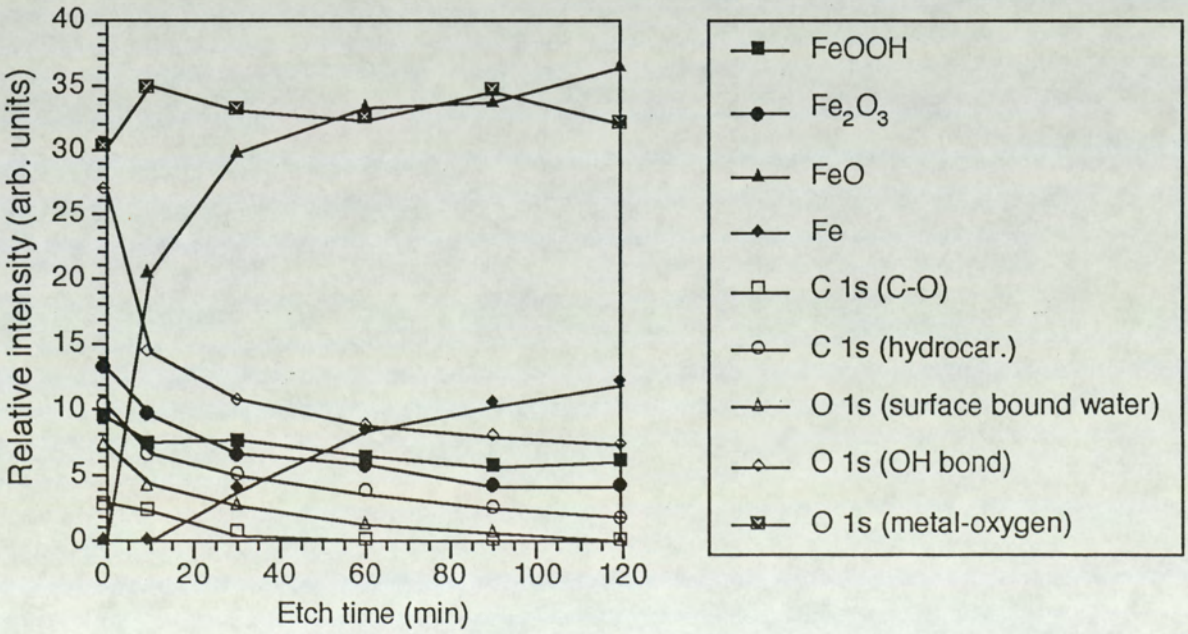

Figure 5.10.

Relative intensity as a function of etch time for FeO.

Further bombardment for periods of 60, 90 and 120 minutes produces changes in the intesity ratio of the components in the Fe $2p_{3/2}$ spectra. For example, the Fe^{II} : Fe^{0} ratio (satellite contribution not taken into account) reduces from 7.7 for 30 minutes of bombardment time to 3.0 after 120 minutes when this ratio stabilises. The Fe^{II} satellite intensity was measured to be within 10-12% of the main peak intensity. Figure (5.9a) shows the spectrum after 120 minutes of ion bombardment. The retention of small amounts of FeOOH and α-Fe_2O_3 in the sample is most probable due to the nature of the powder sample and the low etching rates employed. There may be other reasons for the retention of the Fe^{III} ion but this will be discussed fully later in Chapter 6. In figure (5.10), a plot of the relative intensities for the lines Fe 2p3/2, O1s and C 1s with etch times is shown and table (5.2) includes a list of the measured binding energies with the associated FWHM values for the powder FeO surface. Figure (5.10) also includes a curve showing the variation of M/O (i.e, Metal/Oxygen) ratio with time. The M/O ratio was calculated using purely the total metal intensity contribution from the Fe $2p_{3/2}$ line and the sum of the oxygen contributions due to metal-oxygen bond and the (OH) bond. No account was taken of the atomic sensitivity factors.

5.5.2: Fe_3O_4

The spectral lines, same as for the FeO sample, were recorded and curve-fitting procedure carried out to establish accurate binding energies and chemical shifts for the Fe_3O_4 powder sample. Figures (5.11a, b) and (5.12a, b) show the Fe $2p_{3/2}$, Fe $2p_{1/2}$ and the O1s, C 1s spectra respectively for the unetched surface. In the O 1s spectra two peaks can be seen; the major peak, due to the metal-oxygen bond, appears at binding energy of 530.4 eV, and a much less intense peak at 532.5 eV which is most probably due to surface-bound oxygen. Similarly to the FeO sample, the C 1s spectrum shows the presence of surface hydrocarbons (at binding energy 284.6 eV) and carbon-single oxygen-bond molecules (at 286.1 eV).

The profile of the Fe $2p_{3/2}$ peak corresponding to the unetched state, consists of a single component at binding energy 710.8 eV with FWHM of 3.3 eV. Fe_3O_4 contains both Fe^{III} and Fe^{II} ions in an inverse cubic spinnel structure, with the Fe^{II} ions in octahedral sites and the Fe^{III} ions in octahedral and tetrahedral sites. Therefore, the absence of Fe^{II} contribution in the unbombarded Fe $2p_{3/2}$ indicates that oxidation of the Fe_3O_4 surface has taken place to form α-Fe_2O_3. Unlike the previous case for FeO sample, no subsequent formation of FeOOH has occured. This could be due to storage or production condition of the oxide powder.

The unetched Fe $2p_{1/2}$ spectrum shows the same results as the Fe $2p_{3/2}$ spectrum. Only one peak can be observed at binding energy of 724.5 eV with FWHM of 3.3 eV, showing the surface composition to be entirely α-Fe_2O_3. From the area under the peak, the intensity ratio for $2p_{3/2}$ to $2p_{1/2}$ was calculated to be about 2.2 with a ~10% error (the theoretical value obtained from the ratios of 2j+1 is 2.0 for the 2p line). Close observation of this spectrum also indicates the presence of a very minor peak at a binding energy of approximately 719.1 eV, the origin of this peak is expected to be the satellite associated with the Fe^{III} ionic state of α-Fe_2O_3.

Controlled ion bombardment for different durations causes the Fe 2p peak to sharpen and broaden; while the C 1s spectrum shows gradual removal of both the carbon species. The carbon-single bond-oxygen being completely removed after about 30 minutes. Figures (5.13a and b) show the Fe $2p_{3/2}$ and O 1s spectra after 10 minutes of ion bombardment; in the Fe $2p_{3/2}$ spectrum two distinct peaks are visible, at binding energies of 710.8 eV and 709.2 eV, both with FWHM of 3.3 eV. The latter of these two components is due to Fe^{II} ions from Fe_3O_4 and FeO whilst the former is due to Fe^{III} ions from both Fe_3O_4 and surface α-Fe_2O_3. The shake-up satellite due to Fe^{II} ions is seen at 715.2 eV at an intensity of ~10% of that of the main peak.

For the 10 minutes bombardment period, the peak intensity ratio of Fe^{III}:Fe^{II} is measured to be 0.71 (again satellite contributions neglected). For stochiometric Fe_3O_4, one would expect this ratio to be 2.0 and the presence of substantial amounts of

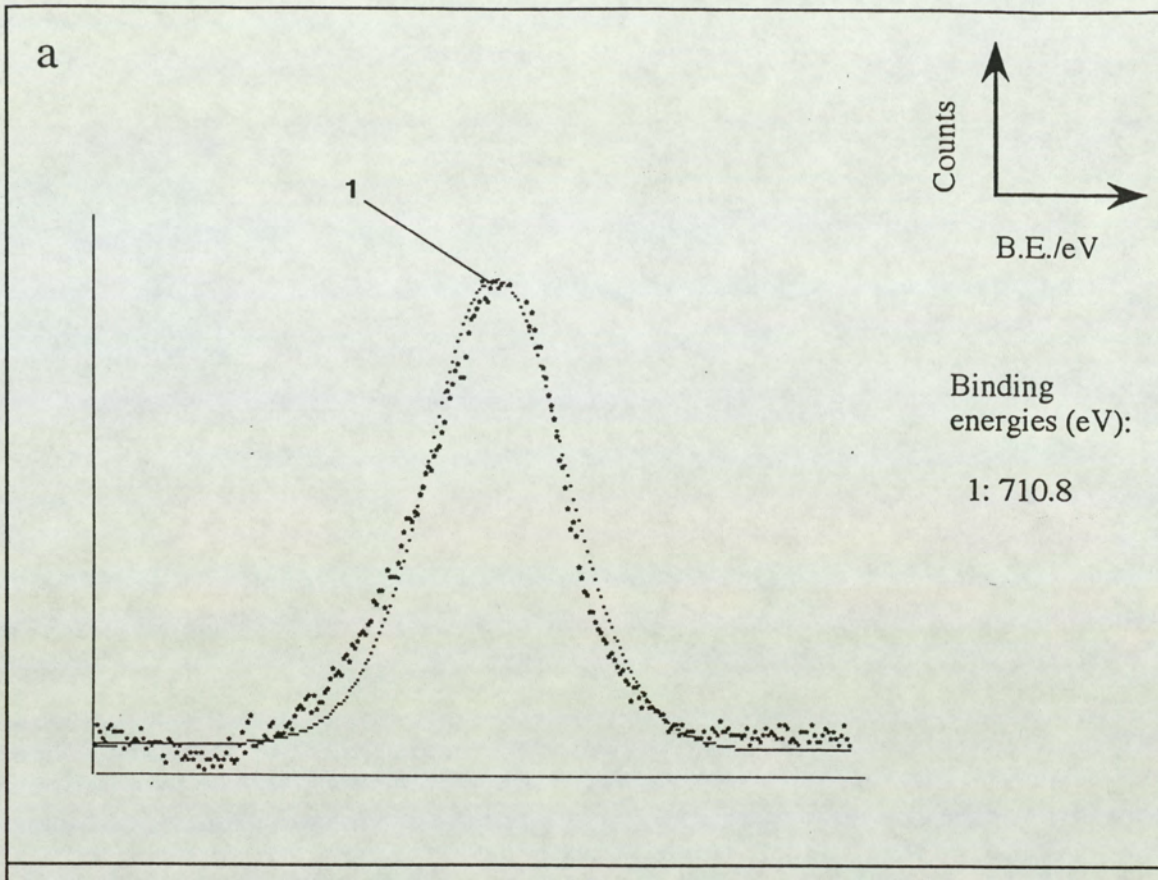

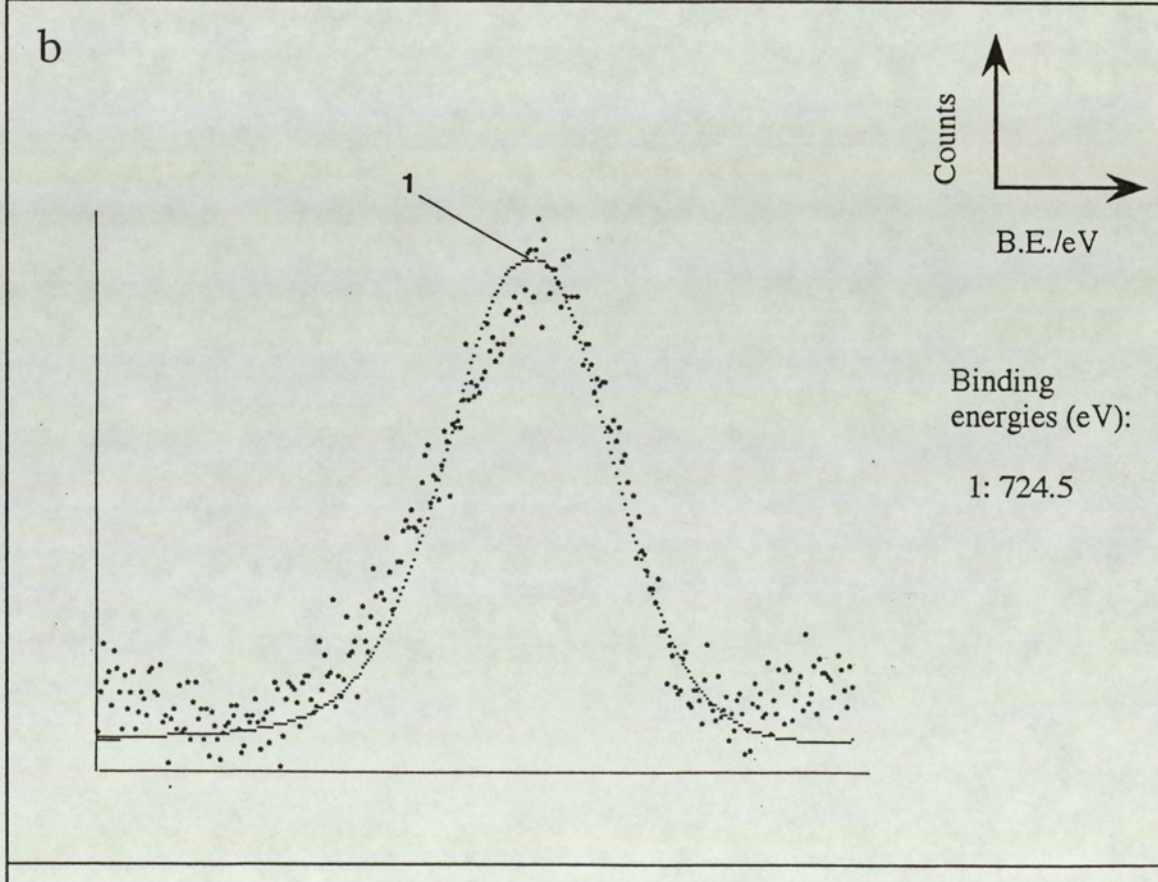

Figure 5.11.

Unbombarded Fe_3O_4 surface.

a) Fe $2p_{3/2}$

b) Fe $2p_{1/2}$

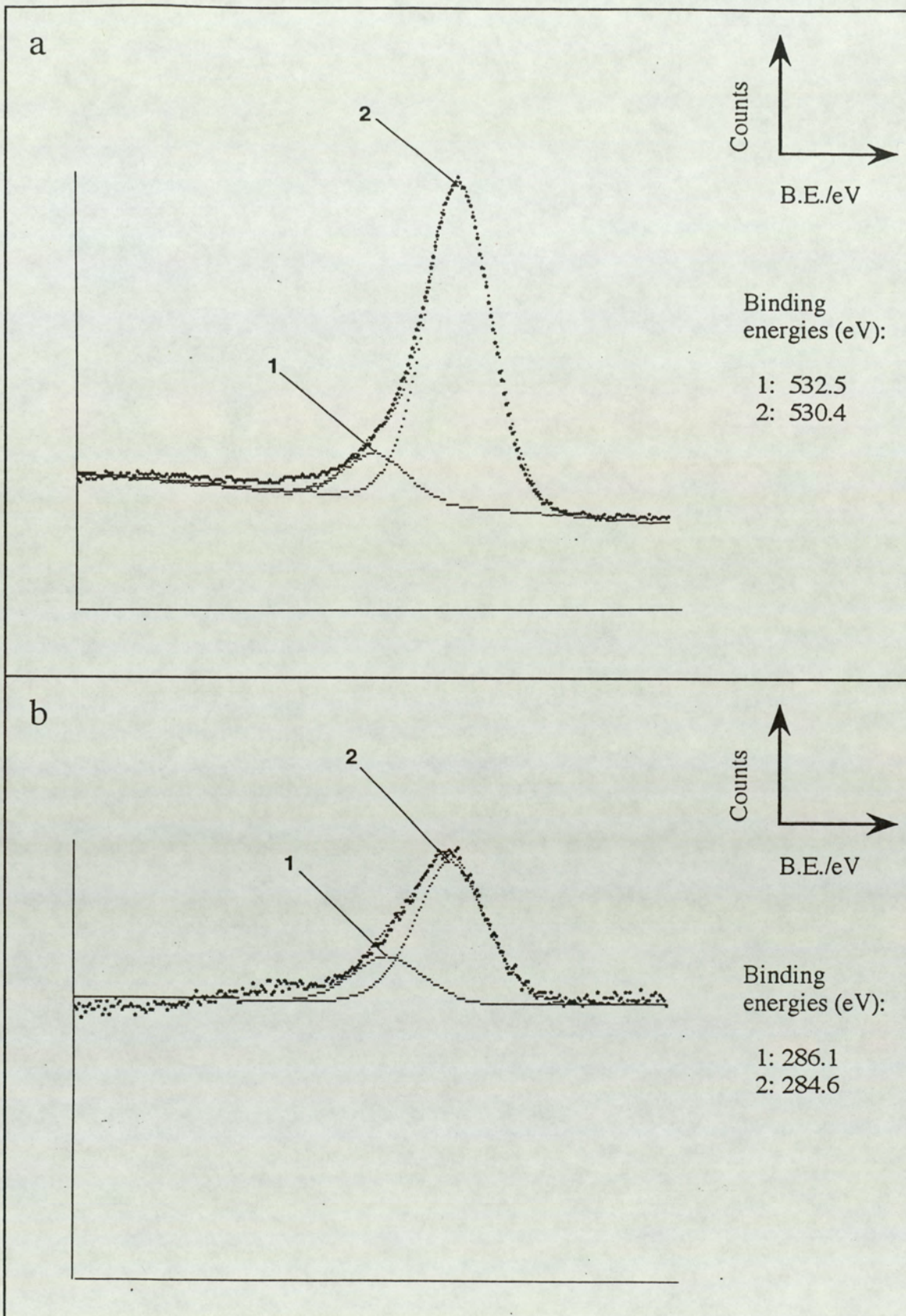

Figure 5.12.

Unbombarded Fe_3O_4 surface.

a) O 1s
b) C 1s

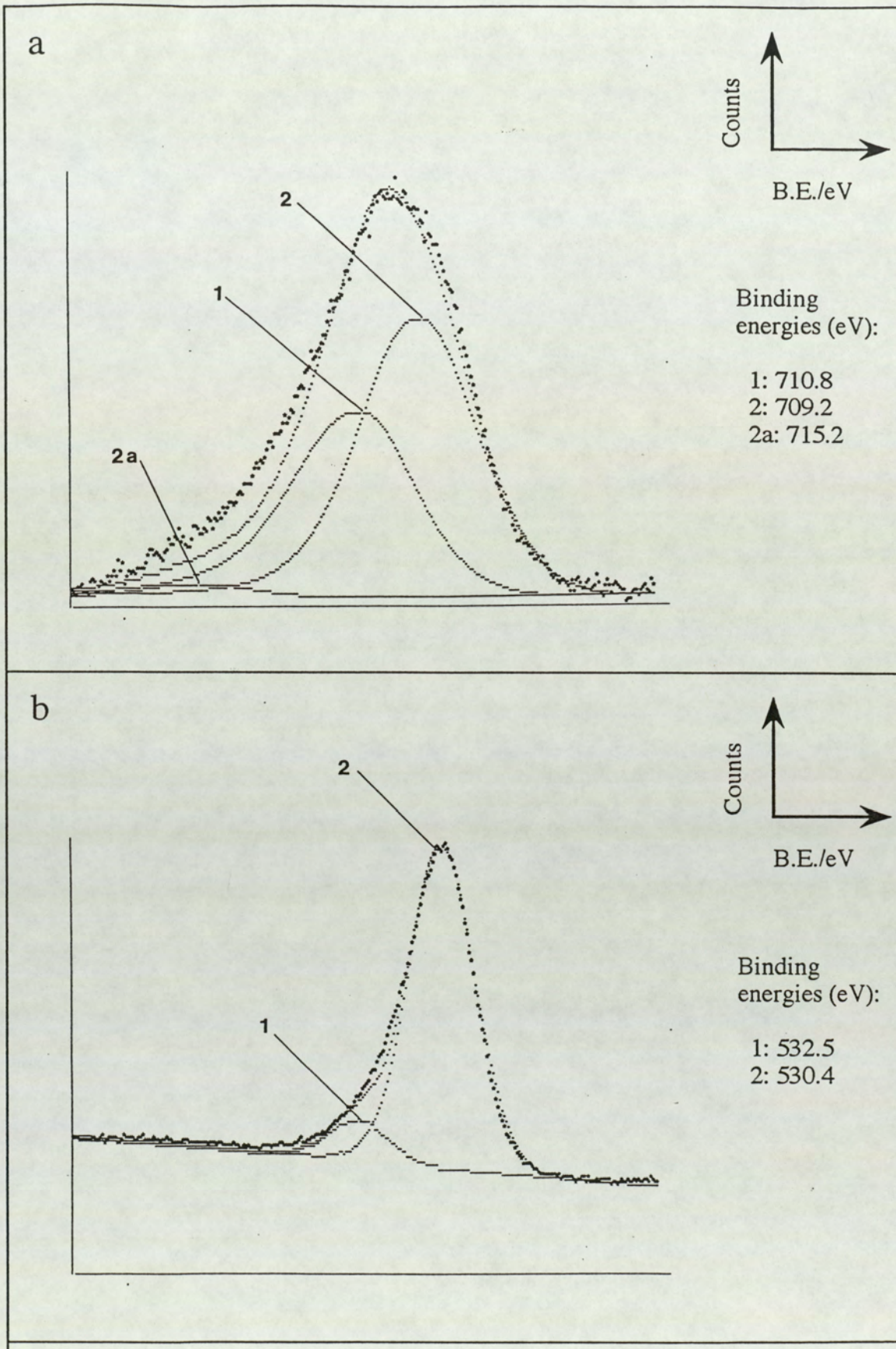

Figure 5.13.

Fe_3O_4 surface after 10 minutes of Ar^+ ion bombardment.

a) Fe $2p_{3/2}$

b) O 1s

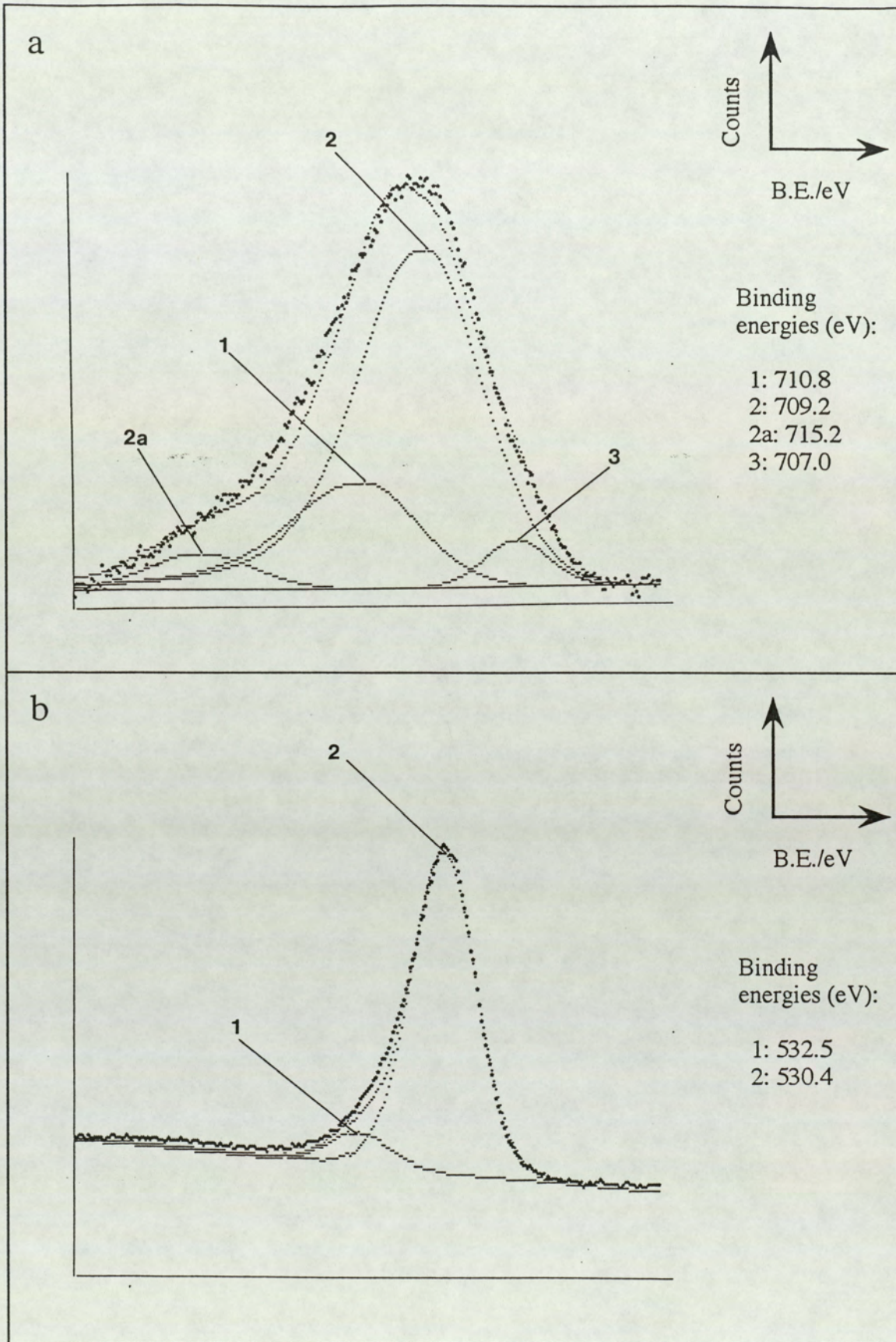

Figure 5.14.

Fe_3O_4 surface after 60 minutes of Ar^+ ion bombardment.

a) Fe $2p_{3/2}$

b) O 1s

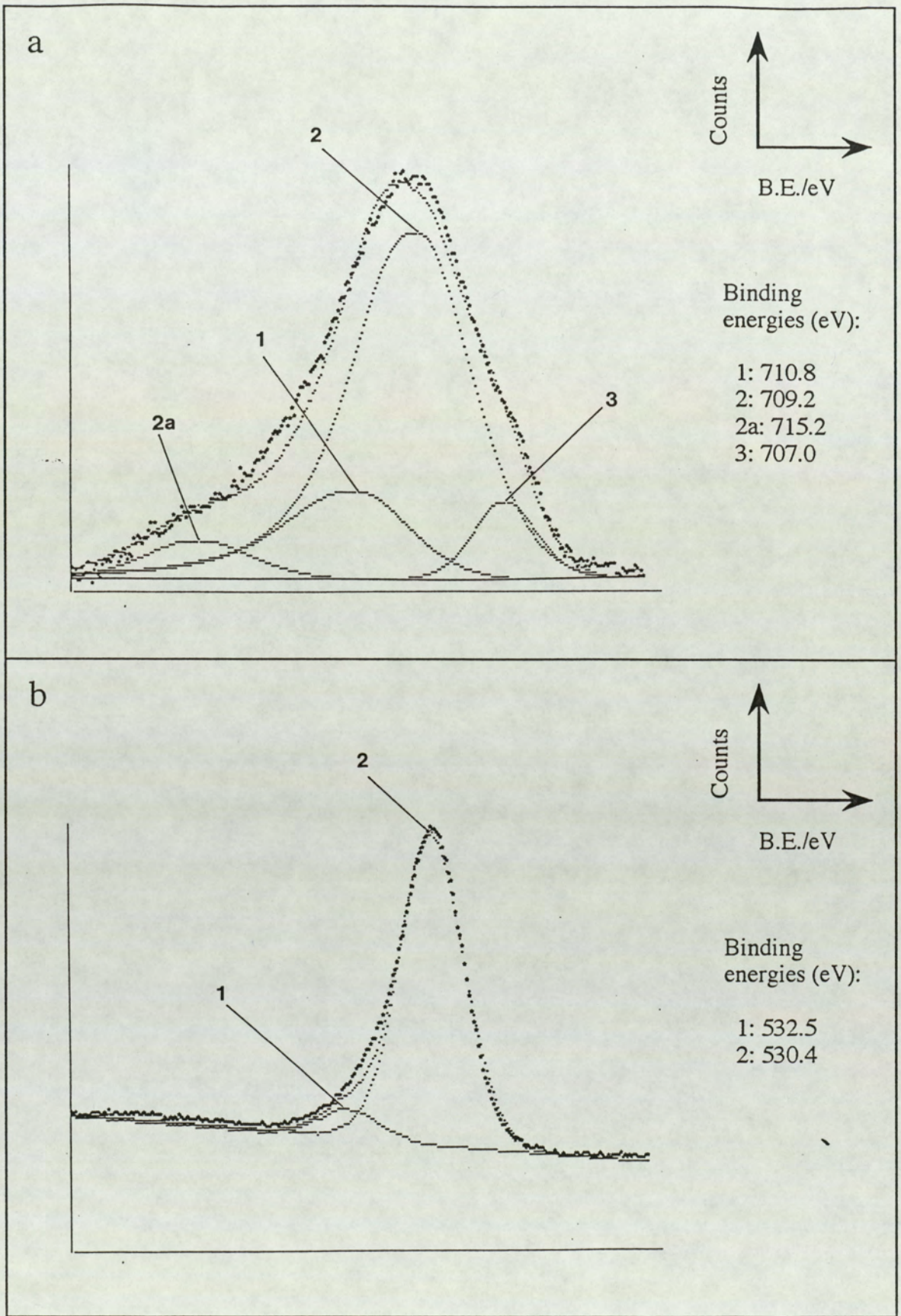

Figure 5.15.

Fe_3O_4 surface after 120 minutes of Ar^+ ion bombardment.

a) Fe $2p_{3/2}$

b) O 1s

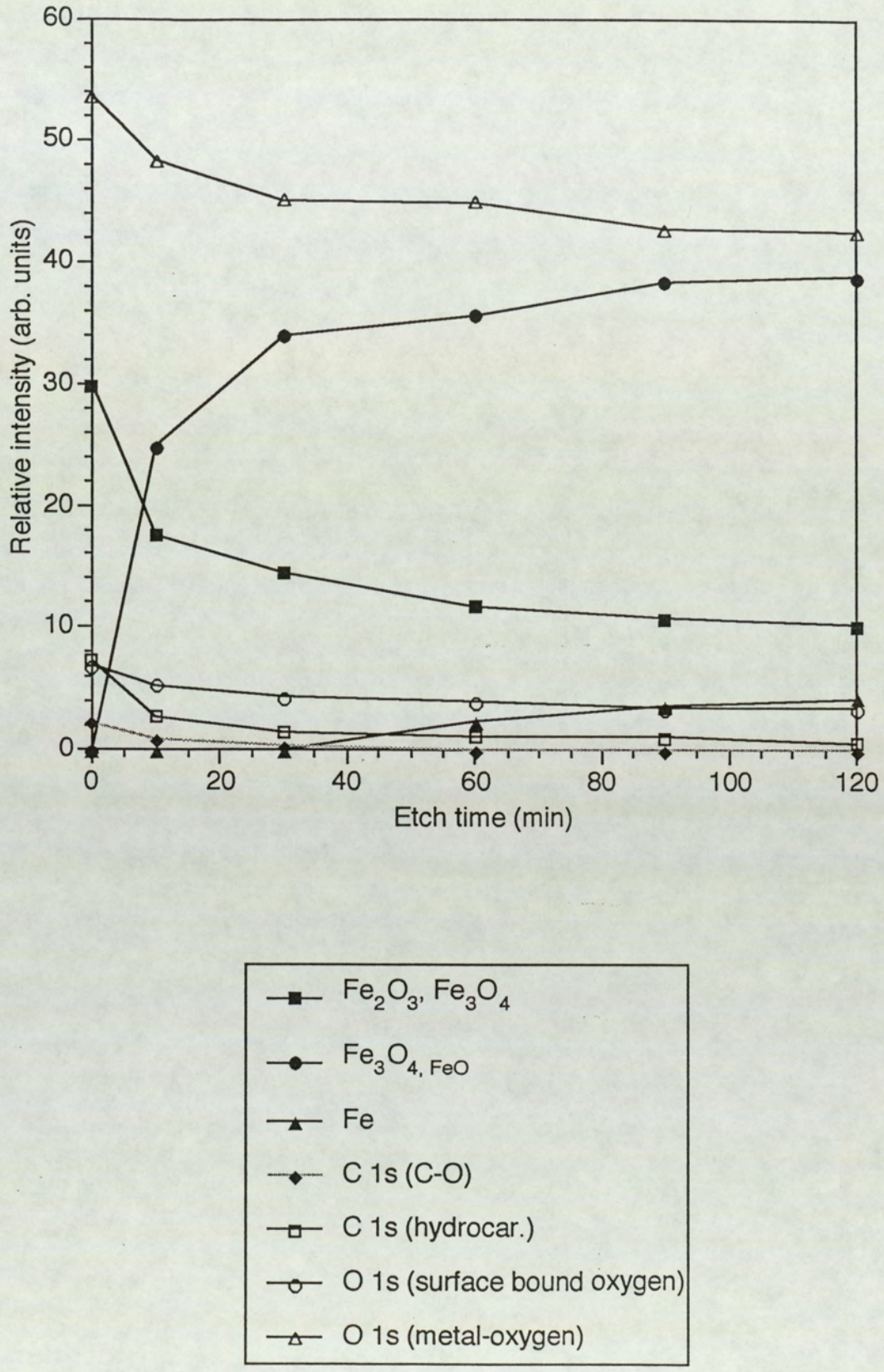

Figure 5.16.

Relative intensity as a function of etch time for Fe_3O_4.

α-Fe_2O_3, containing only Fe^{III}, ions would be expected to increase the ratio further. Thus the only possible explanation for the value of 0.71 for the ratio measured here is that a significant reduction of Fe^{III} to Fe^{II} has occured.

Further ion bombardment for periods of 30, 60, 90 and 120 minutes results in the intensity ratio of Fe^{III} to Fe^{II} decreasing to values of 0.43, 0.33, 0.28 and 0.26 respectively, providing further evidence of ion beam induced reduction of the oxide surface. This evidence is reinforced by the appearence of a narrow, small peak of binding energy 707.0 eV (FWHM = 1.9 eV) in the $Fe2p_{3/2}$ spectra, the intensity of which increases upon further bombardment until a steady state is reached after about 120 minutes of bombardment period. This can be seen clearly in figures (5.14a) and (5.15a) which show the spectra after 60 minutes and 120 minutes of ion bombardment. This narrow peak is due to Fe^0 ions formed partly from the reduction of $Fe^{III} \rightarrow Fe^{II} \rightarrow Fe^0$. The intensity ratio of Fe^{III} to Fe^0 reduces from 5.0 after 60 minutes of bombardment time to 3.0 and 2.4 after 90 and 120 minutes respectively. That for Fe^{II} to Fe^0 reduces from 14.8 after 60 minutes to 10.6 and 9.0 after 90 and 120 minutes respectively. As in the case for FeO, equilibrium conditions are established after approximately 120 minutes of bombardment.

All the binding energy values with their FWHM values are listed in table (5.2). Figure (5.16) shows a plot of the relative intensities against etch times for all peaks appearing in the spectral lines of Fe $2p_{3/2}$, The O 1s and the C 1s. As in the case for FeO, this plot also shows the changes in the M/O intensity ratio against etch time. Only the O 1s contribution due to the metal-oxygen bond has been used in the calculation of M/O.

5.5.3: α-Fe_2O_3

Stochiometric α-Fe_2O_3 contains Fe^{III} ions in a rhombohedral lattice, thus it is expected that the XPS results for the Fe 2p spectra should show only the contribution due to the Fe^{III} ions (unless if surface hydration has taken place). The lines Fe 2p, O 1s, C 1s and Au 4f were recorded and the curve-fitting procedure carried out similarly

to the other iron oxides described above. Figures (5.17a, b) show the Fe 2p lines and figures (5.18a, b) show the oxygen 1s and the carbon 1s spectral lines for the unetched surface. In the O 1s spectrum three peaks can be identified; the major peak at 530.4 eV is due to the metal-oxygen bond and two much smaller peaks at 532.5 eV and at 533.7 eV are due to surface bound oxygen and water molecules respectively. The C 1s spectrum shows the presence of two peaks with FWHM values of 2.0 eV each, separated by an energy difference of 1.5 eV. The origins of these two carbon peaks have already been discussed above for the cases of other iron oxide surfaces. Thus, surface hydrocarbon and carbon contaminations are evident.

The unbombarded spectrum of Fe $2p_{3/2}$, figure (5.17a), shows one major component at 710.8 eV with its associated weak satelite at 719.2 eV, this is as expected being due to Fe^{III} ions from α-Fe_2O_3. The satellite intensity is found to be approximately 4.1% of the main peak intensity. The Fe $2p_{1/2}$ spectrum, figure (5.17b), show the same results; one peak due to the α-Fe_2O_3 state is seen at 724.5 eV. The $2p_{3/2}$ to $2p_{1/2}$ intensity ratio is ~2.3.

Upon subjecting the surface to progressive periods of ion bombardment and carrying out XPS between bombardment periods results in changes to all three spectra of C 1s, O 1s and Fe 2p. The carbon contamination layer is gradually being removed and the Fe 2p spectra showing significant broadening. The O 1s contamination peak due to surface bound water is completely removed within 30 minutes of bombardment, whilst the other oxygen peaks show an intensity reduction. This is accompanied by a gradual colour change of the α-iron (III) oxide surface from brick-red to black.

Figures (5.19a and b) show the Fe $2p_{3/2}$ and O 1s spectra after 10 minutes of ion bombardment. The broadening of the Fe $2p_{3/2}$ spectra can be explained by the appearence of an additional peak at 709.2 eV with its associated satellite at 715.2 eV, showing the presence of Fe^{II} ions due to beam induced reduction. The satellite intensity is found to be ~12% of the main peak intensity. It should be pointed out here that for this bombardment period the weak satellite due to the Fe^{III} ions can not be

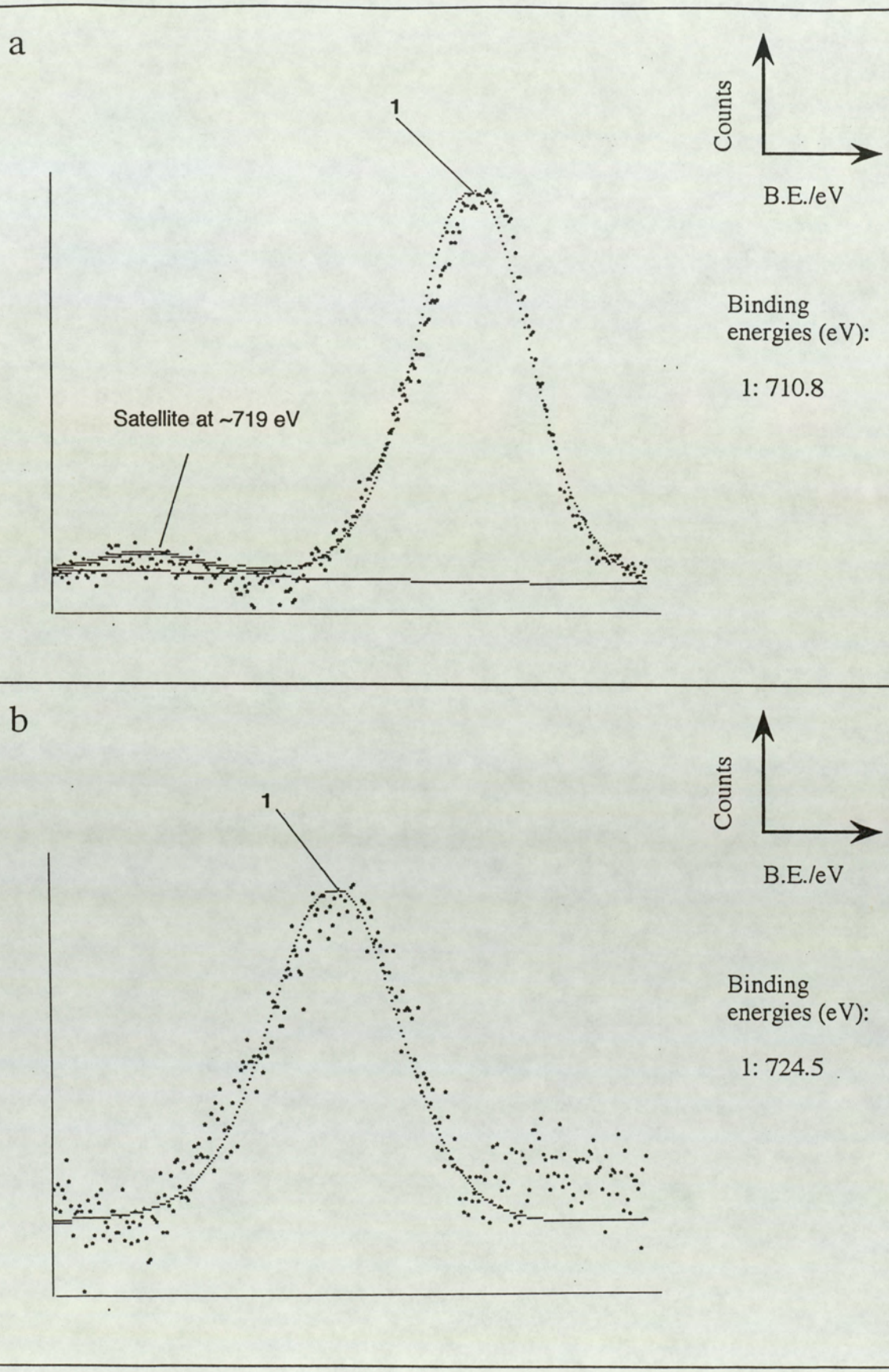

Figure 5.17.

Unbombarded Fe_2O_3 surface.

a) Fe $2p_{3/2}$

b) Fe $2p_{1/2}$

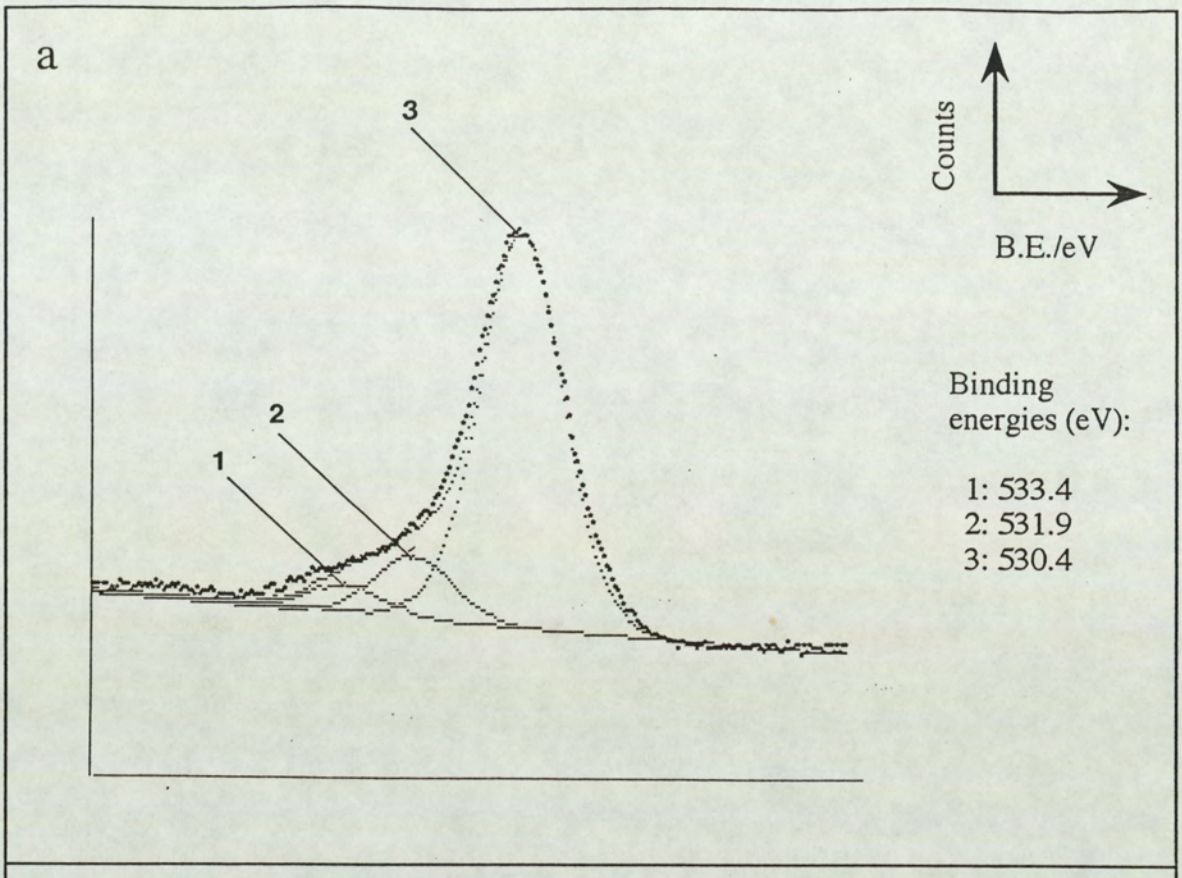

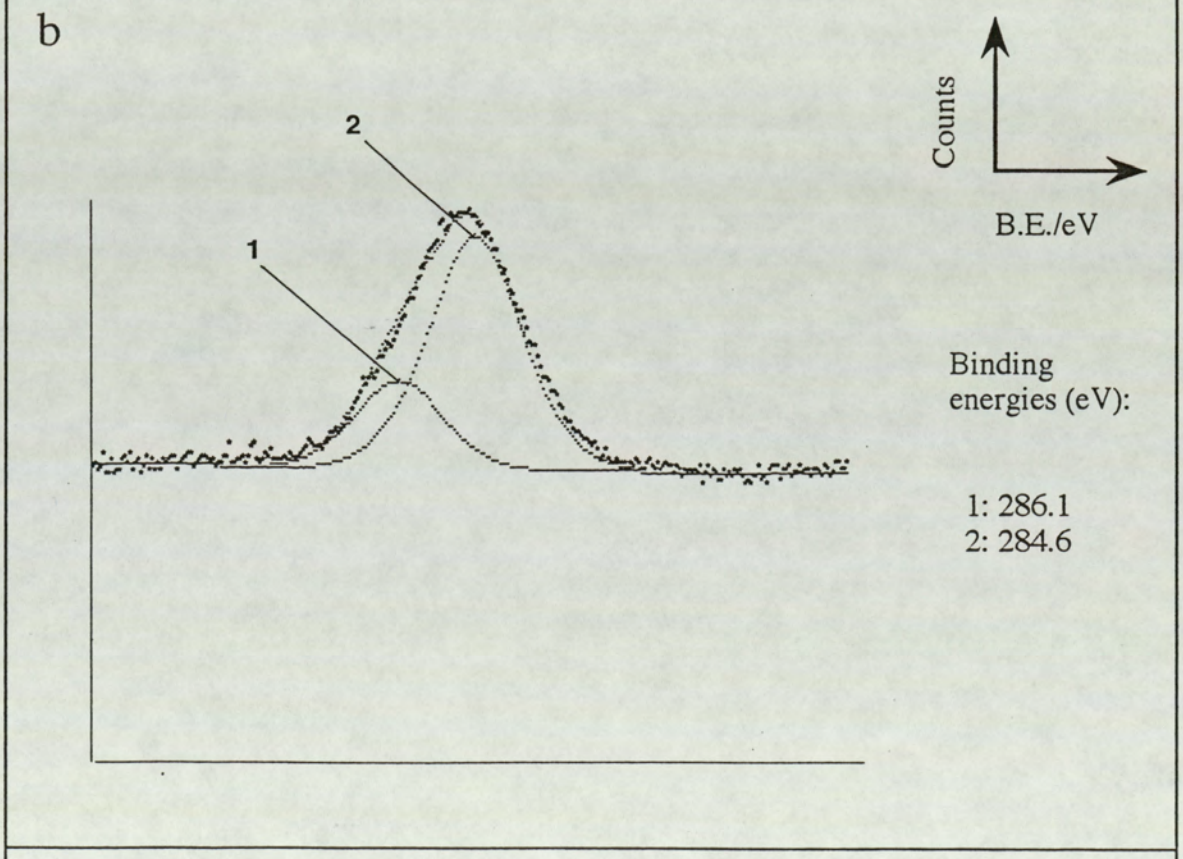

Figure 5.18.

Unbombarded Fe_2O_3 surface.

a) O 1s
b) C 1s

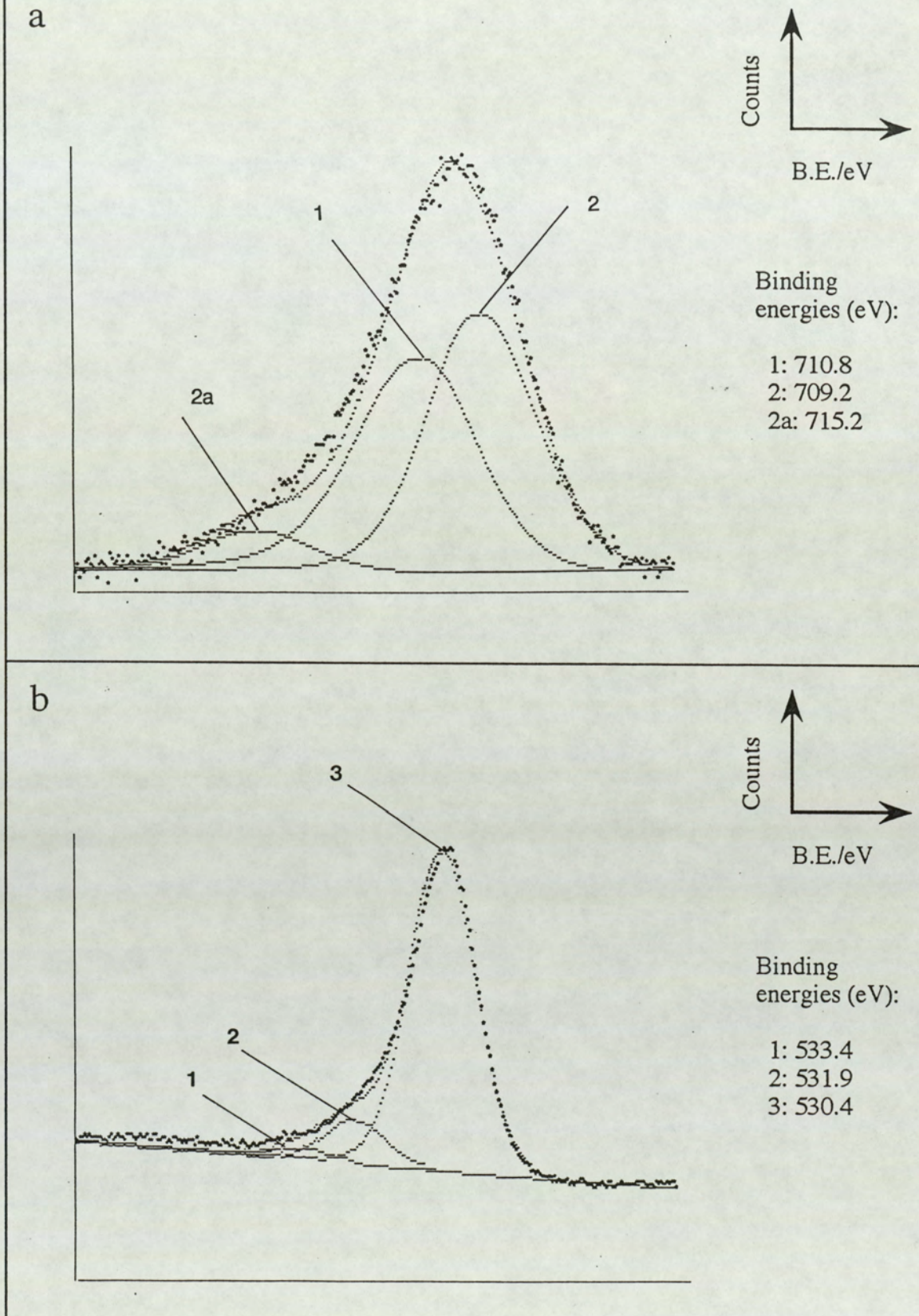

Figure 5.19.

Fe_2O_3 surface after 10 minutes of Ar^+ ion bombardment.

a) Fe $2p_{3/2}$

b) O 1s

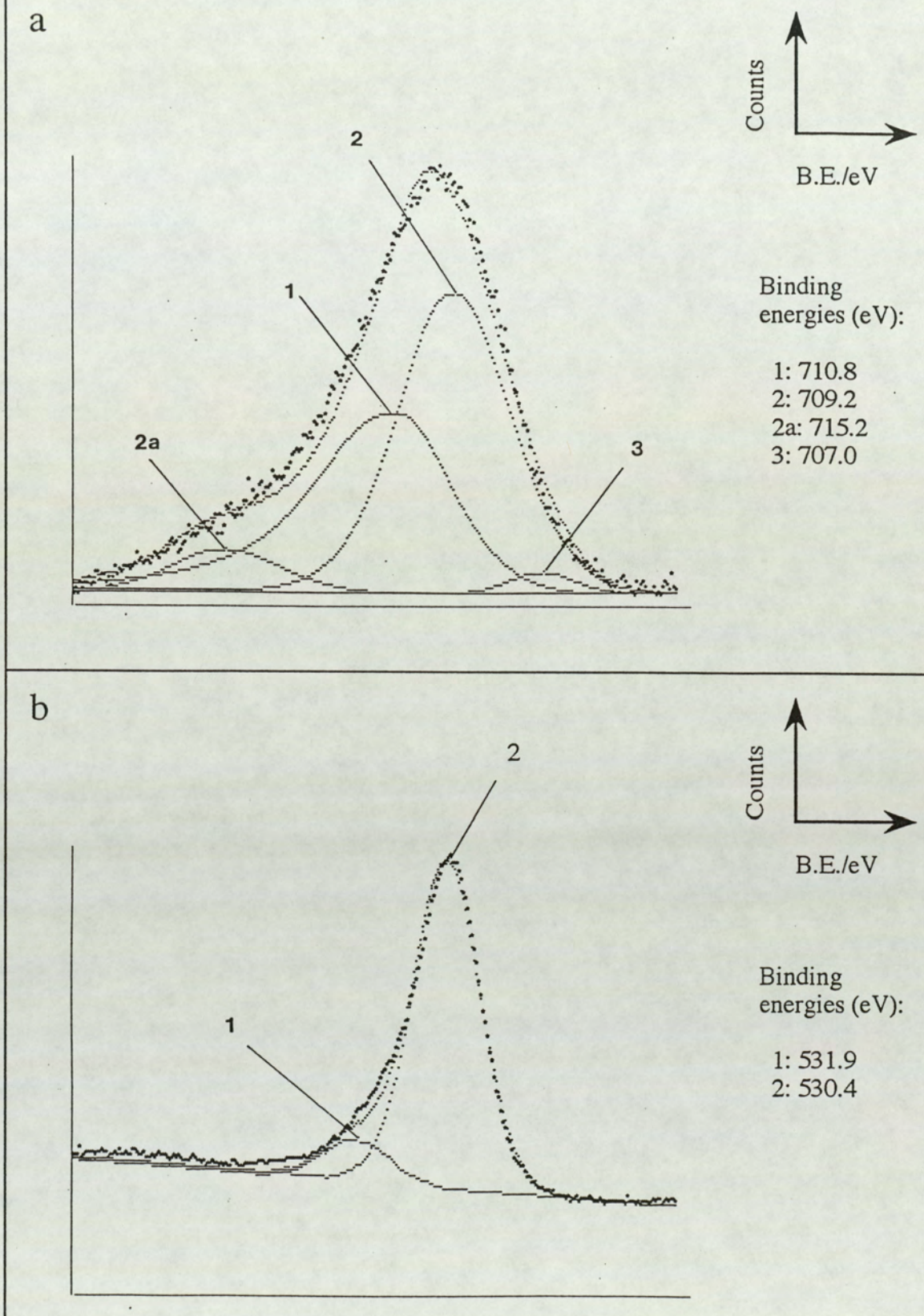

Figure 5.20.

Fe_2O_3 surface after 30 minutes of Ar^+ ion bombardment.

a) Fe $2p_{3/2}$

b) O 1s

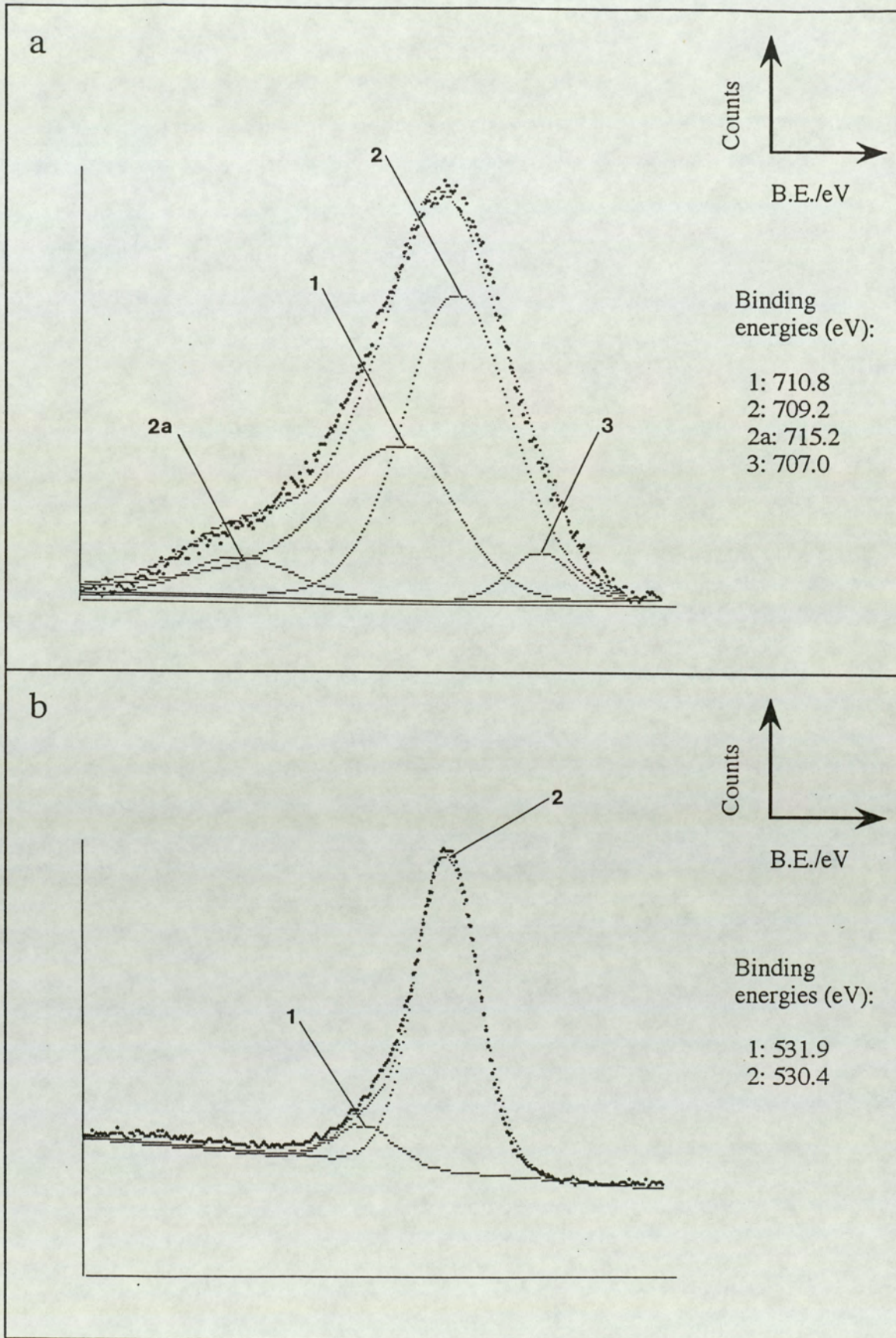

Figure 5.21.

Fe_2O_3 surface after 120 minutes of Ar^+ ion bombardment.

a) Fe $2p_{3/2}$

b) O 1s

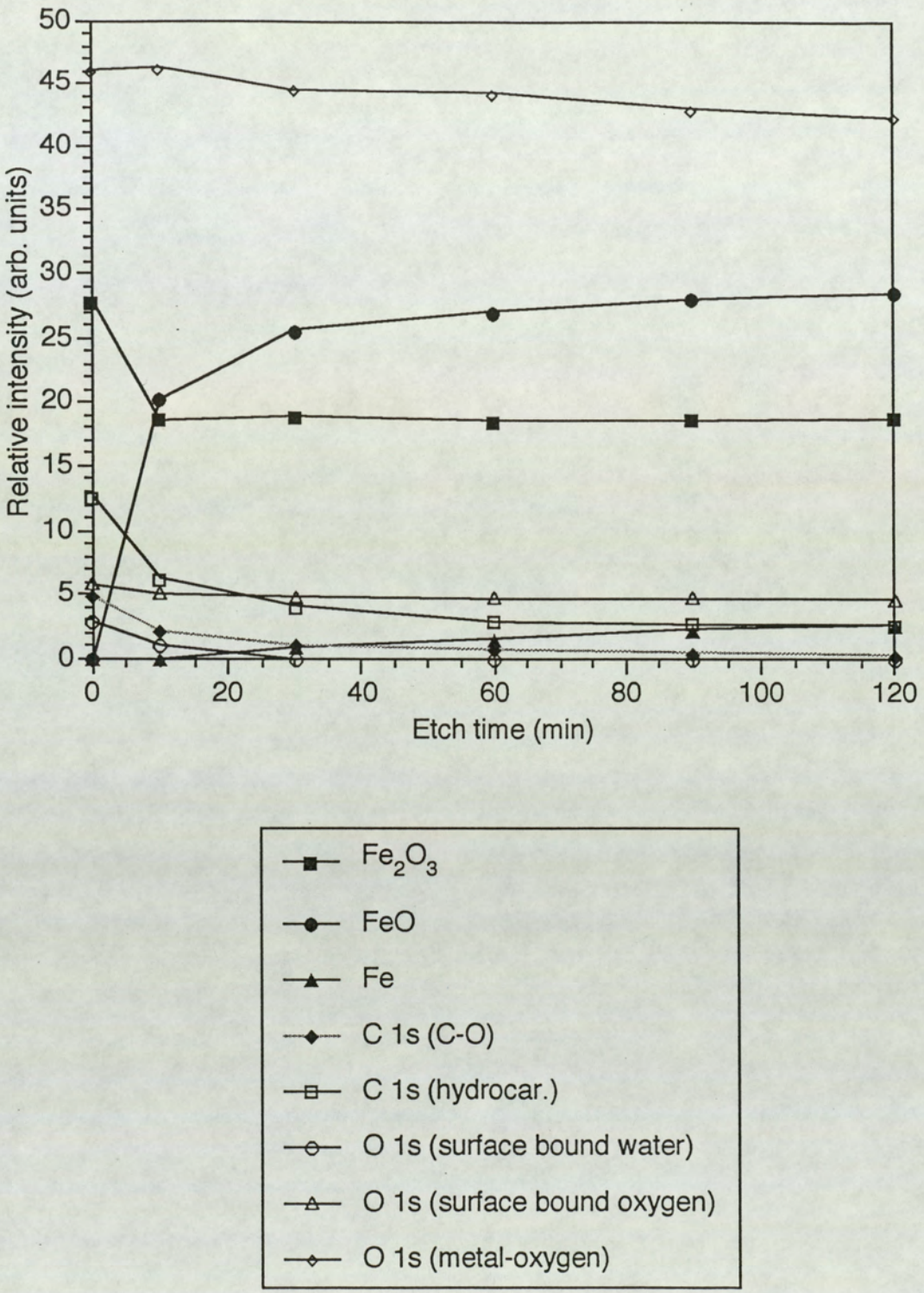

Figure 5.22.

Relative intensity as a function of etch time for Fe_2O_3.

observed. This is because the intensity of the Fe^{III} ions has been greatly diminished and its associated satellite intensity can not be seen above the background.

After 30 minutes of ion bombardment a further peak appears in Fe $2p_{3/2}$ profile, figure (5.20a), at a binding energy of 707.0 eV showing existance of Fe^0, the metallic iron. Thus, full reduction $Fe^{III} \rightarrow Fe^{II} \rightarrow Fe^0$ has taken place. Further bombardment shows an intensity decrease of the Fe^{III} state combined with an intensity increase of the metallic state. Figures (5.21a and b) show the Fe $2p_{3/2}$ and O 1s spectra after 120 minutes of ion bombardment. The intensity ratio of Fe^{III}:Fe^{II} (satellite contributions not taken into account) decreases from 1.1 after 10 minutes of bombardment to 0.74, 0.68, 0.67 and 0.66 after 30, 60, 90 and 120 minutes of bombardment respectively. Similarly the intensity ratio of Fe^{III}:Fe^0 decreases from 20.1 after 30 minutes of bombardment to 11.8, 8.0 and 7.3 after 60, 90 and 120 minutes of bombardment respectively.

The relative intensity of each of the peaks, derived from the results above are shown in figure (5.22). Table 5.2 also lists the binding energy values as found for the α-Fe_2O_3 sample.

5.5.4: CoO

For the investigations carried out on the CoO powder oxide, the photo-electron spectral lines Co $2p_{1/2}$, Co $2p_{3/4}$, C 1s, O 1s and the $Au4f_{7/2}$ were recorded. Figures (5.23a and b) show the O 1s and the C 1s spectral lines for the unbombarded surface. The O 1s spectrum is very similar to that obtained for the FeO surface (for example see figure (5.6a)). The O 1s peak may be resolved into three components at binding energies of 530.1, 531.5 and 533.5 eV, all with FWHM of 1.8 eV. The first of these components is due to the metal -oxygen bond and the second due to the oxygen atom in an OH group (this strongly suggests the presence of a hydroxyl species of the form CoOOH on the CoO powder surface). The third peak at 533.5 eV corresponds to surface bound water.

The C 1s spectrum for the unbombarded surface shows the presence of two peaks. One at ~284.6 eV being due to the surface borne hydrocarbons. The second peak at 286.1 eV is expected to be due to the carbon in a carbon-single bond-oxygen molecule.

Figures (5.24a and b) show the $Co2p_{3/2}$ and Co $2p_{1/2}$ spectra respectively for the unbombarded surface. Three major peaks can be resolved in the Co $2p_{3/2}$ spectrum; two peaks at 780.0 eV and the third peak at 781.3 eV. The latter at 781.3 eV (FWHM = 3.2 eV) is considered to be due to the Co^{II} ions in $Co(OH)_2$. The component at 780.0 eV cannot be due to a single species owing to its extreme width. It is thus interpreted as a double peak, one with a FWHM of 1.8 eV corresponding to the Co^{III} ions in CoOOH and the other with FWHM of 2.8 eV being due to the Co^{II} ions in CoO. The presence of two broad satellites (FWHM = 3.2 eV) at ~7.0 eV and ~5.8 eV above the main CoO peak also confirms the existence of CoO as these satellites are due to the high spin Co^{II} state. The curve-fitting procedure also suggests a third satellite peak due to Co^{II} in CoO at ~2.5 eV above the main peak, i.e., at 782.5 eV. The intensity of each of these satellites was measured to be approximately 24% of the intensity of the main CoO peak.

The Co $2p_{1/2}$ peak (Figure (5.24b)) shows the same trends as described above for the case of Co $2p_{3/2}$. Three major peaks are present, two at 795.4 eV with FWHM of 2.0 eV and 3.0 eV corresponding to the CoOOH and CoO states respectively. The third peak at 796.7 eV (FWHM = 3.4 eV) is the Co $2p_{1/2}$ component of the $Co(OH)_2$ state. The satellite at ~2.5 eV above the CoO peak is also evident. Thus the Co $2p_{1/2}$ spectrum confirms the findings in the Co $2p_{3/2}$ spectrum.

Figures (5.25a and b) show the Co $2p_{3/2}$ and O 1s spectra after 10 minutes of ion bombardment. The Co $2p_{3/2}$ spectrum is broadened and the peak synthesis procedure reveals near removal of the thin layer of surface CoOOH. This is suggested by the presence of only one peak at 780.0 eV (FWHM = 2.8 eV), due to the Co^{II} ions in CoO; however, there may also be a negligible contribution from Co^{III} ions in CoOOH. The presence of predominantly CoO is also indicated by the prominence of

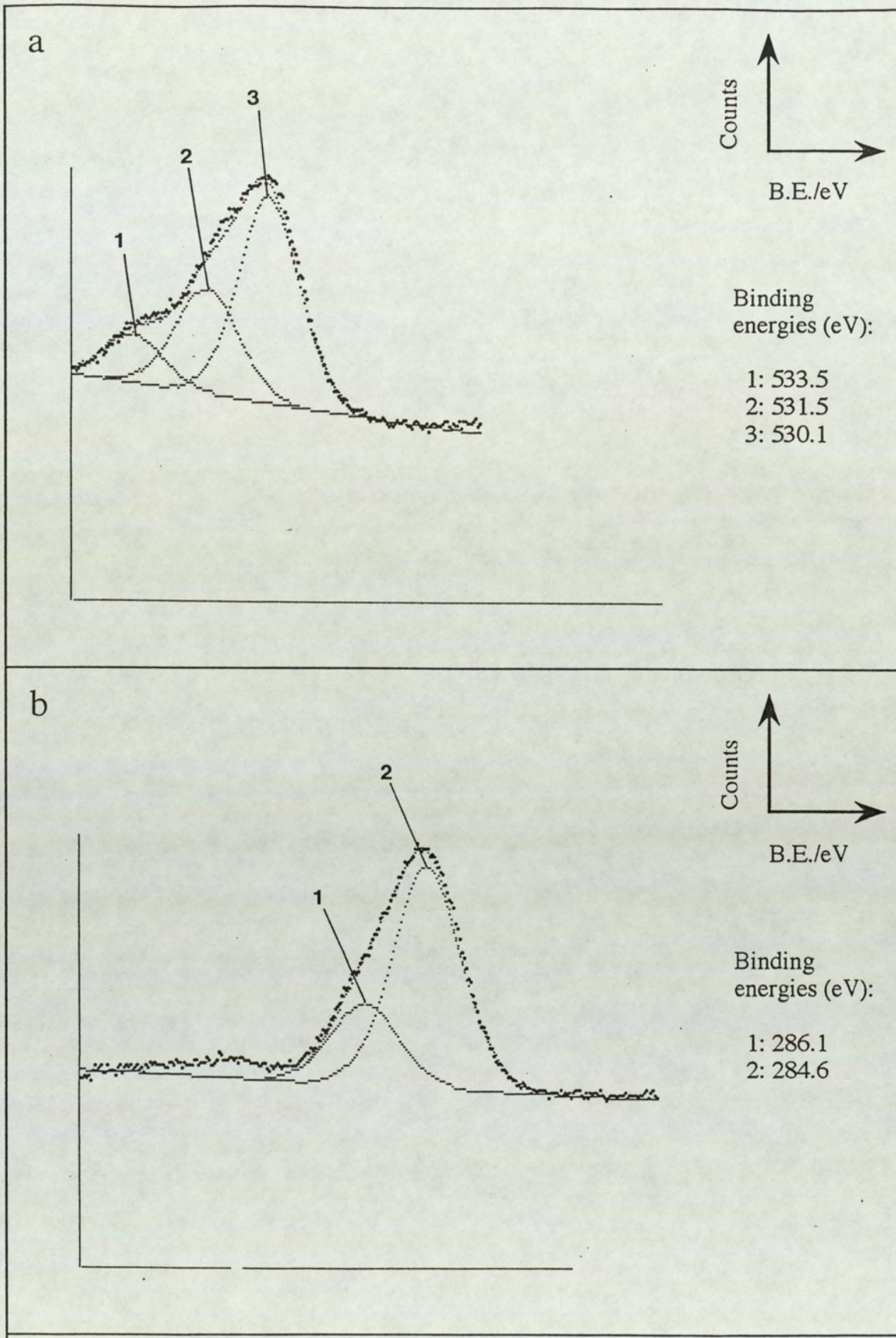

Figure 5.23.

Unbombarded CoO surface.

a) O 1s
b) C 1s

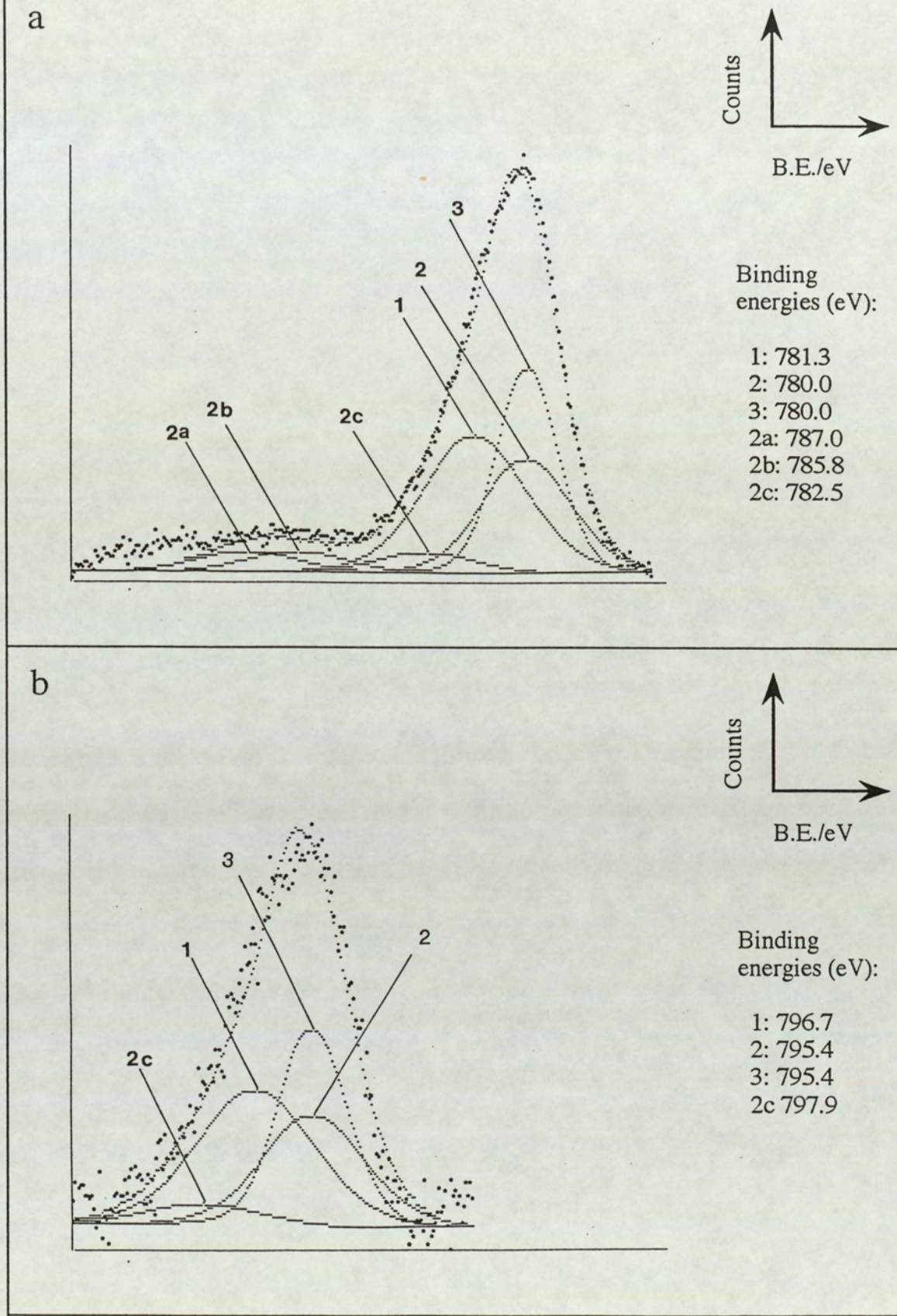

Figure 5.24.

Unbombarded CoO surface.

a) Co $2p_{3/2}$

b) Co $2p_{1/2}$

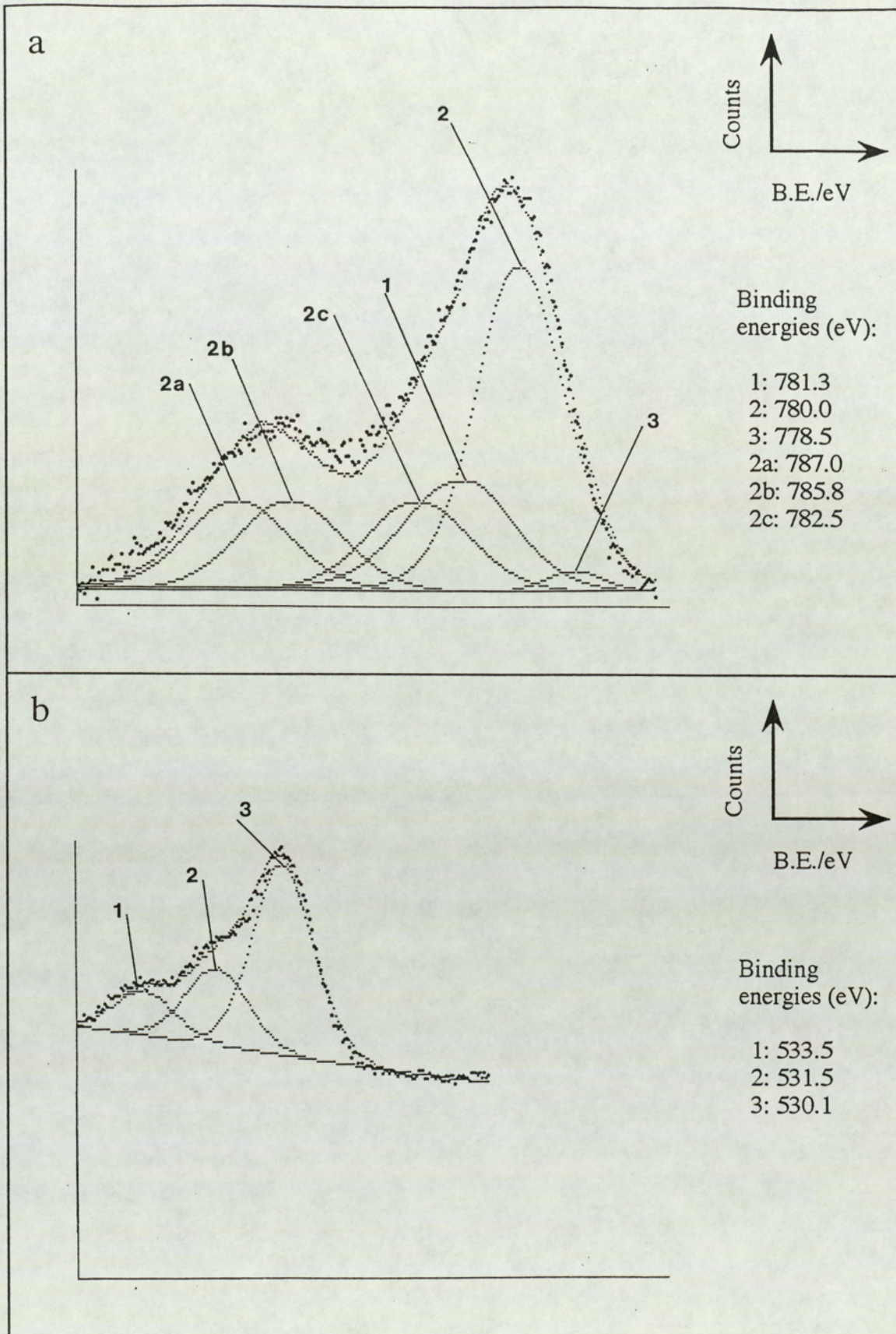

Figure 5.25.

CoO surface after 10 minutes of Ar^+ ion bombardment.

a) Co $2p_{3/2}$

b) O 1s

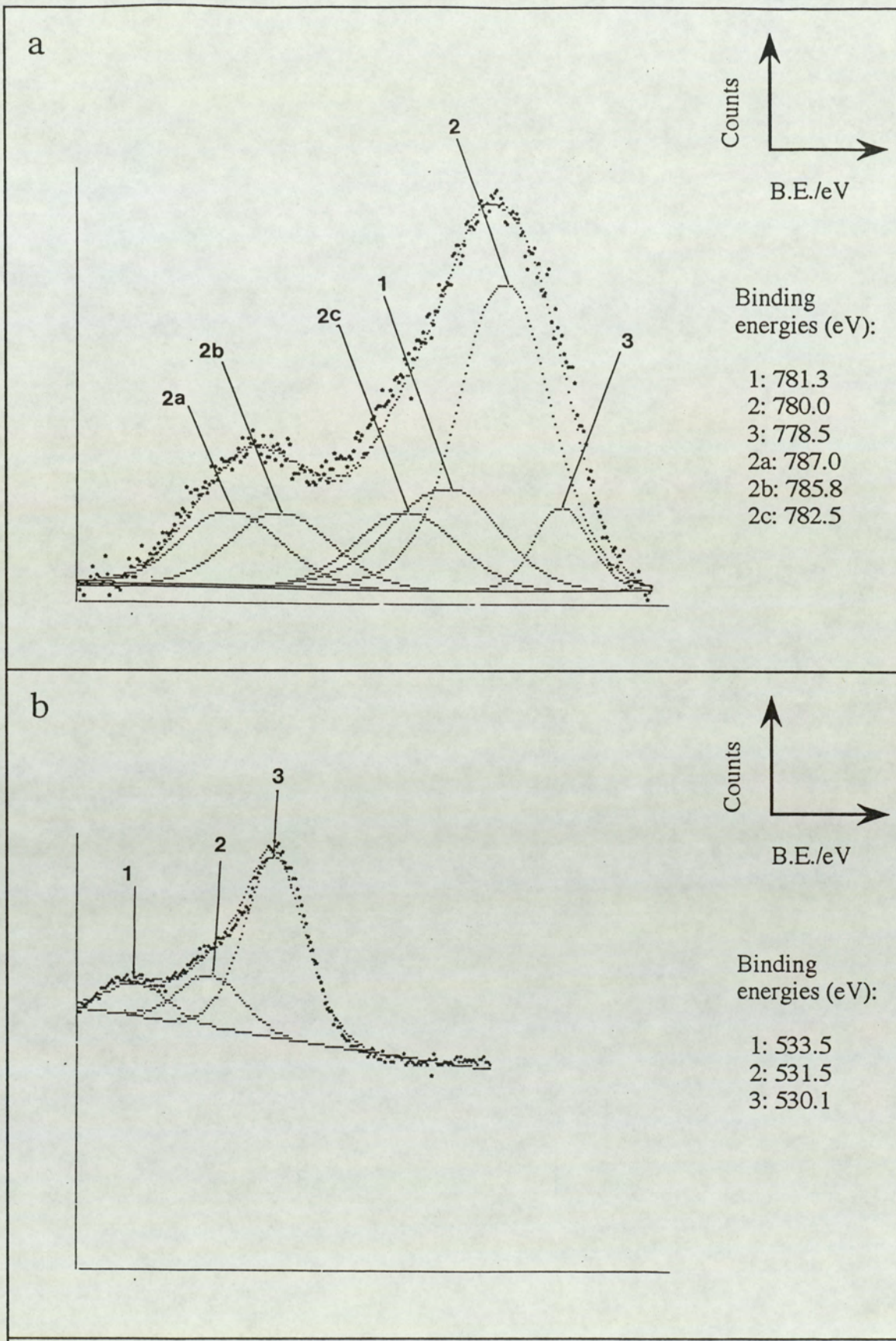

Figure 5.26.

CoO surface after 30 minutes of Ar^+ ion bombardment.

a) Co $2p_{3/2}$

b) O 1s

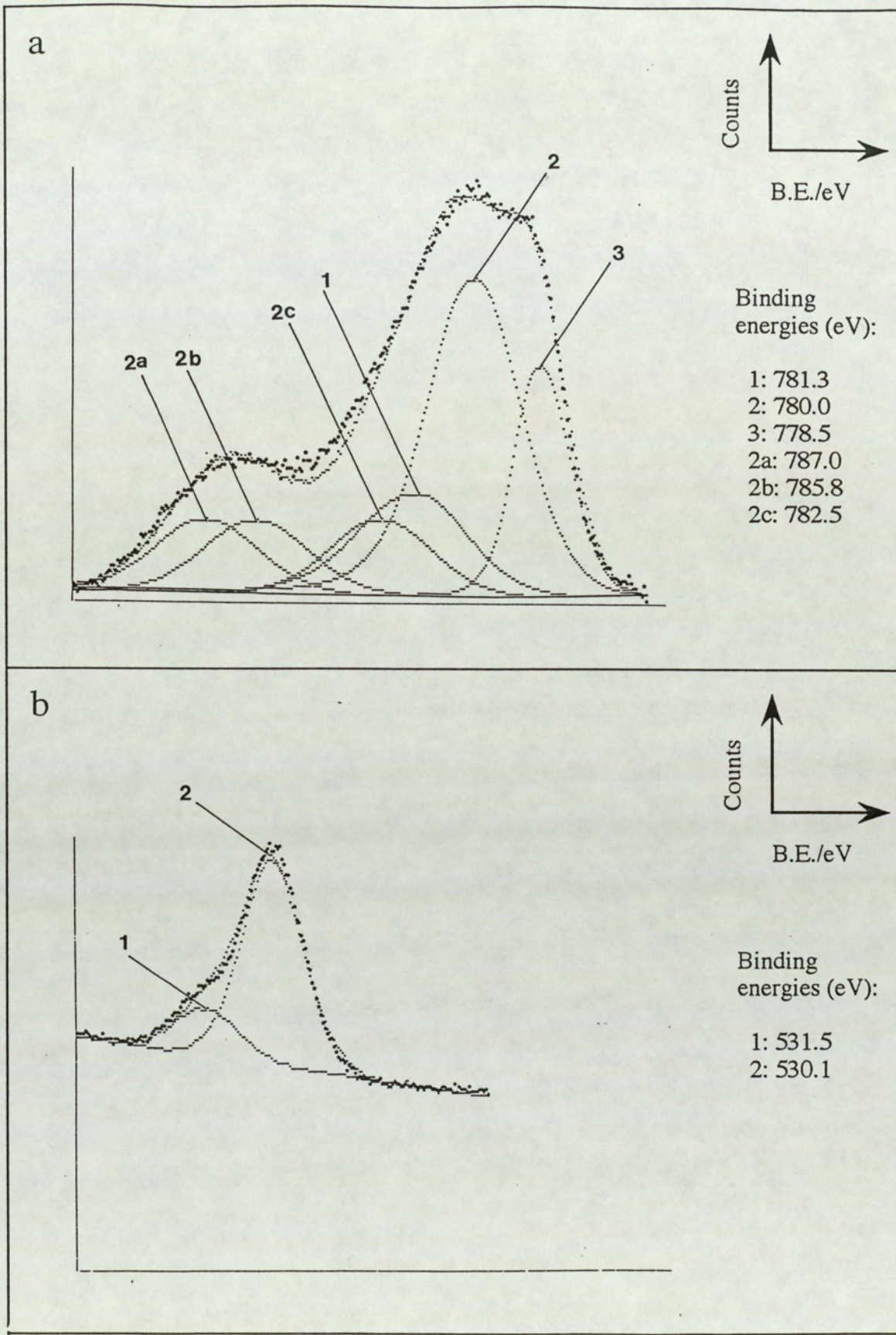

Figure 5.27.

CoO surface after 120 minutes of Ar^+ ion bombardment.

a) Co $2p_{3/2}$

b) O 1s

Table 5.3: Measured binding energy values (±0.2eV) and corresponding FWHM values (±0.2eV) for cobalt and its oxides. Calibration is with respect to the Au $4f_{7/2}$ peak at 84.0 eV.

identity		core level	binding energy (eV)	FWHM (eV)
CoO	Co^{II}	$2p_{3/2}$	780.0	2.8
		$2p_{1/2}$	795.4	3.0
CoOOH	Co^{III}	$2p_{3/2}$	780.0	1.8
		$2p_{1/2}$	795.4	2.0
$Co(OH)_2$	Co^{II}	$2p_{3/2}$	781.3	3.2
		$2p_{1/2}$	796.7	3.4
Co_3O_4	Co^{III}	$2p_{3/2}$	780.0	2.8
		$2p_{1/2}$	795.4	3.0
	Co^{II}	$2p_{3/2}$	780.0	2.8
		2p1/2	795.4	3.0
Co_2O_3	Co^{III}	$2p_{3/2}$	780.0	1.9
Oxygen	metal-oxygen bond	1s	530.1	1.8
	hydroxide bond	1s	531.5	1.8
	surface bound water	1s	533.5	1.8
Carbon	hydrocarbon bond	1s	284.6	2.0
	carbon-oxygen bond	1s	286.1	2.0
	double oxygen bond	1s	287.7	2.0
Satellites	Co^{II}	$2p_{3/2}$	787.0	3.2
(CoO)			785.8	3.2
			782.5	3.2

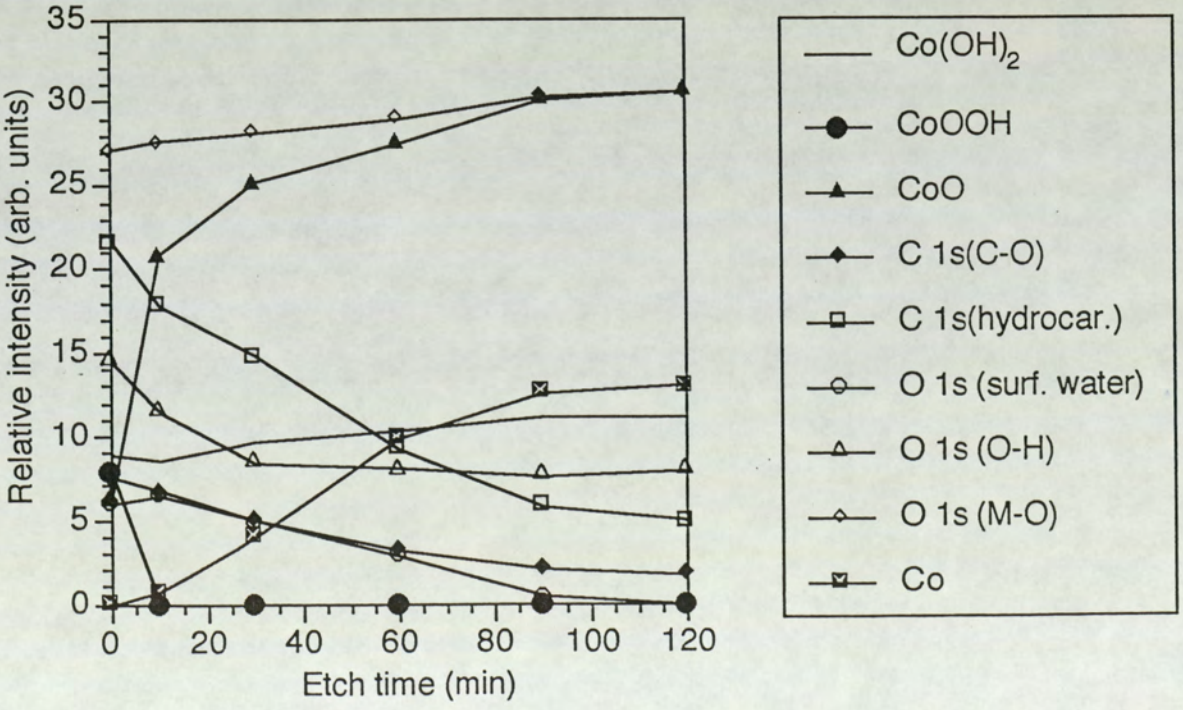

Figure 5.28.

Relative intensity as a function of etch time for CoO.

its satellite peaks. Another important feature of the Co $2p_{3/2}$ spectrum for this bombardment period is the appearence of a peak at 778.5 eV with FWHM of 1.7 eV. This is thought to be due to the presence of metallic cobalt, Co^0. The relative intensity ratio of the Co^{II} ions in CoO to Co^0 is 28.53.

Further bombardment reduces the relative intensity ratio of Co^{II} to Co^0 from 6.34 after 30 minutes to 2.79, 2.39 and 2.35 after 60, 90 and 120 minutes of bombardment respectively. The Co $2p_{3/2}$ and O 1s spectra are shown in figures (5.26a, b) and (5.27a, b) for 30 minutes and 120 minutes of bombardment periods respectively. Figure 5.28 shows a plot of the relative intensities against different etch times for the spectra due to the Co 2p peak of the cobalt and its oxides and hydroxides and the O 1s and the C 1s peaks. Table (5.3) lists all the binding energy values measured for the CoO sample.

5.5.5: Co_3O_4

Binding energies for the lines Co $2P_{3/2}$, Co $2p_{1/2}$, O 1s and C 1s were measured and the spectra recorded for the unetched air-exposed Co_3O_4 powder surface, and curve-fitting procedures were carried out on all peaks. Figures (5.29a and b) show the O 1s and C 1s spectra for the pre-bombardment case. Similar to the CoO samples, the O 1s spectrum contains three peaks. The main peak is due to the metal-oxygen bond at 530.1 eV and the least intense peak at 533.5 eV due to the absorbed water. Presence of cobalt hydroxide is also indicated by the presence of the third oxygen peak at 531.5 eV. In the C 1s spectrum again the presence of three peaks can be seen. The lowest binding energy peak is due to the surface borne hydrocarbons. The second and the third peaks at binding energies 1.5 eV and 3.1 eV above the main peak are due to carbon in single-bond-oxygen molecules and a double-bond-oxygen molecules respectively.

Initially curve-fitting procedures carried out on the unetched Co $2P_{3/2}$ line, figure (5.30a), revealed the presence of two major peaks, one at binding energy 781.3

eV (FWHM=3.2 eV) and the other at 780.0 eV (FWHM=2.8 eV). It is thought that the lower binding energy peak is due to both Co^{III} ions and the Co^{II} ions in Co_3O_4. Since, the Co_3O_4 structure is composed of Co^{III} ions in a octahedral and the Co^{II} ion in tetrahedral site, it would be expected to observe both these ions in the unetched $2P_{3/2}$ spectrum. The presence of the three satellites each with a measured intesity equal to 328 units at approximately 7.0 eV, 5.8 eV and 2.5 eV above the main peak at 780.0 eV (measured intensity equal to 6950 units leading to the satellite intensity being 4.7% of the main peak) indicates that part but not all of this peak is due to Co^{II} ions of Co_3O_4. Considering the case where all contributions to the peak at 780.0 eV is due to Co^{II} ions only, the intensity of its associated satellites would be expected to be higher than the experimentally measured value of 4.7 % (since from the results obtained for CoO powder surface, each of the satellite intensity was measured to be ~24% the value of the main peak intensity). From these observations and from the presence of the OH-bond in the O 1s spectra it can be concluded that the peak at 781.3 eV is due to the Co^{II} ions in $Co(OH)_2$ and the peak at 780.0 is mostly due to the Co^{III} ions in Co_3O_4 with a smaller contribution from Co^{II} ions of Co_3O_4. Thus presence of Only Co_3O_4 on the surface is confirmed.

However a second curve-fitting procedure was also carried out on the unetched Co 2p3/2 spectra to fit two peaks at the binding energy 780.0 eV; one with intensity approximately four times the intensity of one of the satellite lines (the reasons for this second curve-fit are given in chapter 7 on discussion). The fitting parameters for the three satellite peaks and the cobalt hydroxide peak was kept exactly the same as previous, the results of which is shown in figure (5.30b). Thus it is seen that the Co^{III} ions and the Co^{II} ions in Co_3O_4 (also CoO) cannot be resolved separately according to their binding energy or their FWHM value.

A similar curve-fitting procedure carried out on the Co $2p_{1/2}$ peak, (figure (5.30c)), also shows the presence of two peaks at binding energy 795.4 eV with FWHM of 3.0 eV corresponding to the CoII and Co^{III} ions of Co_3O_4 and Co^{II} ions in

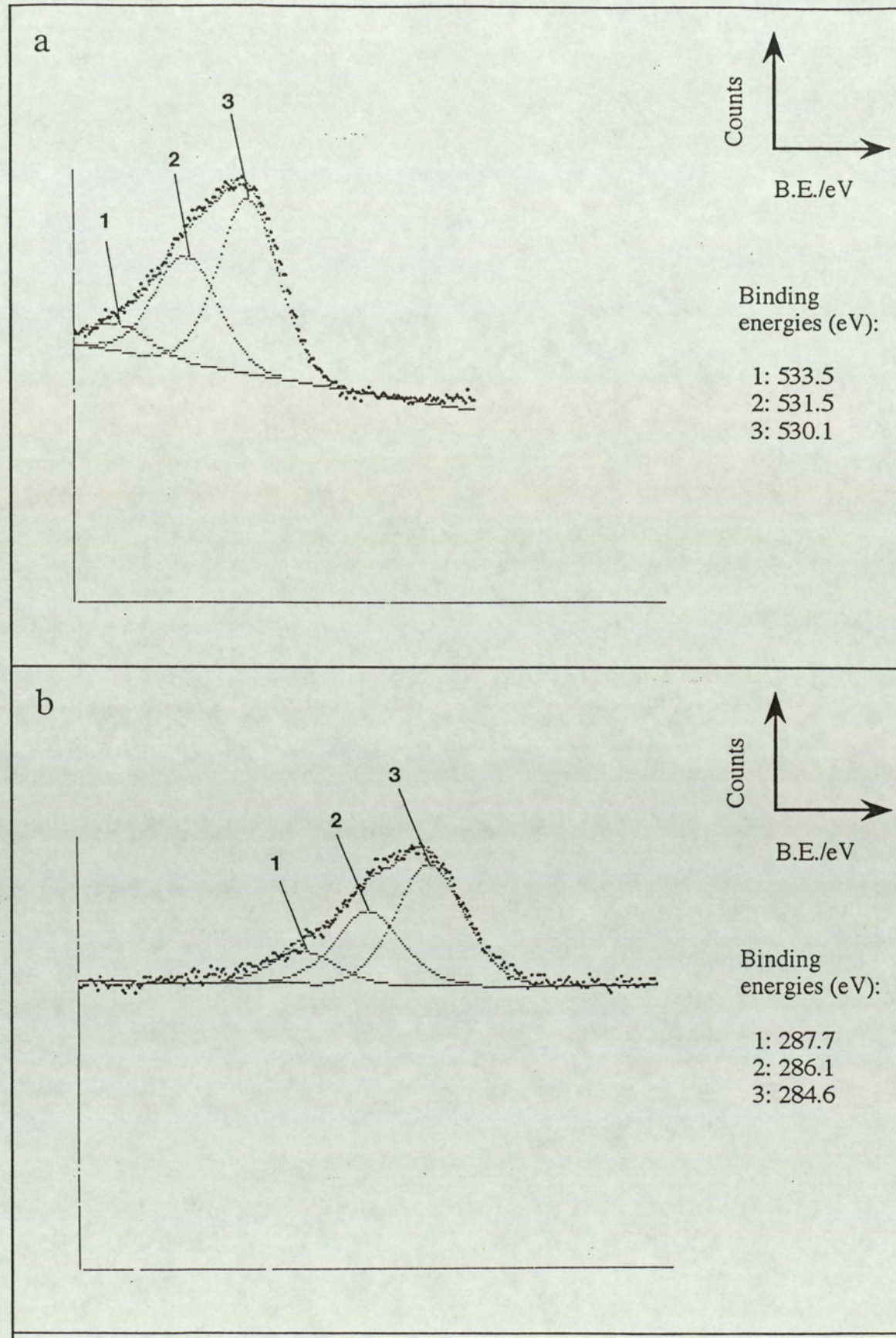

Figure 5.29.

Unbombarded Co_3O_4 surface.

a) O 1s
b) C 1s

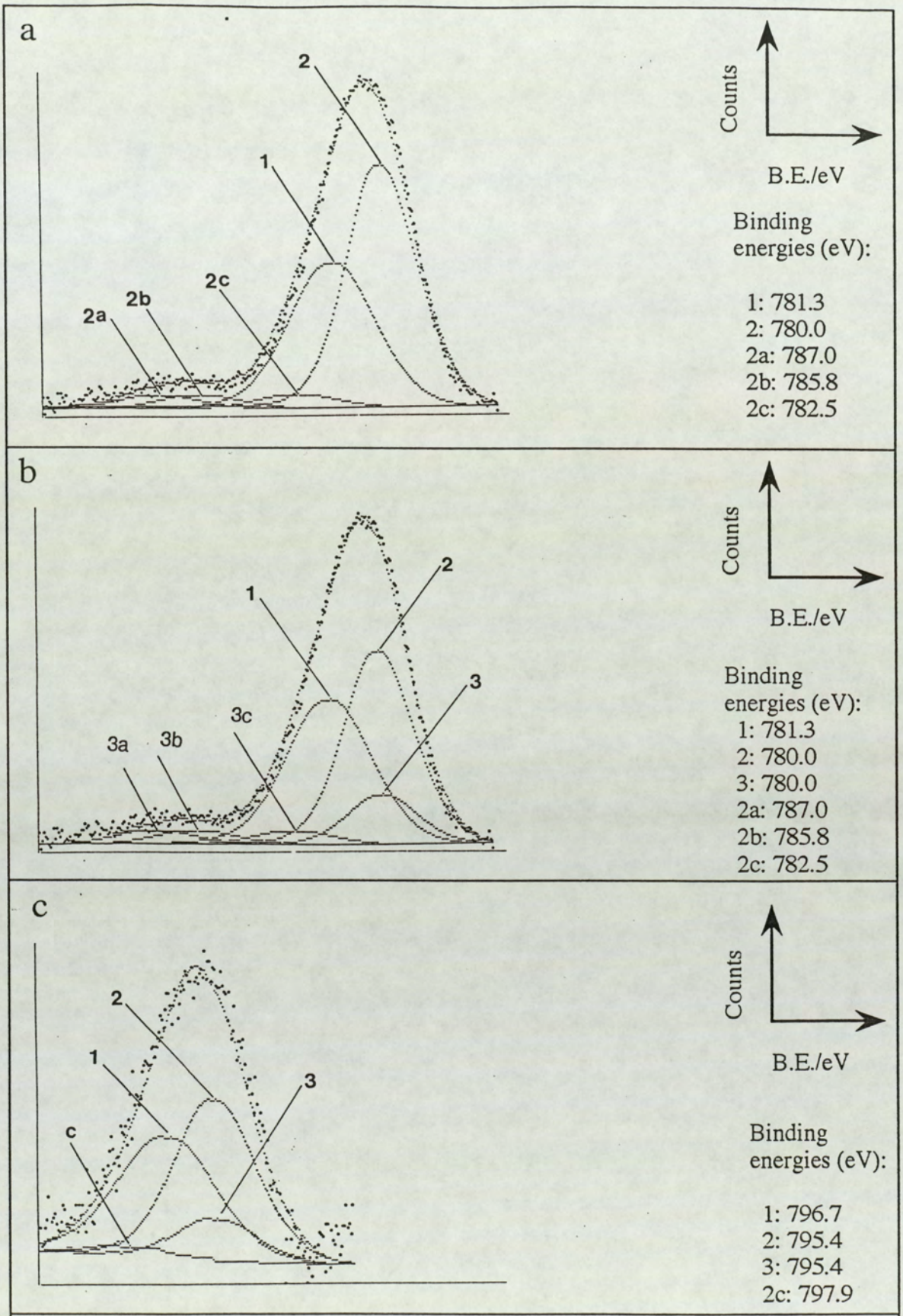

Figure 5.30.

Unbombarded Co_3O_4 surface.

a) initial curve-fit for Co $2p_{3/2}$

b) final curve-fit for Co $2p_{3/2}$

c) Co $2p_{1/2}$

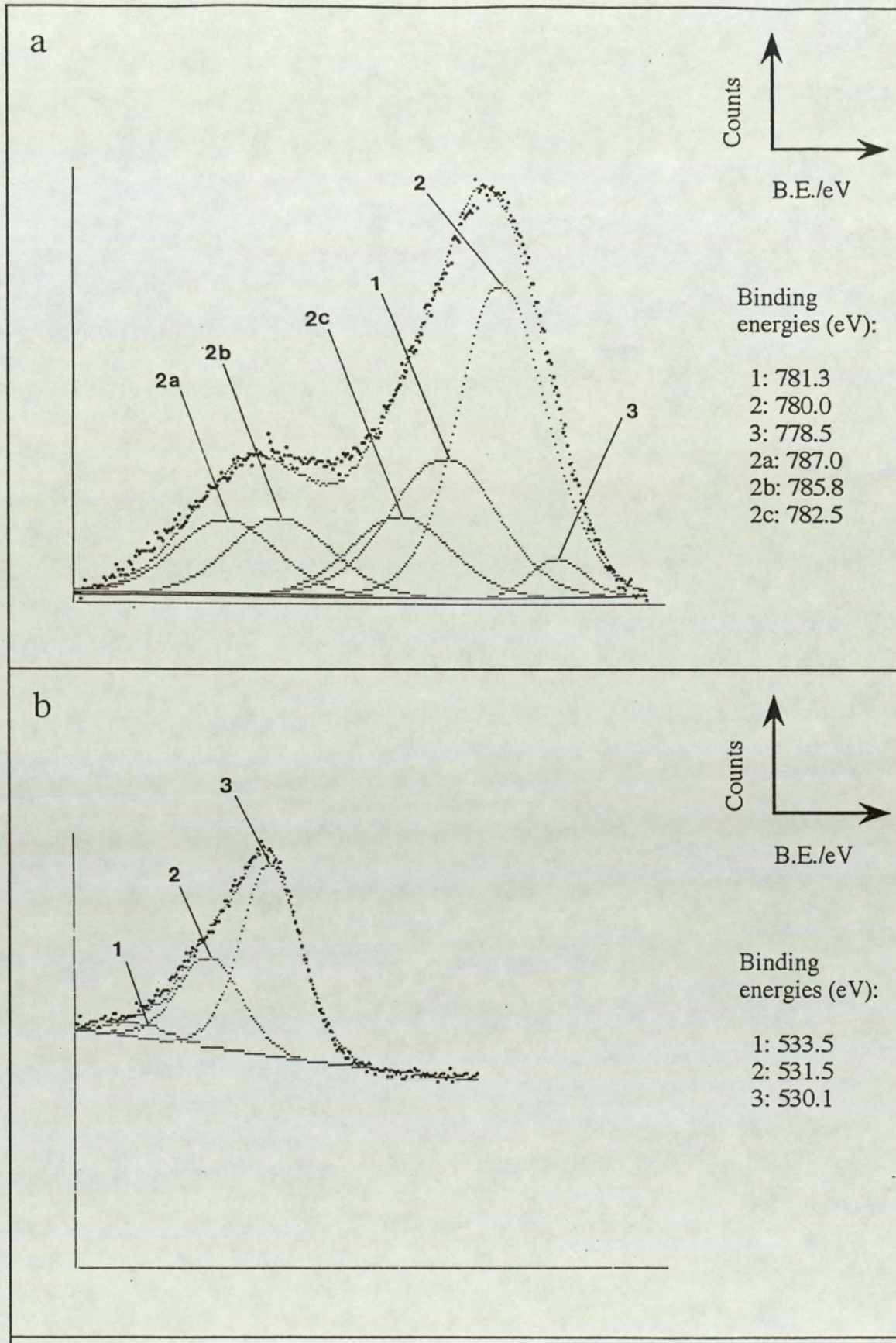

Figure 5.31.

Co_3O_4 surface after 10 minutes of Ar^+ ion bombardment.

a) Co $2p_{3/2}$

b) O 1s

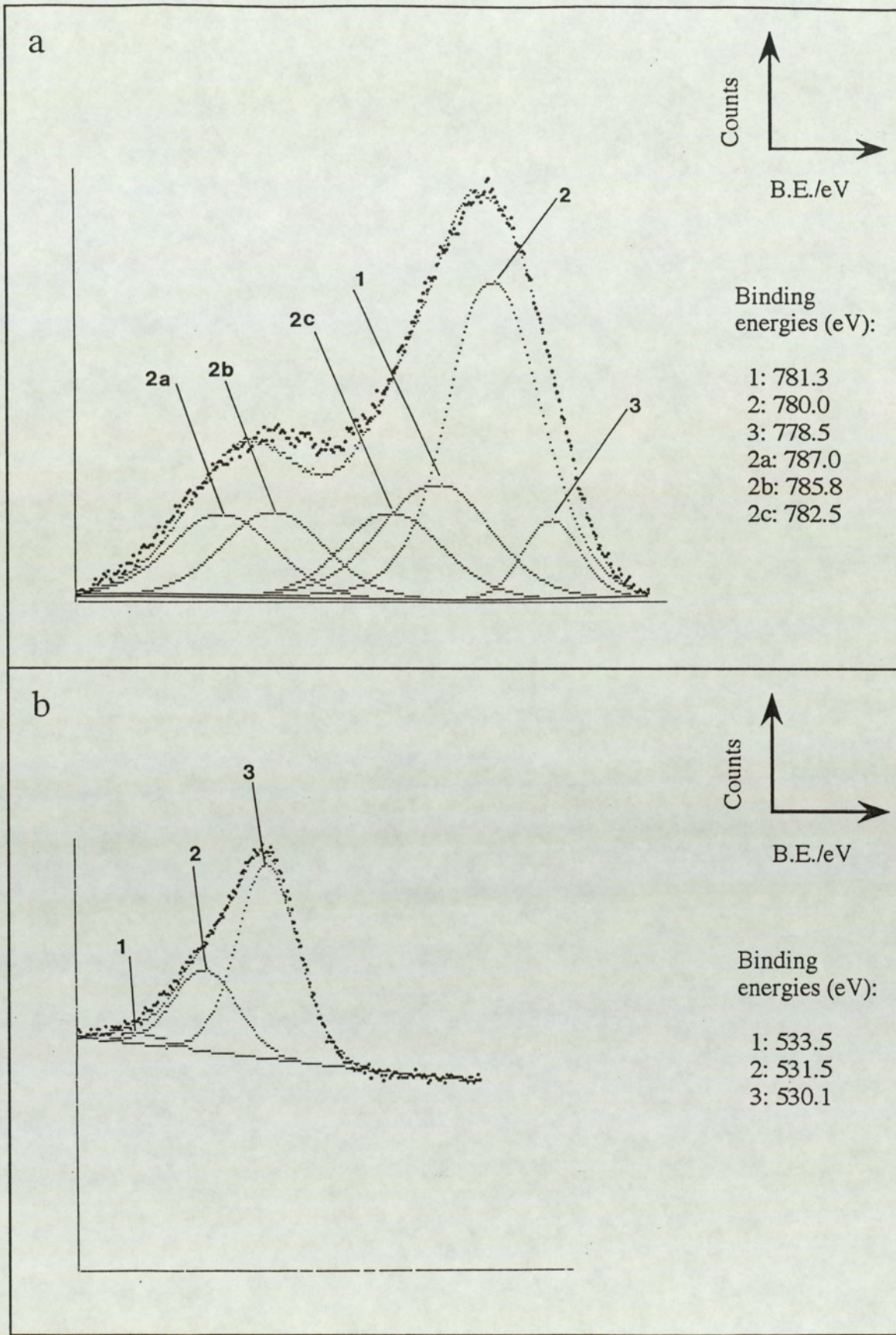

Figure 5.32.

Co_3O_4 surface after 30 minutes of Ar^+ ion bombardment.

a) Co $2p_{3/2}$

b) O 1s

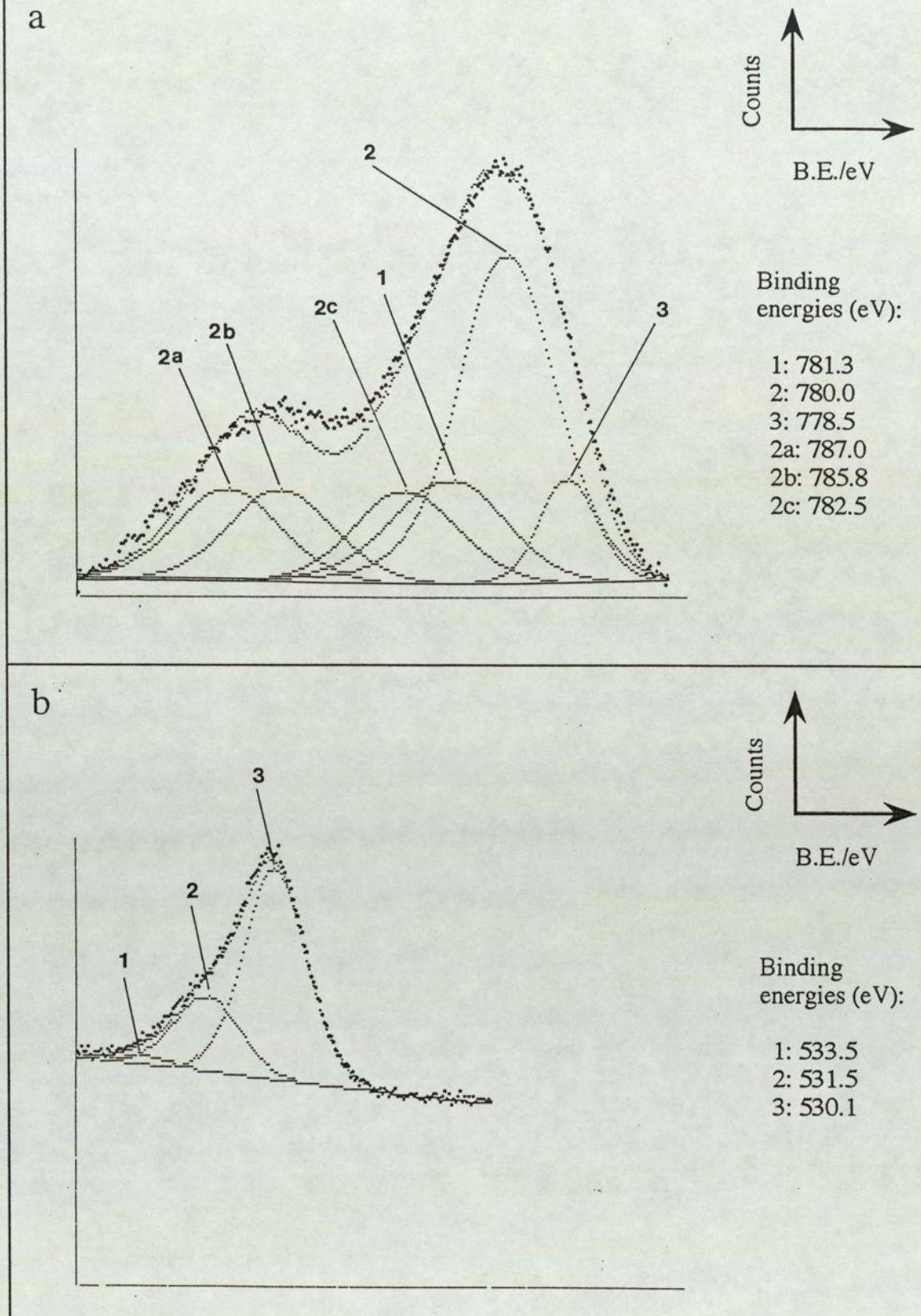

Figure 5.33.

Co_3O_4 surface after 120 minutes of Ar^+ ion bombardment.

a) Co $2p_{3/2}$

b) O 1s

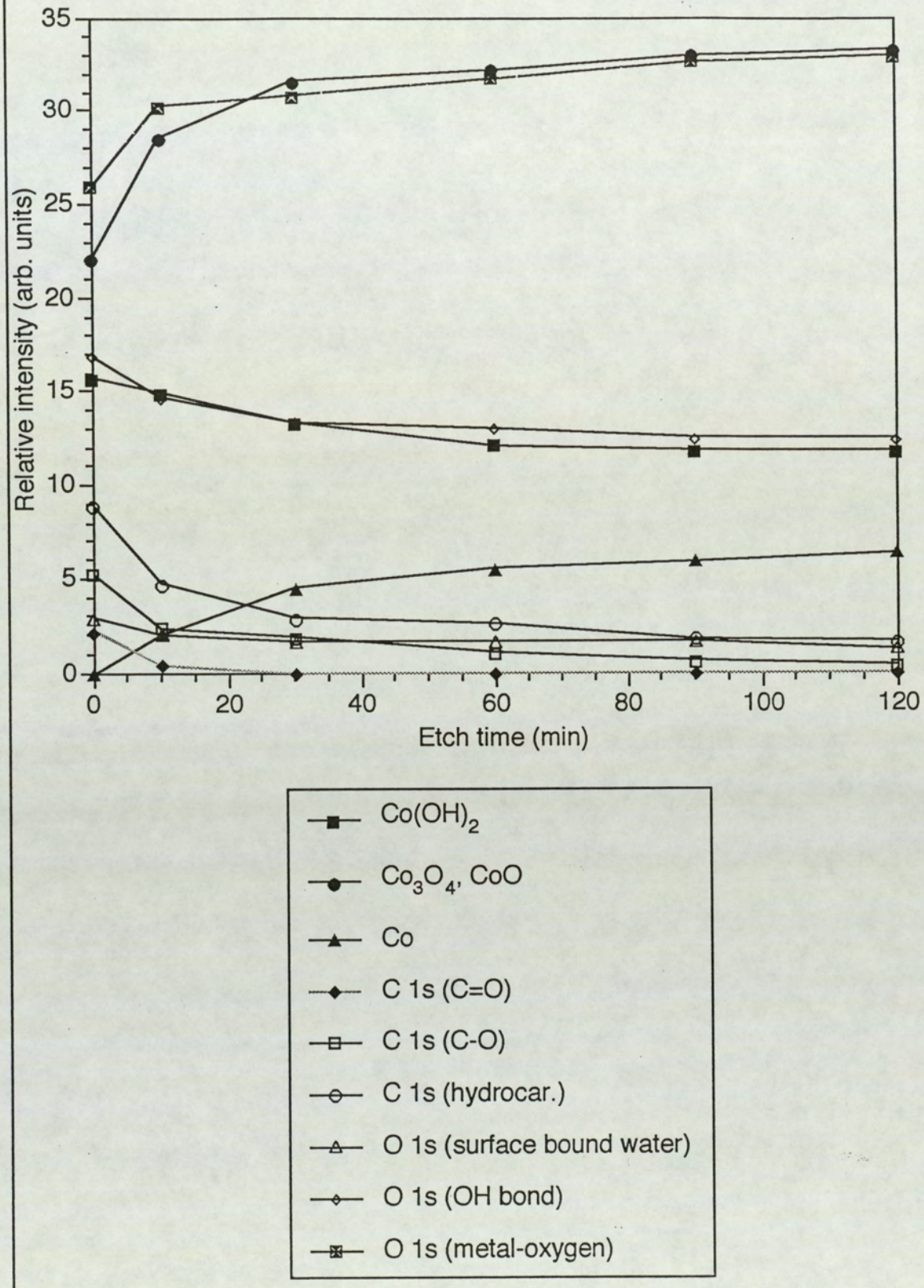

Figure 5.34.

Relative intyensity as a function of etch time for Co_3O_4.

CoO. The 2p line for the $Co(OH)_2$ state appears at 796.7 eV with a FWHM of 3.4 eV. The satellite due to the Co^{II} ions appear at 797.9 eV.

The spectra recorded after argon ion bombardment for 10, 30, 60, 90 and 120 minutes show gradual removal of the carbon species and the surface bound water and the hydroxide species, together with broadening of the Co 2p spectra. Figures (5.31a and b) show the Co $2p_{3/2}$ and O 1s spectra after 10 minutes of ion bombardment. In the Co $2p_{3/2}$ spectra the three satellite structures with their associated main peak at 780.0 eV and the hydroxide peak at 781.3 eV are observed. The three satellite structures for the Co^{II} ions at binding energy 780.0 eV are more prominent than in the case for the unetched surface and the intensity of each satellite is calculated to be ~24% of that for the main peak. Thus it can be assumed that the contributions for the peak at 780.0 eV is entirely due to Co^{II} ions of CoO only, indicating that ion bombardment induced reduction to CoO state has already taken place within 10 minutes of bombardment. This indication is also enhanced by the appearence of the sixth peak at 778.5 eV (FWHM=1.7 eV) showing the presence of metallic cobalt. Further broadening of the Co 2p spectra, to accomodate the increased metallic Co^0 intensity, is observed with increased bombardment times until a steady state is reached after about 120 minutes of etch period. Figures (5.32a,b) and (5.33a,b) show the Co $2p_{3/2}$ and O1s spectra after 30 minutes and 120 minutes of ion bombardment respectively. Figure (5.34) shows a graph of relative intensity against etch time for the lines O 1s C 1s and Co $2p_{3/2}$. Table (5.3) lists all the binding energies obtained with their corresponding fitting parameters.

5.5.6: TiO_2

The TiO_2 powder was obtained by finely grinding commercially obtained high purity chuncks. The spectral lines Ti 2p, O 1s, C 1s and the Au 4f lines were recorded for the investigation on the TiO_2 sample. Figures (5.35a and b) show the oxygen 1s and the carbon 1s spectra for the unbombarded air-exposed surface. In the the O 1s

spectrum three peaks due to: surface bound water, possibly a hydroxide bond (discussed fully later) and the metal-oxygen bond appear at 533.7 eV, 532.0 eV and 530.5eV respectively; all with FWHM value of 1.6 eV. The carbon spectrum shows two peaks separated by an energy of 1.5 eV with FWHM of 2.0 eV. The lower binding energy peak due to surface hydrocarbons being assigned the value 284.6 eV. This line was thus used as the reference line since differential charging effect with gold was observed. The origin of the higher binding energy carbon peak has already been described for other powder samples.

Figure (5.35c) shows the Ti 2p doublet for the unbombarded sample. Two sharp peaks due to the Ti^{IV} ions in TiO_2 appear at binding energies 464.6 eV (FWHM=2.4 eV) and 458.7 eV (FWHM=1.5 eV) corresponding to the $2p_{1/2}$ and $2p_{3/2}$ lines respectively. Absence of a separate doublet in the Ti 2p spectra due to a hydroxide bond yields two possible explanation for the presence of the O 1s peak at 532.0 eV. The first possibility is that this peak is due to surface bound chemisorbed oxygen molecules. The second possibility is that it is a metal-OH bond and that part of the unetched Ti 2p intensity contribution is due to some form of titanium hydroxide bond which cannot be resolved separately from the TiO_2 state.

XPS carried out after 2 minutes of ion bombardment shows the appearence in the 2p spectra, figure (5.36a), of another doublet at binding energy 463.0 eV (FWHM=2.4 eV) and 457.2 eV (FWHM=2.0 eV) due to the $2p_{1/2}$ and $2p_{3/2}$ lines of the Ti^{III} ions in Ti_2O_3. Further ion bombardment shows increased widening of the Ti 2p profile with the shoulder at low binding energy becoming more pronounced; this is accompanied by an intensity reduction of the corresponsing O 1s spectra. A colour change of the TiO_2 powder surface is also observed from white to dark grey, becoming darker with increased etch time.

Figures (5.37a and b) show the Ti 2p and the o 1s spectra after 10 minutes of ion bombardment. Increased broadening of the Ti 2p profile is caused by the appearence of a doublet due to Ti^{II} ions in the second reduced suboxide, TiO. This doublet ($2p_{1/2,3/2}$) appear at binding energies of 461.0 eV (FWHM=2.4 eV) and 455.3

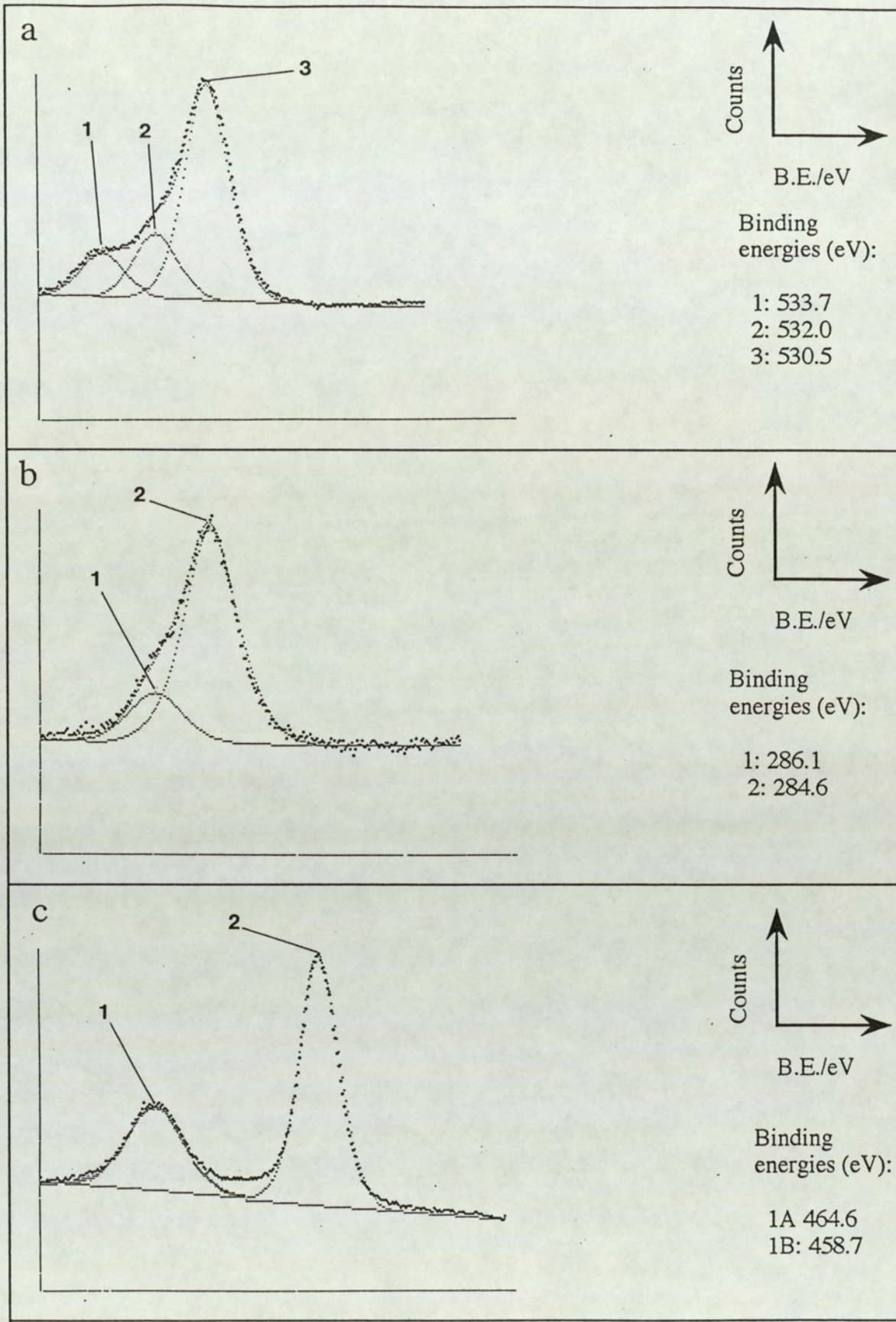

Figure 5.35.

Unbombarded TiO_2 surface.

a) O 1s
b) C 1s
c) Ti 2p ($2p_{1/2}$ is shown by A, and $2p_{3/2}$ is shown by B)

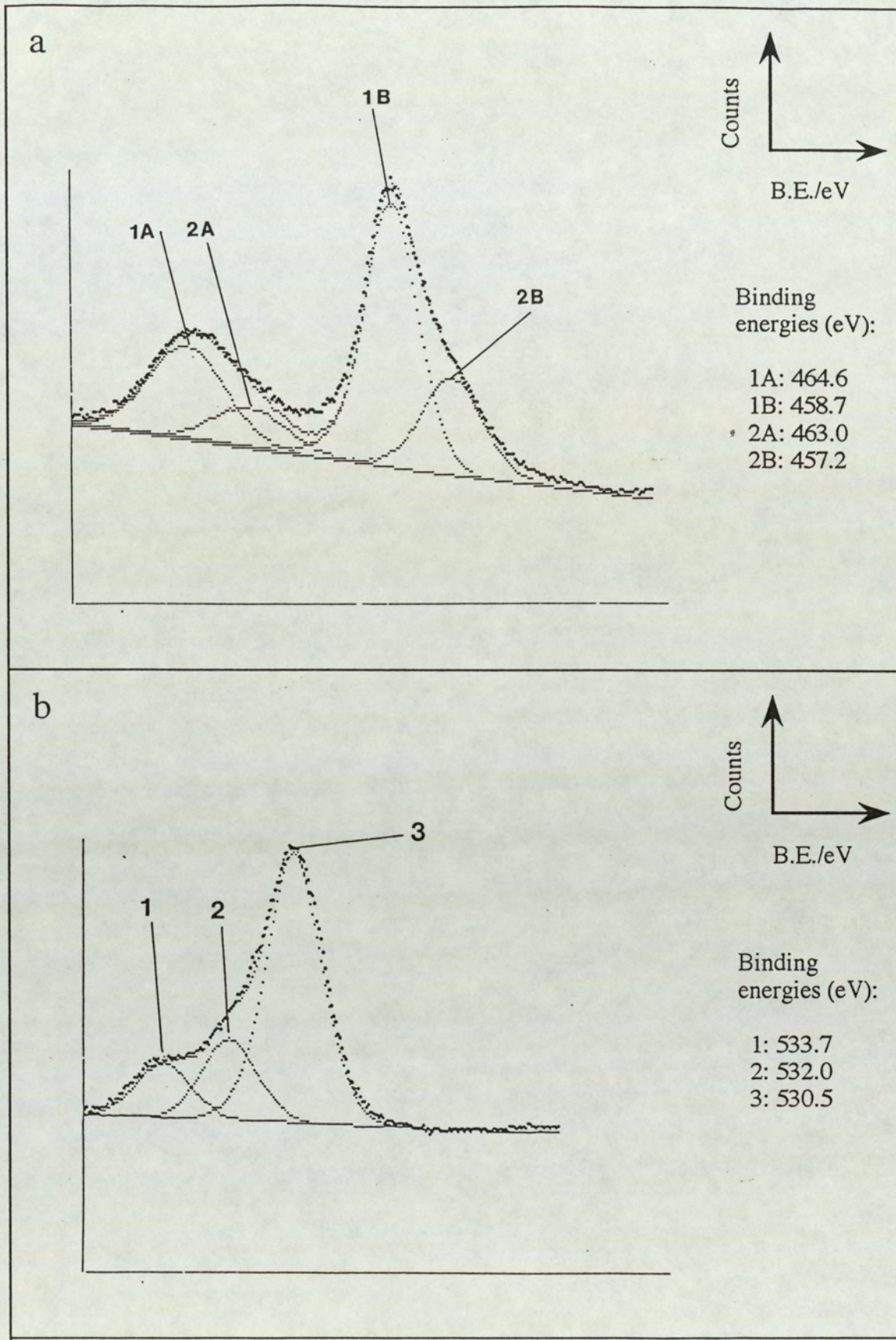

Figure 5.36.

TiO_2 surface after 2 minutes of Ar^+ ion bombardment.

a Ti 2p ($2p_{1/2}$ is shown by A, and $2p_{3/2}$ is shown by B)

b) O 1s

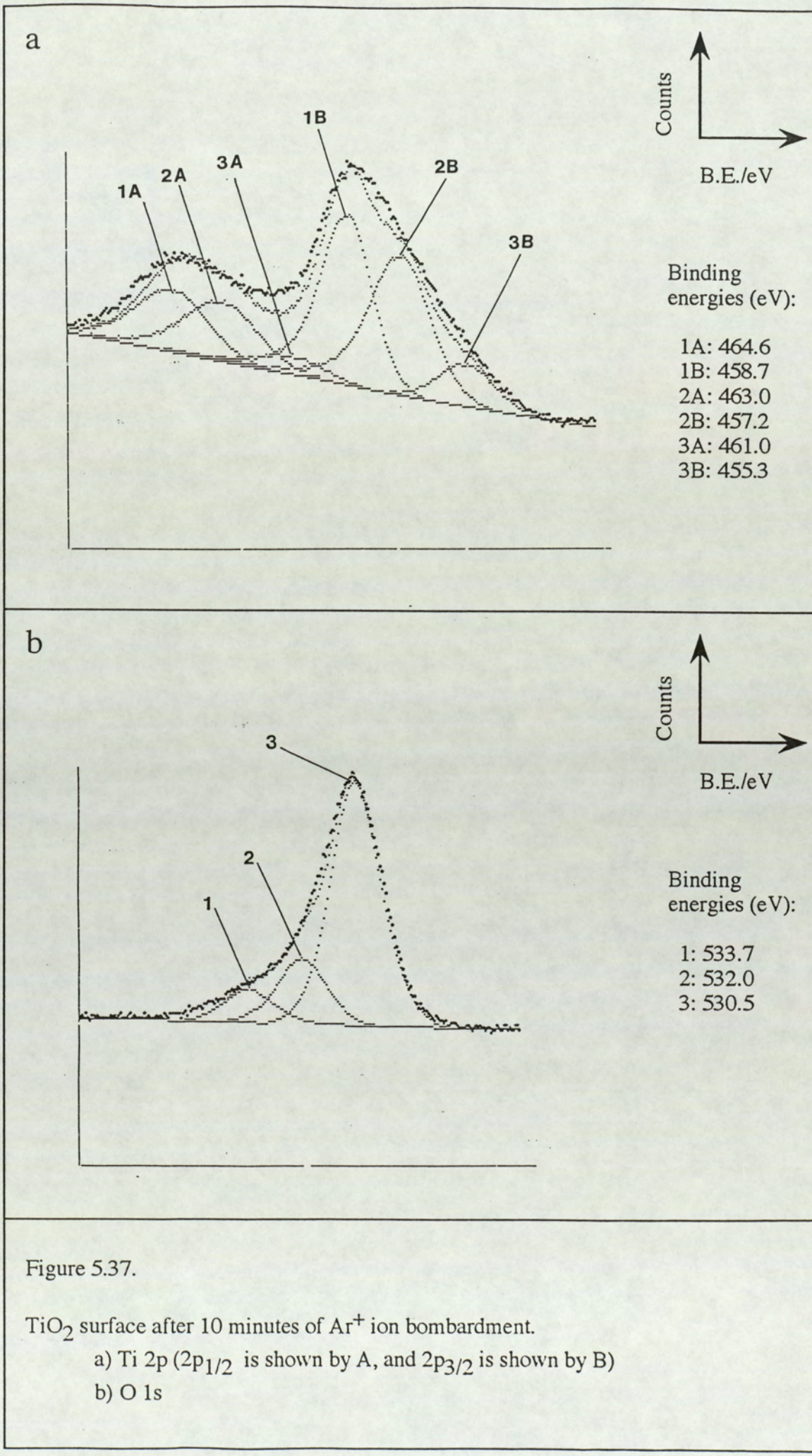

Figure 5.37.

TiO_2 surface after 10 minutes of Ar^+ ion bombardment.

a) Ti 2p ($2p_{1/2}$ is shown by A, and $2p_{3/2}$ is shown by B)

b) O 1s

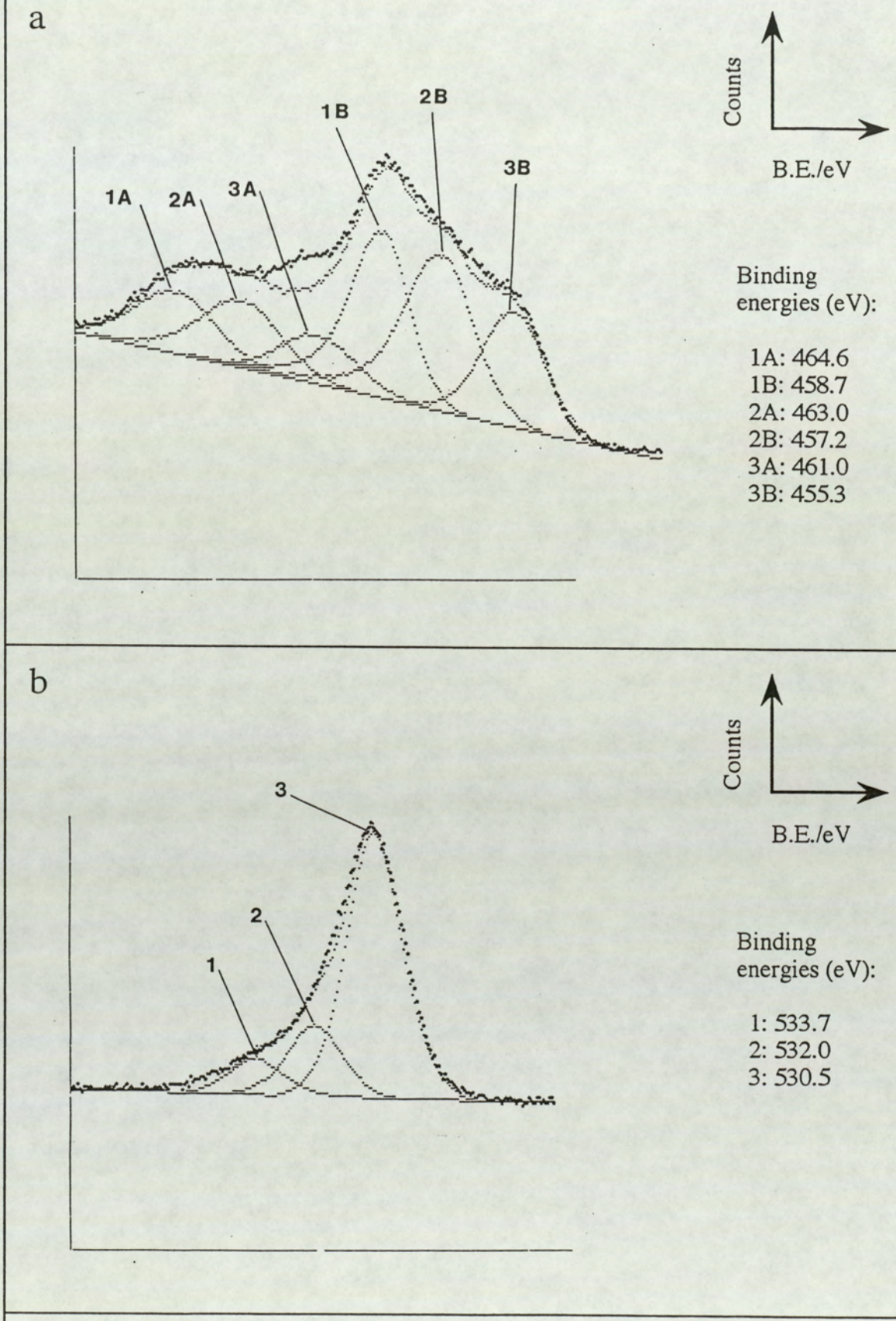

Figure 5.38.

TiO_2 surface after 120 minutes of Ar^+ ion bombardment.

a) Ti 2p ($2p_{1/2}$ is shown by A, and $2p_{3/2}$ is shown by B)

b) O 1s

Table 5.4

Measured binding energy values (±0.2eV) and corresponding FWHM values (±0.2eV) for titanium and its oxides. Calibration is with respect to the C 1s peak at 284.6 eV.

identity		core level	binding energy (eV)	FWHM (eV)
TiO_2	Ti^{IV}	$2p_{3/2}$	458.7	1.5
		$2p_{1/2}$	464.4	2.4
Ti_2O_3	Co^{III}	$2p_{3/2}$	457.2	2.0
		$2p_{1/2}$	463.0	2.4
TiO	Ti^{II}	$2p_{3/2}$	455.3	2.0
		$2p_{1/2}$	461.0	4.0
Oxygen	metal-oxygen bond	1s	530.5	1.6
	surface-bound oxygen	1s	532.0	1.6
	surface bound water	1s	533.7	1.6
Carbon	hydrocarbon bond	1s	284.6	2.0
	carbon-oxygen bond	1s	286.1	2.0

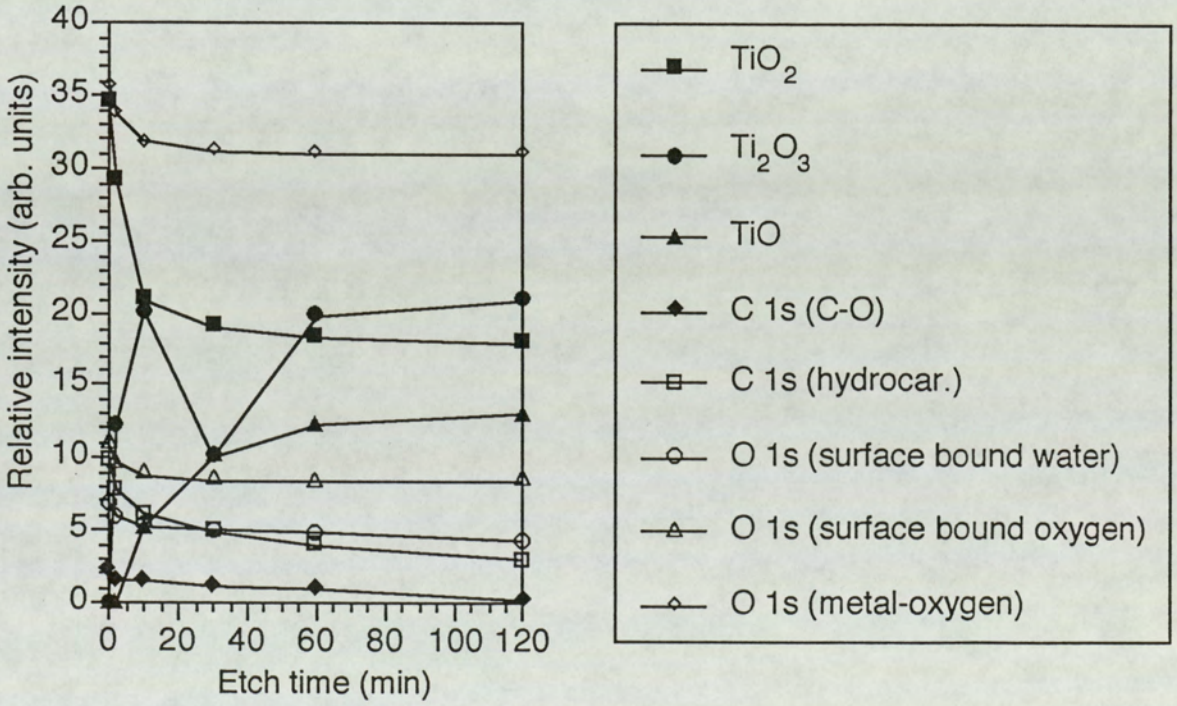

Figure 5.39.

Relative intensity as a function of etch time for TiO_2.

eV (FWHM=2.0 eV) respectively. The TiO state is found to be the final reduced product for this particular ion beam condition (i.e, primary ion energy = 5 keV, beam current = 2μA). Figures (5.38a and b) show the Ti 2p and O 1s spectra after 120 minutes of ion bombardment when a steady state condition of the altered layer has been reached. The Ti^{IV}:Ti^{III} intensity ratio changes from 2.18 after 2 minutes of bombardment to 1.0, 0.98, 0.95 and 0.90 after 10, 30, 60 and 120 minutes respectively. Those due to Ti^{IV}:Ti^{II} decrease from 3.57 after 10 minutes to 1.82, 1.47 and 1.42 for 30, 60 and 120 minutes of bombardment.

The results obtained for the TiO_2 sample thus show ion beam induced partial reduction to Ti_2O_3 and eventually to TiO. A plot of relative intensities against etch times can be seen in figure (5.39). Table (5.4) lists the binding energies and some peak-fitting parameters associated with all peaks observed.

5.5.7: ZrO_2

For the ZrO_2 powder sample the spectral lines Zr 3d, Zr 3p, O 1s, C 1s and the Au 4f were investigated. figures (5.40a and b) show the O 1s and the C 1s spectra for the pre-bombardment situation. In the oxygen profile the three oxygen species are found at 533.4 eV (surface bound water), 531.5 eV (OH-bond) and at 530.2 eV (metal-oxygen bond) all with FWHM of 2.0 eV. This indicates that hydration of the ZrO_2 surface has taken place. The corresponding C 1s spectrum shows two peaks with FWHM of 2.0 eV separated by an energy 1.5 eV, thus showing the existence of surface hydrocarbons and carbon-singly bonded-oxygen. The lower binding energy carbon line being used as the reference line at 284.6 eV.

Figures (5.41a and b) show the Zr 3d and 3p spectra for the unetched surface. The 3d doublet (i.e,$3d_{3/2}$ an $3d_{5/2}$) appears well resolved at binding energies 184.4 eV and 182.0 eV with FWHM value of 2.1 eV; the intensity ratio of the doublet is measured at 1.52 leading to an experimental error of 1.3% (since the ratio of (2j+1) for the d-orbital is 1.5). These lines are due to Zr^{IV} ions in ZrO_2. similarly, the presence

of the Zr^{IV} ions is shown by the the 3p doublet ($3p_{1/2}$ and $3p_{3/2}$) due to the peaks at 346.5 eV and 332.8 eV with FWHM of 3.1 eV (with measured doublet intensity ratio of ~1.98).

However, from the presence of the OH species in the corresponding oxygen spectra and its apparent absence in the Zr 3d and 3p doublets, it is expected that part of the Zr contribution is due to some form of zirconium hydroxide which can not be resolved separately from the ZrO_2 state.

Both the Zr 3d and 3p doublets show changes as the surface is subjected to progressive periods of controlled ion bombardment. Broadening of these peaks are observed with a shoulder to the profiles appering at the low binding energy side. These doublets obtained for the surface after 10 minutes of bombardment can be seen in figures (5.42a and b). The Zr $3d_{3/2,5/2}$ profile show the presence of another doublet at binding energies 182.9 eV and 180.5 eV respectively; those due the $3p_{1/2,3/2}$ profile are found at 344.8 eV and 331.1 eV respectively. These are ascribed to be due to the Zr^{II} ions in ZrO. The intensity ratios of Zr^{IV}:Zr^{II} are 3.79 and 3.64 for the 3d and 3p doublets respectively.

Further bombardment shows increased widening of the Zr lines until a steady state condition is reached. Figures (5.43a,b) show the Zr 3d and 3p lines after 30 minutes of bombardment, an intensity increment of the Zr^{II} state and reduction of the Zr^{IV} state is clearly visible. After 60 minutes of ion bombardment, the appearence of the metallic Zr^0 state in the 3d and the 3p lines can be observed. For the Zr^0 state, the 3d doublet appear at binding energies 180.9 eV and 178.5 eV with FWHM of 1.9 eV. Those due to the corresponding 3p doublet appear at 342.9 eV and 329.2 eV with FWHM of 2.7 eV. Figures (5.44a,b) show the 3d and 3p profiles obtained after 120 minutes of bombardment.

All the binding energy values with their corresponding peak-fitting parameters are listed in table (5.5). A plot of the relative intensities for the different states of zirconium and the different carbon and oxygen species against corresponding

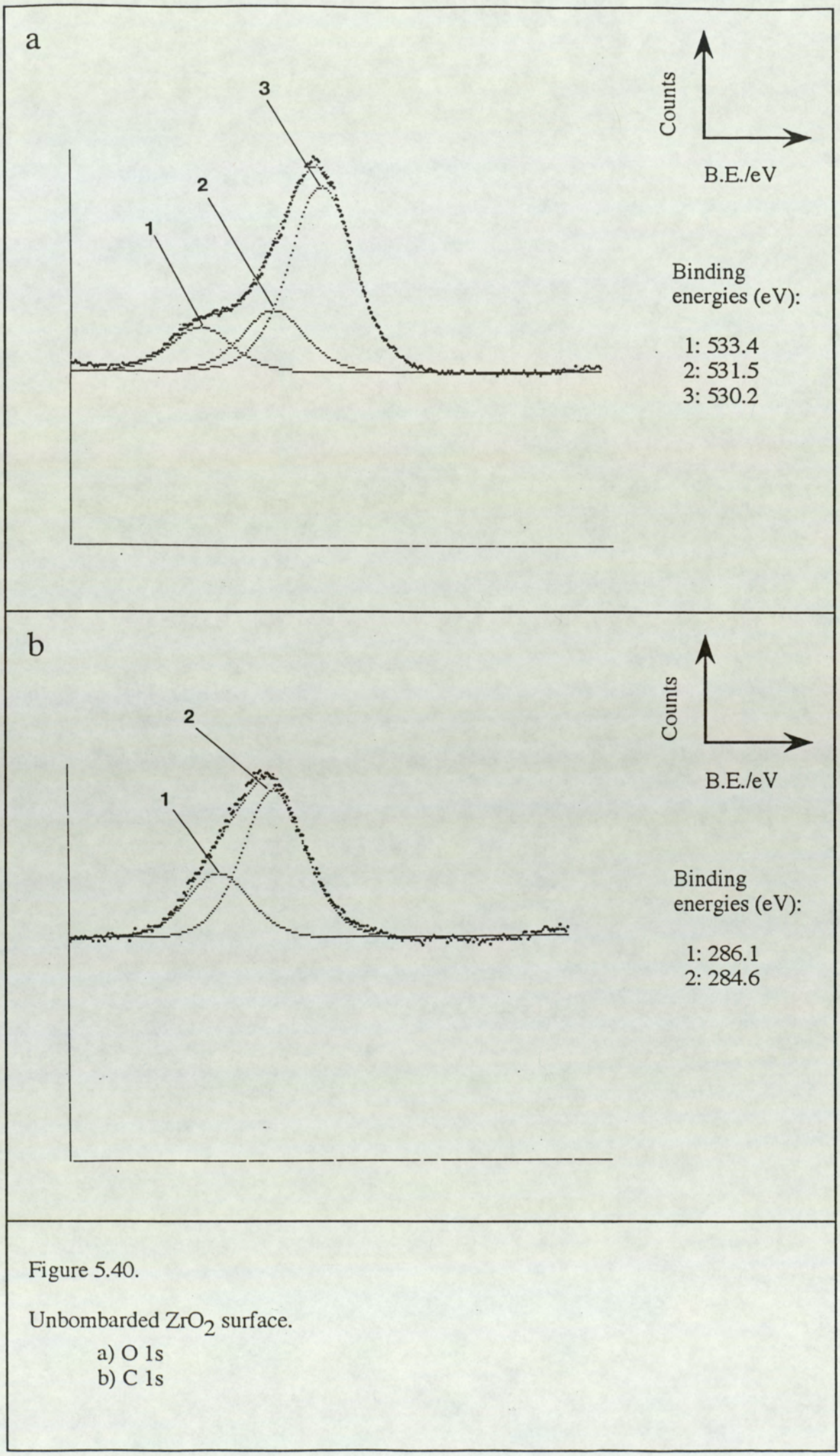

Figure 5.40.

Unbombarded ZrO_2 surface.

a) O 1s
b) C 1s

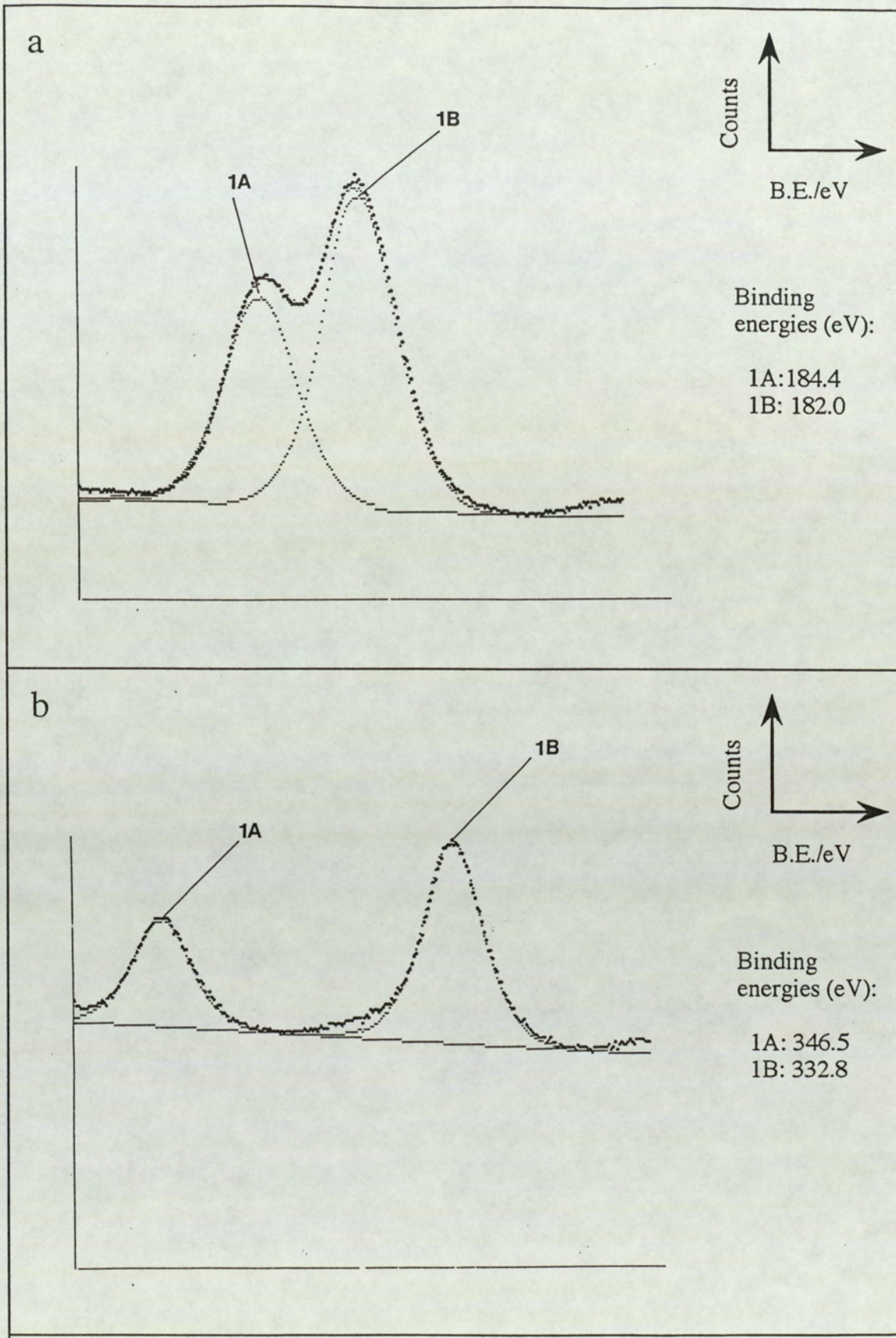

Figure 5.41.

Unbombarded ZrO_2 surface.

a) Zr 3d ($3d_{3/2}$ is shown by A, and $3d_{5/2}$ is shown by B)

b) Zr 3p ($3p_{1/2}$ is shown by A, and $3p_{3/2}$ is shown by B)

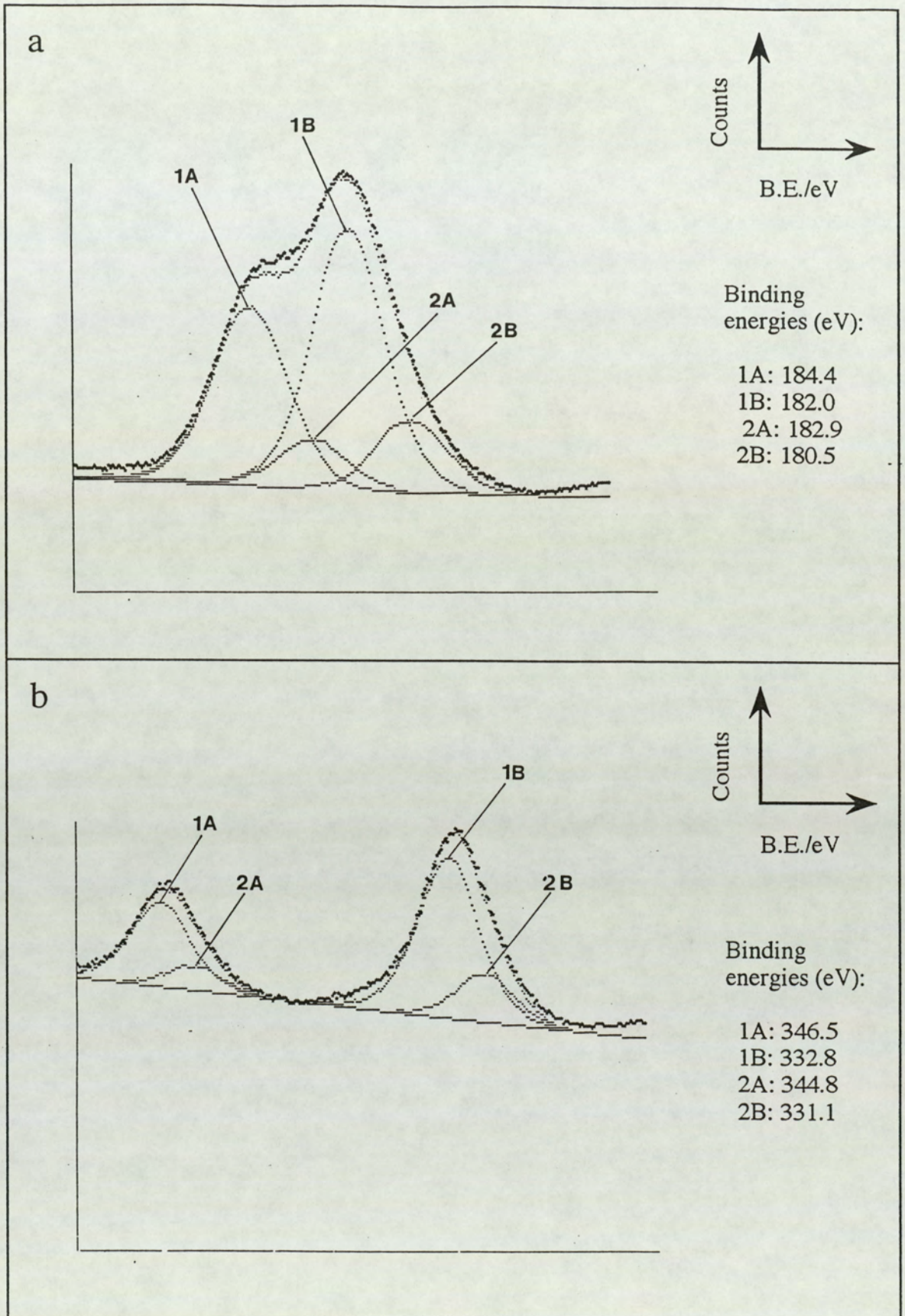

Figure 5.42.

ZrO_2 surface after 10 minutes of Ar^+ ion bombardment.

a) Zr 3d ($3d_{3/2}$ is shown by A, and $3d_{5/2}$ is shown by B)

b) Zr 3p ($3p_{1/2}$ is shown by A, and $3p_{3/2}$ is shown by B)

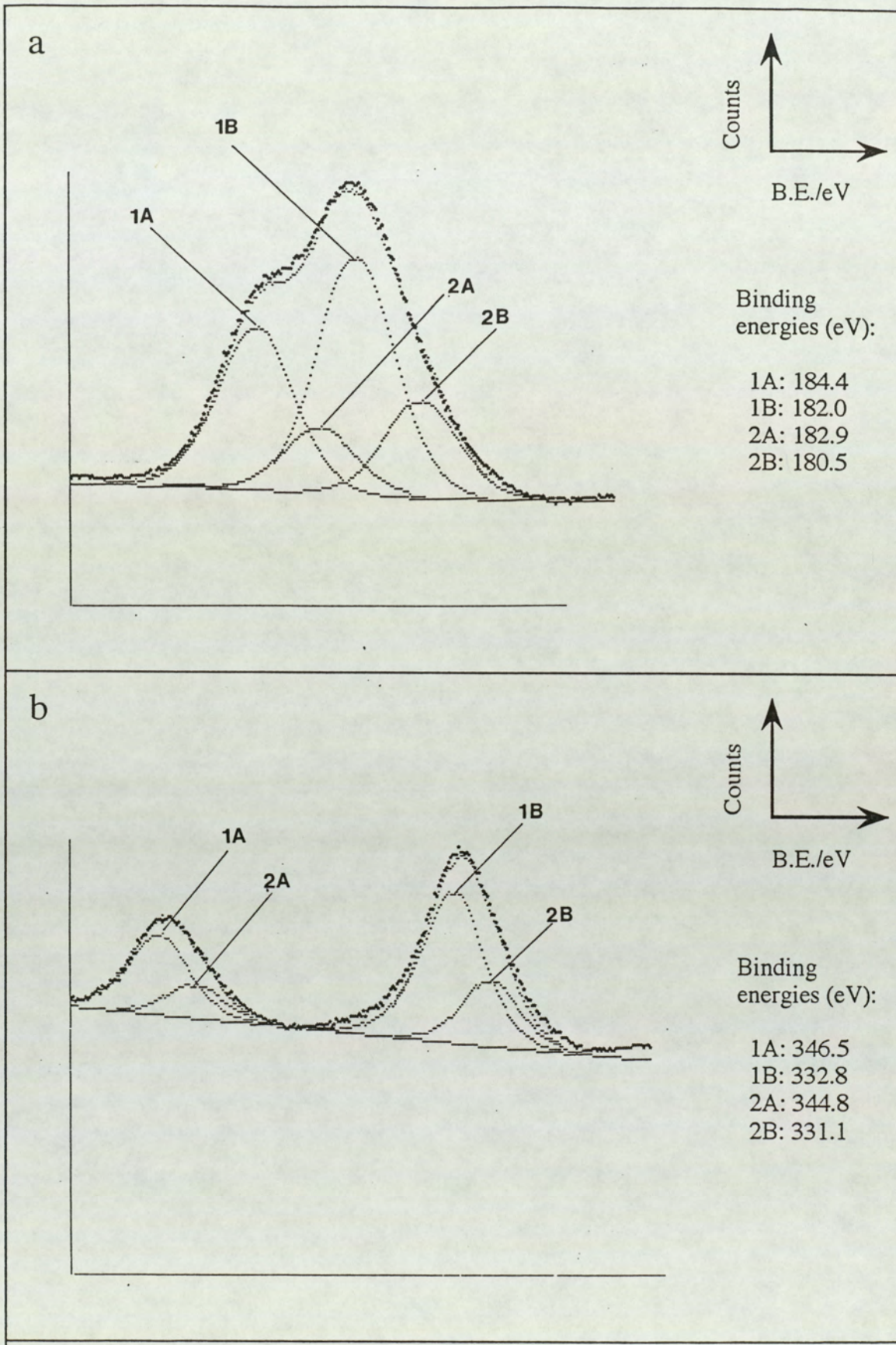

Figure 5.43.

ZrO_2 surface after 30 minutes of Ar^+ ion bombardment.

a) Zr 3d ($3d_{3/2}$ is shown by A, and $3d_{5/2}$ is shown by B)

b) Zr 3p ($3p_{1/2}$ is shown by A, and $3p_{3/2}$ is shown by B)

a

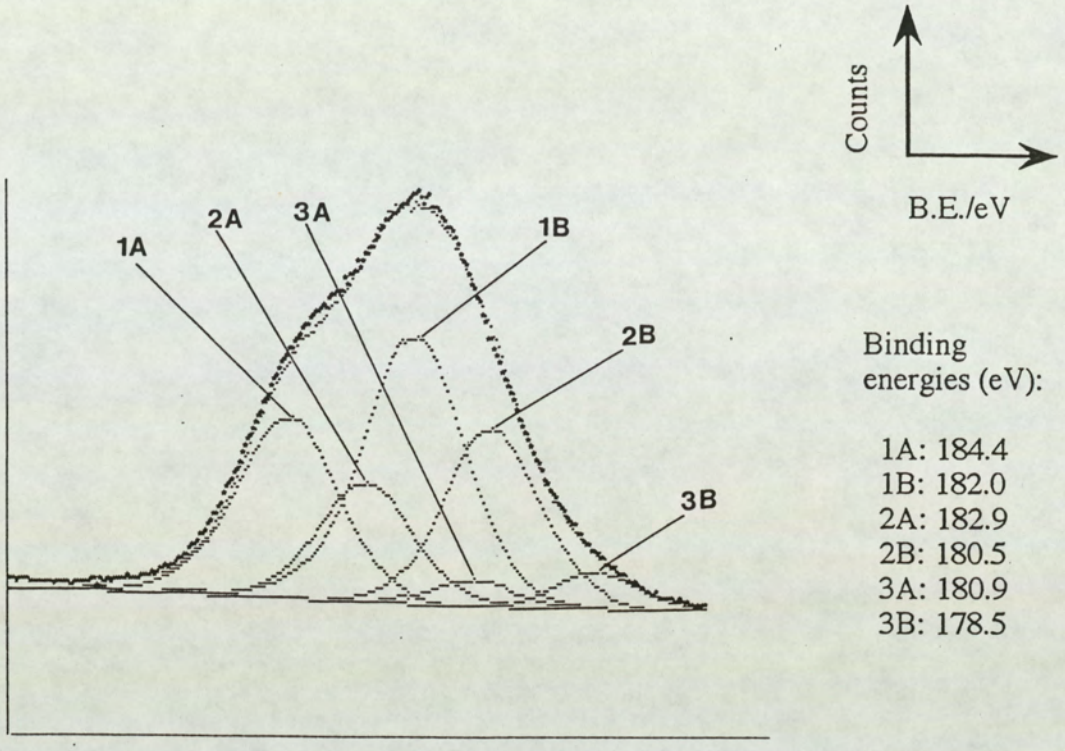

Binding energies (eV):

1A: 184.4
1B: 182.0
2A: 182.9
2B: 180.5
3A: 180.9
3B: 178.5

b

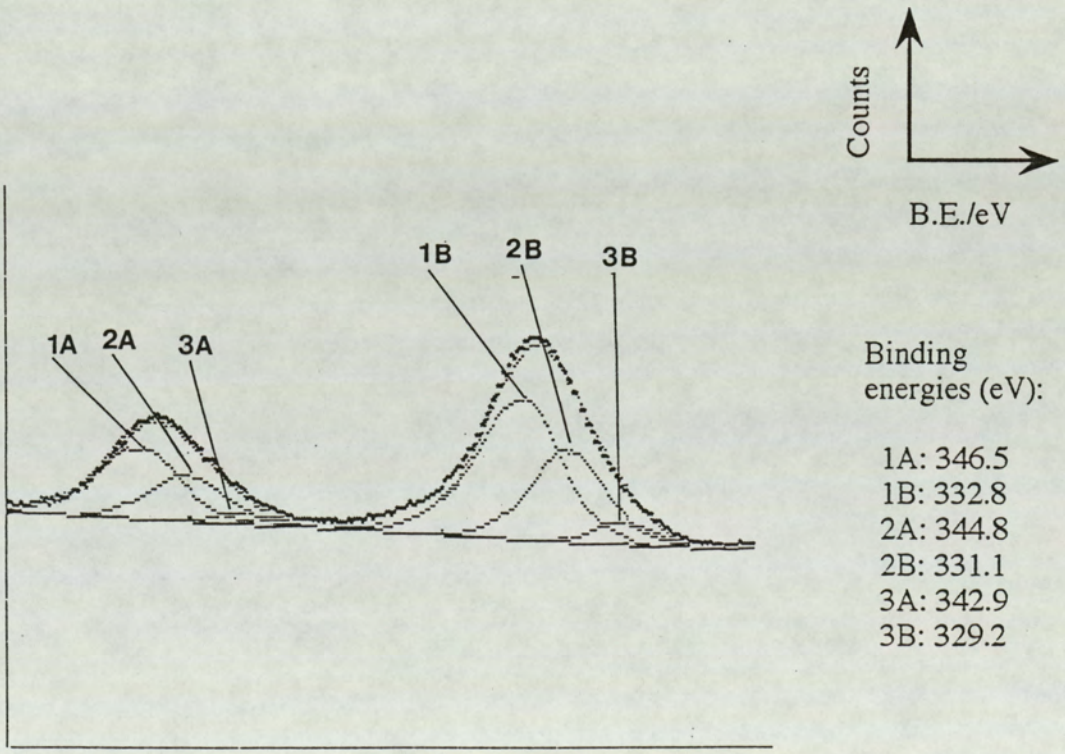

Binding energies (eV):

1A: 346.5
1B: 332.8
2A: 344.8
2B: 331.1
3A: 342.9
3B: 329.2

Figure 5.44.

ZrO_2 surface after 120 minutes of Ar^+ ion bombardment.

a) Zr 3d ($3d_{3/2}$ is shown by A, and $3d_{5/2}$ is shown by B)

b) Zr 3p ($3p_{1/2}$ is shown by A, and $3p_{3/2}$ is shown by B)

Table 5.5

Measured binding energy values (±0.2eV) and corresponding FWHM values (±0.2eV) for zirconium and its oxides. Calibration is with respect to the C 1s peak at 284.6 eV.

identity		core level	binding energy (eV)	FWHM (eV)
ZrO_2	Zr^{IV}	$3d_{5/2}$	182.0	2.1
		$3d_{3/2}$	184.4	2.1
		$3p_{3/2}$	332.8	3.1
		$3p_{1/2}$	346.5	3.1
ZrO	Zr^{II}	$3d_{5/2}$	180.5	2.1
		$3d_{3/2}$	182.9	2.1
		$3p_{3/2}$	331.1	3.1
		$3p_{1/2}$	344.8	3.1
Zr-metal	Zr^0	$3d_{5/2}$	178.5	1.9
		$3d_{3/2}$	180.9	1.9
		$3p_{3/2}$	329.2	2.7
		$3p_{1/2}$	342.9	2.7
Oxygen	metal-oxygen bond	1s	530.2	2.0
	hydroxide bond	1s	531.5	2.0
	surface bound water	1s	533.4	2.0
Carbon	hydrocarbon bond	1s	284.6	2.0
	carbon-oxygen bond	1s	286.1	2.0

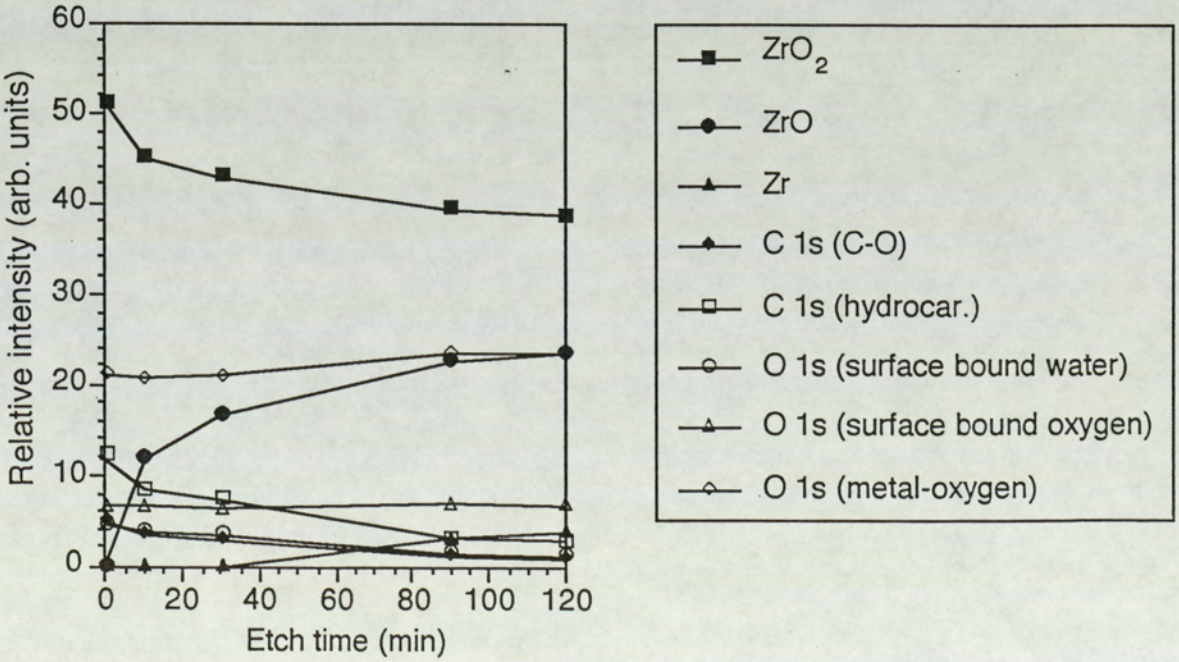

Figure 5.45.

Relative intensity as a function of etch time for ZrO_2.

bombarding times is shown in figure (5.45).

5.5.8: Nb_2O_5

The powder surface of Nb_2O_5 undergoes extensive chemical changes when subjected to progessive periods of ion bombardment. This is detected by the results from XPS investigations and also by the colour change from white to dark grey. The photo-electron lines Nb $3d_{(3/2, 5/2)}$, Nb $3p_{(1/2, 3/2)}$, O 1s, and Au 4f were recorded before and after each period of ion bombardment and curve-fitting procedures carried out. Figure (5.46a) shows the Nb 3d doublet for the unbombarded surface. Two well-resolved peaks are visible at 210.3 eV and 207.6 eV, both with FWHM of 1.9 eV, associated with the $3d_{3/2}$ and $3d_{5/2}$ lines of Nb^V ions. For the 3d doublet the intensity ratio is 1.492, giving a very good fit to the peaks (the theoretical value is 1.5). The corresponding O 1s spectrum, figure (5.46b), shows evidence of surface hydration with the presence of the bound water peak at 533.3 eV. The major oxygen peak due to the metal-oxygen bond appear at 531.0 eV.

Figures (5.47a,b) show the pre-bombarded Nb 3p peaks. The $3p_{1/2}$ line appears at 381.3 eV and the $3p_{3/2}$ line appears at 365.8 eV both with FWHM of 2.9 eV; this doublet intensity being measured at ~1.9 (compared with a value of 2 given by theory). This again shows good fit to the curves.

Within 2 minutes of ion bombardment, a partial reduction of the Nb_2O_5 state to NbO_2 is found. This is detected in the Nb 3d spectra, figure (5.48a), by the appearence of a doublet at 208.6 eV and 205.9 eV due to the Nb^{IV} ions. The corresponding Nb $3p_{1/2}$ and $3p_{3/2}$ spectra, figures (5.49a,b), confirm this by showing the additional presence of two peaks at 379.5 eV and 364.1 eV respectively. The Nb^V:Nb^{IV} intensity ratio for this etch period is ~8.7 for both the 3d lines and ~8.4 for both the 3p lines.

The second reduced suboxide, NbO, appears within 10 minutes of ion bombardment as can be seen in Figures (5.50a,b) and (5.51a,b). Additional broadening of the 3d doublet is accounted for by the presence of two lines at 207.1 eV

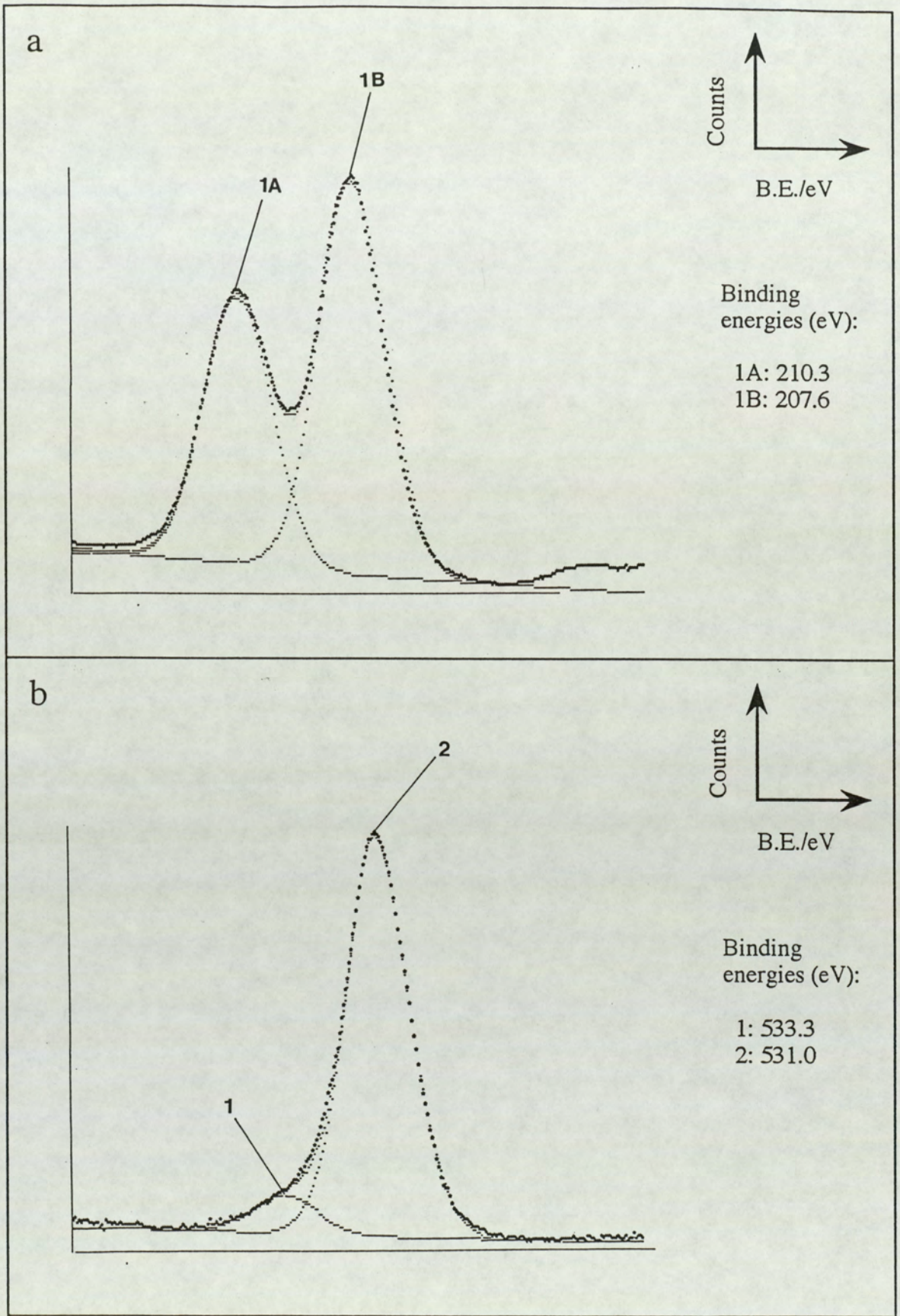

Figure 5.46.

Unbombarded Nb_2O_5 surface.

a) Nb 3d ($3d_{3/2}$ is shown by A, and $3d_{5/2}$ is shown by B)

b) O 1s

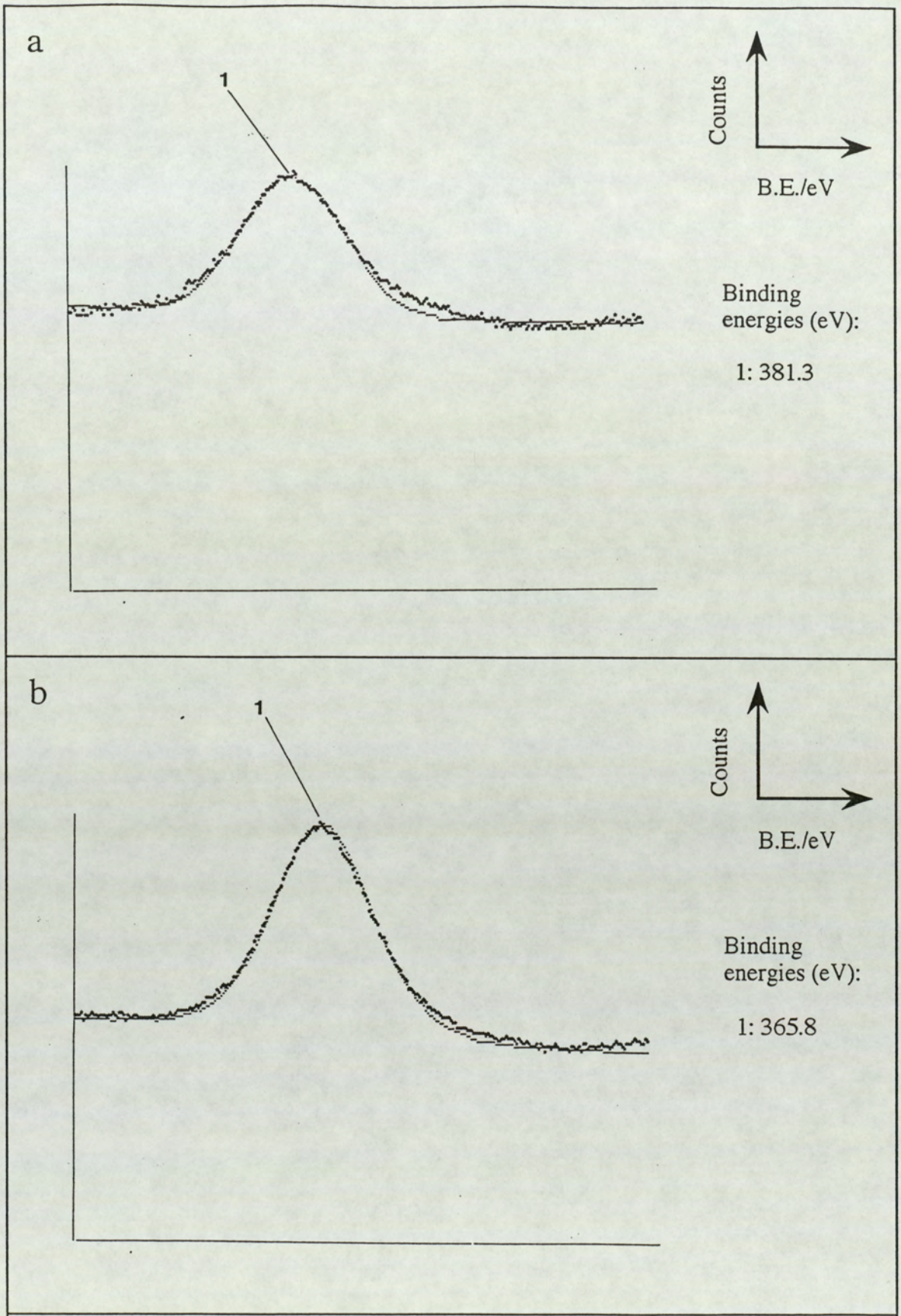

Figure 5.47.

Unbombarded Nb_2O_5 surface.

a) Nb $3p_{1/2}$

b) Nb $3p_{3/2}$

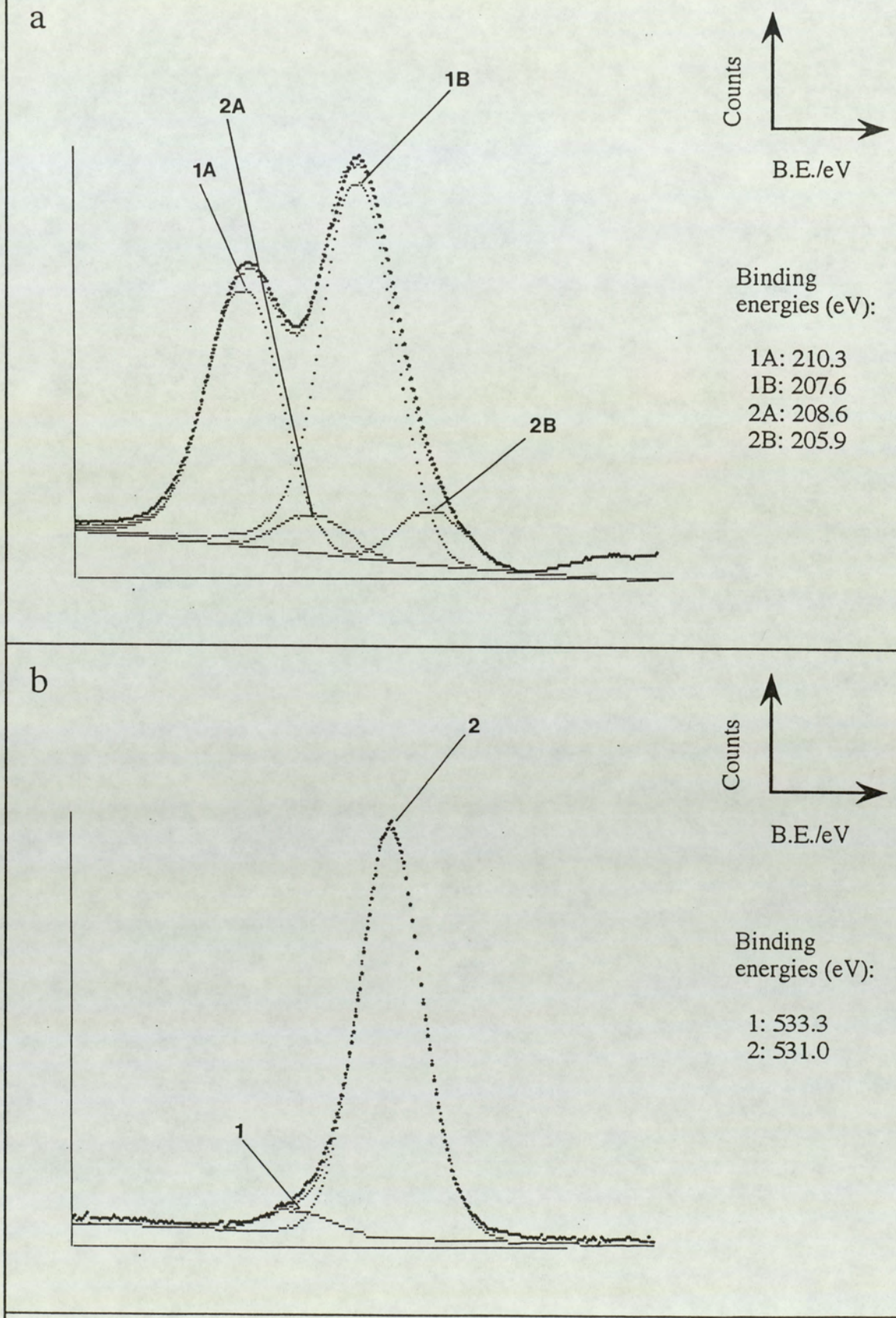

Figure 5.48.

Nb_2O_5 surface after 2 minutes of Ar^+ ion bombardment.

a) Nb 3d ($3d_{3/2}$ is shown by A, and $3d_{5/2}$ is shown by B)

b) O 1s

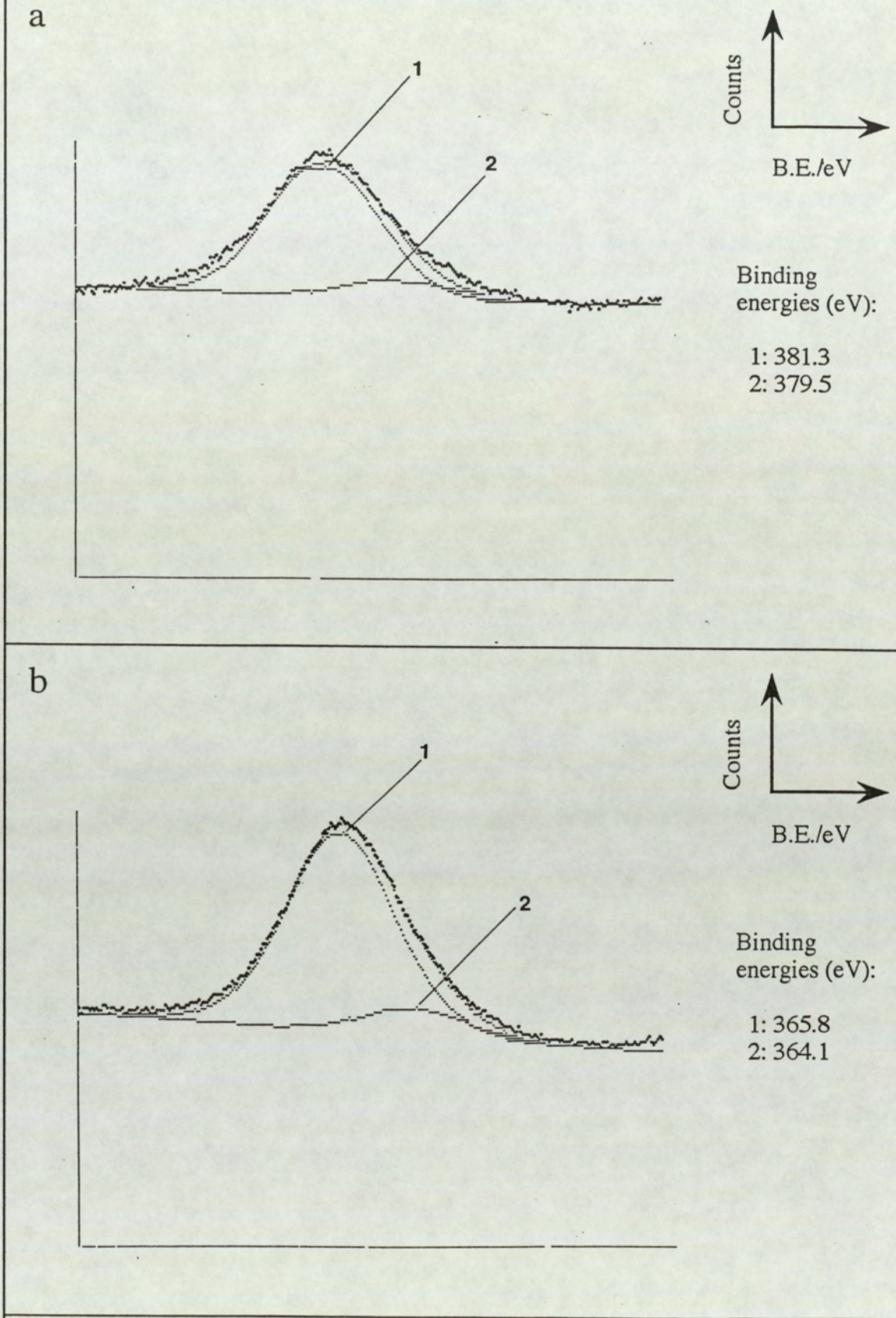

Figure 5.49.

Nb_2O_5 surface after 2 minutes of Ar^+ ion bombardment.

a) Nb $3p_{1/2}$

b) Nb 3p3/2

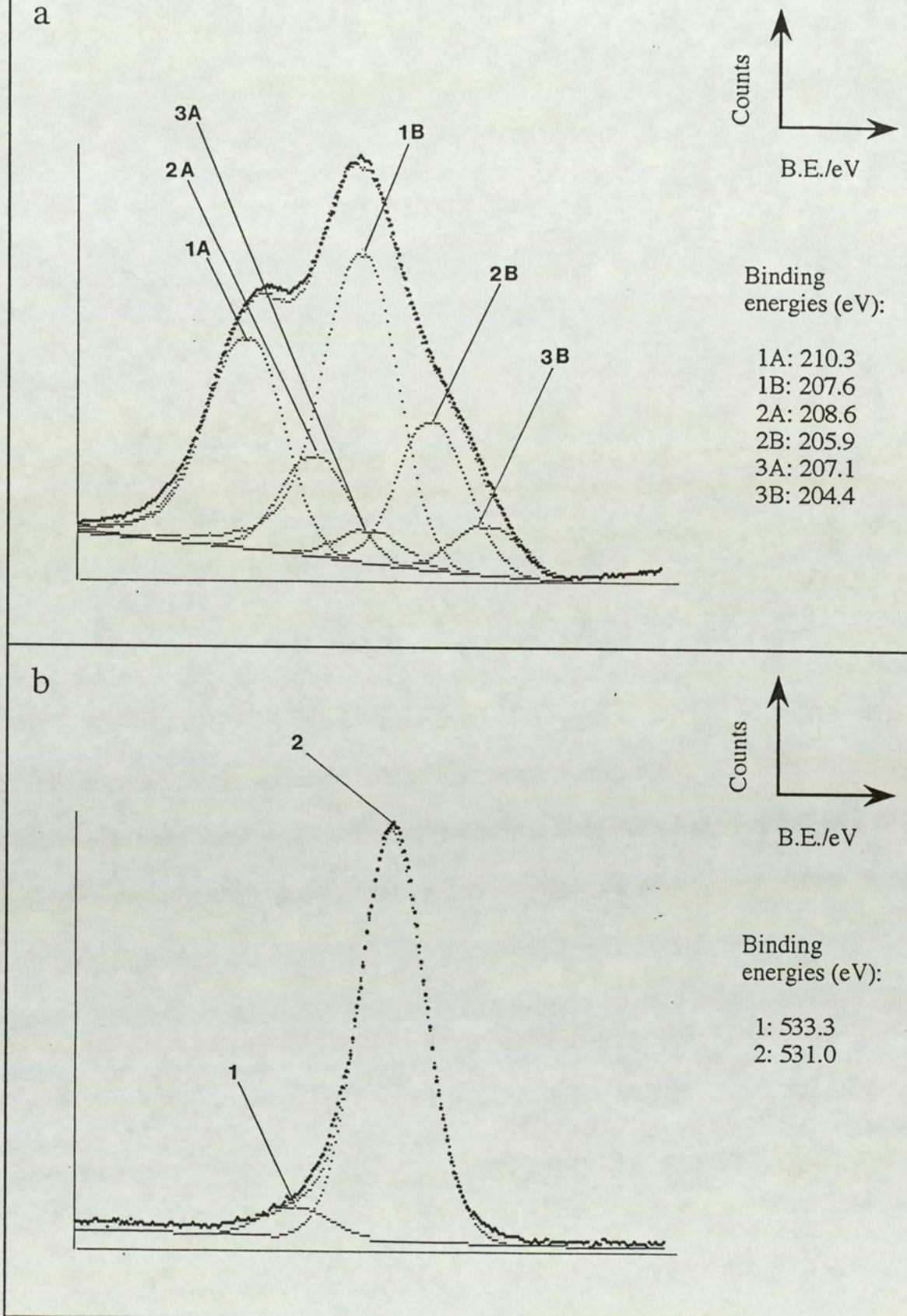

Figure 5.50.

Nb_2O_5 surface after 10 minutes of Ar^+ ion bombardment.

a) Nb 3d ($3d_{3/2}$ is shown by A, and $3d_{5/2}$ is shown by B)

b) O 1s

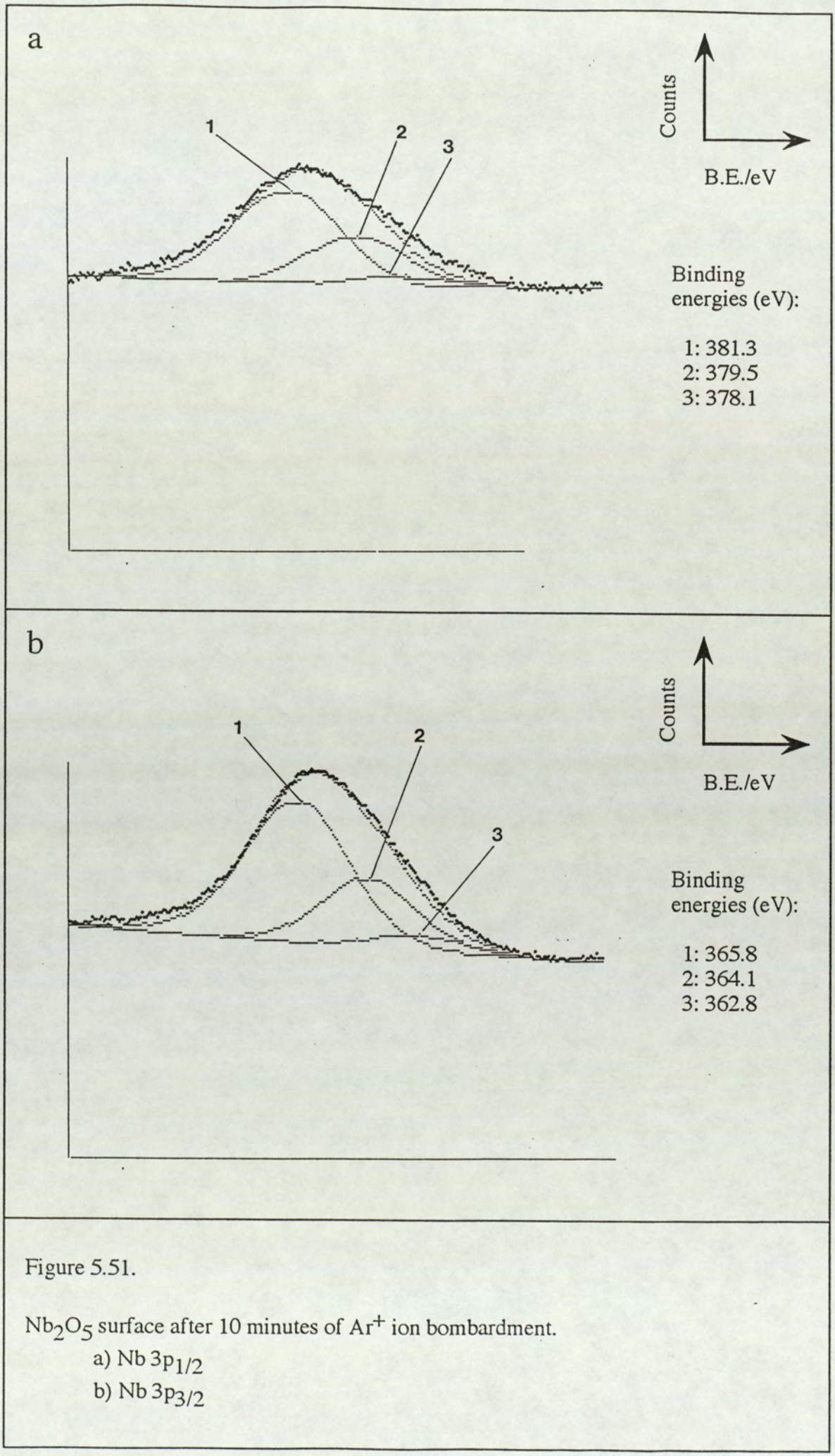

Figure 5.51.

Nb_2O_5 surface after 10 minutes of Ar^+ ion bombardment.

a) Nb $3p_{1/2}$

b) Nb $3p_{3/2}$

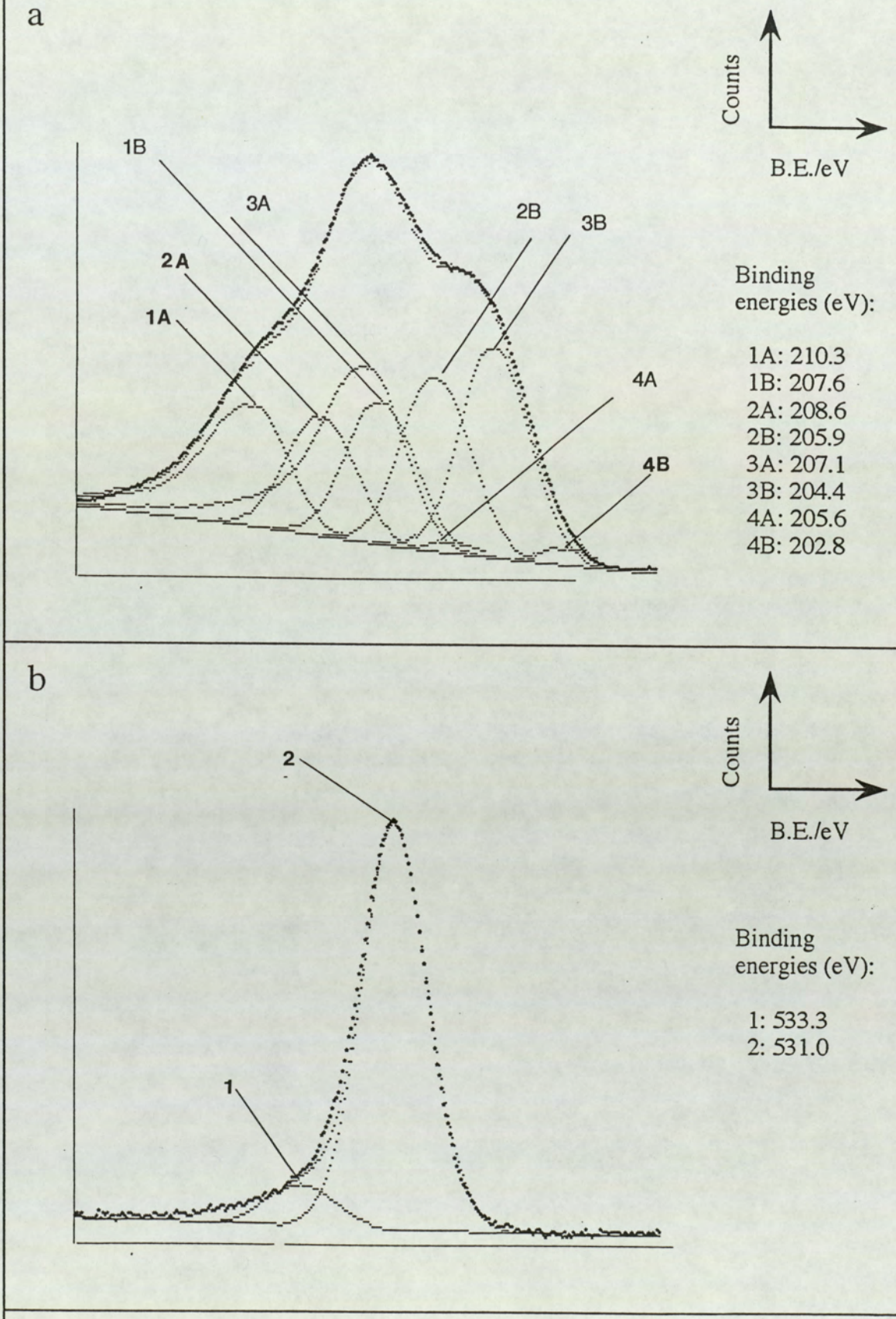

Figure 5.52.

Nb_2O_5 surface after 120 minutes of Ar^+ ion bombardment.

a) Nb 3d ($3d_{3/2}$ is shown by A, and $3d_{5/2}$ is shown by B)

b) O 1s

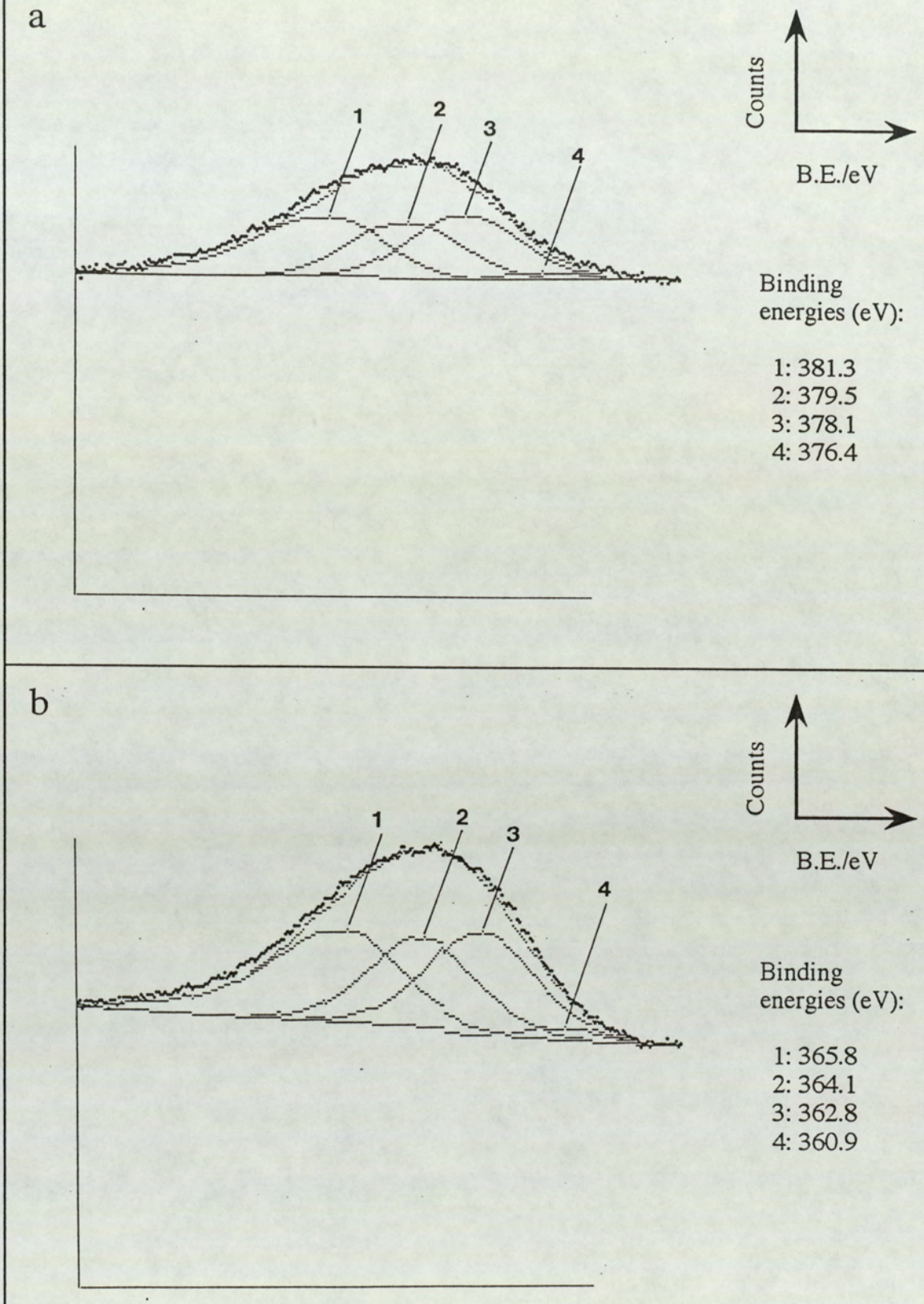

Figure 5.53.

Nb_2O_5 surface after 120 minutes of Ar^+ ion bombardment.

a) Nb $3p_{1/2}$

b) Nb $3p_{3/2}$

Table 5.6

Measured binding energy values (±0.2eV) and corresponding FWHM values (±0.2eV) for niobium and its oxides. Calibration is with respect to the C 1s peak at 284.6 eV.

identity		core level	binding energy (eV)	FWHM (eV)
Nb_2O_5	Nb^V	$3d_{5/2}$	207.6	1.9
		$3d_{3/2}$	210.3	1.9
		$3p_{3/2}$	365.8	2.9
		$3p_{1/2}$	381.3	2.9
NbO_2	Nb^{IV}	$3d_{5/2}$	205.9	1.9
		$3d_{3/2}$	208.6	1.9
		$3p_{3/2}$	364.1	2.9
		$3p_{1/2}$	379.5	2.9
Nb_2O_5	Nb^{II}	$3d_{5/2}$	204.4	1.9
		$3d_{3/2}$	207.1	1.9
		$3p_{3/2}$	362.8	2.9
		$3p_{1/2}$	378.1	2.9
Nb-metal	Nb^0	$3d_{5/2}$	202.8	1.3
		$3d_{3/2}$	205.6	1.3
		$3p_{3/2}$	360.9	2.0
		$3p_{1/2}$	376.4	2.0
Oxygen	metal-oxygen bond	1s	530.0	1.8
	surface bound water	1s	533.3	1.8
Carbon	hydrocarbon bond	1s	284.6	2.0

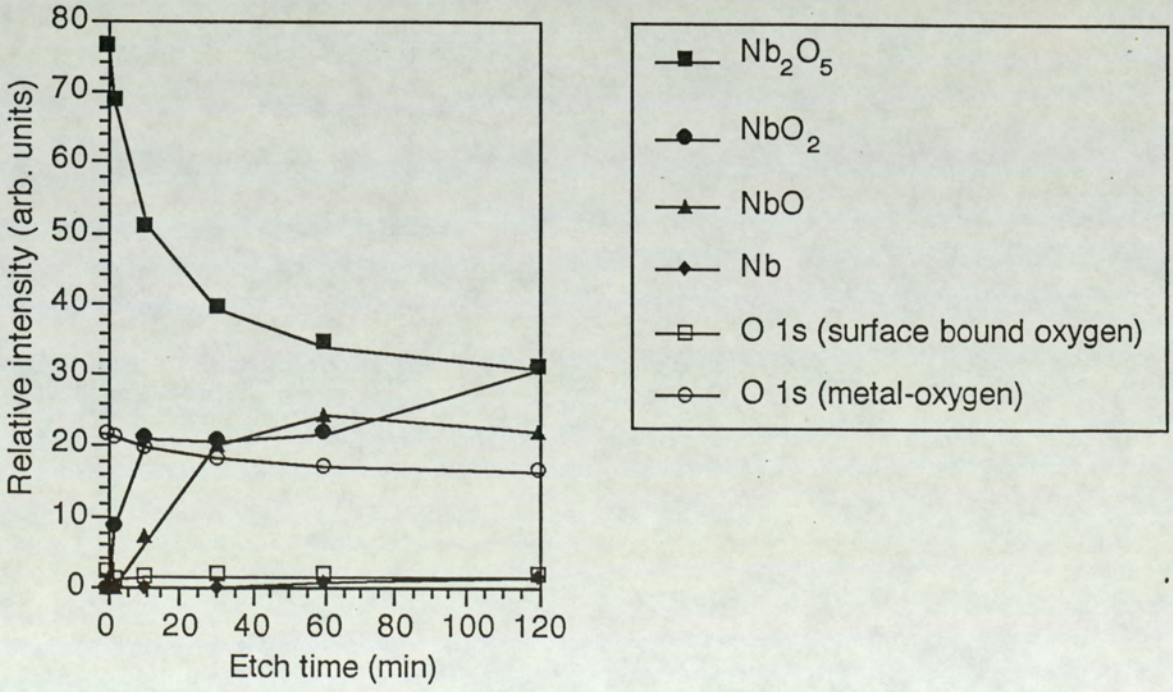

Figure 5.54.
Relative intensity as a function of etch time for Nb_2O_5.

and 204.4 eV due to the $3d_{3/2}$ and $3d_{5/2}$ lines of the Nb^{II} ions In NbO. The associated $3p_{1/2}$ and $3p_{3/2}$ lines appear at 378.1 eV and 362.8 eV.

Further exposure to incident ion beam causes increments to the measured suboxide intensities with the appearence of the metallic state, Nb^0, after 60 minutes of ion bombardment. For the metallic state the $3d_{(3/2, 5/2)}$ lines appear at binding energies 205.6 eV and 202.8 eV (FWHM=1.3 eV) and those due to the $3p_{(1/2, 3/2)}$ lines appear at 376.4 eV and 360.9 eV (FWHM=2.0 eV). This investigation thus clearly demonstrates ion beam induced reduction of Nb^V to Nb^{IV}, Nb^{II} and eventually to Nb^0. Figures (5.52a,b) and (5.53a,b) show the spectra for the 120 minutes of bombardment which exhibit the existence of a steady state surface layer containing all four states of niobium. An indication of the variation of surface composition with etch time can be seen in figure (5.54) where relative intensity against etch time is plotted. Table (5.6) lists all the peaks observed with their associated FWHM values.

5.5.9: WO_3

To investigate the effects of ion bombardment on the tungsten tri-oxide powder sample, it was found that addition of gold powder was not necessary to counteract against charging effects. Thus the sample was prepared without addition of the gold powder and binding energies were measured with respect to the carbon 1s peak due to the surface hydrocarbons. The photo-electron lines W4f, W4d, O 1s and the C 1s lines were recorded for the unetched surface and after different durations of bombardment. Curve-fitting procedures carried out on these spectral profiles yielded the following results.

Figure (5.55a and b) show the O 1s and C 1s spectra for the unbombarded surface. In the O 1s spectrum two peaks are seen; a peak due to the metal oxygen bond appearing at 531.4 eV (FWHM=1.8 eV) and a peak due to surface bound water at 533.3 eV. The carbon peak also shows two peaks with FWHM of 2.0 eV separated by energy of 1.5 eV. The lower binding energy peak is the major peak and is assigned a

value of 284.6 eV. The peak at 1.5 eV higher binding energy is due to the carbon-single bond-oxygen molecule.

Figures (5.56a and b) show the W 4f and W 4d profiles for the unbombarded surface. Two peaks can just be resolved in the W 4f spectrum prior to curve-synthesis, these are the W $4f_{5/2}$ and $4f_{7/2}$ lines. Curve-synthesis procedure yields the binding energies to be 37.8 and 35.6 eV respectively, both with FWHM of 1.9 eV; their intensity ratio measured as 1.324 (the theoretically calculated value for f-orbitals using the ratio of (2J+1) is 1.33). The W 4d spectrum show two clearly resolved peaks due to the $4d_{3/2}$ and $4d_{5/2}$ lines at 260.3 eV and 247.8 eV with FWHM value of 4.1 eV (their measured intensity ratio being 1.507 compared with 1.5 which is the theoretical value obtained for d-orbitals). All four peaks are due to the 4f and 4d lines of W^{VI} ions in WO_3.

Controlled ion bombardment for duration of 10 minutes brings about drastic changes in the in both the 4f and 4d profiles, as shown in figures (5.57a,b), accompanied by a colour change of the WO_3 surface from yellow to dark grey. The 4f lines show extensive broadening with a shoulder to the low binding energy. Curve-fitting results show that this broadening can be accounted for by the addition of three pairs of peaks. The first pair at binding energies of 36.1 and 33.9 eV are expected to be due to the $4f_{5/2}$ and $4f_{7/2}$ lines of tungsten perhaps in the form W_2O_5 (i.e. the W^V ionic state). The second pair appear at binding energies of 34.4 and 32.2 eV being due to the two 4f lines of W^{IV} ions In WO_2, which is a chemically stable form under normal temperature and pressure conditions. The last pair shows the existance of metallic tungsten W^0, appearing at 33.3 and 31.1 eV for the $4f_{5/2}$ and $4f_{7/2}$ lines respectively. The first two pairs have FWHM value equal to that of the original bulk oxide at 1.9 eV and the peaks due to the metallic state have FWHM of 1.5 eV. Thus the results obtained for the 4f lines show full reduction to the metallic state.

The 4d spectrum for the 10 minutes etching period show the same results as the 4f spectrum. Broadening of the $4d_{3/2}$ and $4d_{5/2}$ lines is observed which is

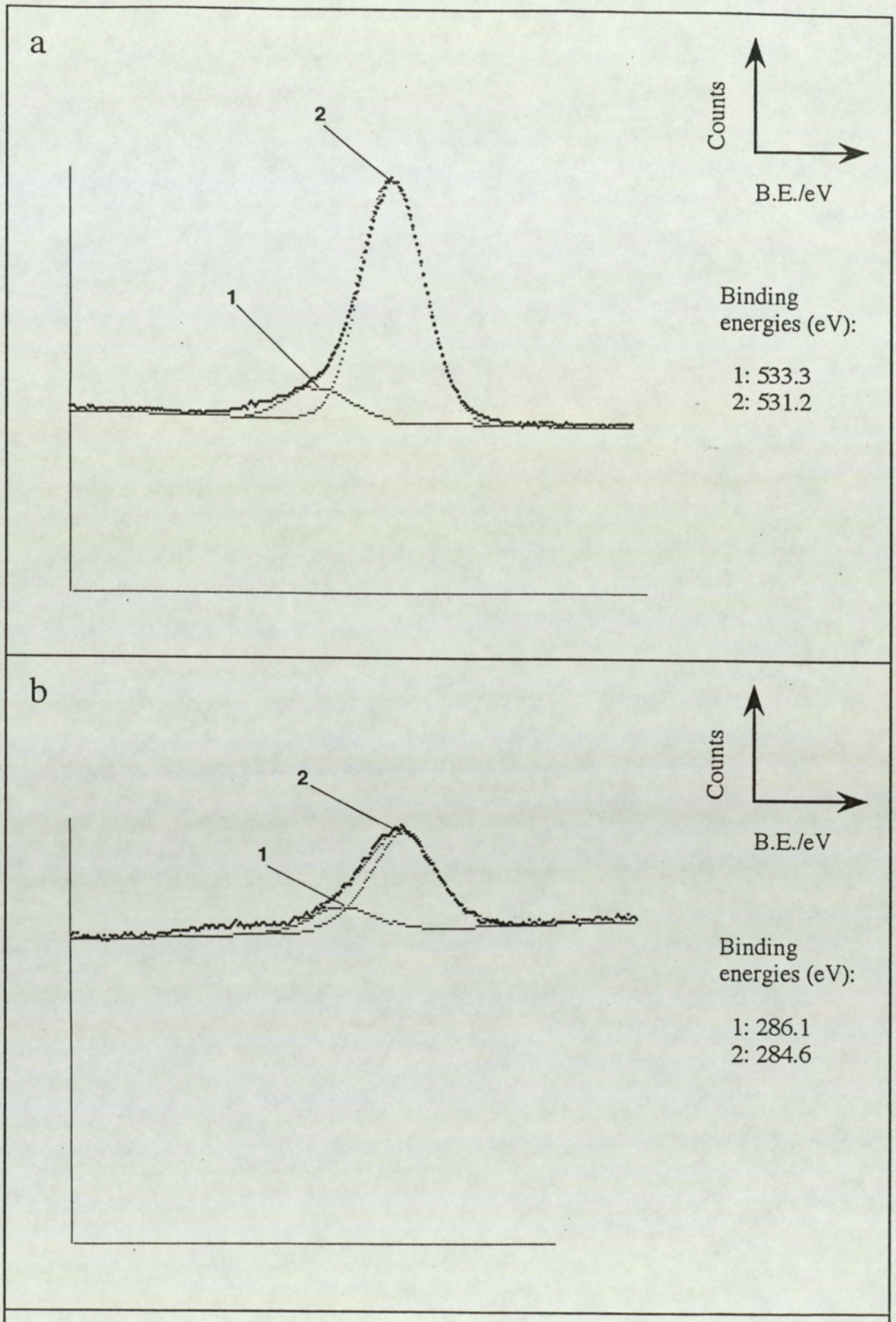

Figure 5.55.

Unbombarded WO_3 surface.

a) O 1s
b) C 1s

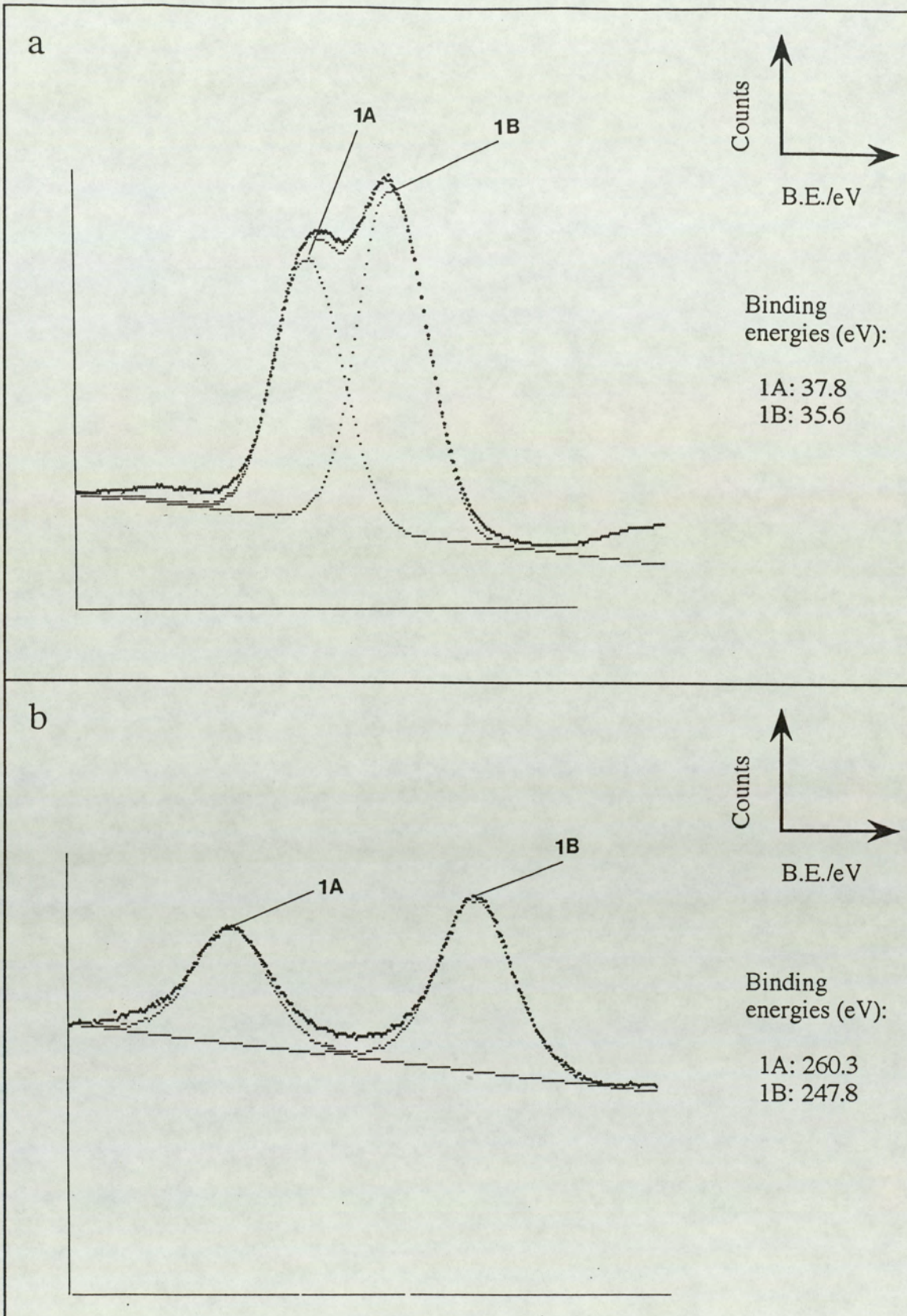

Figure 5.56.

Unbombarded WO_3 surface.

a) W 4f ($4f_{5/2}$ is shown by A, and $4f_{7/2}$ is shown by B)

b) W 4d ($4d_{3/2}$ is shown by A, and $4d_{5/2}$ is shown by B)

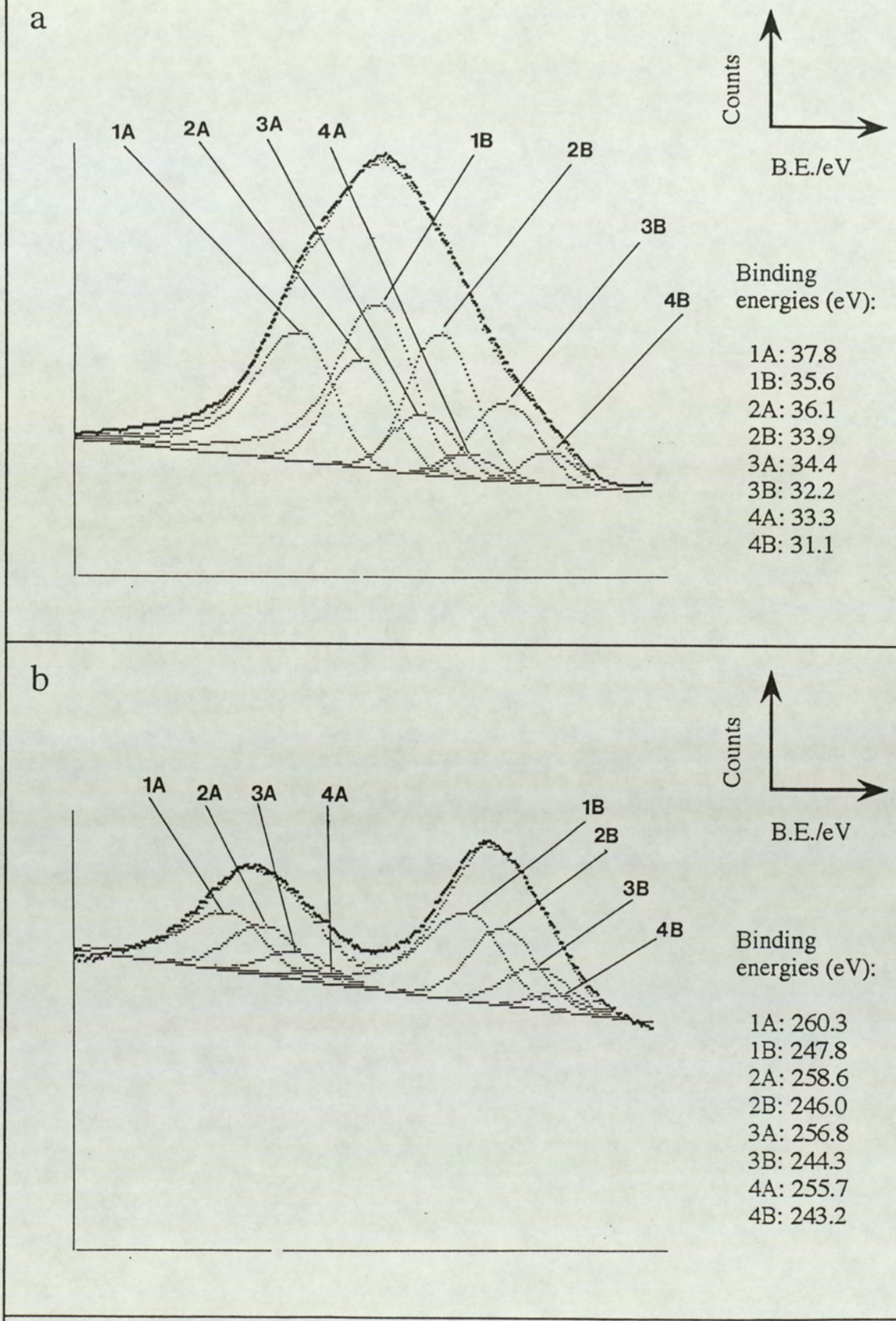

Figure 5.57.

WO_3 surface after 10 minutes of Ar^+ ion bombardment.

a) W 4f ($4f_{5/2}$ is shown by A, and $4f_{7/2}$ is shown by B)

b) W 4d ($4d_{3/2}$ is shown by A, and $4d_{5/2}$ is shown by B)

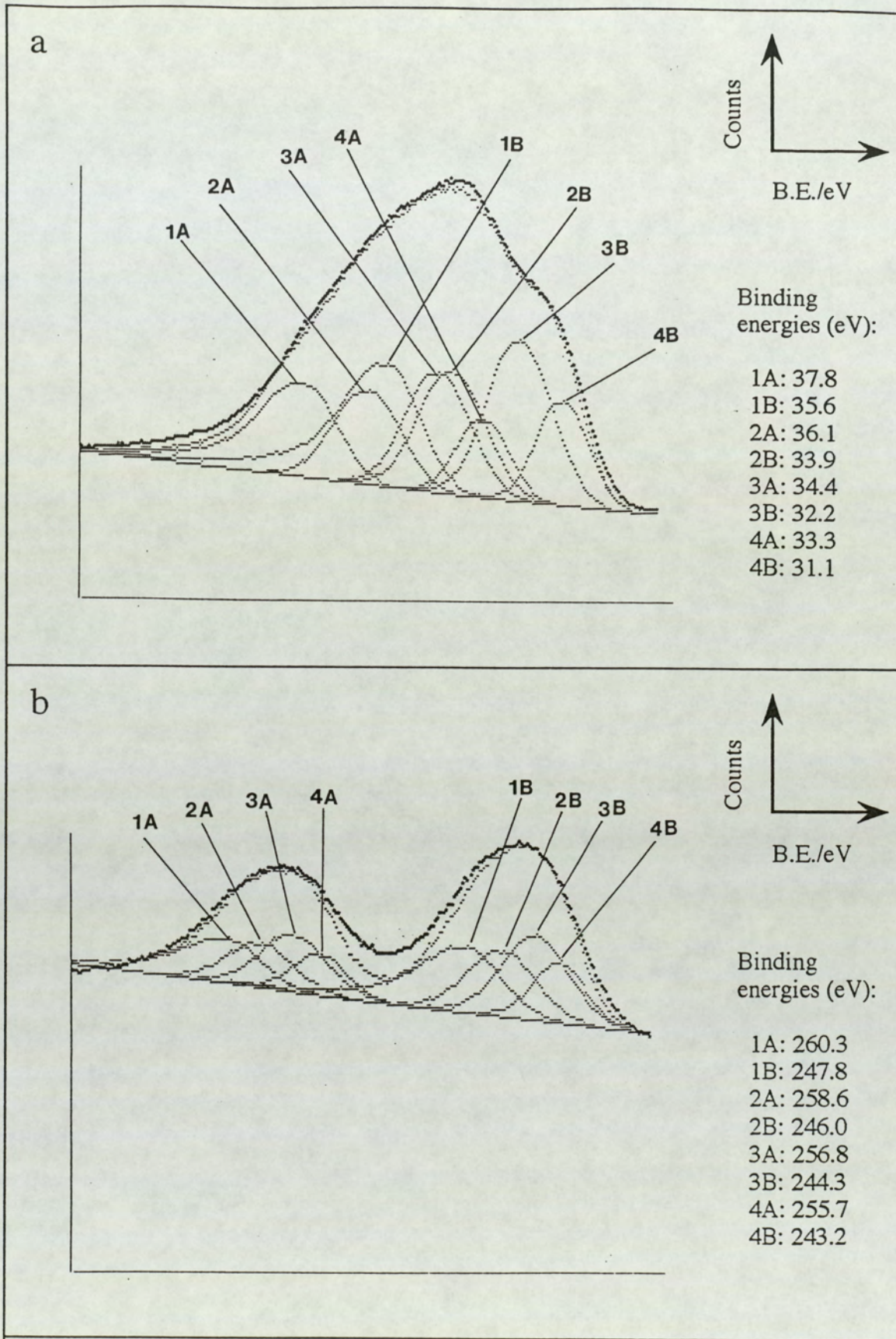

Figure 5.58.

WO_3 surface after 120 minutes of Ar^+ ion bombardment.

a) W 4f ($4f_{5/2}$ is shown by A, and $4f_{7/2}$ is shown by B)

b) W 4d ($4d_{3/2}$ is shown by A, and $4d_{5/2}$ is shown by B)

Table 5.7

Measured binding energy values (±0.2eV) and corresponding FWHM values (±0.2eV) for tungsten and its oxides. Calibration is with respect to the C 1s peak at 284.6 eV.

identity		core level	binding energy (eV)	FWHM (eV)
WO_3	W^{VI}	$4f_{7/2}$	35.6	1.9
		$4f_{5/2}$	37.8	1.9
		$4d_{5/2}$	247.8	4.1
		$4d_{3/2}$	260.3	4.1
W_2O_5	W^{V}	$4f_{7/2}$	33.9	1.9
		$4f_{5/2}$	36.1	1.9
		$4d_{5/2}$	246.0	4.1
		$4d_{3/2}$	258.6	4.1
WO_2	W^{IV}	$4f_{7/2}$	32.2	1.9
		$4f_{5/2}$	34.4	1.9
		$4d_{5/2}$	244.3	4.1
		$4d_{3/2}$	256.8	4.1
W-metal	W^{0}	$4f_{7/2}$	31.1	1.5
		$4f_{5/2}$	33.3	1.5
		$4d_{5/2}$	243.2	3.2
		$4d_{3/2}$	255.7	3.2
Oxygen	metal-oxygen bond	1s	531.4	1.8
	surface bound water	1s	533.3	1.8
Carbon	hydrocarbon bond	1s	284.6	2.0
	single oxygen bond	1s	286.1	2.0

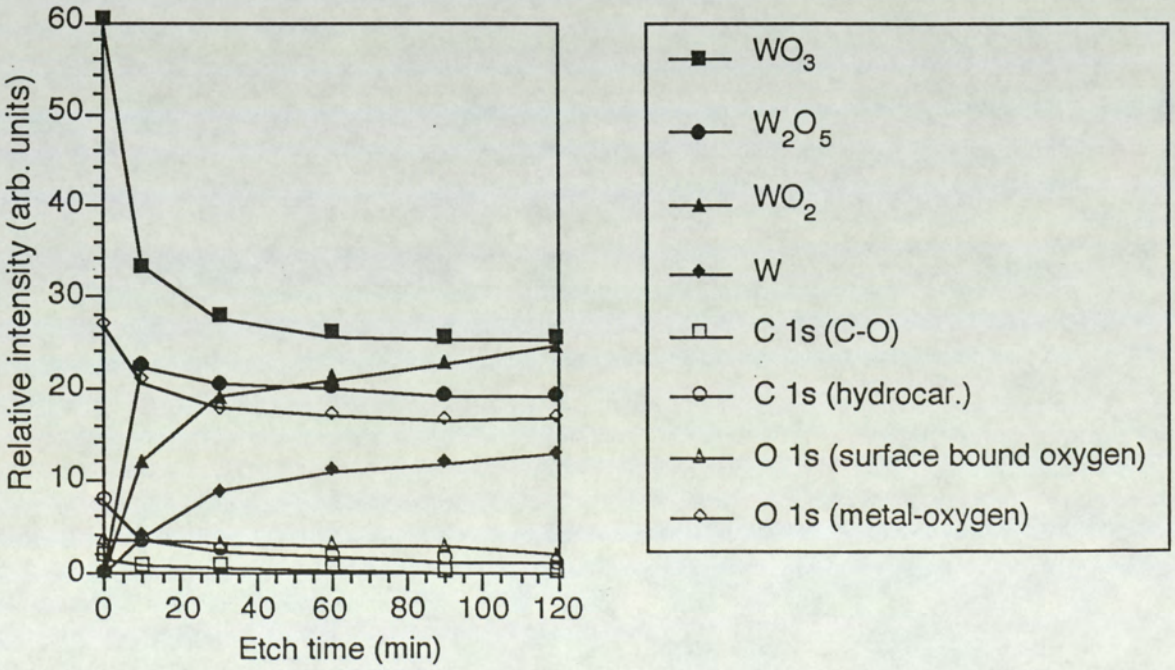

Figure 5.59.

Relative intensity as a function of etch time for WO_3.

accounted for by the appearence of the W_2O_5, WO_2 and metallic W states. These lines for the W_2O_5 state appear at 258.6 and 246.0 eV, for WO_2 at 256.8 and 244.3 eV and those due to metallic tungsten at 255.7 and 243.2 eV. The peaks due to the 4d lines of the sub-oxides have FWHM of 4.1 eV and those due to the metallic state have FWHM of 3.2 eV.

For the 10 minutes of bombardment the intensity ratio of W^{VI}:W^{V}, W^{VI}:W^{IV} and W^{VI}:W^{0} are measured to be 14.75, 2.76 and 8.41. With further bombardment these ratios change to 1.36, 1.47 and 3.20 after 30 minutes; to 1.30, 1.23 and 2.35 after 60 minutes; to 1.32, 1.12 and 2.13 after 90 minutes and eventually to 1.32, 1.03 and 2.0 after 120 minutes of bombardment. Equilibrium conditions seem to have been reached within 120 minutes of bombardment. Figures (5.58a,b) show the 4f and 4d spectra after 120 minutes of ion bombardment. Figure (5.59) shows a plot of the relative intensities against etch times and Table (5.7) shows all the binding energy values with its appropriate FWHM values.

5.5.10: Ta_2O_5

For the unbombarded Ta_2O_5 sample, the lines Ta 4f, Ta 4d, O 1s and the C 1s were recorded and curve-fitting procedures were employed on all peaks. Figures (5.60a,b) show the Ta 4f and the Ta 4d spectra. Considering the Ta 4f spectrum, curve-fitting reveals the presence of two peaks both with FWHM of 2.0 eV at 28.5 eV and at 26.6 eV due to the $4f_{5/2}$ and $4f_{7/2}$ lines of the Ta^{V} ions in Ta_2O_5. The same results can be concluded by observing the Ta 4d lines; two peaks at 242.5 eV (FWHM=4.2 eV) and 230.9 eV (FWHM=4.1 eV) are seen due to the $4d_{3/2}$ and $4d_{5/2}$ lines of the Ta^{V} ions.

The O 1s and C 1s lines obtained from XPS studies of the unbombarded surface are shown in figures (5.62a,b). The carbon 1s spectrum shows the presence of two peaks; the lower binding energy one being due to the surface borne hydrocarbons (at 284.6 eV,used here as the reference energy). The second carbon line due to the carbon in the carbon-single bond-oxygen molecule appears at 1.5 eV above the

hydrocarbon line. The oxygen 1s spectrum shows the presence of three peaks: the main peak at 530.8 eV and two others at 533.7 and 532.2 eV indicating the presence of surface bound water and oxygen.

Figures (5.62a,b) show the O 1s and the Ta 4f spectra for the surface obtained after 30 minutes of ion bombardment. The Ta 4f spectrum shows the appearence of six additional peaks, these are due to the $4f_{5/2}$ and $4f_{7/2}$ lines of the Ta^{IV}, Ta^{II} and Ta^{0} ions in TaO_2, TaO and metallic tantalum respectively. The binding energies for the $4f_{5/2}$ and $4f_{7/2}$ lines are 27.7 eV and 25.8 eV for the Ta^{IV}, 25.6 eV and 23.8 eV for the Ta^{II} and 23.62 eV and 21.9 eV for the metallic Ta^{0}. The peaks due to the $4f_{5/2}$ and $4f_{7/2}$ lines of Ta^{IV} and Ta^{II} have the same FWHM value as those due to the Ta^{V} state, i.e. 2.0 eV and those due to Ta^{0} state have FWHM value of 1.8 eV. All these binding energy values with their FWHM values are listed in Table (5.8).

The corresponding O 1s spectrum shows an intensity reduction of all three oxygen peaks; the reduction for the bound water state, i.e. at binding energy 533.7 eV, being the most evident. Thus, a depletion of the total surface oxygen content has been obtained together with a reduction of the oxidation states. The evidence of which is apparent from the presence of the lower oxidation states of TaO_2, TaO and metallic tantalum. The peak intensity ratios of (Ta^{V}:Ta^{IV}), (Ta^{V}:Ta^{II}) and (Ta^{V}:Ta^{0}) are calculated to be 2.26, 2.57 and 10.48 respectively. These values are calculated using the results obtained for the areas under the peaks of both the $4f_{5/2}$ and $4f_{7/2}$ for each of the oxidation states and then taking the average of the two values obtained.

Further ion bombardment for periods of 60, 90 and 120 minutes shows progressive intensity reduction of the Ta_2O_5 state and increment of the TaO_2, TaO and metallic Ta states. This is evident from the progressive decrease of the intensity ratio of (Ta^{V}:Ta^{IV}) to 1.83, 1.63 and 1.51 after durations 60, 90 and 120 minutes of bombardment. Similar behaviour is also observed for the intensity ratios of (Ta^{V}:Ta^{II}) and (Ta^{V}:Ta^{0}). The ratio (Ta^{V}:Ta^{II}) decreases to 2.12, 1.82 and 1.62 and the ratio (Ta^{V}:Ta^{0}) decreases to 5.93, 4.50 and eventually to 3.43 after the bombardment

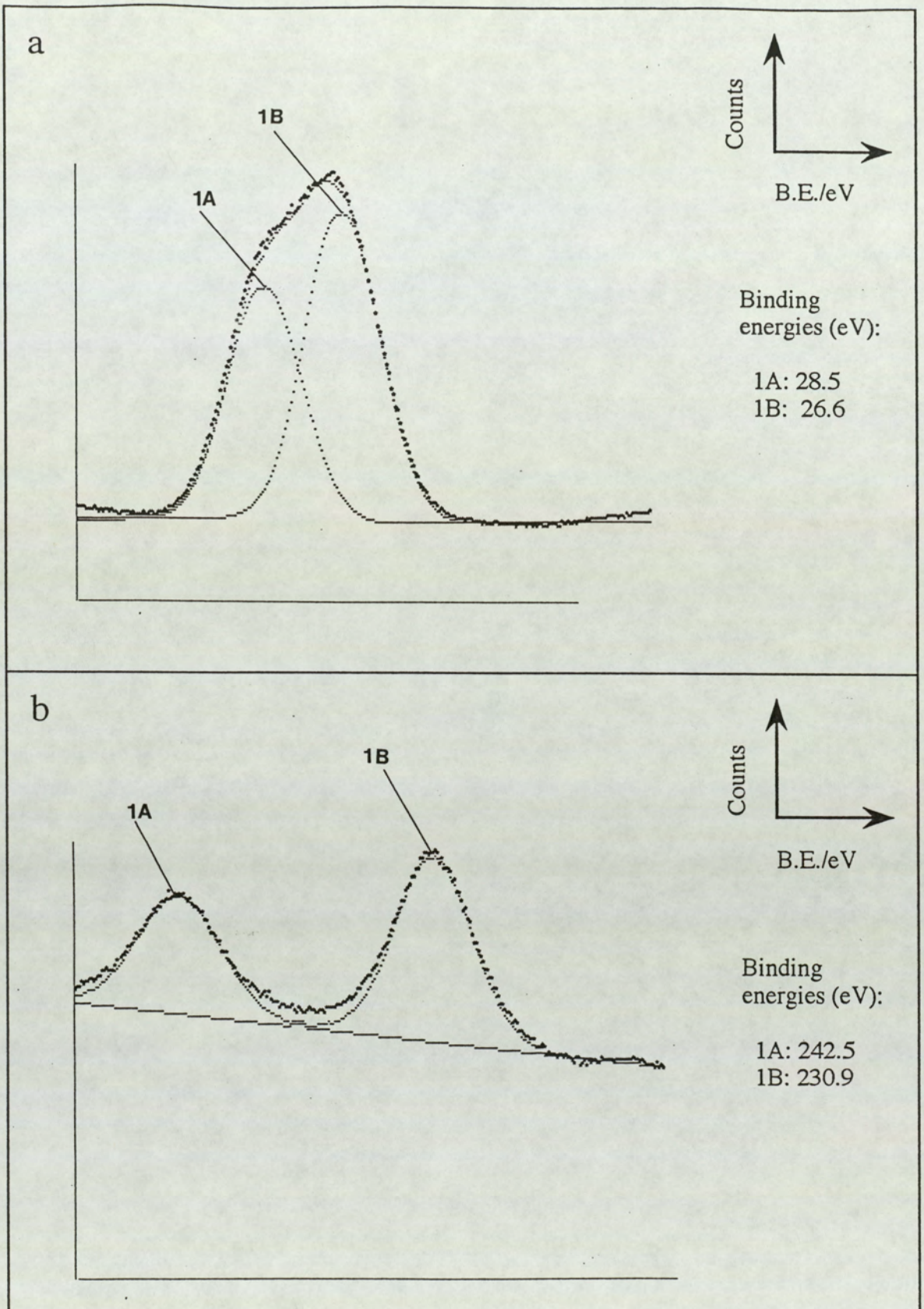

Figure 5.60.

Unbombarded Ta_2O_5 surface.

a) Ta 4f ($4f_{5/2}$ is shown by A, and $4f_{7/2}$ is shown by B)

b) Ta 4d ($4d_{3/2}$ is shown by A, and $4d_{5/2}$ is shown by B)

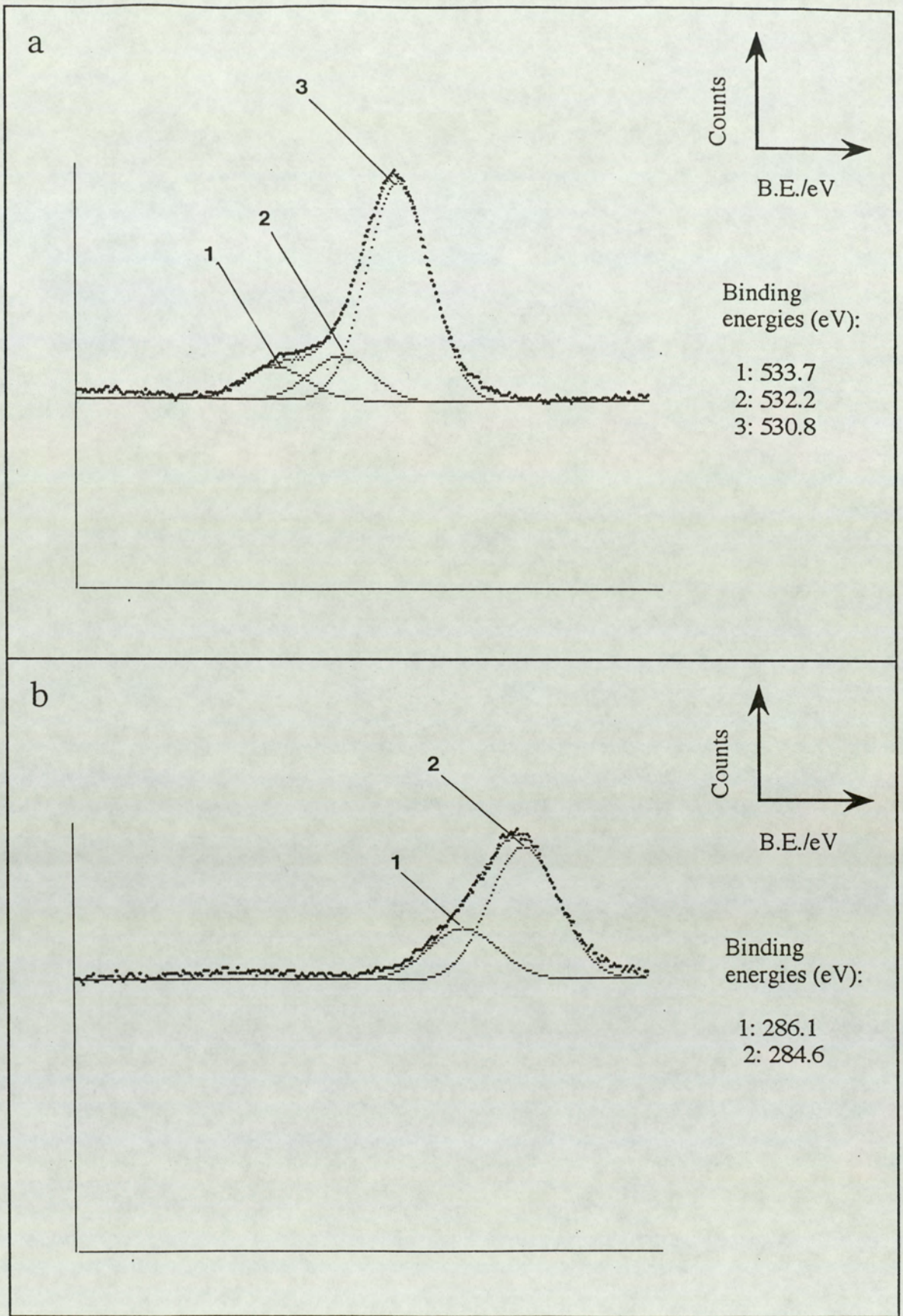

Figure 5.61.

Unbombarded Ta_2O_5 surface.

a) O 1s
b) C 1s

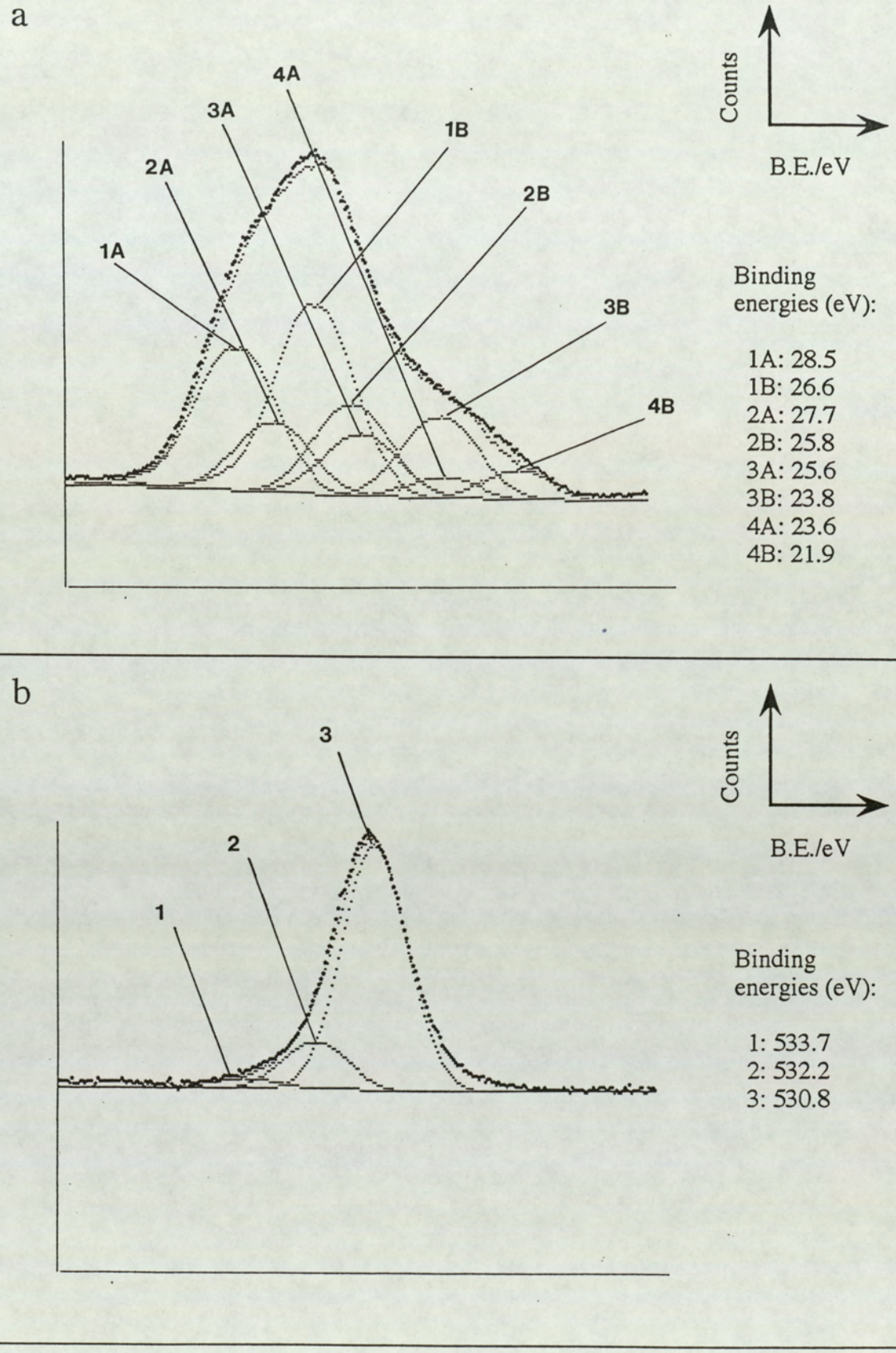

Figure 5.62.

Ta_2O_5 surface after 30 minutes of Ar^+ ion bombardment.

a) Ta 4f ($4f_{5/2}$ is shown by A, and $4f_{7/2}$ is shown by B)

b) O1s

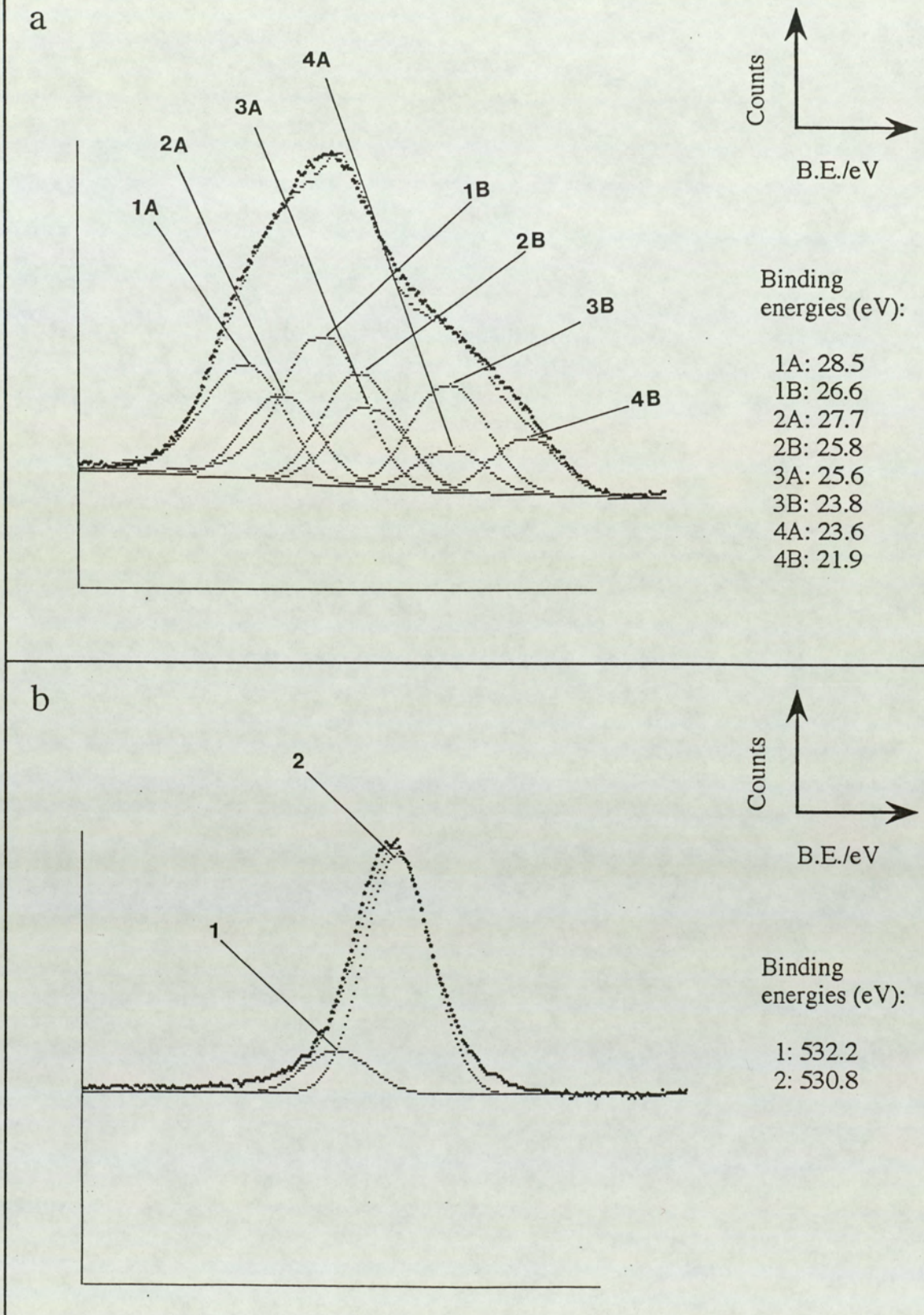

Figure 5.63.

Ta_2O_5 surface after 120 minutes of Ar^+ ion bombardment.

a) Ta 4f ($4f_{5/2}$ is shown by A, and $4f_{7/2}$ is shown by B)

b) O1s

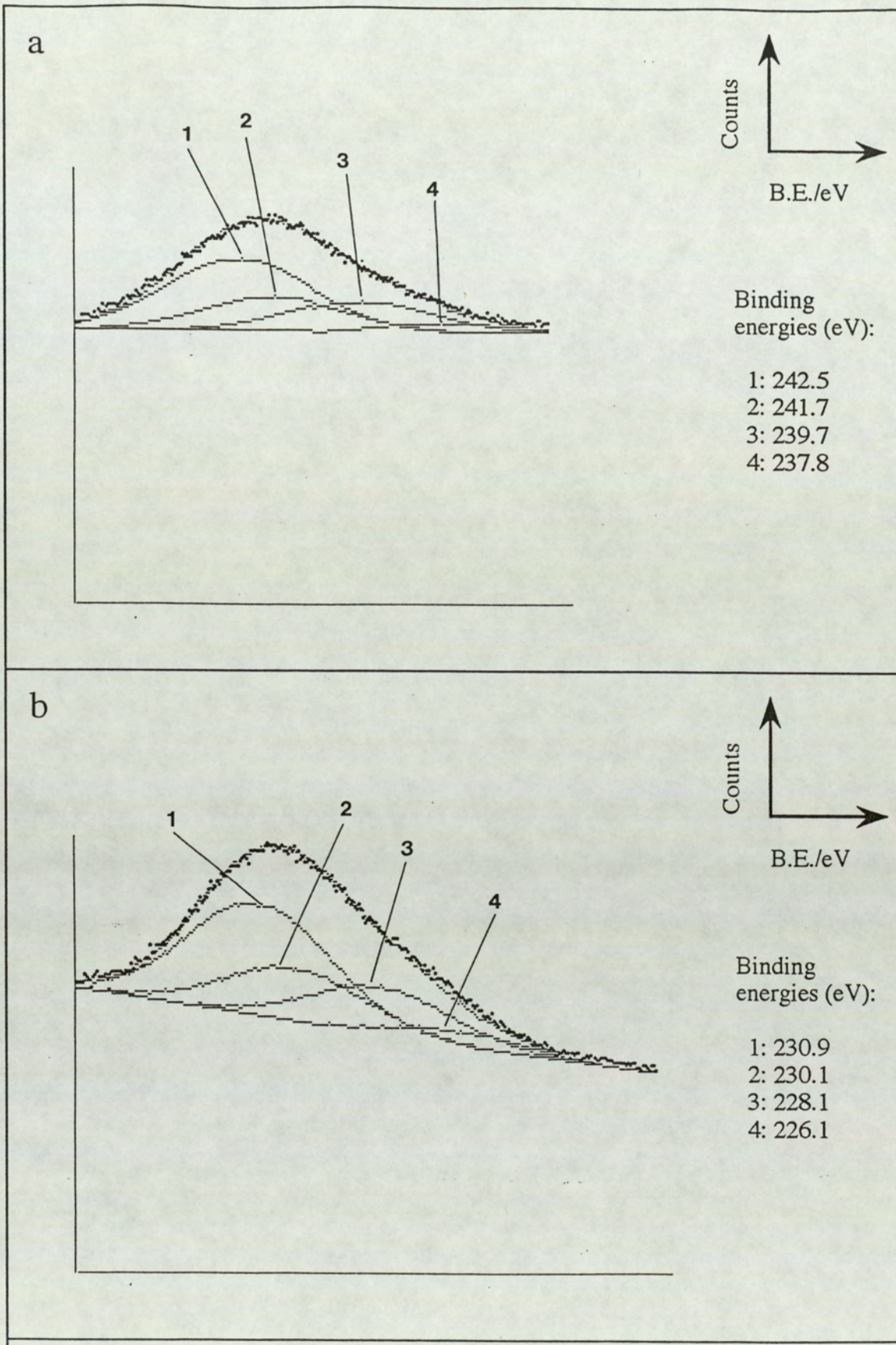

Figure 5.64.

Ta_2O_5 surface after 30 minutes of Ar^+ ion bombardment.

a) Ta $4d_{3/2}$

b) Ta $4d_{5/2}$

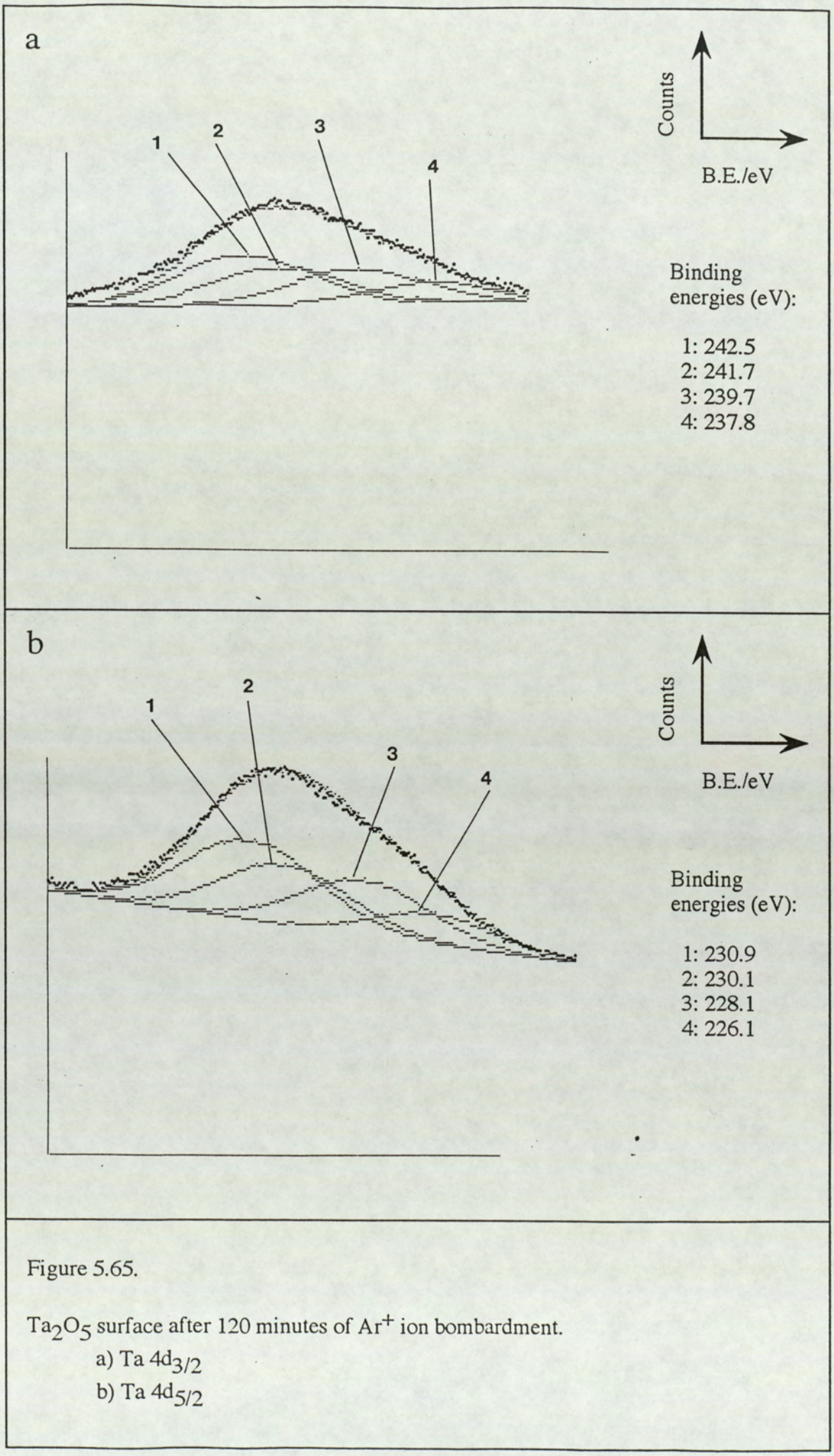

Figure 5.65.

Ta_2O_5 surface after 120 minutes of Ar^+ ion bombardment.

a) Ta $4d_{3/2}$

b) Ta $4d_{5/2}$

Table 5.8

Measured binding energy values (±0.2eV) and corresponding FWHM values (±0.2eV) for tantalum and its oxides. Calibration is with respect to the C 1s peak at 284.6 eV.

identity		core level	binding energy (eV)	FWHM (eV)
Ta_2O_5	Ta^V	$4f_{7/2}$	26.6	2.0
		$4f_{5/2}$	28.5	2.0
		$4d_{5/2}$	230.9	4.1
		$4d_{3/2}$	242.5	4.2
TaO_2	Ta^{IV}	$4f_{7/2}$	25.8	2.0
		$4f_{5/2}$	27.7	2.0
TaO	Ta^{II}	$4f_{7/2}$	23.8	2.0
		$4f_{5/2}$	25.6	2.0
Ta-metal	Ta^0	$4f_{7/2}$	21.9	1.8
		$4f_{5/2}$	23.6	1.8
Oxygen	metal-oxygen bond	1s	530.8	1.8
	surface bound oxygen	1s	533.2	1.8
	surface bound water	1s	533.7	1.8
Carbon	hydrocarbon bond	1s	284.6	2.0
	single oxygen bond	1s	286.1	2.0

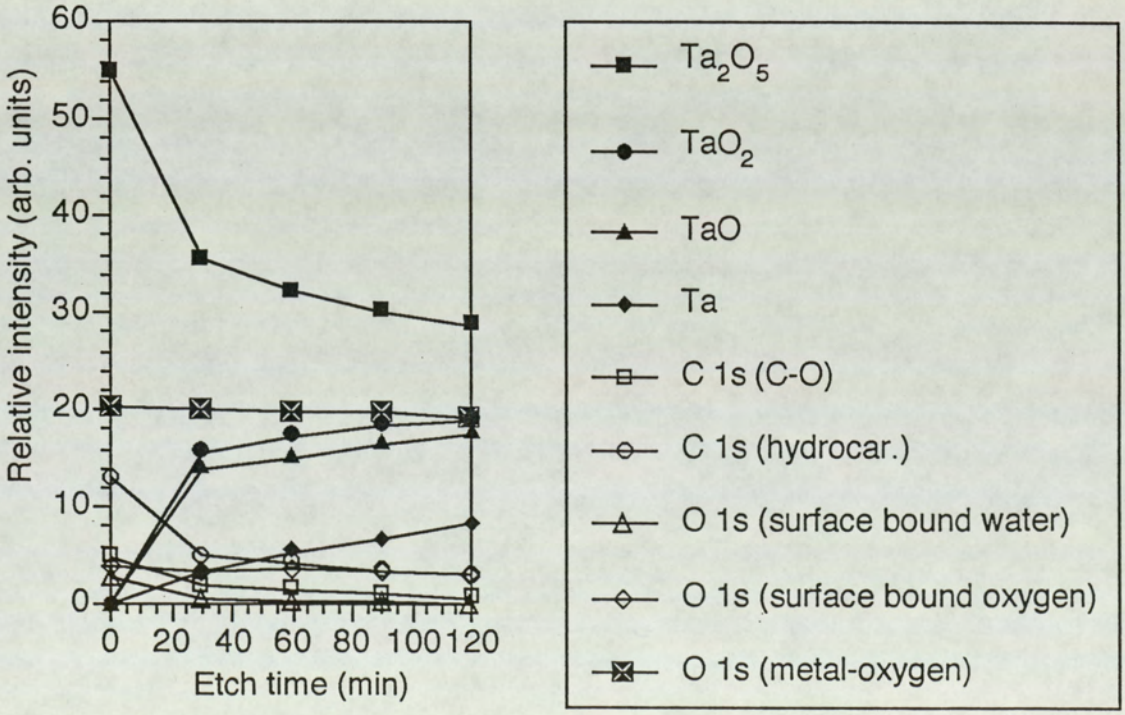

Figure 5.66.

Relative intensity as a function of etch time for Ta_2O_5.

periods of 60, 90 and 120 minutes respectively. The O 1s spectra for each of the bombardment periods mentioned above shows gradual decrease of all three oxygen peaks and the spectra for 90 minutes of bombardment shows complete removal of the surface bound water peak at 533.7 eV. Figures (5.63a,b) show the Ta 4f and O 1s spectra obtained after 120 minutes of ion bombardment.

The Ta 4d spectrum upon bombardment show the same trends as the Ta 4f spectra. Figures (5.64a,b) and (5.65a,b) show the Ta $4d_{3/2}$ and $4d_{5/2}$ spectra after 30 and 120 minutes of ion bombardment. The binding energies for the $4d_{3/2}$ and $4d_{5/2}$ lines of TaO_2 state are found to be 230.12 eV and 241.72 eV; those due to TaO state are 228.07 eV and 239.67 ev and the binding energies of 226.17 and 237.77 are assigned to be those due to the metallic tantalum. All these binding energies and their associated FWHM values are also listed in table (5.8)

A relative intensity for the oxidation states Ta_2O_5, TaO_2,TaO and metallic Ta, together with the three oxygen peaks and the two carbon peaks, are calculated for all the bombardment periods and a plot of these relative intensities against the bombardment times is given in Figure (5.66).

5.5.11: The effect of ion bombardment on the metal oxides MgO and Al_2O_3.

This investigation on these materials were carried out with the intention of observing the preferential sputtering effects on oxides in which the mass difference between the binary constituents is low. Thus MgO and Al_2O_3 are ideal oxides for this investigation having a mass difference of 8 a.m.u. and 11 a.m.u. respectively. The results are described below:

a) MgO

Figures (5.67a and b) show the Mg 1s and O 1s spectra respectively for the unbombarded surface. The Mg 1s spectrum shows the existence of the Mg^{II} ionic state at 1303 eV. The corresponding O 1s spectrum shows the existence of surface bound

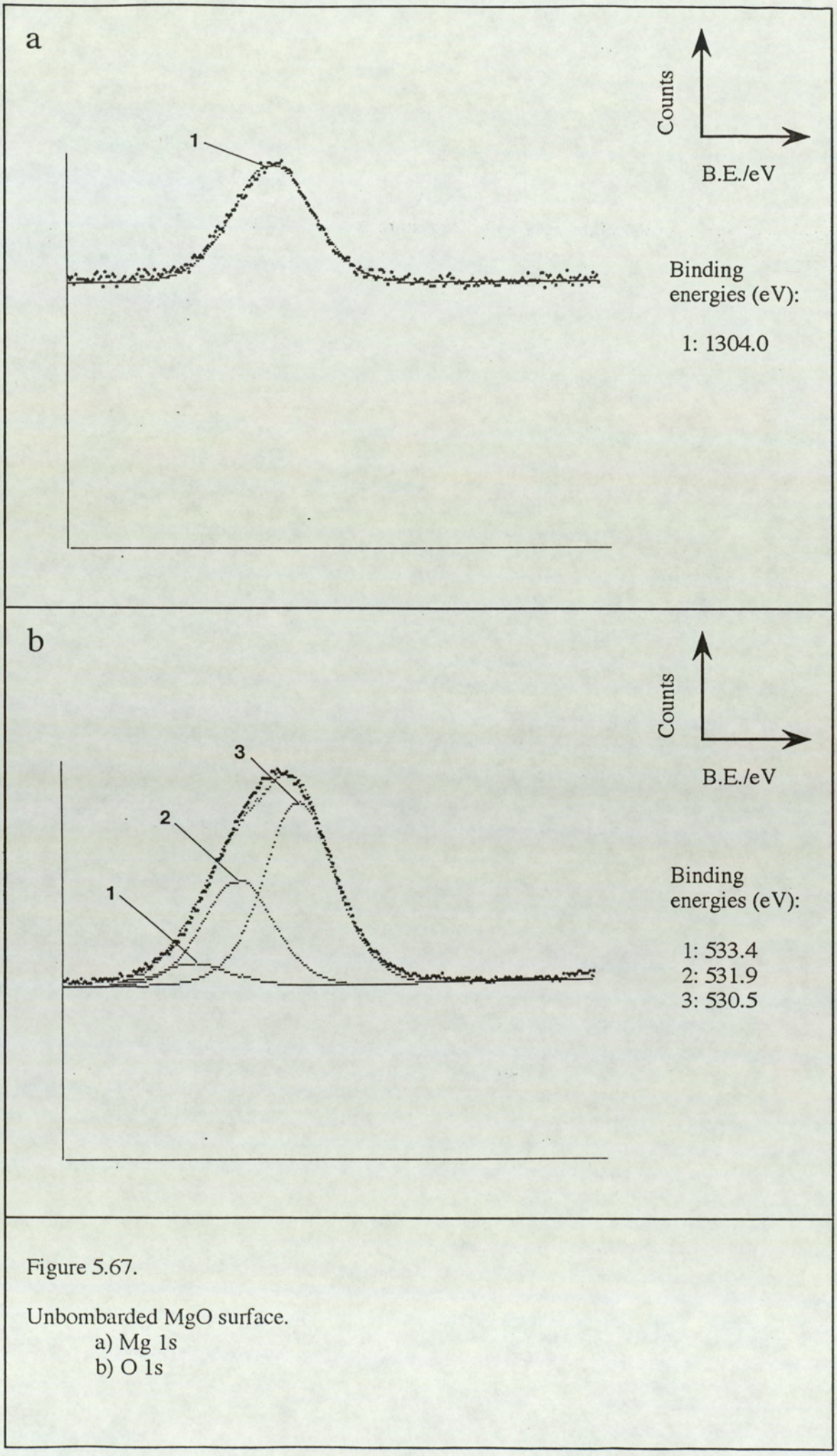

Figure 5.67.

Unbombarded MgO surface.
a) Mg 1s
b) O 1s

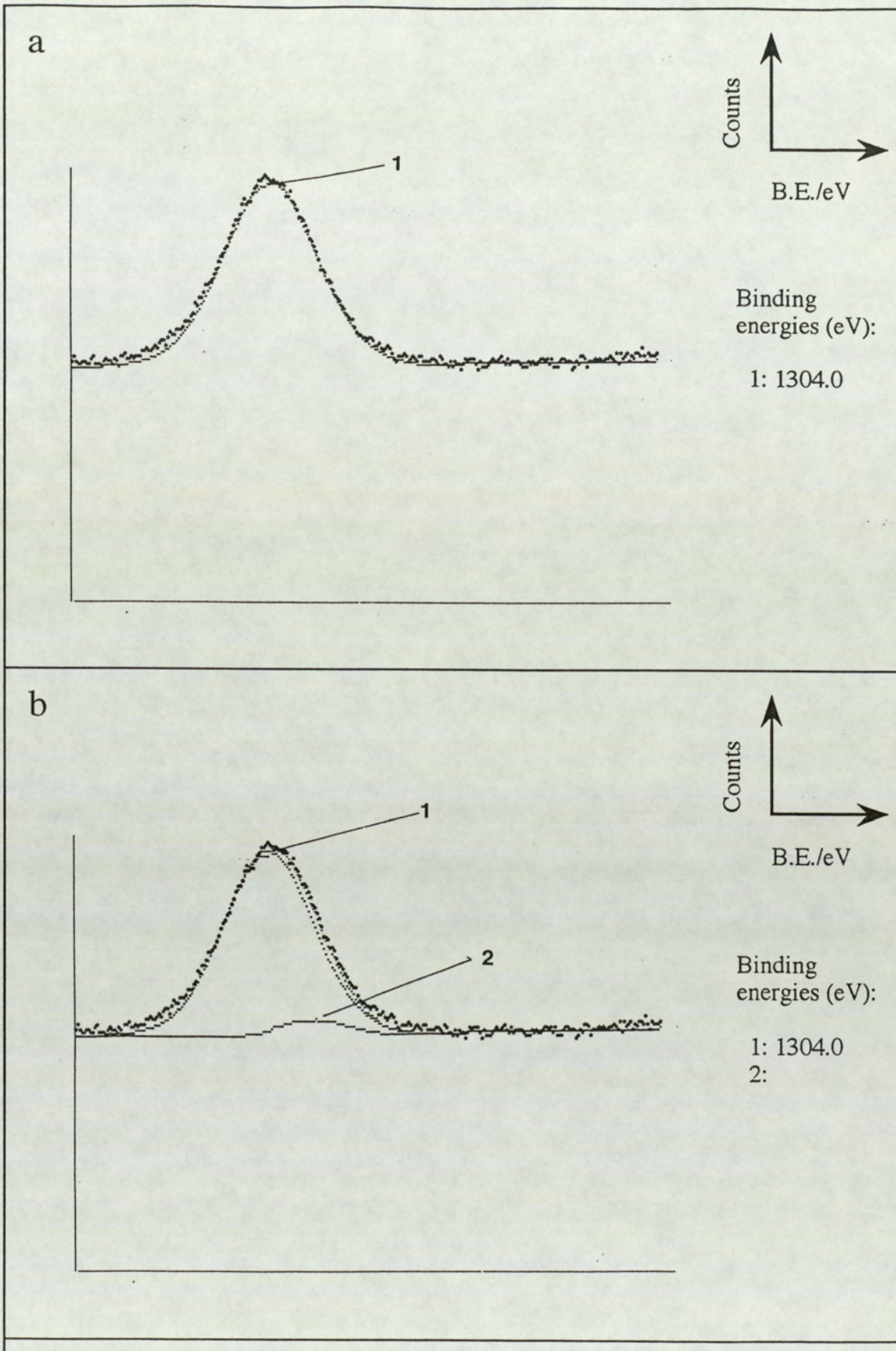

Figure 5.68.

MgO surface after 30 minutes of Ar^+ ion bombardment.
a) Mg 1s, one peak fitted
b) Mg 1s, two peaks fitted

Table 5.9

Measured binding energy values (±0.2eV) and corresponding FWHM values (±0.2eV) for MgO. Calibration is with respect to the C 1s peak at 284.6 eV.

identity		core level	binding energy (eV)	FWHM (eV)
MgO	Mg^{II}	1s	1304.0	2.5
Mg (metal)		1s	1302.0	1.9
Oxygen	metal-oxygen bond	1s	530.5	2.1
	surface bound water		533.4	2.1
	surface bound oxygen		531.9	2.1

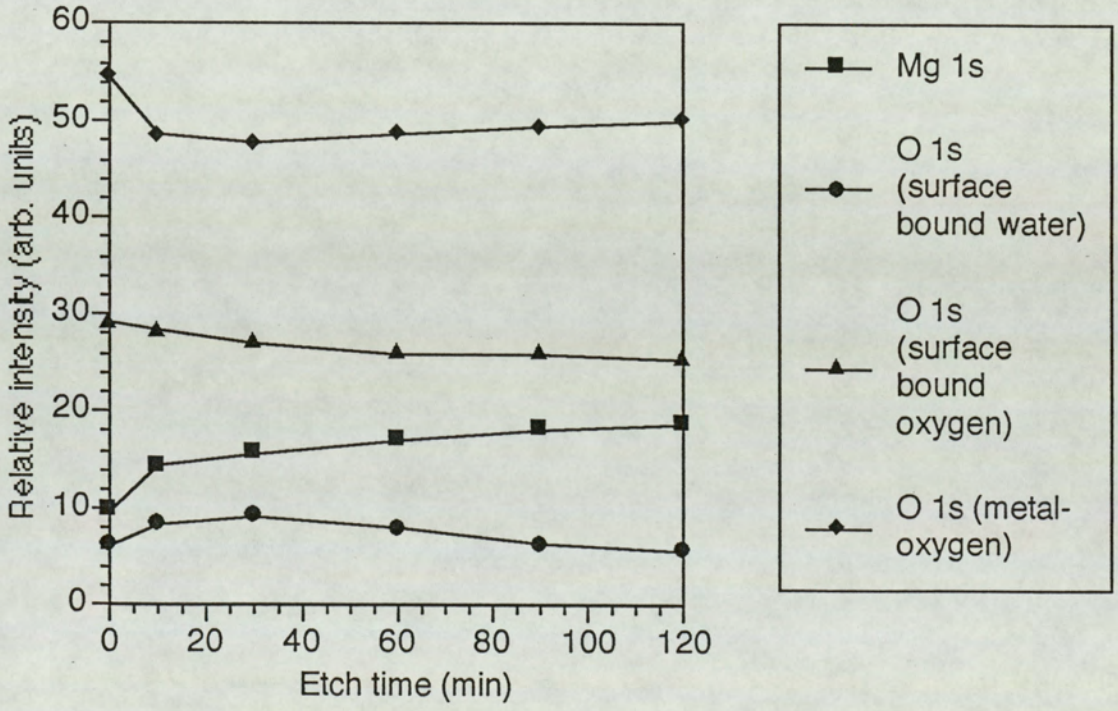

Figure 5.69.

Relative intensity as a function of etch time for MgO.

water peak at 533.4 eV, surface bound oxygen at 531.9 eV and the peak due to the metal-oxygen bond at 530.5 eV.

Subjecting the surface to progressive periods of ion bombardment does not show the extensive broadening of the metal peak as seen previously with the transition metal oxides (which have higher mass difference). However, an interesting aspect can be observed after curve-synthesis procedures are carried out. An ion bombardment induced peak widening of 0.2 eV is seen in the Mg 1s spectrum. This small increase in peak width has two possible explanations. Figures (5.68a,b) show the Mg 1s spectrum after 30 minutes of etching but with two different curve-synthesis results. The small peak widening can be accomodated by either fitting, in-additon to the first peak, a smaller peak at a binding energy of 1302.6 eV corresponding to the metallic Mg^0 state; or only one peak at the original binding energy value is fitted with a wider peak than that for the unbombarded surface being assumed to be caused by a phase change of the MgO state.

Figure (5.69) show the relative intensities of the Mg 1s and O 1s spectra plotted against etch times. A very small increase in the M/O intensity ratio can be seen. Table (5.9) tabulates all the binding energy and the FWHM values obtained.

b) Al_2O_3

The results obtained with this oxide are very similar to those obtained with MgO surface. Figures (5.70a,b and c) show the Al 2p, 2s and O 1s spectra for the unbombarded surface. The Al 2p and 2s peaks appear at binding energies of 74.7 eV and 119.5 eV respectively. The O 1s profile show the Metal-oxygen bond at 530.5 eV and the presence of surface bound oxygen at 533.4 eV.

Upon ion bombardment, an increase of 0.2 eV is seen in both the 2p and 2s peak widths. This 0.2 eV increase in the peak width is also measured for the O 1s peak due to the metal-oxygen bond. Figures (5.71a, b, c) show these peaks after 30 minutes of bombardment. Figure (5.72) shows the relative intensity of the Al 2p and 2s and O

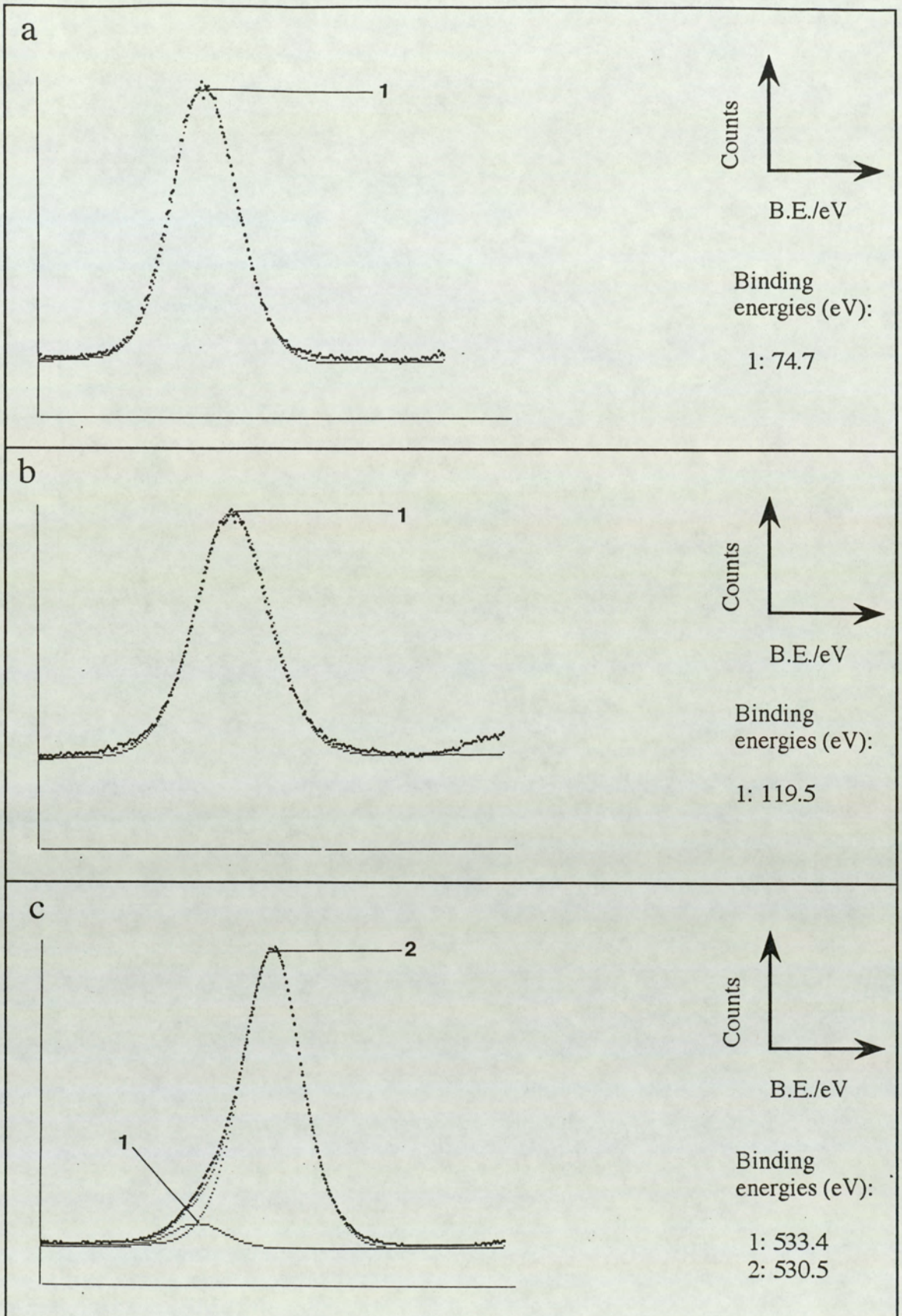

Figure 5.70.

Unbombarded Al_2O_3 surface.

a) Al 2p
b) Al 2s
c) O 1s

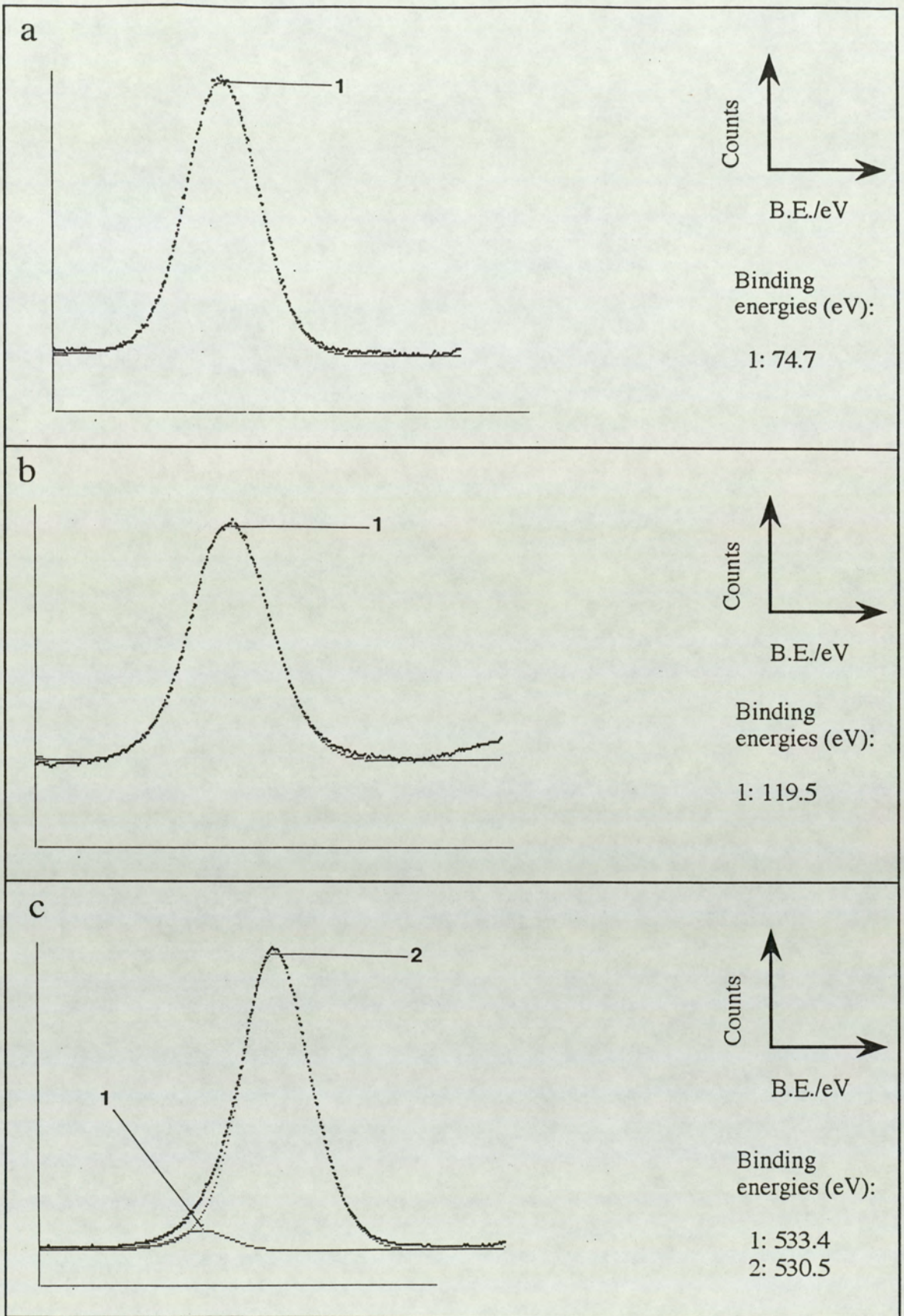

Figure 5.71.

Al_2O_3 surface after 30 minutes of Ar^+ ion bombardment.

a) Al 2p
b) Al 2s
c) O 1s

Table 5.10

Measured binding energy values (±0.2eV) and corresponding FWHM values (±0.2eV) for Al_2O_3. Calibration is with respect to the C 1s peak at 284.6 eV.

identity		core level	binding energy (eV)	FWHM (eV)
Al_2O_3	Al^{III}	2p	74.7	2.3
		2s	119.5	2.7
Oxygen	metal-oxygen bond	1s	530.5	2.2
	surface bound water	1s	533.4	1.9

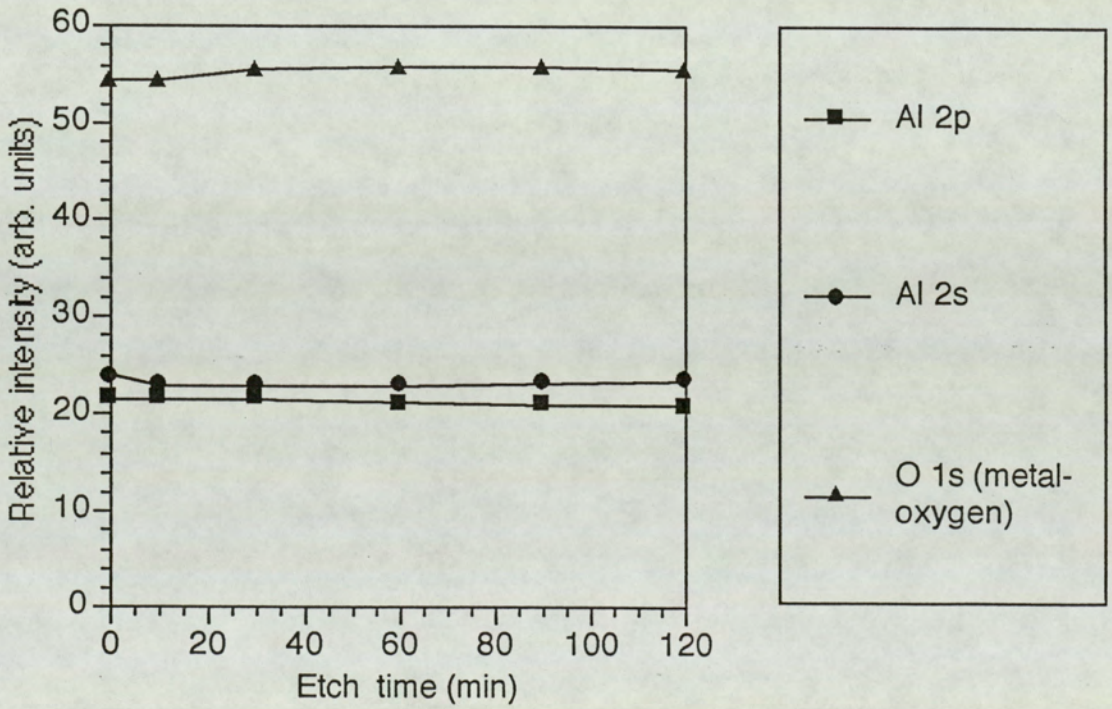

Figure 5.72.

Relative intensity as a function of etch time for Al_2O_3.

1s as a function of etch time. Similar to the case for MgO surface, a small increas in the metal to oxygen intensity ratio can be seen. Table (5.10) lists all the binding energy values.

5.5.12: Summary of the effect of ion bombardment

In any XPS study, the binding energies obtained of the core levels are dependent on the oxidation states of the element. When XPS is applied to definite chemical identifications, as in the investigations of this thesis, a knowledge of the chemical shifts of various elements in approximately the same binding state is desirable. Data available in current literature on the measured shifts for oxides are few and differing. During the investigations here, an attempt was made to accurately define the shifts measured in the various oxidation states of the elements concerned. All binding energies measured have been tabulated.

A reduction effect due to ion bombardment is observed on the transition metal oxides. The reduction path taken is indicated to be as follows:

1) $FeO\,(Fe^{II}) \Rightarrow Fe^{0}$

2) $Fe_2O_3\,(Fe^{III}) \Rightarrow FeO\,(Fe^{II}) \Rightarrow Fe^{0}$

3) $Fe_3O_4\,(Fe^{III}, Fe^{II}) \Rightarrow FeO\,(Fe^{II}) \Rightarrow Fe^{0}$

4) $Co_3O_4\,(Co^{III}, Co^{II}) \Rightarrow CoO\,(Co^{II}) \Rightarrow Co^{0}$

5) $CoO\,(Co^{II}) \Rightarrow Co^{0}$

6) $TiO_2\,(Ti^{IV}) \Rightarrow Ti_2O_3\,(Ti^{III}) \Rightarrow TiO\,(Ti^{II}) \Rightarrow Ti^{0}$

7) $ZrO_2\,(Zr^{IV}) \Rightarrow ZrO\,(Zr^{II}) \Rightarrow Zr^{0}$

8) $Nb_2O_5\,(Nb^{V}) \Rightarrow NbO_2\,(Nb^{IV}) \Rightarrow NbO\,(Nb^{II}) \Rightarrow Nb^{0}$

9) $WO_3\,(W^{VI}) \Rightarrow W_2O_5\,(W^{V}) \Rightarrow WO_2\,(W^{IV}) \Rightarrow W^{0}$

10) $Ta_2O_5\,(Ta^{V}) \Rightarrow TaO_2\,(Ta^{IV}) \Rightarrow TaO\,(Ta^{II}) \Rightarrow Ta^{0}$

For the 'low mass difference' oxides, i.e. MgO and Al_2O_3, The indications are that chemical states other than the original state is not clearly detected after ion bombardmen, although a peak widening of ~0.2 eV is observed for both the Mg 1s and Al 2p peaks. This may be due to ion bombardment induced phase changes of the

oxides.

The next step in this investigation is to quantify the extent of the chemical changes caused to the surface. Hence for each sample, the metal to oxygen surface to bulk concentration ratio, $\{(X_M/X_O)^S/(X_M/X_O)^B\}$, is calculated for the ion bombardment period of 120 minutes. This concentration ratio is a means of quantification of the chemical changes. Table (5.11) shows these ratios of $\{(X_M/X_O)^S/(X_M/X_O)^B\}$ values after 120 minutes of bombardment, for each of the oxides investigated together with the theoretically calculated and experimentally obtained values due to Malherbe et al [47]. Figure (5.73) shows the surface to bulk (X_M/X_O) ratio obtained in this investigation plotted against the corresponding transition metal mass number.

As an example, the steps undertaken in determining the (X_M/X_O) surface to bulk ratio, using the experimental data obtained for Nb_2O_5, are now outlined as follows:

(1) Under steady state conditions, the curve-fitting procedure carried out on the Nb 3d peak yields areas under each of the Nb components for Nb_2O_5, NbO_2, NbO and metallic Nb^0 to be 26400, 19115, 23246 and 1241 units respectively. Hence the constituents are calculated to be 37.7% Nb_2O_5, 27.3% NbO_2, 33.2% NbO and 1.8% Nb^0. Thus the intensity ratio is :

$$Nb^V : Nb^{IV} : Nb^{II} : Nb^0 = 37.7 : 27.3 : 33.2 : 1.8$$

(2) Letting the total number of niobium ions and/or atoms = 1, namely

0.377 part due to Nb_2O_5

0.273 part due to NbO_2

0.332 part due to NbO

0.018 part due to Nb^0

The associated total number of oxygen ions and/or atoms can be found by considering that:

Table 5.11. X_M/X_O surface to bulk ratio found here, compared to Malherbe et al [47].

Sample	cation mass (a.m.u.)	(X_M/X_O) S-B	calc. from ref. [47]	results from ref.[47]
Al_2O_3	27	1	1	1
Mg	24	1	1.09	1
FeO	56	1.18	1.45	1.05
Fe_3O_4	56	1.35	1.44	1.05
Fe_2O_3	56	1.32	1.44	1.05
CoO	59	1.31		
Co_3O_4	59	1.51	1.51	1.33
TiO_2	48	1.29	1.32	1.5
ZrO_2	91	1.3	1.81	2.26
Nb_2O_5	93	1.38	2.04	2.22
WO_3	184	1.42		
Ta_2O_5	181	1.45	2.56	2.5

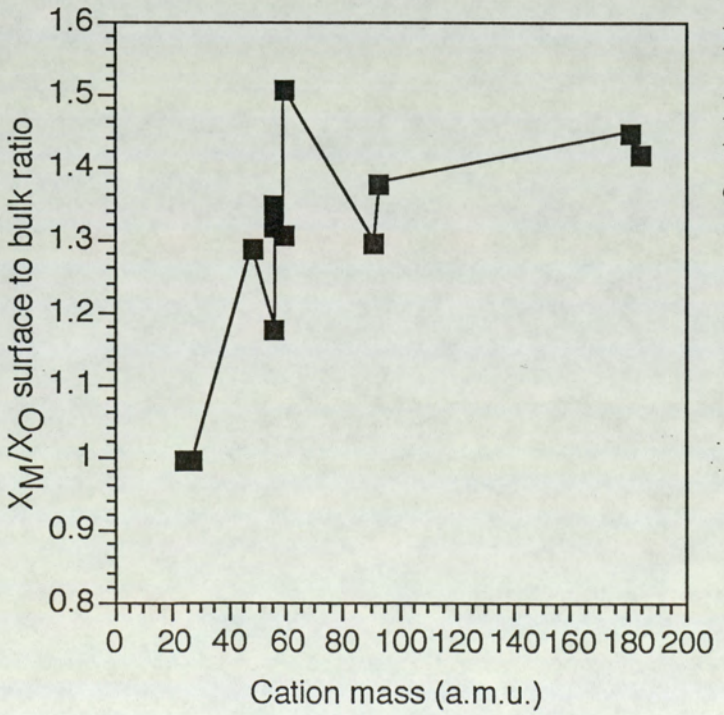

Figure 5.73.

Measured X_M/X_O surface to bulk ratio as a function of cation mass.

each Nb in Nb_2O_5 has 5/2 associated oxygen atoms

each Nb in NbO_2 has 2 associated oxygen atoms

each Nb in NbO has 1 associated oxygen atom

each Nb in Nb^0 has no associated oxygen atom.

(3) Hence the total number of associated oxygen atom is given by:

$\{(5/2 \times 0.377) + (2 \times 0.273) + 0.332\} = 1.82$

This yields a value for $(X_M/X_O)^S$ to be (1/1.82) and the $\{(X_M/X_O)^S/(X_M/X_O)^B\}$ ratio to be 1.375. This ratios can be determined in a similar manner for the other oxides.

(4) Calculation of the (X_M/X_O) surface to bulk ratio using the above method eliminates the need for the use of various atomic sensitivity factors and thus removing unnecessary errors.

5.5.13: Comparisons of linear and non-linear background subtraction

Figures (5.74) and (5.75) show some curve-fitted spectra from Nb_2O_5 and TiO_2 samples respectively. These are the spectra that have been measured after ion bombardment with a beam energy of 5 keV and current density of 56 mA/m^2. Figure (5.74) show the Nb 3d spectra after 10 minutes of bombardment and figure (5.75) show the Ti 2p spectra after 2 minutes of bombardment. Thus, figure (5.74) shows the same spectra as shown in figure (5.50a), but the curve-fitting is carried out after employing a non-linear background subtraction. Comparing these two figures it is seen that for the case of the Nb_2O_5, the type of background subtraction employed does not have a profound effect on the intensities and the appearence of the reduced states. The maximum variation in intensities obtained from the two modes of background subtraction is approximately 6% which is comparable to experimental errors.

However, for the case of the TiO_2, it can be seen that the non-linear subtraction under-estimates the background at the low binding energy side of the peak (figure (5.75) shows the same spectra as that shown in figure (5.36), but for the case of a non-linear background subtraction). The effect of this on the results obtained with

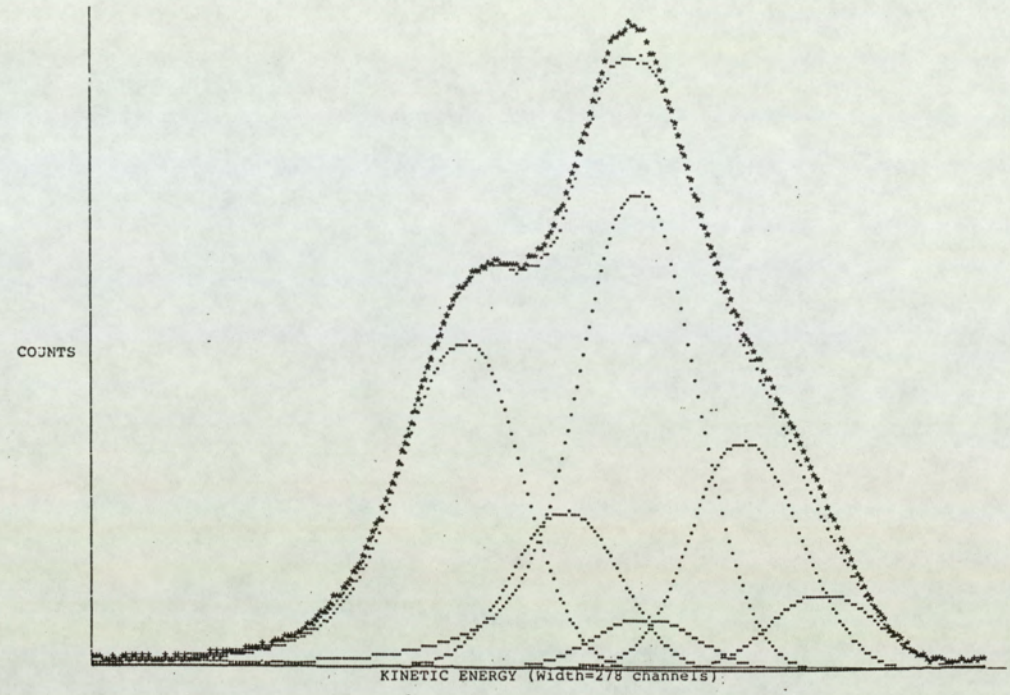

Figure 5.74.

Nb 3d spectra showing curve-fitting results after a non-linear background substraction.

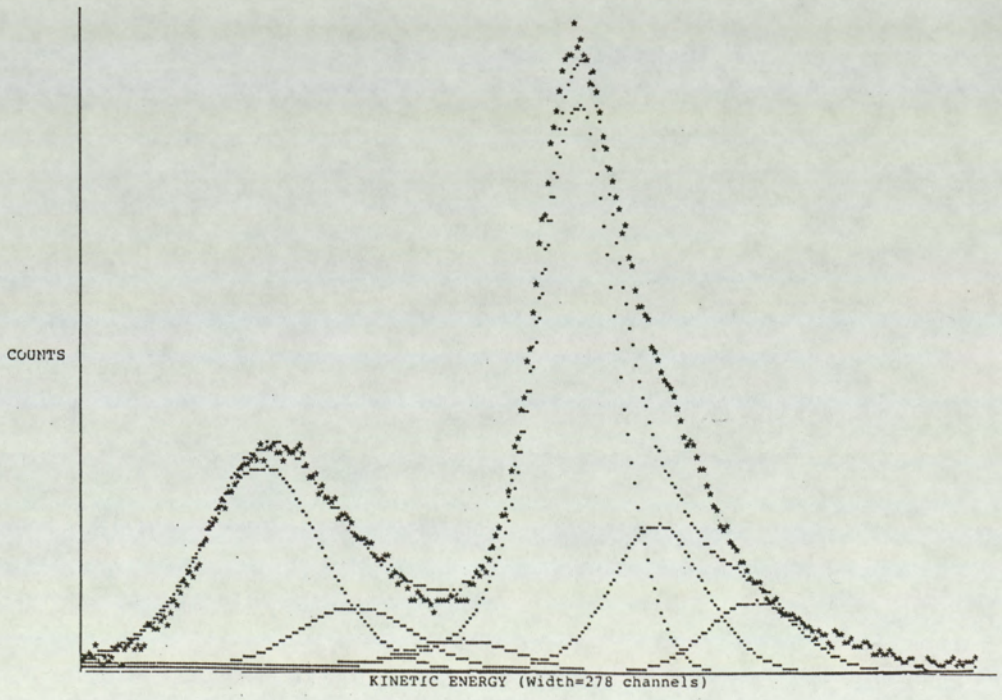

Figure 5.75.

Ti 2p spectra showing curve-fitting results after a non-linear background substraction.

the unetched surface where only one state is present is not too drastic. However, after the surface is subjected to ion bombardment, when other chemical states appear in the peak profile, the under-estimation of the background at the low binding energy side can lead to significant errors in the measured intensities and also perhaps indicating falsely the existence of reduced states within a short bombardment period of 2 minutes. For this thesis, it is critical that no uncertainty exists with regard to the presence of reduced states. It is necessary that any implications casting doubts to the presence or origin of the reduced states is eliminated. Observation of the Ti 2p peak after a linear line subtraction indicates an underestimation of the background at the high energy side of the peak. The generated peak envelope, superimposed on the experimental peak leaves gaps on the high energy side due to contributions of the the low energy loss electrons not being subtracted. It is thought that the errors in the intensities due to this are negligible for the purpose of this thesis and a non-linear background subtraction was thus decided to be employed.

For the cases with oxides of iron and cobalt, it is found that a non-linear background subtraction is necessary. The peak shapes for the 2p peaks are too assymmetric for obtaining meaningful curve-fit results after carrying out a linear subtraction. Figures (5.76a,b) show the Fe 2p spectra for the unbombarded bulk Fe_2O_3 surface and after 10 minutes of bombardment. The assymetric peak shapes and the high background at the low kinetic energy side of the peak is clearly visible.

5.6: The dependency of the extent of surface chemical changes on the primary beam energy and current density

A series of experiments were carried out on the oxides α-Fe_2O_3, TiO_2, Nb_2O_5, ZrO_2 and WO_3 to investigate the effect of beam energy variation and current density variation to the extent of chemical changes caused. For the set of experiments investgating the effect of beam energy variation, the current density was kept constant at ~28 mA/m^2. Similarly, the incident beam energy was kept constant at 5 keV during the investigations carried out to observe the effect of current density variation. The

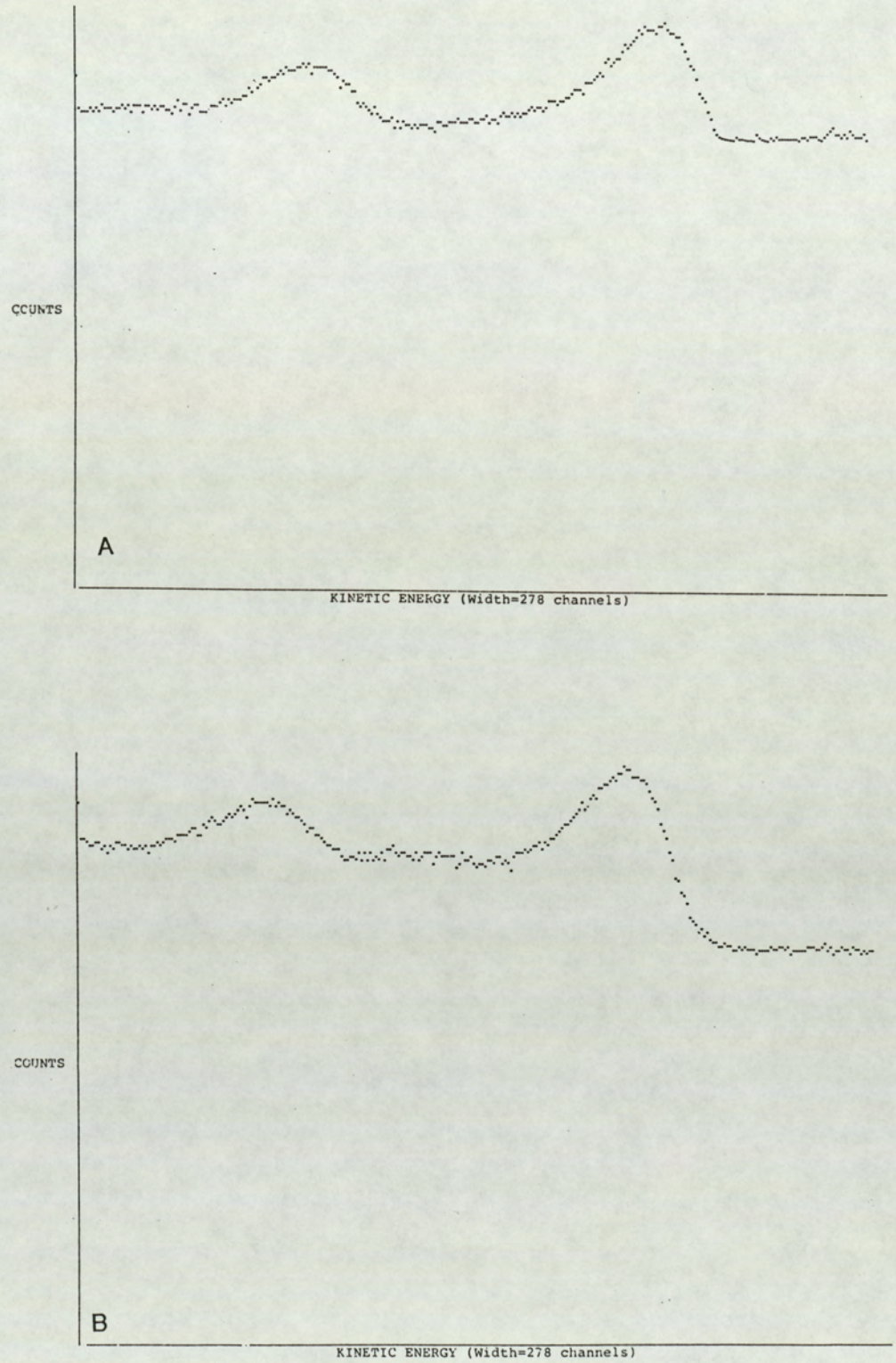

Figure 5.76.

The raw data from Fe 2p spectra, showing :
a) unbombarded surface
b) after 10 minutes of bombardment.

ranges of beam energy and current density, for each of the oxides concerned, has already been described in chapter 4.

In each experiment, the percentage relative intensites of the various metal components in the spectrum have been measured using the most intense photo-electron line. Thus, for example, for the Nb_2O_5 samples the Nb 3d ($_{3/2,\ 5/2}$) doublet contribution for each of the states Nb^V, Nb^{IV}, Nb^{II} and Nb^0 have been considered such that the percentage relative intensity of the Nb^V component is given by:

$$\frac{\text{relative intensity of}}{\text{the } Nb^V \text{ component}} = \frac{I(Nb^V) \times 100}{\{ I(Nb^V) + I(Nb^{IV}) + I(Nb^{II}) + I(Nb^0) \}}$$

Where the intensity, I(x), of the different components is obtained after employing the curve synthesis procedure on the Nb 3d doublet. This percentge relative intensity is calculated using the XPS results of both the $3d_{3/2}$ and $3d_{5/2}$ lines and an average of these two values obtained and tabulated. Similarly the relative intensities of the components Nb^{IV}, Nb^{II} and Nb^0 are also obtained and tabulated. The variations in these relative intensities can be regarded as indications of the degree of chemical reduction created on the oxide surfaces.

In the following a survey of the results of XPS depth profiling for the variations of beam parameters (i.e., energy and current density) is reported, in the order of carrying out the investigations:

5.6.1: Nb_2O_5

a) Beam energy dependency

As mentioned before, for each of the states Nb^V, Nb^{IV}, Nb^{II} and Nb^0, the relative intensities have been determined after each experiment. Figure (5.77a) shows a graph of the relative intensity of Nb^V ions in Nb_2O as a function of bombardment time for the different beam energies considered. A decrease in the Nb^V state is observed due

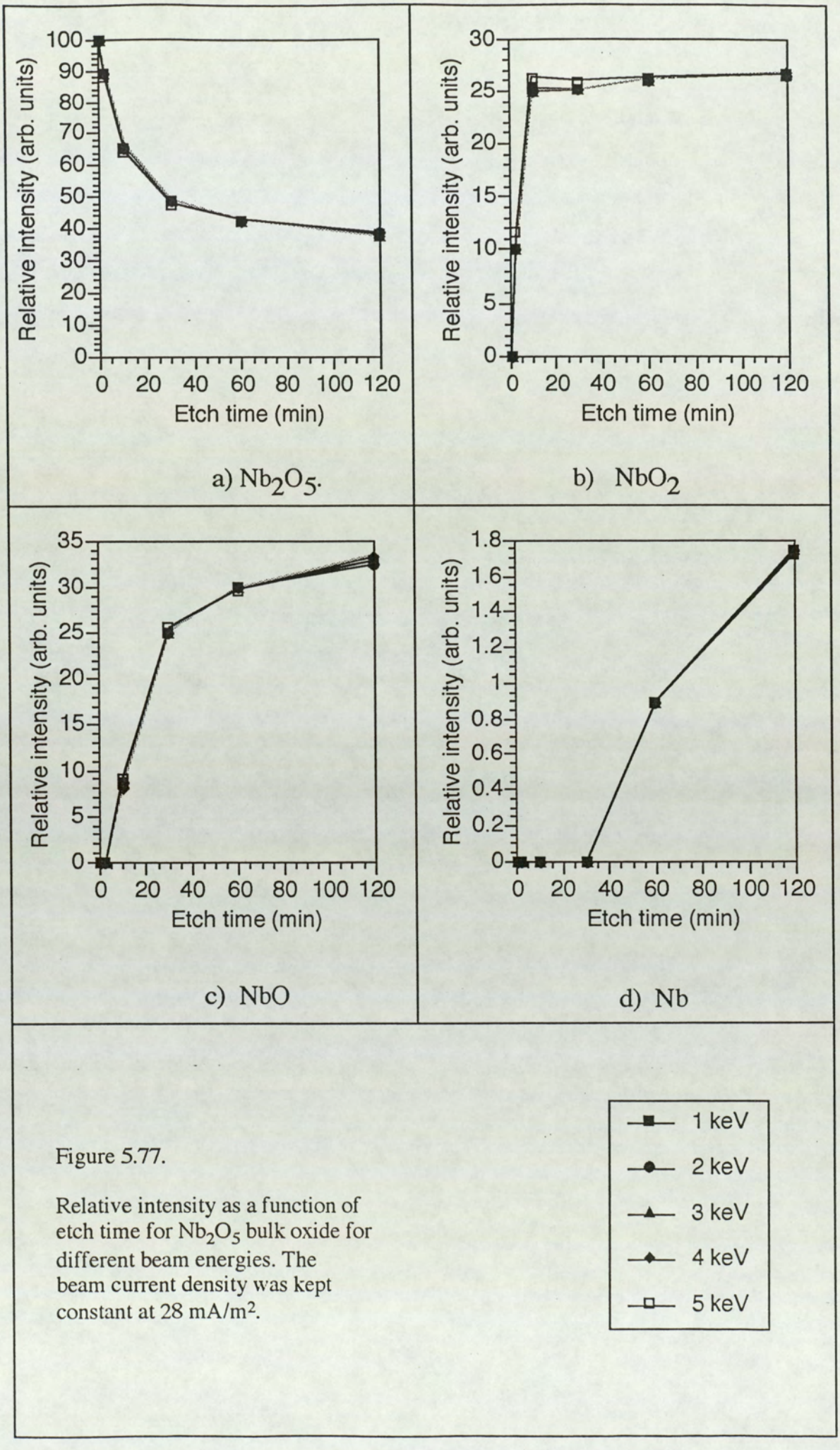

Figure 5.77.

Relative intensity as a function of etch time for Nb_2O_5 bulk oxide for different beam energies. The beam current density was kept constant at 28 mA/m^2.

to beam induced reduction untill a steady state condition is reached after approximately 120 minutes of bombardment. It is thus evident that in this primary energy range (i.e, 1 to 5 keV), the time taken to reach steady state is independent of beam energy. Also, at each bombardment period, very little or no changes in relative intensity with beam energy is observed. Maximum variation at the steady state being ~3% which is well within the range of experimental errors that may be expected for measured XPS intensities.

Figures (5.77b, c and d) show the appearence and growth of the sub-oxides NbO_2, NbO and the metallic state Nb^0 respectively. The surface sputtering time necessary for the appearence of each of these reduced states is found to be the same for all the primary energies investigated. Again, time taken to reach steady state is found to be constant with primary energy and the maximum variations in relative intensities obtained at steady state are 1.3%, 2.9% and 1.7% for Nb^{IV}, Nb^{II} and Nb^0 states respectively (which are again well within experimental errors). Another important aspect is that this negligible relative intensity variation is purely random and not related to the primary energies, i.e, the maximum variation is not obtained for the minimum and maximum primary energies.

Thus, the results obtained show no significant changes on the extent of the chemical changes with varying the primary energy for the range considered.

b) Dependency on ion current density

For a constant primary energy of 5 keV the current density is varied between 8 to 139 mA/m^2. The time taken for each of the ionic states to reach steady state in this case is found to be inveresely related to the current density. Figure (5.78a) shows the decrease in relative intensity of the Nb^V state as a function of bombardment time. At the lowest current density of 8 mA/m^2, up to 120 minutes of bombardment is not sufficient to reach steady state conditions. Also, after 120 minutes, minimum reduction (and removal) of the Nb^V ion is observed for the lowest current density.

Between the current densities of 8 and 28 mA/m^2, a significant increase in the

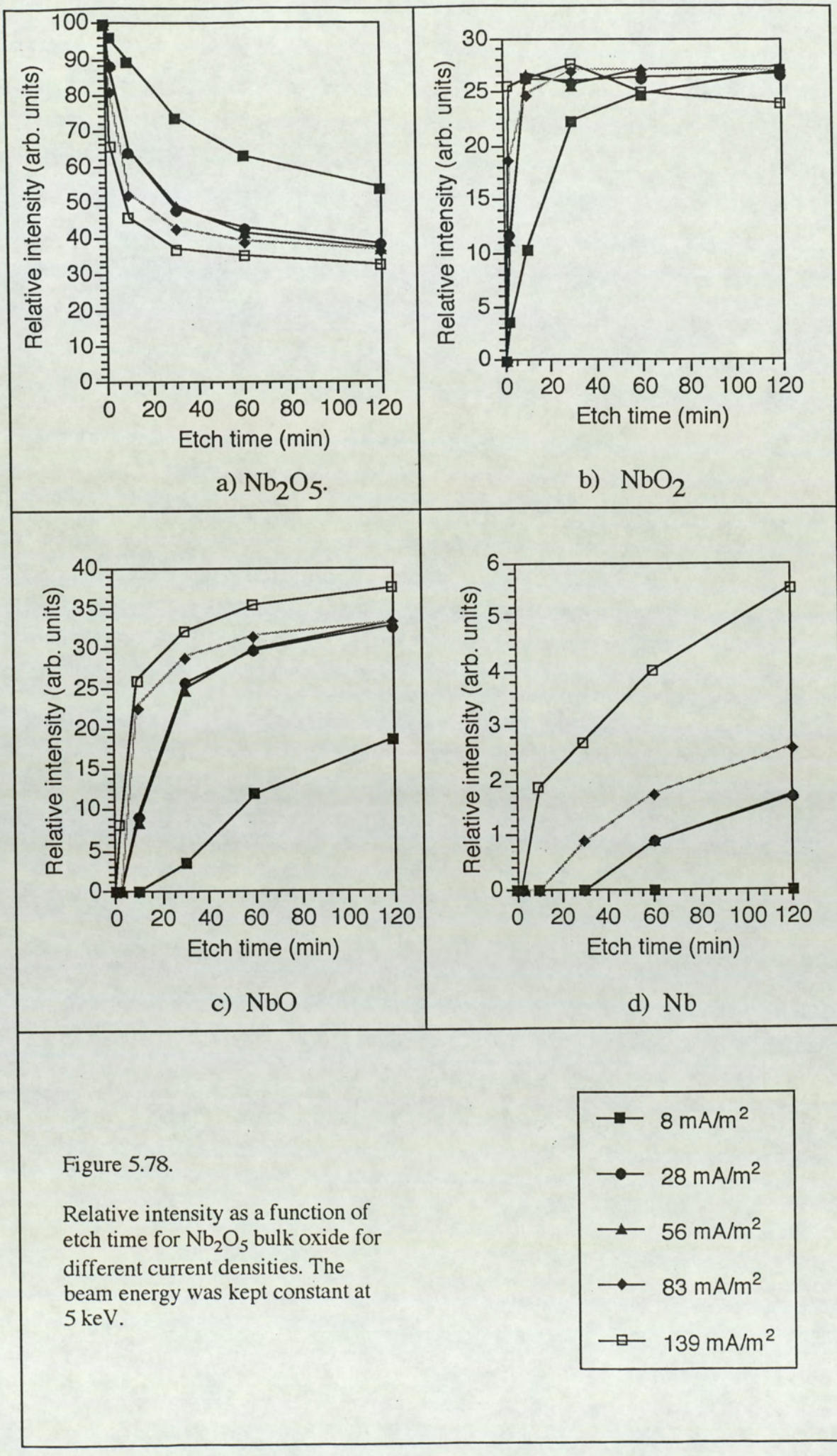

Figure 5.78.

Relative intensity as a function of etch time for Nb_2O_5 bulk oxide for different current densities. The beam energy was kept constant at 5 keV.

reduction of the Nb^{V} state can be seen. However, at 28 and 56 mA/m^2, the intensity reductions are found to be quantitatively similar. Further increases in current density to 83 mA/m^2 and 139 mA/m^2 showed additional relative intensity reduction of the original ionic state. These findings do not imply that the amount of chemical damage produced on the surface is the same between the current densities 28 and 56 mA/m^2, as consideration of all four states (i.e, Nb^{V}, Nb^{IV}, Nb^{II} and Nb^{0}) is required to determine the quantity of surface damage for any given bombardment condition.

Figures (5.78b, c and d) show the relative intensities of the respective metal components in the sub-oxides NbO_2, NbO and the metallic state Nb^{0} versus bombardment time, for the range of the current densities mentioned. Considering figure (5.78b), a number of observations can be made. Most importantly, it is seen that increase in current density decreases the etching time required for the appearence of the Nb^{IV} state. For the current densities of 8, 28 and 56 mA/m^2, after the appearence of the Nb^{IV} state, a gradual increment in its relative intensity can be observed until steady state is reached. However, for the higher current densities, the relative intensity of the Nb^{IV} state initially increases rapidly and then decreases. This indicates the occurence of reduction to the Nb^{IV} state itself. The extent of chemical damage to the Nb^{IV} state can be seen to be highest for the maximum current density of 139 mA/m^2.

The pattern for the rate of increment of the Nb^{II} ion in NbO, figure (5.78c), is found to be similar to the rate of reduction of the Nb^{V} ion in Nb_2O_5. The etch time necessary for the relative intensity of the Nb^{II} to reach a steady state is found to vary inversely with current density. Similarly, for the case of the lowest current density employed, up to 120 minutes of bombardment is not sufficient for steady state condition to be attained. Again, the relative intensities for Nb at steady state can be seen to be approximately the same at 28 and 56 mA/m^2.

The variations in relative intensity (after a given bombardment period) as a function of current density for the metallic niobium state (figure (5.78d)) follows similar pattern as those due to the three oxidation states already discussed. Reduction

to the metallic state is not observed at the lowest current density of 8 mA/m^2. At current densities of 28 and 56 mA/m^2, the relative intensities of Nb^0 are the same. Further increase in current density increases the relative intensity.

c) Accumulative effect

As mentioned previously in the last section, the resulting relative intensities with varying bombardment time for one state alone is not adequate to give a full account of the extent of absolute surface chemical changes. A full quantitative consideration of all the reduced states in addition to the corresponding original state data is necessary. Thus, to quantify the degree of damage caused on the surface, the metal to oxygen surface to bulk concentration ratio, $\{(X_M/X_O)^S/(X_M/X_O)^B\}$, is calculated using the procedure described in section 5.5. These results are presented in figures (5.79a,b) which show the values plotted against corresponding etch times for the different beam energies and beam current densities respectively.

The summary of the results is that the amount of chemical damage created to the surface at a constant current density is found to be approximately independent of the beam energy in the range 1 to 5 keV. However, for the variation of current density within the range 8 to 139 mA/m^2, the extent of surface chemical damage is found to increase with current density. To confirm these findings a third set of experiments were carried out for the current density variation (8 to 83 mA/m^2) at a lower constant beam energy of 2 keV. The results obtained shows the same trends as those for the set of experiments carried out at the constant beam energy of 5 keV.

The $\{(X_M/X_O)^S/(X_M/X_O)^B\}$ values obtained after 120 minutes of ion bombardment (a steady state of the surface altered layer is reached after this bombardment period) are plotted as a function of the beam energy in figure (5.80a), and as a function of beam current density in figure (5.80b). Figure (5.80b) also displays the current density variation results at the lower constant beam energy of 2 keV. For these constant primary energy cases, the variations in the (X_M/X_O) surface to

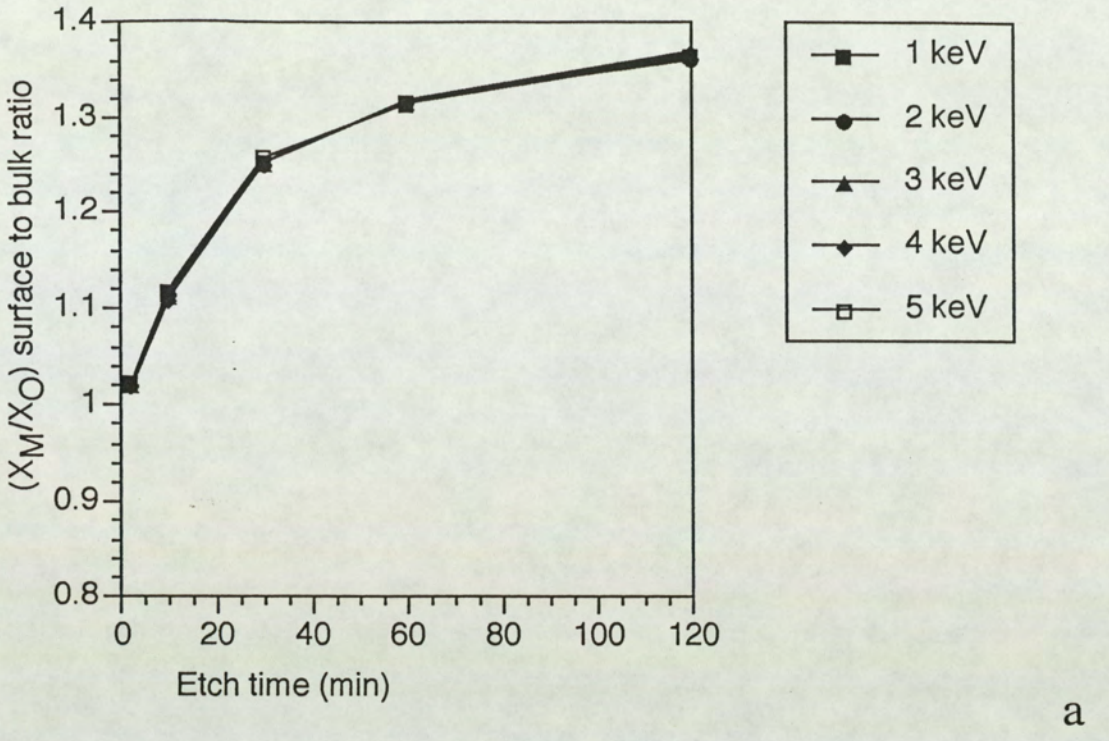

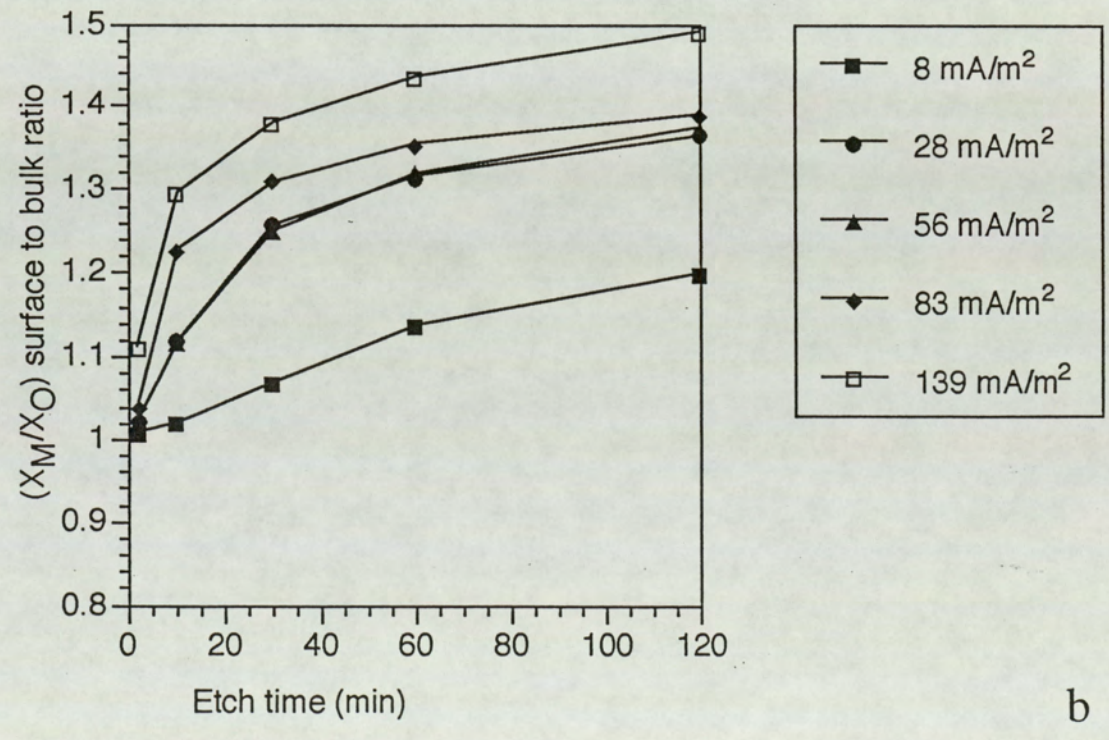

Figure 5.79.

Nb_2O_5 (X_M/X_O) surface to bulk ratio as a function of etch time.

a) current density; 28 mA/m_2, various beam energies

b) beam energy: 5 keV various curent densities

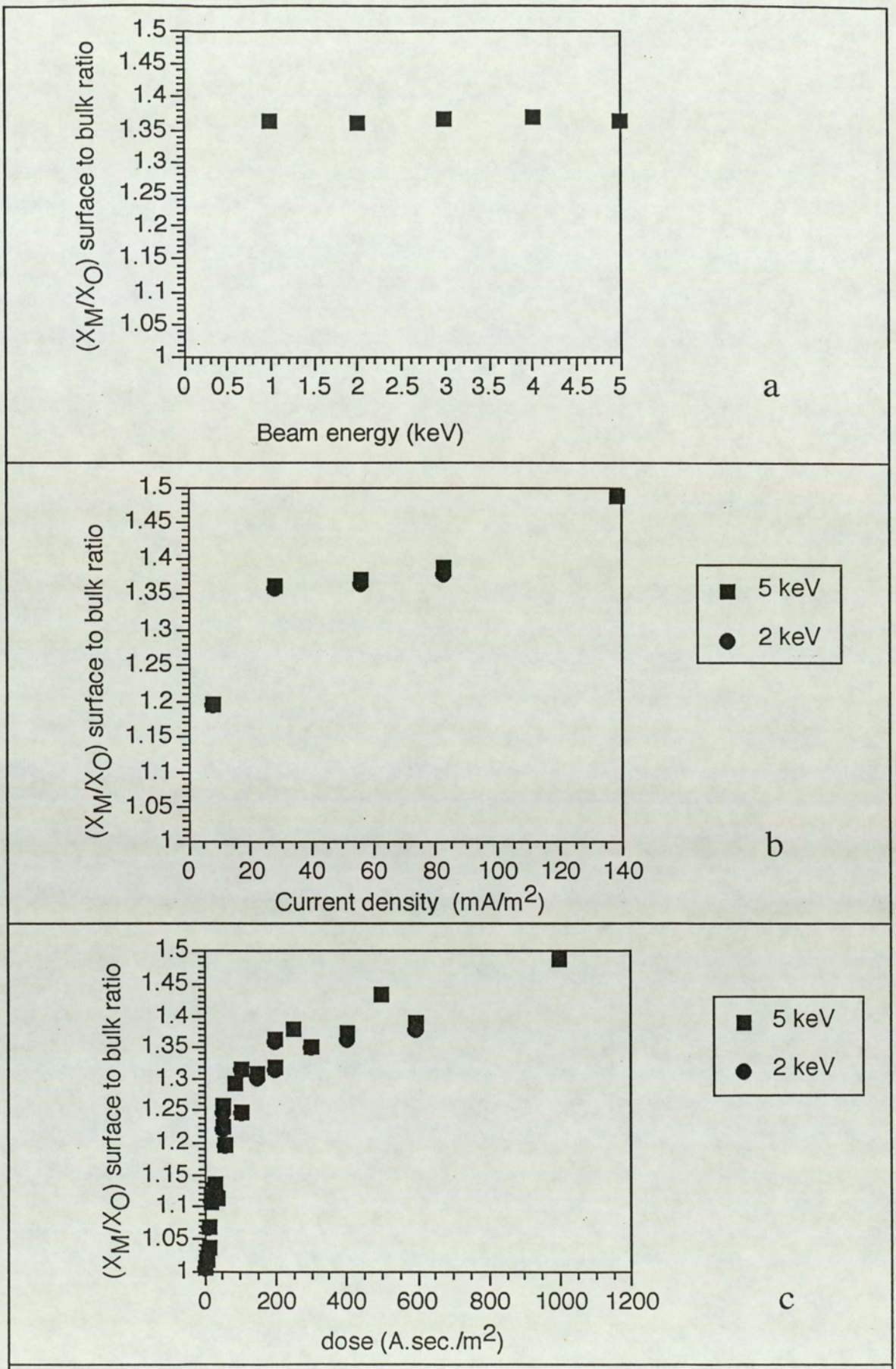

Figure 5.80.
Nb_2O_5 (X_M/X_O) surface to bulk ratio as a function of :

a) beam energy
b) current density (for 120 min. etch duration)
c) dose

bulk ratio ratio are found to be less than 1%. This value is well within the typical range of experimental errors that may be expected in quantitative surface analysis using XPS. Hence a single curve is drawn to demonstrate the variation of (X_M/X_O) surface to bulk ratio with beam current density. The ratio initially increases rapidly with current density and then gradually towards a steady state situation; although a plateau has not yet been attained for the highest current density of 139 mA/m^2.

Since it has been established that variation of beam current density has an effect on the extent of the chemical damage on the surface, it was decided to differentiate whether this relationship is current density dependent or dose dependent. For each of the constant beam energies (5 and 2 keV) the surface to bulk (X_M/X_O) ratio is then plotted against the corresponding primary ion dose. The dose value is obtained by multiplying the current density with the exposure time; i.e:

Dose = Current density x bombardment time

Figure (5.80c) shows the graph of surface to bulk (X_M/X_O) ratio against dose; the variation observed in the concentration ratio is similar to that with current density at the given bombardment period of 120 minutes. Thus a dose dependency has been clearly established.

5.6.2 TiO_2

The effect of beam energy and current density variation with TiO_2 is found to be very similar to that with Nb_2O_5. Figure (5.81a) show the variation in relative intensity of the Ti^{IV} state with etch time for the range of different primary energies between 1 to 5 keV (keeping the current density constant at 28 mA/m^2). All the relative intensities have been calculated using the Ti 2p spectrum considering both the $2p_{1/2}$ and $2p_{3/2}$ contributions and then taking the average value. The time necessary for the Ti^{IV} intensity to reach steady state is found to be the same for each of the energy cases. After a bombardment period of 120 minutes the Ti^{IV} relative intensity has changed by ~2.6%, clearly suggesting that the extent of the surface chemical changes for titanium pentaoxide does not depend on the energy (within the energy range considered).

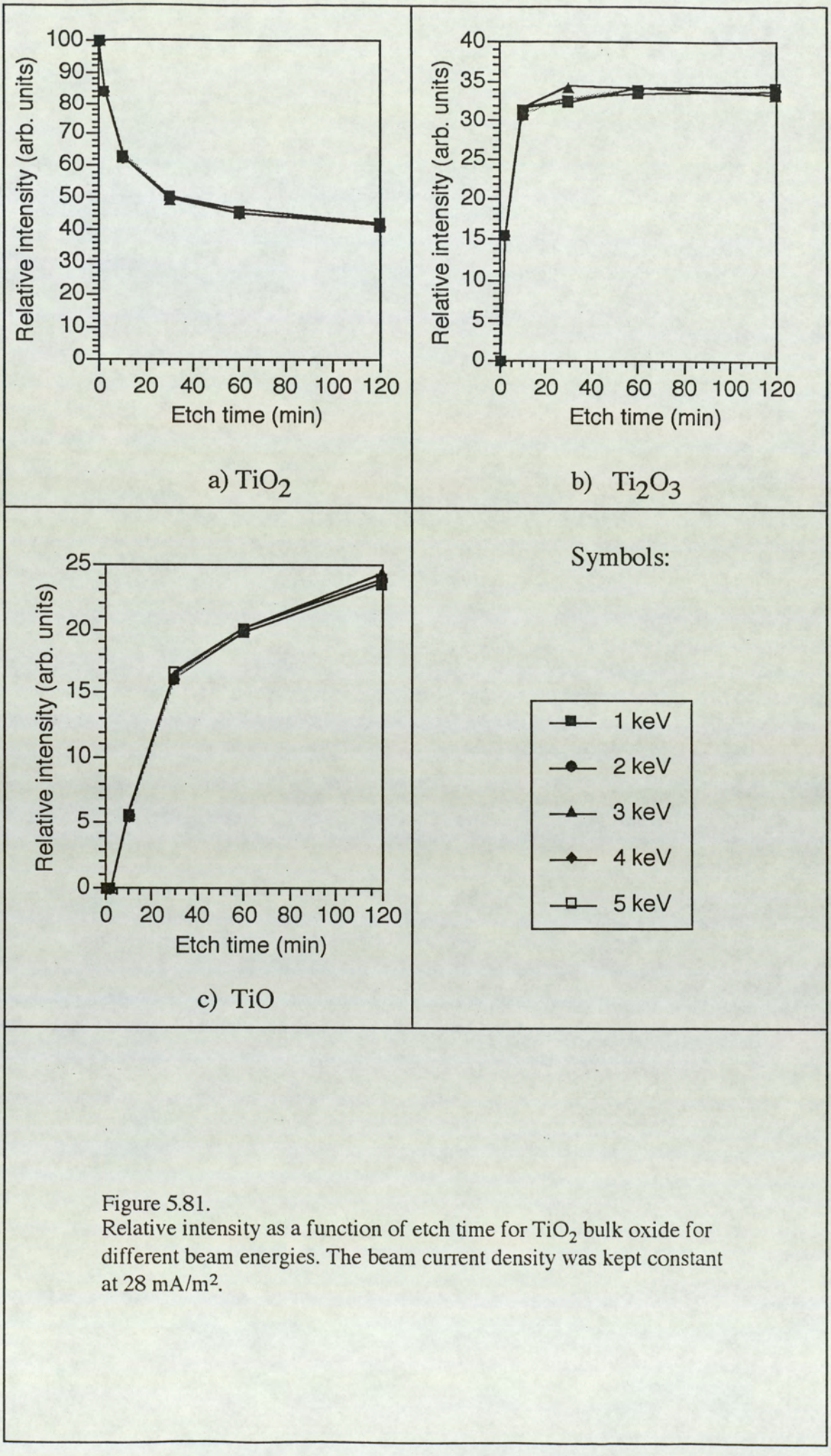

Figure 5.81.
Relative intensity as a function of etch time for TiO_2 bulk oxide for different beam energies. The beam current density was kept constant at 28 mA/m^2.

Figures (5.81b, c) show the corresponding Ti^{III} and Ti^{II} relative intensities plotted against the etching times. The same conclussions as above can be made. After 120 minutes, the maximum variations in the Ti^{III} and Ti^{II} relative intensities are 2.9% and 3.2% respectively; which is well within the range of experimental errors that can be expected.

Figure (5.82a) shows the relative intensities due to the Ti^{IV} state as a function of etch time for the different current densities used (each experiment was carried out at a constant beam energy of 5 keV). An increase in the chemical reduction in the TiO_2 state can be observed the beam current density is increased from 8 mA/m^2 to about 83 mA/m^2. Further increase of the current density to 111 mA/m^2 and eventually to 139 mA/m^2 yields a rate of reduction of the Ti^{IV} state approximately the same as that for 83 mA/m^2.

The corresponding current density variation results for the Ti_2O_3 and TiO states can be seen in Figures (5.82b,c). Similar to the case of The Nb_2O_5 samples, the etch time, after which the first reduced state (i.e. Ti_2O_3) appears on the surface, decreases with increasing current density. The second important aspect that can be observed in figure (5.83b) is that with increasing current density, increased chemical damage to the Ti_2O_3 state itself is also achieved. This damage to the Ti_2O_3 state is lowest for the lowest value of the current density (8 mA/m^2). The etch time required for the appearence of the second (and final) state, i.e. TiO, is again seen to be dependent on the current density. For the current densities of 139, 111, 83 and 56 mA/m^2 a steady state of the relative intensity value seems to have been obtained within 120 minutes of bombardment whereas for 28 and 8 mA/m^2 the indication is that further increase in bombardment time would increase the relative intensity.

A third set of experiments carried out on the TiO_2 powder surface, at a constant beam energy of 2 keV but for the different current densities of 8, 28, 56 and 83 mA/m^2, yields the same conclusions as described above for the constant beam energy case of 5 keV. This set of experiments for the variation of current density at the

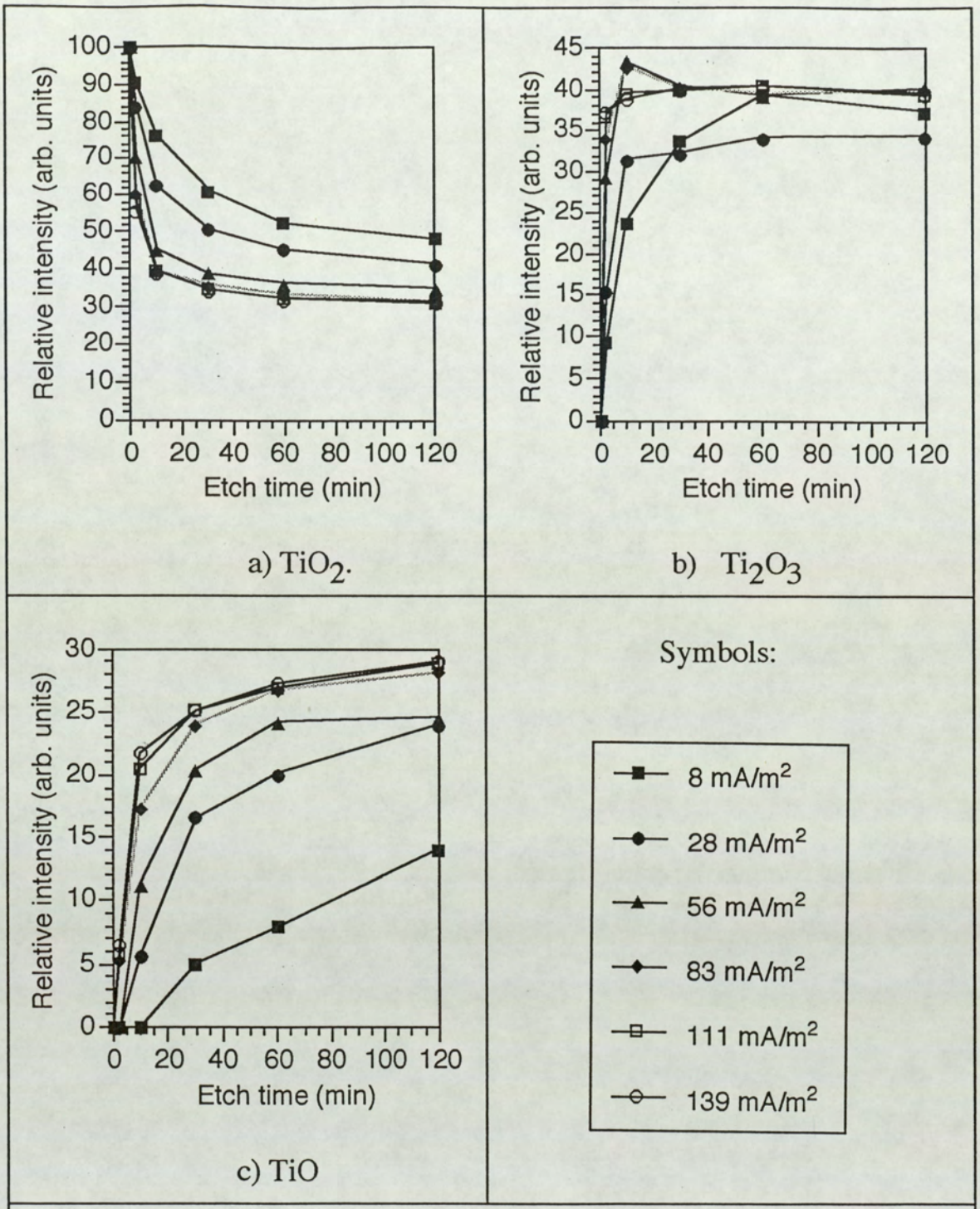

Figure 5.82.

Relative intensity as a function of etch time for TiO_2 bulk oxide for different current densities. The beam energy was kept constant at 5 keV.

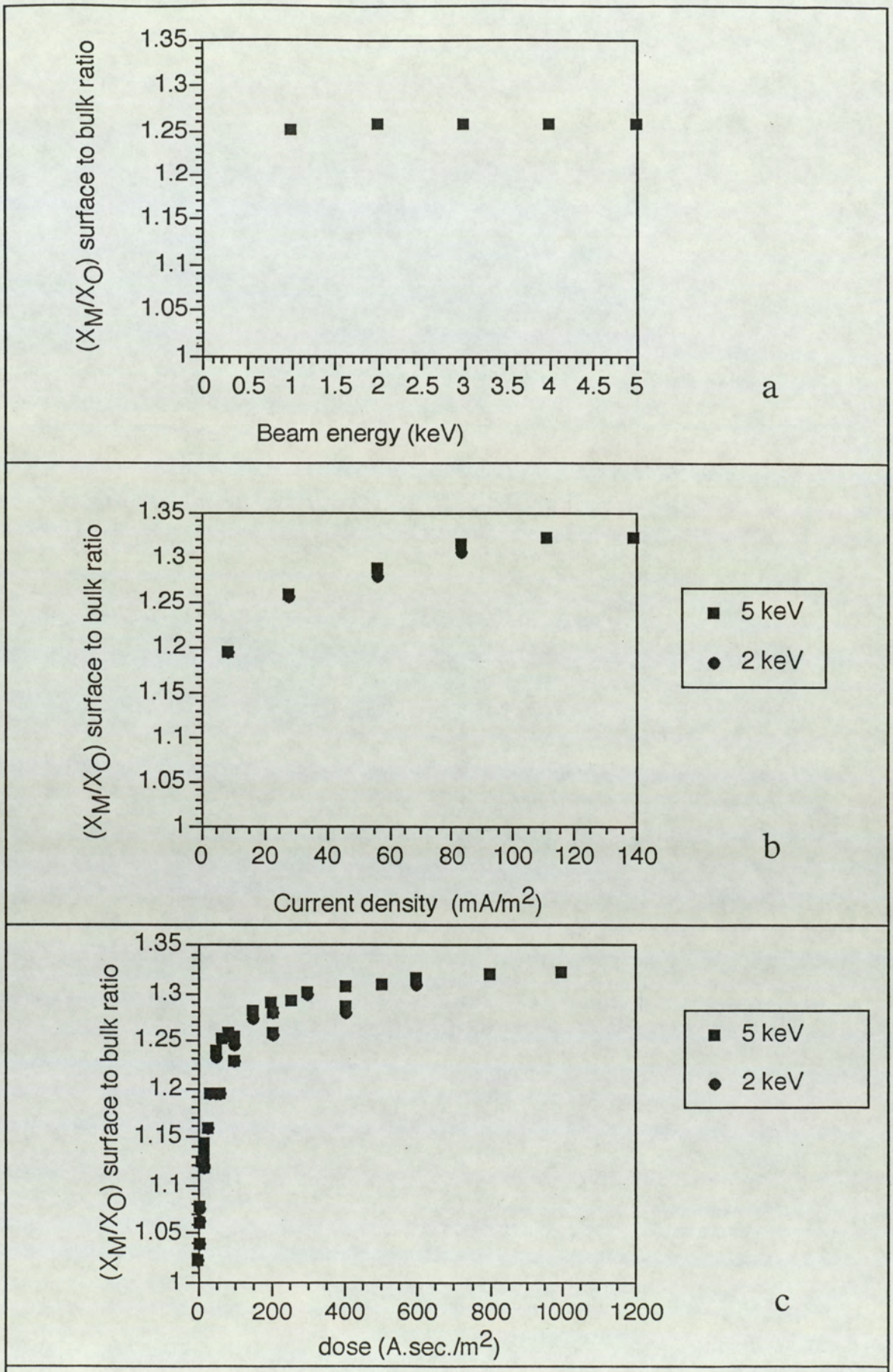

Figure 5.83.
TiO_2 (X_M/X_O) surface to bulk ratio as a function of :

a) beam energy
b) current density (for 120 min. etch duration)
c) dose

lower beam energy has been carried out to confirm the results obtained for the variation of the beam energy.

For the three set of experiments described above, i.e. beam energy variation at 28 mA/m^2, current density variation at 5 keV and at 2 keV the concentration ratios of $\{(X_M/X_O)_S/(X_M/X_O)_B\}$ are measured. Figures (5.83a,b) show this ratio plotted against beam energy and current density respectively. In figure (5.83b) the values obtained for both the constant beam energies 5 and 2 keV can be seen; a single curve is drawn as the maximum diffenence in the $\{(X_M/X_O)_S/(X_M/X_O)_B\}$ concentration ratio for the two sets is found to be ~%0.7. Figure (5.83c) shows the $\{(X_M/X_O)_S/(X_M/X_O)_B\}$ concentration ratio plotted against the corresponding dose value. A dose dependency of the extent of surface chemical changes is clearly established.

5.6.3: Fe_2O_3

Figures (5.84a, b, c) show the relative intensity as a function of etch time for the original oxide Fe_2O_3 and the reduced oxide FeO and the metallic state Fe^0 respectively for the range of beam energies between 1 to 5 keV. The relative intensities of each of these states are independent of the beam energy. These relative intensities have been calculated using the Fe $2p_{3/2}$ line. Figures (5.85a, b, c) show the relative intensity plotted against etch times for the above chemical states, for the various current densities between 8 to 139 mA/m^2. Similar to the case for the Nb_2O_5 and TiO_2 samples, significant increase in chemical reduction is observed with increasing current density.

To quantify the above results in terms of the metal to oxygen concentrations the surface to bulk ratio, i.e, $\{(X_M/X_O)^S/(X_M/X_O)^B\}$, is determined for each bombardment time. Figure (5.86a) shows this ratio plotted against beam energy for the steady state case (i.e., after 120 minutes of bombardment). The overall effect is that the quantity of chemical damage is constant with primary energy for the range considered.

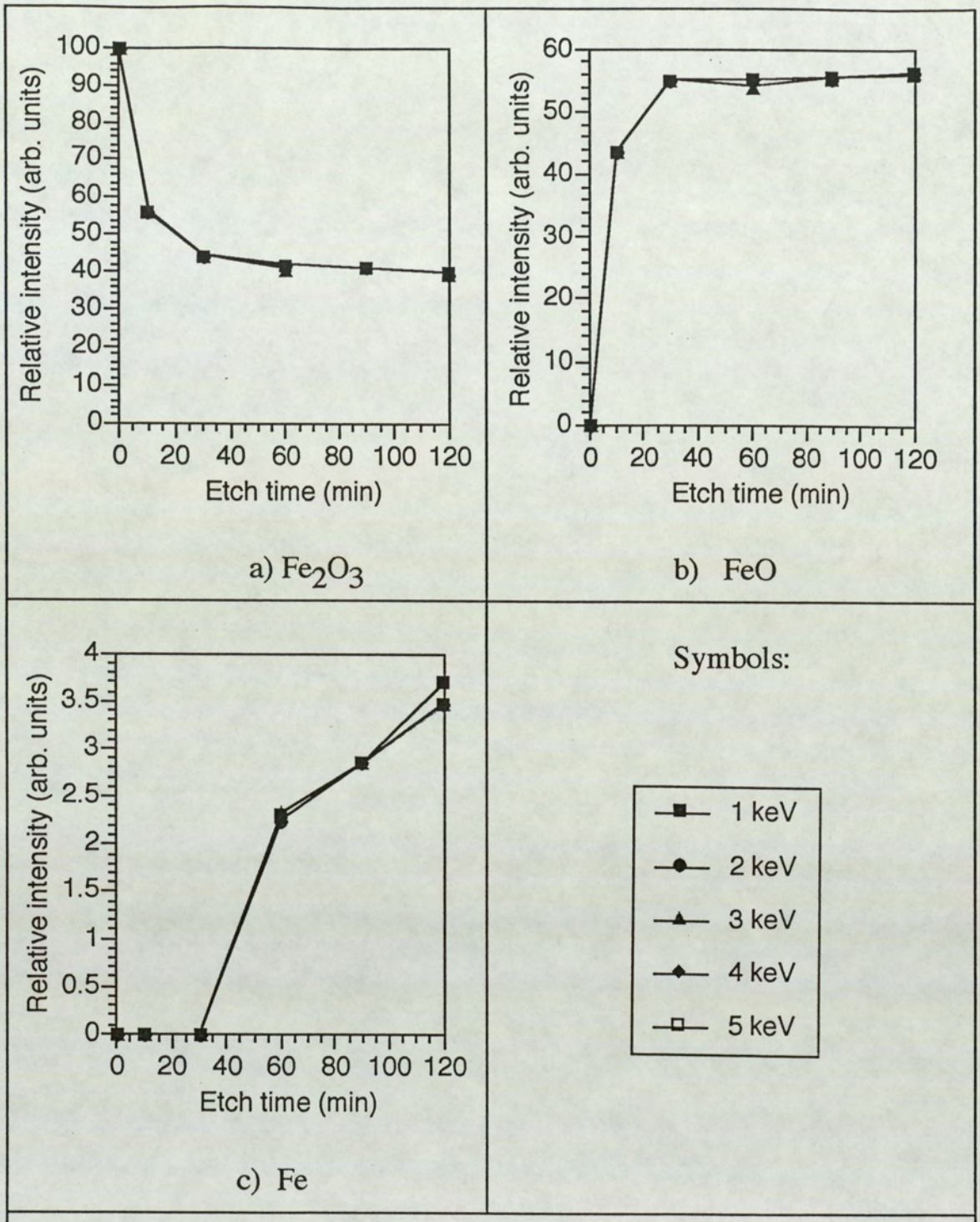

Figure 5.84.
Relative intensity as a function of etch time for Fe_2O_3 bulk oxide for different beam energies. The beam current density was kept constant at 28 mA/m^2.

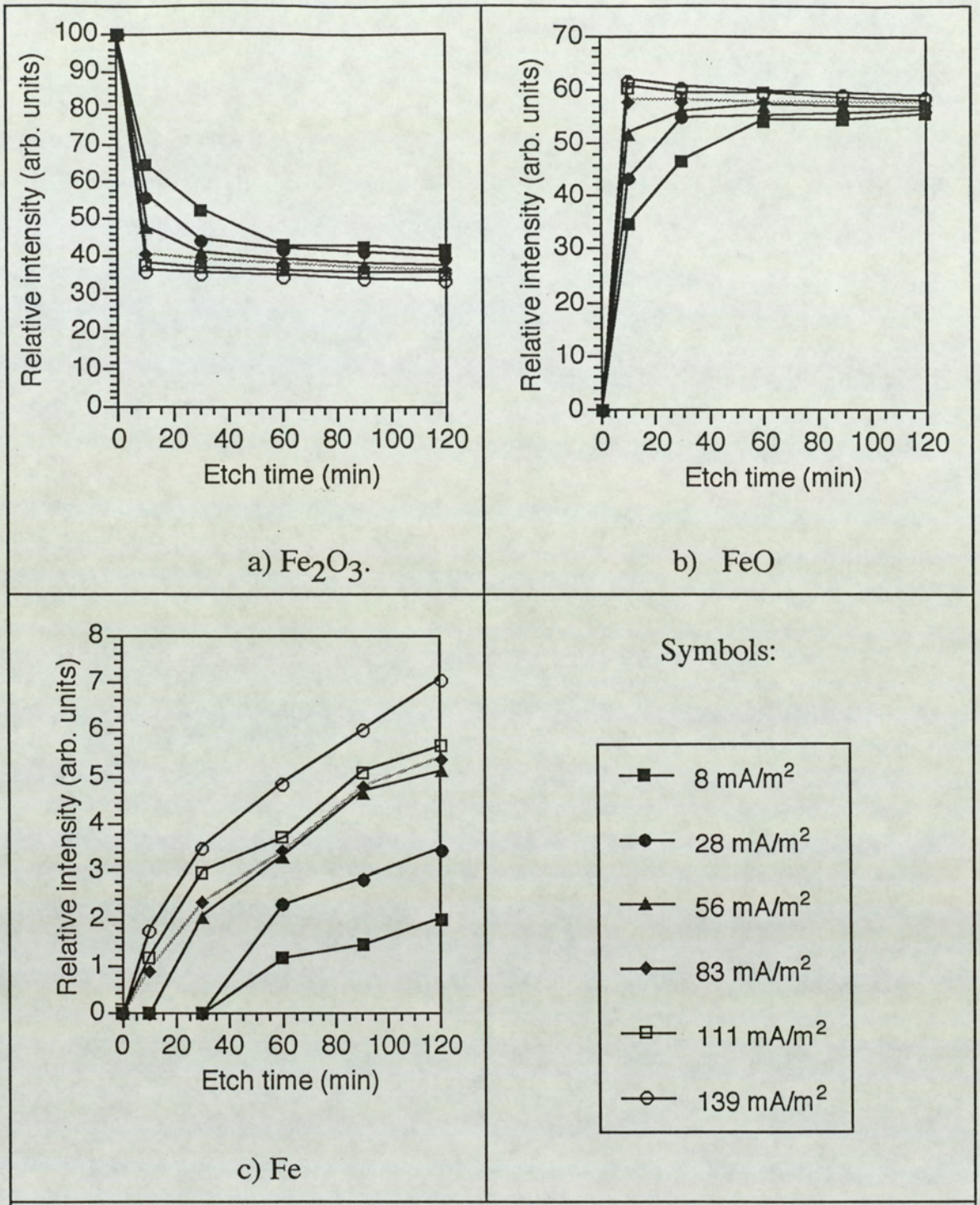

Figure 5.85.

Relative intensity as a function of etch time for Fe_2O_3 bulk oxide for different current densities. The beam energy was kept constant at 5 keV.

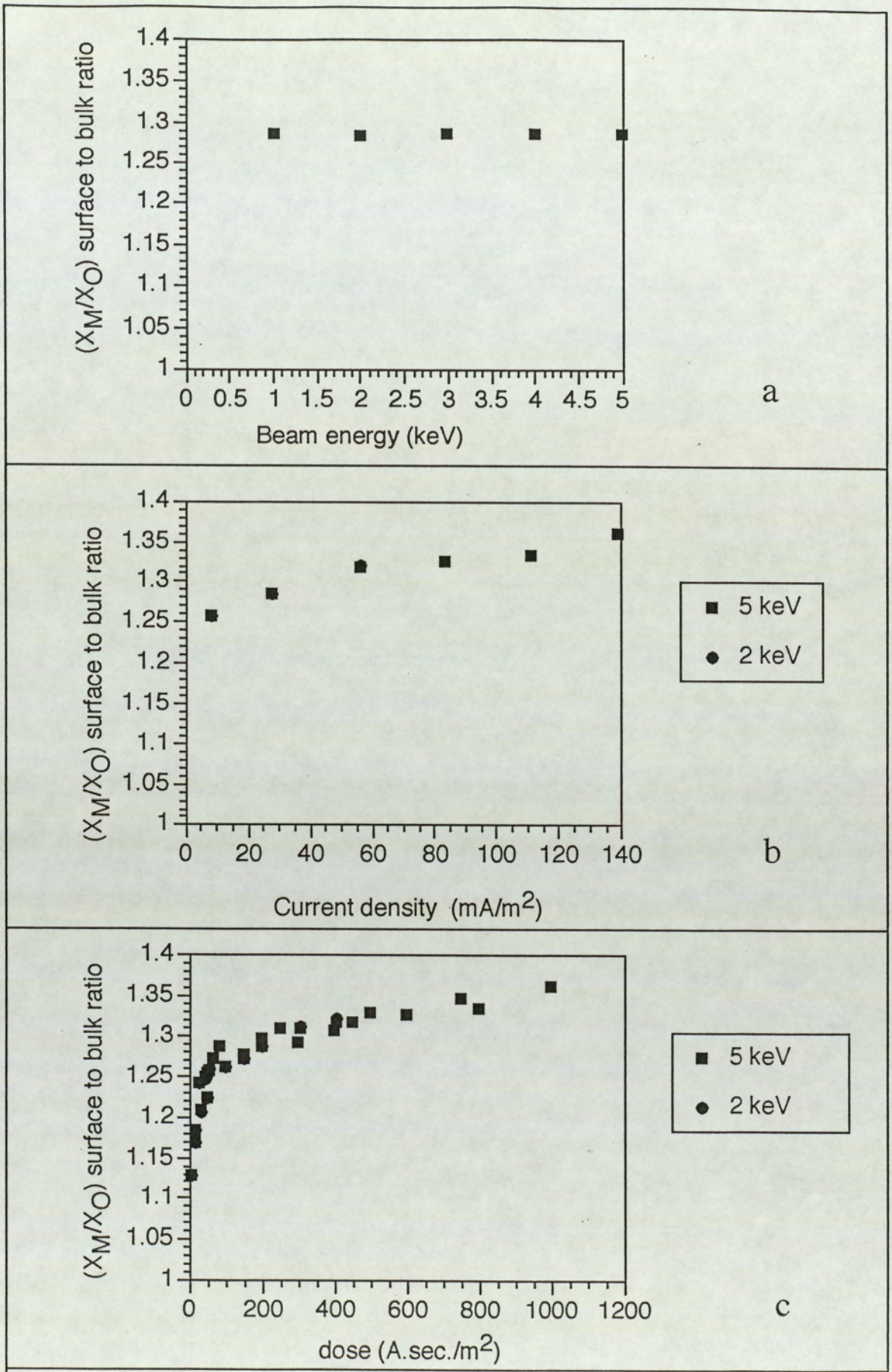

Figure 5.86.
Fe_2O_3 (X_M/X_O) surface to bulk ratio as a function of :

a) beam energy
b) current density (for 120 min. etch duration)
c) dose

Figure(5.86b) shows this ratio as a function of the beam current densitiy for the two constant beam energies of 5 and 2 keV(after 120 minutes of bombardment). For this two cases of the constant beam energies, the treands for the dependency on current density are approximately the same. The $\{(X_M/X_O)^S/(X_M/X_O)^B\}$ ratio is seen to increase significantly with current density and then gradually seems to be reaching towards a steady state. In figure (5.86c), the concentration ratio is plotted as a function of the dose, which is very similar to that plotted against the current density (at 120 minutes), confirming that the extent of surface chemical changes is dependent on the dose.

5.6.4: ZrO_2

Figures (5.87a, b, c) show the relative intensities of the ZrO_2, ZrO and the metallic Zr^0 respectively as a function of etch times for the different beam energies within the range 1 to 5 keV. Very little changes in relative intensities are again observed between 2 to 5 keV for the ZrO_2 and ZrO states. However this oxide has been found to the only exception since it shows a higher percentage of ZrO_2 present at the surface after 120 minutes of bombardment for the 1 keV case. Also, the appearence of metallic Zr takes the longest bombardment time for the 1 keV beam energy.

Figures (5.88a, b, c) show a series of graphs for the relative intensities of the above mentioned oxidational states as a function of etch times for current densities within the range 8 to 111 mA/m^2. The higher the current density the greater is the observed degree of chemical damage.

The above results are summarised in figures (5.89a, b, c) which show the $\{(X_M/X_O)_S/(X_M/X_O)_B\}$ ratio plotted against beam energy, beam current density and dose respectively. The figures (5.89b, c) also include the results obtained from a third set of experiments investigating the effect of current density variation at the lower constant beam energy variation of 2 keV.

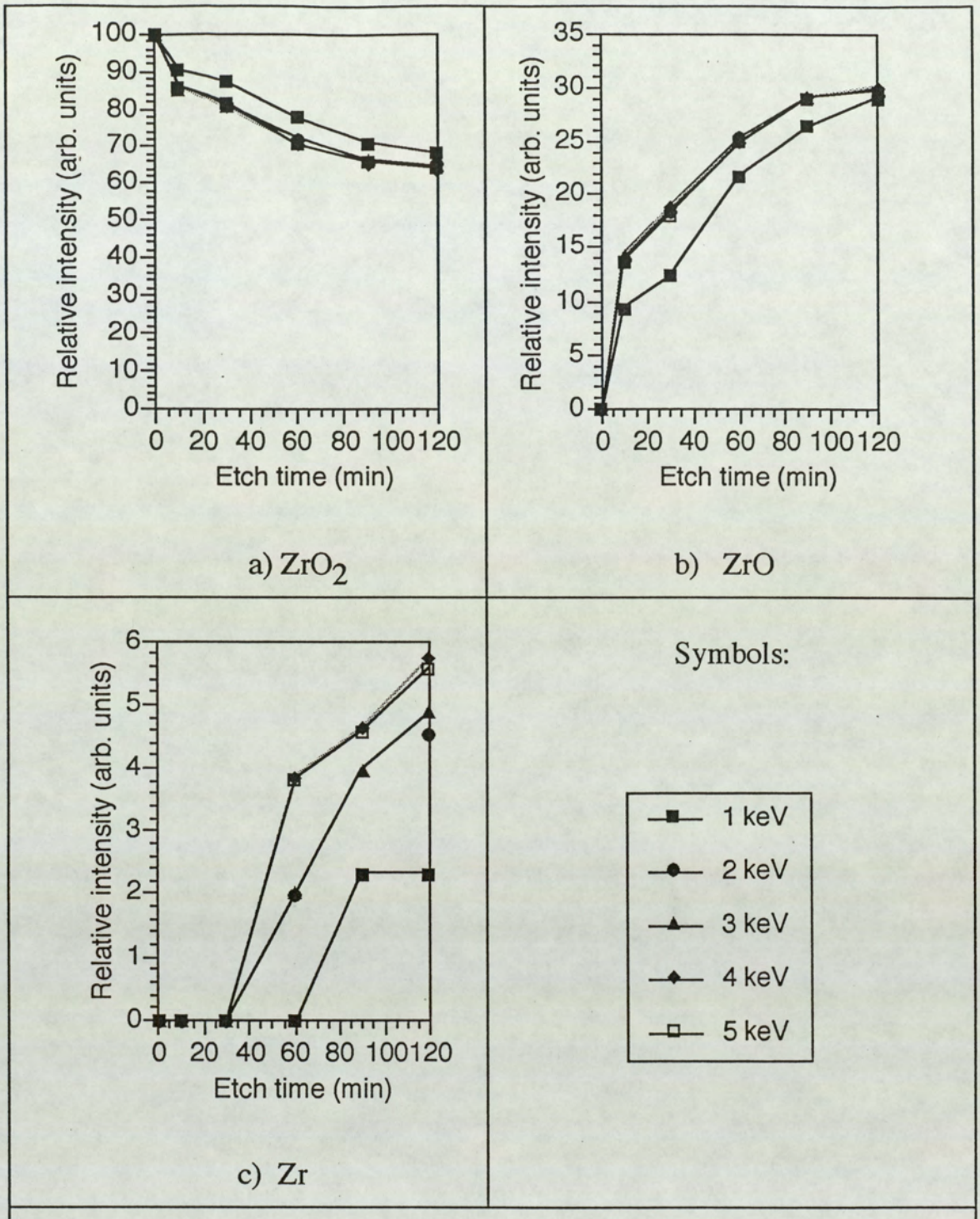

Figure 5.87.
Relative intensity as a function of etch time for ZrO_2 bulk oxide for different beam energies. The beam current density was kept constant at 28 mA/m^2.

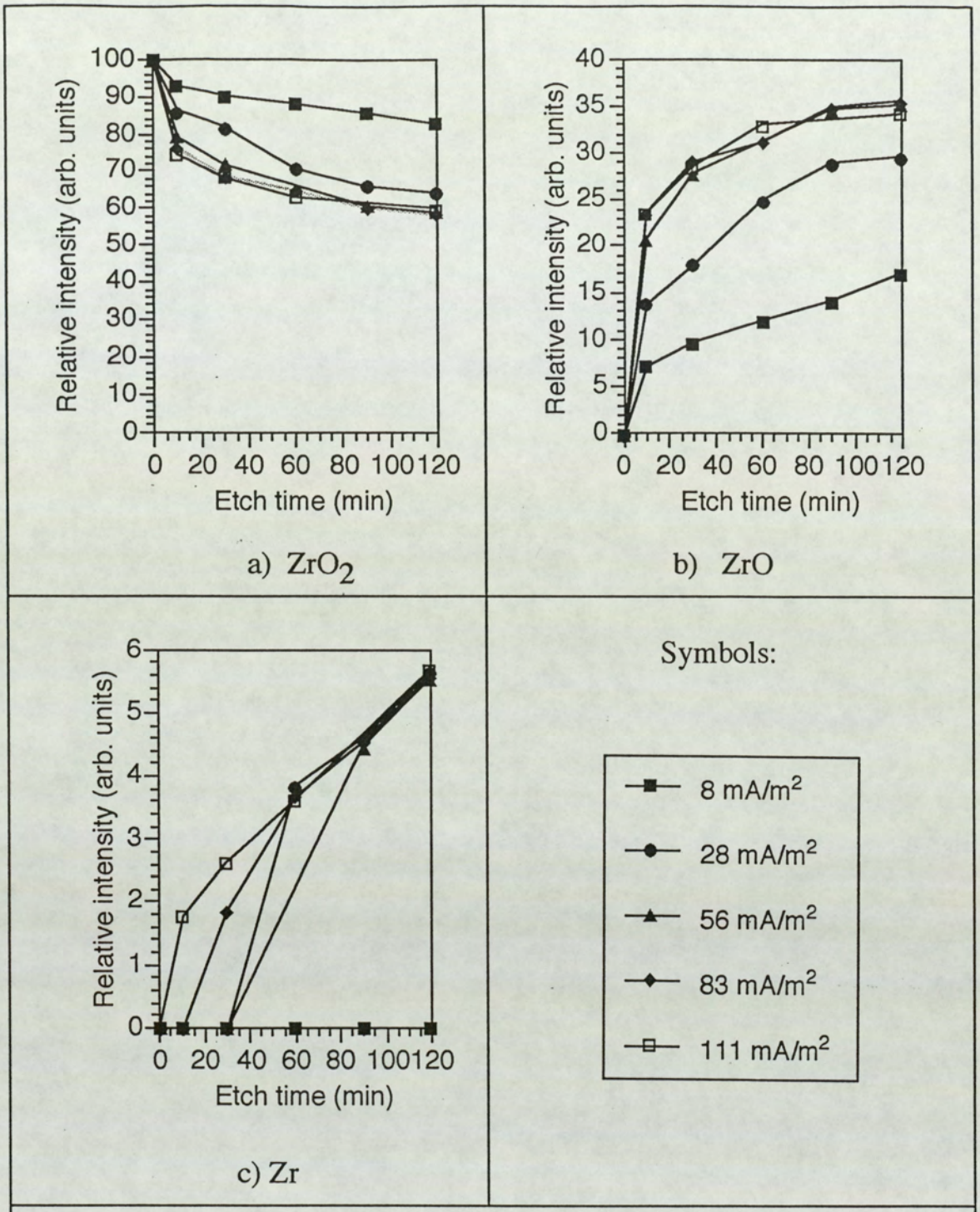

Figure 5.88.

Relative intensity as a function of etch time for ZrO_2 bulk oxide for different current densities. The beam energy was kept constant at 5 keV.

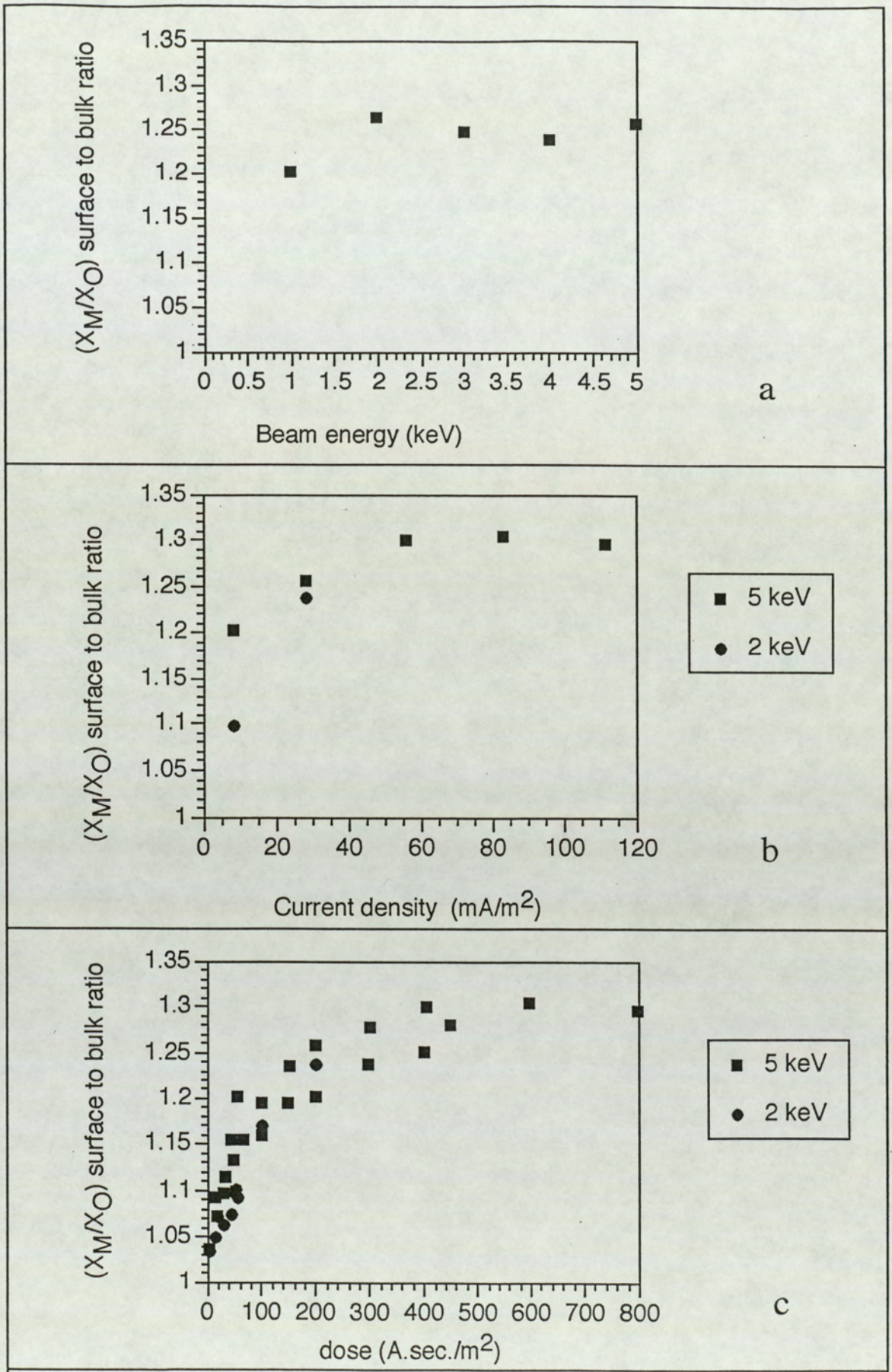

Figure 5.89.
ZrO_2 (X_M/X_O) surface to bulk ratio as a function of :

a) beam energy
b) current density (for 120 min. etch duration)
c) dose

5.6.5: WO_3

The primary beam energy and current density variation results obtained with the WO_3 surface is very similar to those due to the Nb_2O_5 and TiO_2 samples. Figure (5.90a) shows the chemical reduction of the WO_3 relative intensity as a function of etch time for the range of beam energies between 1 to 5 keV (for a constant current density of 28 mA/m^2). The relative intensities have been calculated using the W $4f_{7/2,5/2}$ lines and then taking the average of the two values. The variation of the relative intensity of the WO_3 state with etch time is found to be the same for each of the beam energies employed. After 120 minutes of bombardment period, the difference between the maximum and the minimum value of the relative intensity is 1.4%, which is negligible compared to experimental errors.

In figures (5.90b, c, d) the corresponding relative intensities for the W_2O_5, WO_2 and metallic W^0 are seen plotted against etching time. For the different beam energies employed, the etch time needed for the appearence of these states is found to be the same. Also, the intensities at steady state are not dependent on the beam energy in the range 1 to 5 keV. The maximum changes in relative intensity as a function of beam energy are 4.4%, 3.8% and 3.2% for the W_2O_5, WO_2 and W^0 states respectively. These variations are again purely random with respect to the beam energy and not related to the maximum and minimum beam energy cases. Thus occurence of the same amount of chemical damage with beam energy in the range 1 to 5 keV is seen.

Next the effect of current density variation in the range 8 to 139 mA/m^2 is considered for a constant beam energy of 5 keV. Figure (5.91a) shows the results obtained for the original surface oxide WO_3 as a function of the etch time. The minimum reduction to the WO_3 state is found at the lowest current density of 8 mA/m^2 and after 120 minutes of a steady state condition for the relative intensity is not yet reached. With increment in the current density, the etch time necessary for attainment of steady state decreases until a current density of about 111 mA/m^2 is reached. For the cases of 111 and 139 mA/m^2, this time needeed to reach steady state and the value of intensity at the steady state is approximately the same.

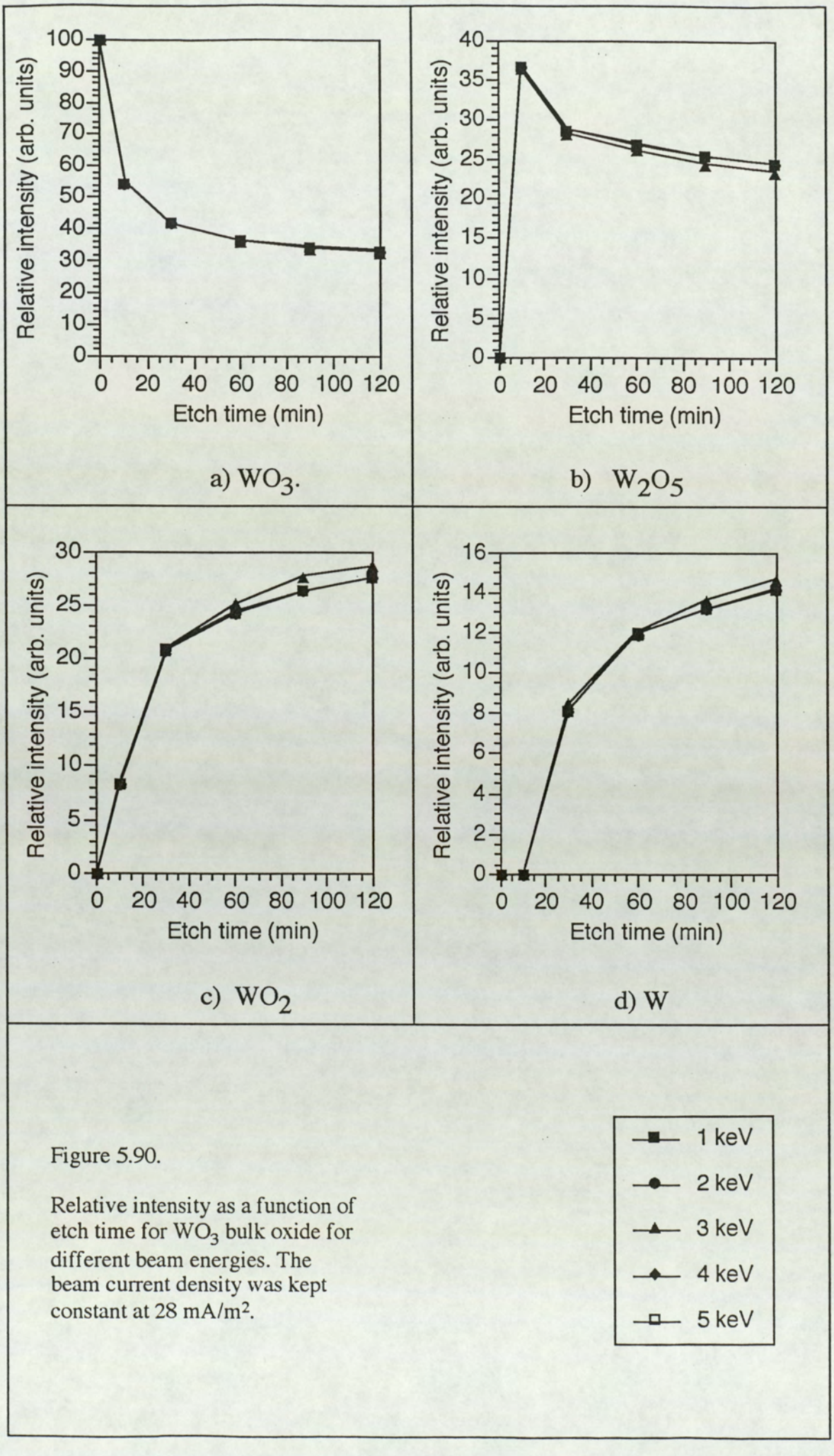

Figure 5.90.

Relative intensity as a function of etch time for WO_3 bulk oxide for different beam energies. The beam current density was kept constant at 28 mA/m^2.

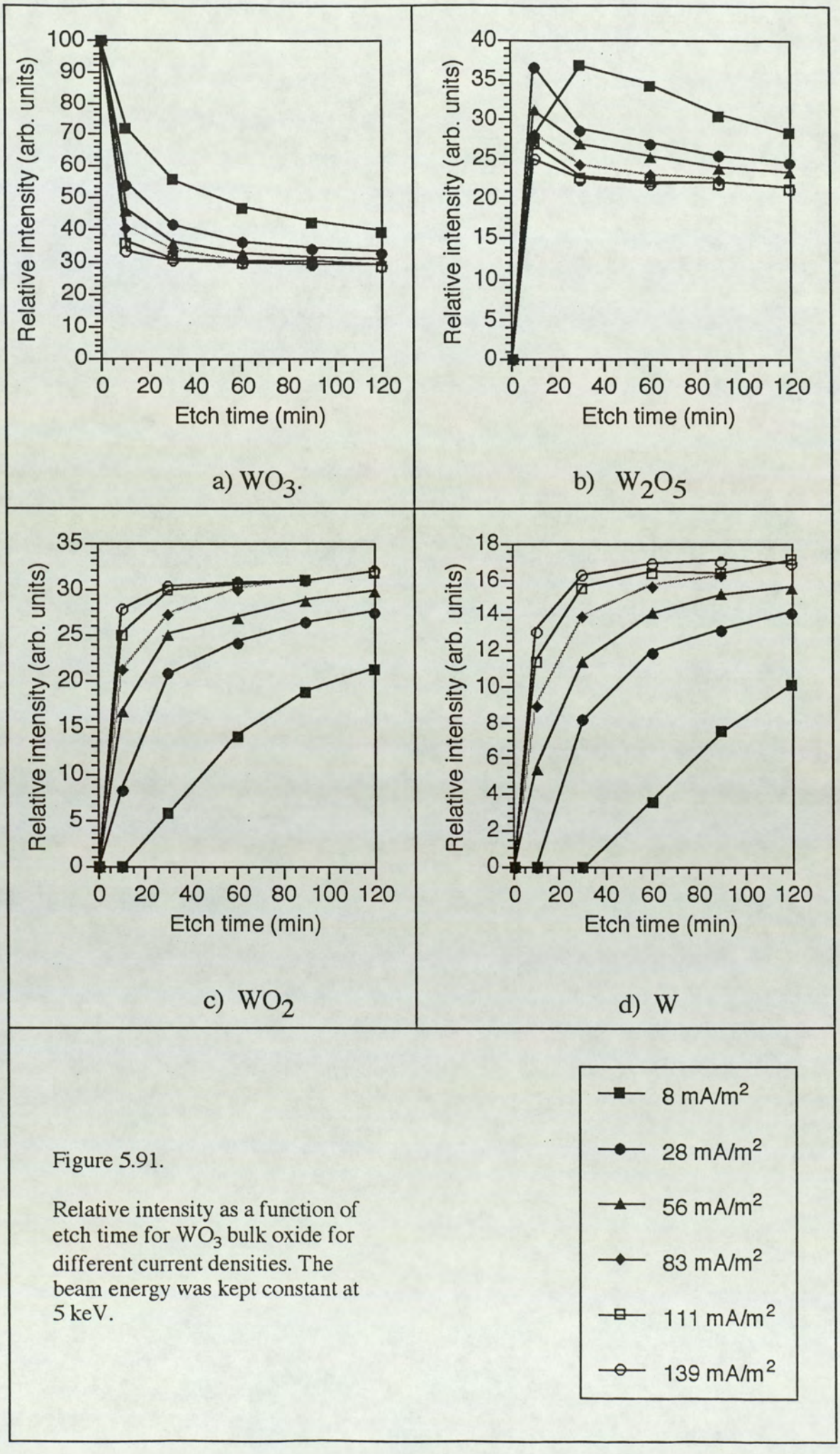

Figure 5.91.

Relative intensity as a function of etch time for WO_3 bulk oxide for different current densities. The beam energy was kept constant at 5 keV.

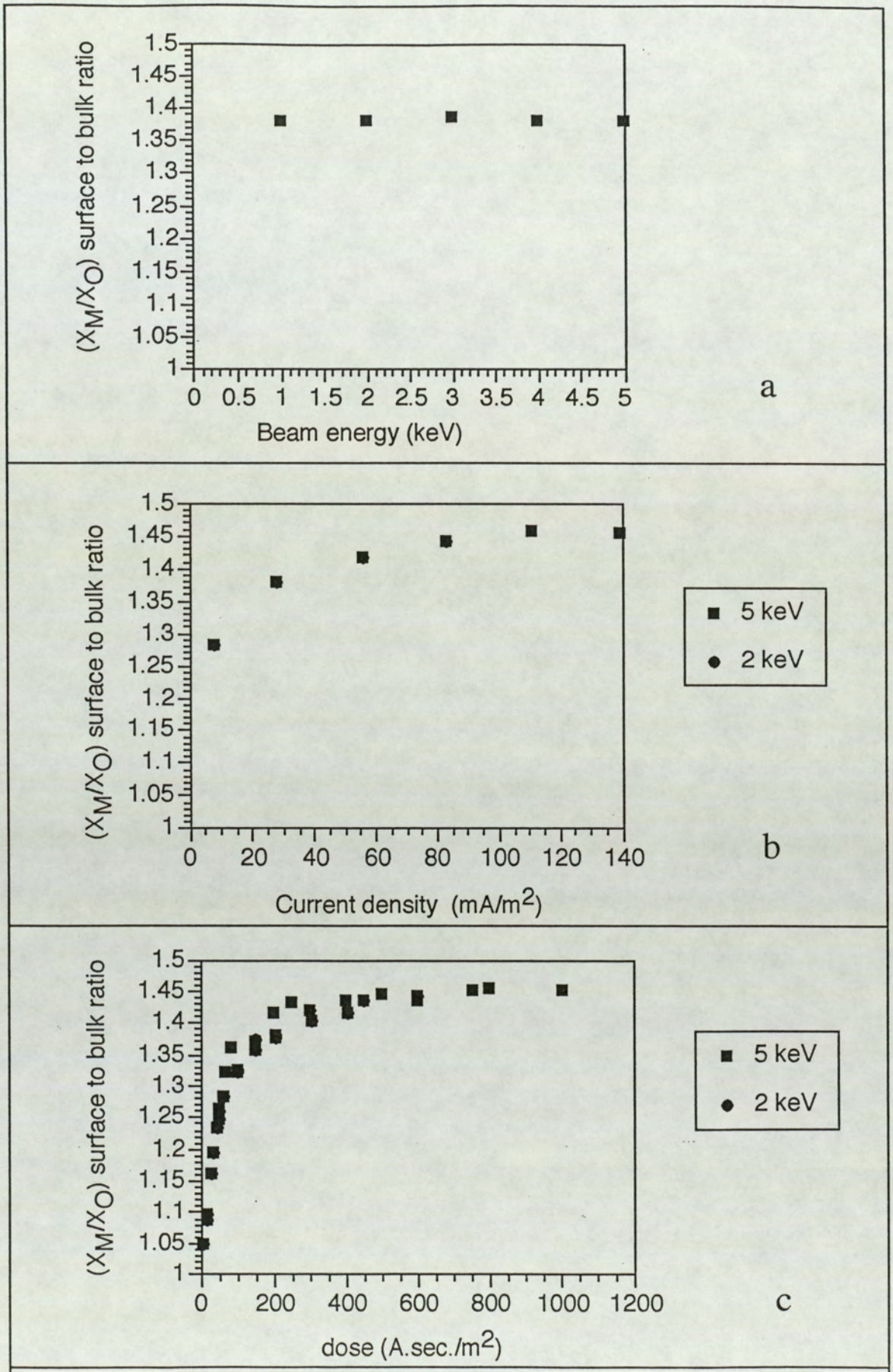

Figure 5.92.
WO_3 (X_M/X_O) surface to bulk ratio as a function of :

a) beam energy
b) current density (for 120 min. etch duration)
c) dose

Figures (5.91b, c, d) show the relative intensity for the states W_2O_5, WO_2 and W^0 as a function of etch time. These figures all show an increase of surface chemical damage with increasing beam current density. The first reduced state, i.e. W_2O_5 shows an initial (i.e., with respect to etch time) increase in relative intensity and then gradual decrease; thus chemical reduction of this state is apparent. Similar to the WO_3 state, reduction caused to the W_2O_5 state is a minimum for the lowest current density and a maximum for the highest current density. The second and the final reduced states, that of WO_2 and metallic W^0 respectively, for higher current densities require a shorter etch time for their appearence in the surface layer; also, the etch time required for attainment of a steady stateis again less for the higher current densities.

The above results together with those from a third set of experiments carried out to investigate the variation of beam current density (8 to 83 mA/m^2) at a lower constant beam energy of 2 keV is summarised in figures (5.92a, b, c). Figure (5.92a) shows the variation of $\{(X_M/X_O)_S/(X_M/X_O)_B\}$ concentration ratio plotted against the corresponding beam energies; a linear-relationship with beam energy is seen. In figure (5.92b), the $\{(X_M/X_O)_S/(X_M/X_O)_B\}$ ratio is plotted against current density for both sets of experiments at 5 keV and 2keV. In figure (5.92c) this surface to bulk (X_M/X_O) ratio is presented as a function of the dose. The dose dependency of the surface chemical changes is thus demonstrated.

5.7: The effect of atom versus ion bombardment

As stated before in chapter 4, this investigation has been carried out at two different beam current densities to characterise fully the comparisons made. The powder oxide used for the purpose of this investigation was TiO_2. The high primary current was chosen to be 10 μA and the low to be 1 μA. The two different inert gases used for the bombardment were Ar and He. This choice for the bombarding gas species was made with the intention that the charge and mass effects of the incident particles might be effectively separated. For example, if the charge is important, one

would expect to have a greater differential effect with the low mass particle.

In this investigation, XPS spectra were recorded for the TiO_2 samples initially for the unbombarded air-exposed surface and then after 2, 10, 30, 60 and 120 minutes of bombardment. It was found that the more reliable and consistent results were obtained for the shorter periods of bombardment. For the longer etch periods, it was difficult to maintain the source currents at constant levels. All sample bombardment was carried out at a mean beam energy of 5 keV.

To illustrate the comparisons made for ion versus atom bombardment, the most intense metal peak, the Ti 2p, is considered. The effect of the two types of particle bombardment on the Ti $2p_{1/2,3/2}$ lines are illustrated in figures (5.93) and (5.94). These figures represent the most mild and the most severe conditions of bombardment used. Figure (5.93) shows the spectra recorded for He atom bombardment for the case of low beam fluence (i.e, equivalent to a current density of 1.3×10^{-2} Am^{-2}). It can be seen that the there is little change in the 2p profile even after 120 minutes of neutral bombardment. Figure (5.93) may be contrasted with figure (5.94), which shows a similar series of Ti 2p spectra for the Ar ion bombardment at high current conditions (equivalent to a current density of 1.3×10^{-1} Am^{-2}). The latter series of spectra shows substancial peak shape changes within a short period of bombardment of 2 minutes. A broadening of the spectra caused by the reduction of the Ti^{IV} state producing a shift of the core level photoelectron lines to the lower binding energies is clearly visible. Thus under these conditions of bombardment, by a relatively massive ion at high current density, a considerable degree of oxide reduction has occured. The two series of spectra shown here represent the extremes of the bombardment conditions applied, all other conditions produces spectral changes in between these two.

Next, a curve-synthesis procedure was carried out to clarify whether reduction had taken place and to distinguish quantitatively the contributions due to each oxidation state. Figures (5.95) to (5.98) show the Ti 2p spectra, after 10 minutes of

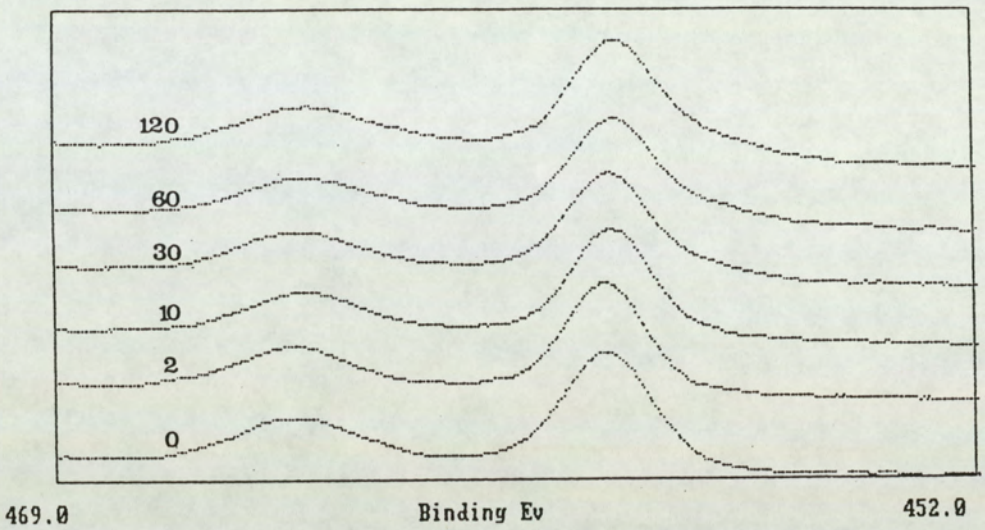

Figure 5.93.

A series of Ti 2p spectra after Helium atom bombardment with a current density of 1.3×10^{-2} A/m^2.

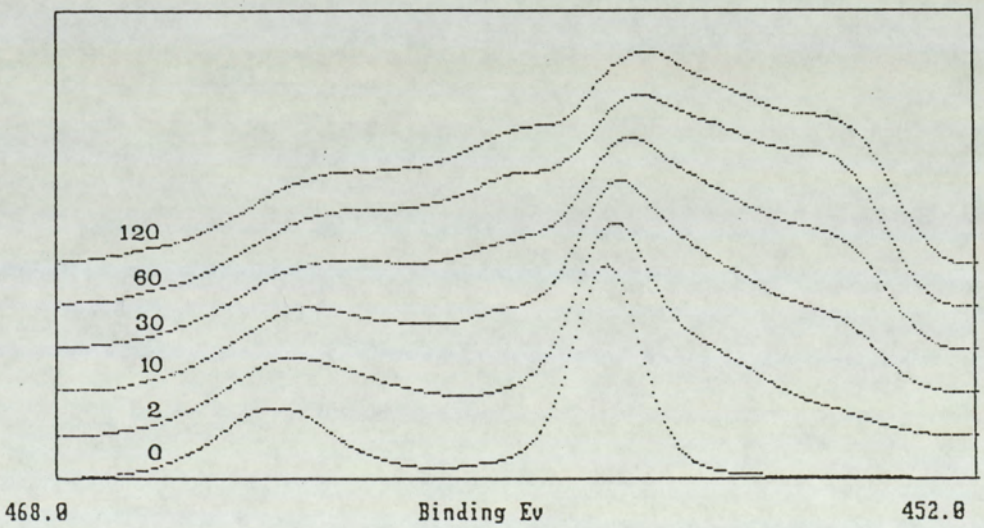

Figure 5.94.

A series of Ti 2p spectra after Ar^+ ion bombardment with a current density of 1.3×10^{-1} A/m^2.

bombardment, on which the curve-synthesis procedure has been employed. In these figures reduction of the TiO_2 to Ti_2O_3 and then to TiO can be seen. The binding energies and their corresponding FWHM values of the different components have already been stated in section 5.5. Considering each of these figures in turn, figure (5.95a) shows the spectra for He atom bombardment at the low equivalent current density of 1.3×10^{-2} Am^{-2}. Curve-synthesis procedure reveals the presence of Ti_2O_3 state and also suggests a small contribution due to the presence of TiO. Figure (5.95b) shows the corresponding Ti 2p spectra for He ion bombardment with similar beam current. The presence of the two reduced states as mentioned above is very prominent in this case. Thus, bombardment with ions creates substantially more chemical reduction than bombardment with atoms. To compare quantitatively the degree of reduction in each case, the ratio of the sum of intensities of the reduced oxide lines to the intensity associated with the original oxide, $\{I(Ti^{IV})+I(Ti^{III}) / I(Ti^{II})\}$, is determined. This value expressed as a percentage is shown in Table (5.12); also listed in this table is the ratio of the ion to atom reduction.

Figures (5.96a, b) show the Ti 2p spectra for He neutral and ion bombardment respectively at the higher current density of 1.3×10^{-1} Am^{-2}. Again, chemical damage due to atom bombardment is seen to be less than that due to ion bombardment. Thus in this case for the light mass projectiles it is seen that the charge has a profound effect on the differencial sputtering process. Similar to section 5.6 for the higher current density a greater degree of reduction is seen. In both cases of atom and ion bombardment, a ten times increase in the current density produces about four times the percentage reduction.

Figures (5.97) and (5.98) shows the spectra obtained for a similar set of experiments carried out with Ar atoms and ions at the low and the high current densities. Again, reduction to the Ti^{II} state is seen for both neutrals and ions. For both the current densities employed, the spectra indicate that the difference between atom induced and ion induced reduction is not nearly as pronounced as in the case for He. With He bombardment, fast atoms produces about 2.5 times less chemical reduction

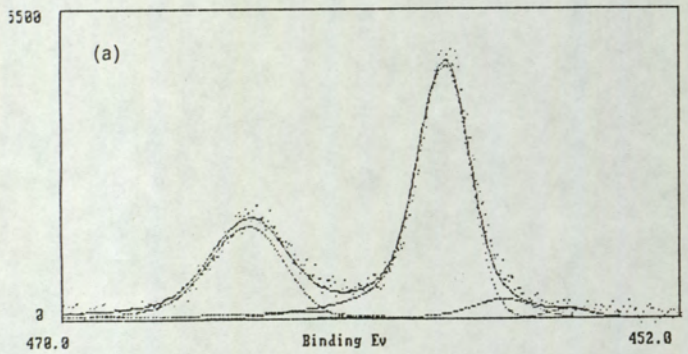

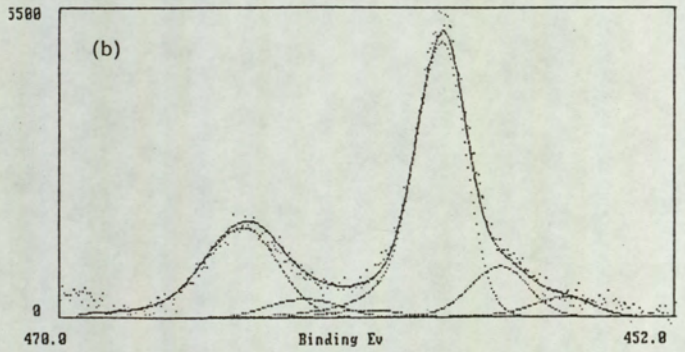

Figure 5.95.

Helium atom and ion bombardment with a current density of 1.3×10^{-2} A/m^2.

a) atoms
b) ions

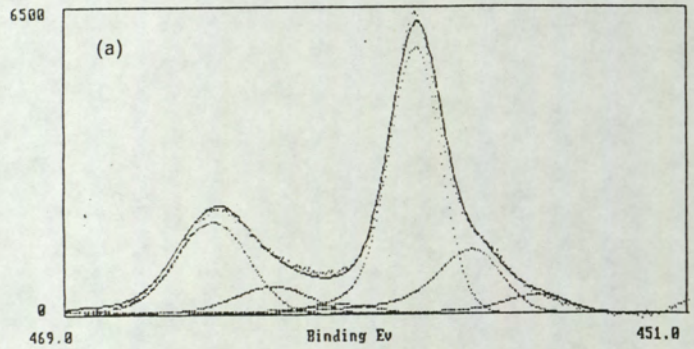

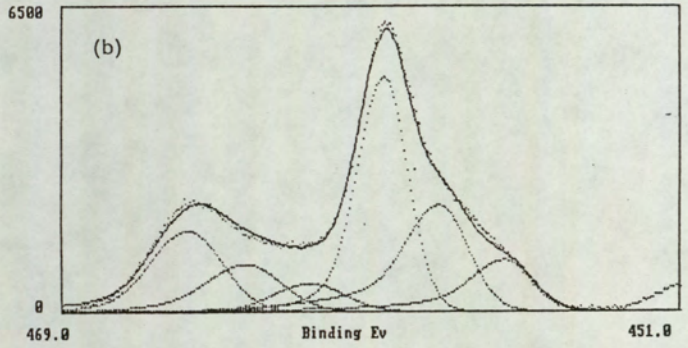

Figure 5.96.

Helium atom and ion bombardment with a current density of 1.3×10^{-1} A/m^2.

a) atoms
b) ions

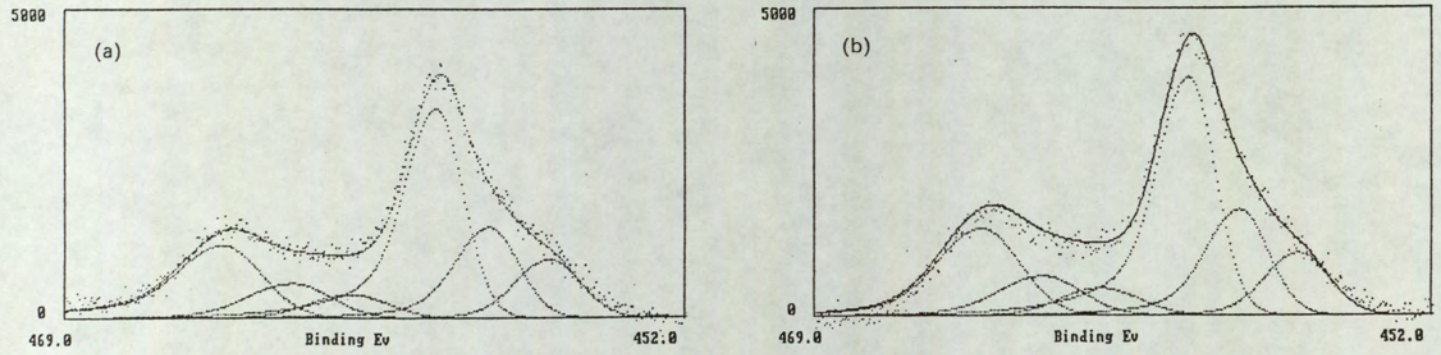

Figure 5.97.

Argon atom and ion bombardment with a current density of 1.3×10^{-2} A/m^2.
a) atoms
b) ions

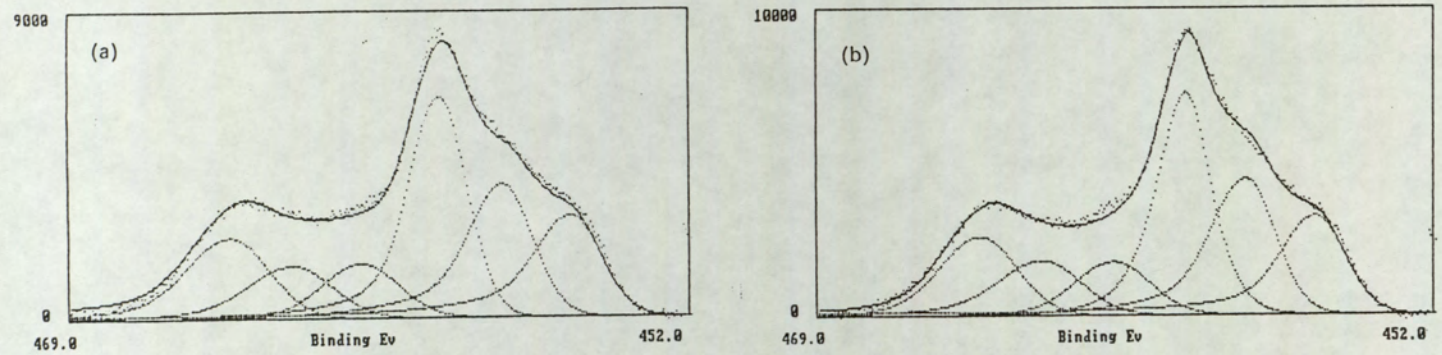

Figure 5.98.

Argon atom and ion bombardment with a current density of 1.3×10^{-1} A/m^2.
a) atoms
b) ions

than ions as compared with Ar bombardment which produces about 1.1 times less. It should be noted here that for both the incident gas species the 'ion' beam contains ~20% atoms. Hence, the difference in the degree of reduction obtained in this investigation between ion beam and the fast atom beam bombardment is expected to be far less than if the 'ion' beam was wholly composed of charged particles. Also, for Ar a ten times increase in the current density approximately doubles the degree of reduction. The more massive Ar particles produce the greater overall degree of reduction. All thes results are tabulated in Table 5.12.

This investigation clearly demonstrates that there is a difference in chemical damage produced in an insulating surface due to charge on the incident particle.

5.8: The effect of electron bombardment

Electron bombardment carried out the on oxides Nb_2O_5 and TiO_2 respectively at ~ 5 keV showed no compositional changes after bombardment up to 120 minutes.

Table 5.12.

The percentage reduction and ratio of ion to atom reduction for the various bombarding species after 10 minutes exposure to bombardment

bombarding species	current density A/m^2	percentage reduction	ratio to ion atom reduction
He^0	1.3×10^{-2}	11	2.5 : 1
He^+		28	
He^0	1.3×10^{-1}	43	2.3 : 1
He^+		98	
Ar^0	1.3×10^{-2}	73	1.5 : 1
Ar^+		77	
Ar^0	1.3×10^{-1}	127	1.12 : 1
Ar^+		142	

CHAPTER 6: Theoretical considerations

6.1: Introduction

An overview of the basic concepts behind low energy ion induced chemical changes of oxides has already been described in chapter 1. Also it has been expressed that none of the models describe fully the causes of the surface chemical changes in metal oxides. Two of the most favoured models are those due to Malherbe et al [47] and Kelly [49]. Only these two models will be considered in this chapter. Both models have been proposed to account for the ion induced oxide reduction based on Sigmund's classification of sputtering events and sputtering yield equation [1,2]. The model due to Malherbe [47] uses a collisional approach to explain the average composition in terms of the metal to oxygen concentration ratio, C_M/C_O, whereas in the model due to Kelly [49] a thermal approach is favoured in attempting to explain specific stochiometries.

6.2: Model due to Malherbe et al

In this model Malherbe, Hofmann and Sanz [47] incorporate a mass difference effect and surface binding effects to lead to explain the preferential sputtering of metal oxides. The outline of the basic concepts used are as follows:

The initial equation is taken from the simple models for preferential sputtering as developed by several other authors [14,15]. In which for the case of the steady state, the ratio of the surface fractional composition X_i^S of a metallic oxide to a bulk fractional composition X_i^b is given by :

$$(X_M/X_O)^S = (X_M/X_O)^B (Y_O/Y_M) \qquad \ldots. (6.1)$$

where Y_i represents the component sputter yield of the metal (M) or of oxygen (O).

The second equation is taken from Sigmund's sputtering theory [1] assuming the linear cascade regime in which the ratio of the component sputter yield is approximated

by:

$$Y_O/Y_M = (A_M/A_O)^{2m} (U_M/U_O)^{1-2m} \quad \ldots. (6.2)$$

where A_i and U_i denote the atomic masses and surface binding energy respectively and m is the atom potential parameter. Substitution of (6.2) into (6.1) leads to the following equation:

$$(X_M/X_O)^S = (X_M/X_O)^B \ (A_M/A_O)^{2m} \ (U_M/U_O)^{1-2m} \quad \ldots. (6.3)$$

The exact value of the atom potential parameter, m, is uncertain since it depends on the energy. The origin of m in equations (6.2) and (6.3) comes from the particular form of the power cross sections (for elastic collision between an incident atom and a target atom) that Sigmund used in his theory. For this cross-section, m=1 at high energies while for medium energies (10 - 100 keV) m=0.5 and for lower energies, the value of m ranges between 0 and 0.5. The energy of the incident particle that results in the sputtering of target atoms is usually small. therefore, for applications in sputtering, the relevant values of m should lie in the range $0<m<0.2$ [1,2].

The next step in the theory due to Malherbe et al was to calculate the surface binding energies of the oxygen and the metal atoms. The determination of the surface binding energy applicable for the case of oxide sputtering is an extremely difficult one due to the lack of reliable experimental data and also because these di-atomic compounds do not sputter stoichiometrically in molecular fragments. Malherbe et al [47] concluded that under the given circumstances the best that can be achieved is to obtain a reasonable approximation to real energies. To do this, they proposed a simple model based on a gross modification of the Pauling formalism [180] for the bond energies in a covalent bond. In the Pauling formalism the average covalent bond energy of a di-atomic oxide molecule is the arithmatic mean of the metal-metal and oxygen molecule bond energies. To account for the polarity of the ionic character of the bond, Pauling included another term in the equation, which is the difference in electronegativities ε. In the Malherbe et al [47] extension of this formalism to account for a molecule M_xO_y, the average bond energy is given by:

$$D(M_xO_y) = \{x/(x+y)\ D(M\text{-}M) + y/(x+y)\ D(O\text{-}O) + x/(x+y)\ D(M\text{-}O) + 1/2\ (\varepsilon_M\text{-}\varepsilon_O)^2\} \quad \ldots. (6.4)$$

where D(M-M) denotes the metal-metal bond energy, D(O-O) the dissociation energy of the oxygen molecule and D(M-O) the metal-oxygen bond energy of the di-atomic oxide MO. The average energy necessary to remove only one oxygen atom from this molecule is thus given by:

$$U_O = x/(x+y)\ D(M\text{-}O) + y/(x+y)\ D(O\text{-}O) + 1/2\ (\varepsilon_M\text{-}\varepsilon_O)^2 \ldots. (6.5)$$

The above equation for U_O is found by substituting in values for the bond energies obtained from ref. [181] and the electronegativities obtained from ref. [182].

In the case of binary alloys the surface binding energy U_M of a metal atom is usually taken to be equal to be the sublimation energy, H_S, of the metal [183]. In particular for oxides, Malherbe et al [47] predict that the value of the surface binding energy of the metal must be modified to account for the effect of chemical binding energy between the metal and oxygen atoms. They achieved this by assuming an approach similar to the Pauling scheme [180] such that:

$$U_M = H_S + 1/2(\varepsilon_M\text{-}\varepsilon_O)^2 \quad \ldots. (6.6)$$

Using the above approach of combined mass difference and surface binding energy effects, Hofmann and co workers compared thier experimental results [50] with those due to the theory. Their findings are reproduced in Table 6.1. To obtain the theoretical values, the exponent parameter 2m=0.33 was chosen in accordence with the range suggested by Sigmund [1,2] and mostly since it gave a satisfactory fit to their experimental results.

6.3: Model due to Kelly and co. workers

This model as proposed by Kelly and co workers [40,49,87] would be described here, however it is noted that the experimental evidence obtained in this thesis and due

to other workers [50] are contradictory to this theory. In this model it is assumed that the mass difference effect, as far as the preferential sputtering of oxides is concerned, can be neglected. Also that only binding energy effects being related to the cascade and thermal sputtering which are thought in this theory to be the most important copmonents for oxide sputtering.

For the cascade component the linear cascade regime as defined by Sigmund [1] is assumed, i.e, the sputtering yield is inveresely proportional to the surface binding energy U. At the steady state it is then assumed that:

$$\{\alpha_{A(3)} / \alpha_{B(3)}\} = \{\alpha^{\infty}_{A(2)} U_B / \alpha^{\infty}_{B(2)} U_A\} \quad \ldots. (6.7)$$

i.e. the loss ratio of the surface equals the bulk concentration ratio. In the above equation "2" stands for outer surface, "3" for bulk and "∞" for steady state. α_i and U_i are the atom concentration and binding energy respectively for the components A and B.

However, the problem with oxides is the definition of the quantity U. Kelly [87] proposes that an identification of U with the average total and partial heats of atomisation ΔH^a, can predict oxygen loss for a given oxide. For example for TiO_2, the average total ΔH^a is assumed to relate to:

$$TiO_2(l) = Ti(g) + 2\,O(g)$$

$$U_{Ti} = U_O = \Delta H^a_{TiO_2} = 1/3[-\Delta H^f_{TiO_2} + \Delta H^a_{Ti} + 2\Delta H^a_O] = 6.4 \text{ eV/atom.} \quad \ldots. (6.8)$$

The average partial ΔH^a relates to:

$$2\,TiO_2(l) = Ti_2O_3(s) + O(g);$$

$$U_O = \Delta H^a_{TiO_2\text{-}Ti_2O_3} = -2\Delta H^f_{TiO_2} + \Delta H^f_{Ti_2O_3} + \Delta H^a_O = 5.1 \text{ eV/gas atom.} \quad \ldots. (6.9)$$

Here s stands for solid (i.e. crystalline), l for liquid (amorphous) and g for gas (i.e. sputtered) and ΔH^f is the heat of formation. The reasoning would be that since U in equation (6.9) is less than U in equation (6.8), TiO_2 will tend to lose oxygen when bombarded. Thus equal sputtering of both components with no changes in surface composition should be observed if the average total ΔH^a is smaller than all possible

values of the partial ΔH^a.

There are some difficulties with the above predictions; one of the important ones being that the total and partial ΔH^a are sufficiently similar (which implies that Y_A/Y_B is near to unity), so that major changes such as a reduction of TiO_2 to Ti_2O_3 should not occur. However to account for the above difficiencies in the theory Kelly [49] proposes that for oxides the predominant sputtering process is that of a thermal origin rather than collisional. This thermal component is also related to the bonding through the proportionality equation:

$$Y_{i(thermal)} \alpha M_i^{-1/2} T^{3/2}(\Delta H^a_i)^{-2} \exp(-\Delta H^a_i / kT) \quad .... (6.10)$$

where T is the "thermal spike" temperature and M is the atomic weight. For oxides, the appropriate quantity for comparison is taken to be the decomposition pressure, P_d. The decomposition pressure is the partial pressure of the oxygen over the oxide. The decomposition pressure versus 1/T graph due to ref [49] is shown in figure (6.1). As a rough criterion, kelly gives an estimate for the value of $Y_{thermal}$, which would be the limiting case for thermal sputtering to be significant such that:

$$Y_{thermal} \geq 1 \text{ if } P_d(T) \geq 10^{2\pm1} \text{ bar.}$$

Taking the decomposition pressure of the oxide at assumed spike temperatures of 2000-4000 K, preferential loss of oxygen from the surface of oxides is predicted. In figure (6.1)., oxides with the decomposition pressure greater than 10^2 bar at approximately 3000 K are predicted to lose oxygen preferentially, while those with lower decomposition pressure should sputter such that the surface composition remains equal to the bulk composition.

Experimental results are too contradictory to make a clear decision as to whether the proposed criterion for losing or not losing oxygen from oxides is correct. This will be further discussed in the next chapter.

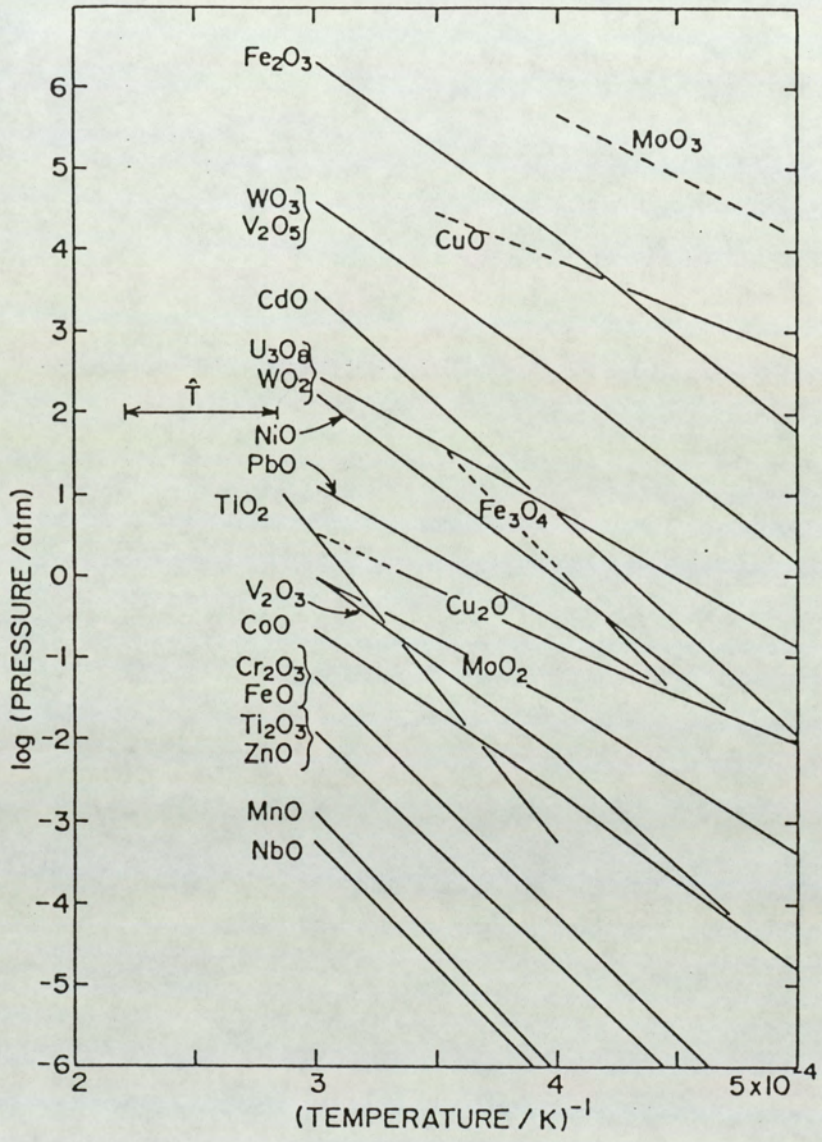

Figure 6.1.

Decomposition pressure versus 1/T for oxides at high temperatures [49].

CHAPTER 7: Discussion

7.1: Introduction

From the results described in chapter 5, the discussions for all investigations carried out will be divided into three main groups: a) the effect of ion bombardment on the transition and non-transition metal oxides as detected by x-ray photoelectron spectroscopy, b) the effect of variation of incident beam conditions i.e. variation of beam energy and beam current density on the extent of surface chemical damage, and c) comparison of ion bombardment with neutral bombardment. Sections 7.2, 7.3 and 7.4 discuss the results obtained for the three main groups of investigations. In section 7.5, comparisons are made of the results with the predictions due to the existing models.

7.2: The effect of ion bombardment

Although ion induced reduction of binary oxides has been studied in recent years by many research workers using a variety of different detection techniques [37-46], there exist few quantitative investigations comparable with this work. In most cases the conclusions are restricted to affirmative or negative comments. There has been a lack of extensive quantitative work on the influence of the beam parameters.

Another important factor is that the standard data available for the core level binding energies of the transition metals and their different oxidation states are not complete. Also there exists only a limited number of reports [56,57,58,68,102,] that give any additional information such as binding energy values for the satellite structures and the width of the main and the satellite peaks. However, it is well understood that this extra information can be important for characterization of the binding states [70,71]. Hence the results obtained here give up to date and extensive XPS data to add to the current literature, in addition to the information obtained for the effect of ion bombardment. In the following these results are discussed for each of the oxides.

7.2.1: Iron and its oxides

As mentioned in chapter 5 (section 5.5.13), it was found necessary to carry out a non-linear background subtraction of the Fe 2p spectra. This was done to ensure that meaningful information could be obtained from the curve-synthesis data. This is mostly due to the reason that the base line climbs steeply in this region. In itself this would not normally present any experimental difficulty provided that the observed peaks were relatively sharp and well defined. However, due to the multiplet splitting effects, the maxima assigned to Fe $2p_{1/2}$ and $2p_{3/2}$ each have a number of satellites which combine to almost the height of the maxima. This leads to a wide peak and a too assymetric peak shape; additional complexicity arises when presence of more that one valence state of the Fe ion enhances the assymetry of the peak shape. So employment of a non-linear background subtraction prior to curve-synthesis becomes an absolute necessity.

In the iron-oxygen system two conditions are present which maximize the multiplet splitting. Firstly many of the iron oxides contain iron which has a formal oxidation number of three and all are high spin, with a maximum of five unpaired 3d electrons. Secondly, the ligand around the Fe atom is oxygen which has no orbitals available for overlap that could lead to metal electron delocalisation. Hence the measured peak width of 3.3 eV for the Fe 2p spectra is to be expected. This value is in good agreement with that of approximately 3 eV due to McIntyre and Zetaruk [68]. Allen et al [57] also suggests, in view of their experimental findings, that due to the multiplet splitting components the half widths of the 2p iron oxide spectra could be expected in the region up to 3.8 eV to 4.4 eV. The data reported in this thesis, similar to those due to McIntyre et al [68], had been obtained under higher resolution than employed by Allen et al.

Considering the results for the FeO powder first, the unbombarded surface showed presence of FeOOH (at the $2p_{3/2}$ binding energy of 711.8 eV) and α-Fe_2O_3 (710.8 eV). The high possibility of formation of surface Fe_2O_3 from air-exposed FeO

has been described by Allen et al [57] to take the following route:

$$FeO + (1/4)\ O_2(air) \leftrightarrow (1/2)\ Fe_2O_3$$

The presence of FeOOH on the surface is also indicated by the O 1s peak at 531.9 eV; the other oxygen peak at 530.4 eV are due to the metal-oxygen bond. This view is supported by the work of Mills and Sullivan [53] and Allen et al [57]; although Brundle et al [70] suggest that the higher energy peak could be due to non-stoichiometric surface oxidational states. The third and the smallest O 1s peak at 533.4 eV has been allocated to be due to some form of surface bound water. Although the presence of this peak has often been noted in current literature, its identity has been ignored. The only known confirmed presence of this peak is that due to McIntyre [184] who suggests that the broad O 1s peak centred at 533.2 eV is most probably due to a multiplicity of chemically and physically bonded water on and within the surface.

The binding energies for the corresponding Fe $2p_{1/2}$ line are found to be 725.5 and 724.5 eV for the FeOOH and Fe_2O_3 states respectively. Similar results for the binding energies of the $2p_{1/2,3/2}$ lines for these oxides have been obtained by Brundle et al [70], McIntyre et al [68] and Allen et al [57,58].

Within 10 minutes, argon ion bombardment exposes the underlying bulk FeO, which is indicated by the appearence of an additional peak at binding energy of 709.4 eV with its associated shake-up satellite at 715.2 eV. Brundle et al [70], McIntyre et al [68] and Mills and Sullivan [53] quote binding energies of 709.7, 709.5 and 709.6 eV respectively; also these authors suggest that the satellite appears at about 6 eV above the main peak. It is also highly likely that part of the FeO contribution is due to "ion induced reduction" of the FeOOH and Fe_2O_3 states, since appearence of metallic Fe^0 is detected with further ion bombardment. Part of the Fe^0 contribution in the 2p spectrum is from the contaminant Fe which is detected in the bulk powder by X-ray diffraction technique. But, most of the Fe^0 contribution is due to the ion bombardment induced reduction process, since in the XRD powder photograph only weak lines due to metallic iron is seen, whereas in Fe 2p spectrum at steady state more than 30% of the

intensity contribution is due to the Fe^0 ions. The binding energy value obtained for Fe^0 at 707.0 eV again agrees well with those due to other workers, for example McIntyre et al [68] at 707.3 ev and Allen et al [57] at 706.9 eV.

The retention of small amounts of the contaminants (i.e. FeOOH and Fe_2O_3) has been explained, in the last chapter on results, as being due to the nature of the powder sample and the low etching rates employed. However it should also be noted that FeO is thermodynamically unstable below about 500 °C and that the beam may have brought about the appropriate changes through the reaction:

$$4\,FeO \rightarrow Fe_3O_4 + Fe.$$

This reaction requires that a substantial amount of Fe^{III} (at binding energy 710.8 eV) should persist which is not observed in this case. In addition, a higher concentration of Fe^0 than observed would be expected for the beam initiated break-down of FeO to Fe_3O_4 and Fe. thus retention of Fe_2O_3 is the most likely explanation of the results.

Next, the results obtained for the Fe_3O_4 powder are considered. Spectra for the pre-etched condition showed that air oxidation has occurred to a sufficient extent to convert the surface region, examined by XPS, entirely to Fe_2O_3. This is indicated by the $2p_{3/2}$ line at binding energy of 710.8 eV with a very weak satellite at 719.1 eV. If some of the contribution for the component at 710.8 eV is due to the Fe^{III} ions of Fe_3O_4 (rather than entirely due to the Fe^{III} ions of Fe_2O_3) then a component at ~709.4 eV associated to the Fe^{II} ions of Fe_3O_4 would also be observed. The same results are seen by Allen et al [57] who report that the room temperature spectra of Fe_3O_4 are indistinguishable from many of those obtained for Fe_2O_3 at room temperature. They suggested that the high susceptibility of Fe_3O_4 to air oxidation to Fe_2O_3 is reflected by the free energy of formation (-95.9 kJ/mol) through the following reaction:

$$Fe_3O_4 + (1/4)\,O_{2(air)} \leftrightarrow 3/2\,Fe_2O_3.$$

Ion bombardment for different durations cause the removal of the thin contaminant Fe_2O_3 and expose the Fe_3O_4 surface underneath. Reduction to the metallic state has also been established. Another important feature observed is that the Fe^{III} and Fe^{II} binding energies in the state Fe_3O_4 could not be resolved separately from those

associated with the Fe^{III} ions of Fe_2O_3 and Fe^{II} ions in FeO.

The last iron oxide considered is α-Fe_2O_3. This is the most stable of the iron-oxides. Thus the presence of only the Fe_2O_3 state on the unetched surface is not surprising. The O 1s peak at 532.5 eV (also observed with the previous case of Fe_3O_4) is thought to be due to surface bound oxygen since this binding energy is too low to fall within the range expected for surface bound water (i.e, 533 to 534 eV). Allen et al [57,58], after carrying XPS of in-situ heated Fe_2O_3, report the presence of an oxygen peak at about 532.2 eV. They also attribute this peak to be due to absorbed oxygen rather than absorbed water. A Similar conclusion has been made by Kim and Davies [185] when they obtained an O 1s peak at 532.7 eV from a fresh surface of annealed polycrystal nickel (heated to 800 °C in air and then sanded).

Again, subjecting the surface to progressive periods of ion bombardment reduction of the oxide to the metallic state has been observed which followed the sequence: $Fe^{III} \rightarrow Fe^{II} \rightarrow Fe^0$. This form of reduction behaviour is also reported by Lad and Henrich [72], Mills and Sullivan [53], Chung et al [71] and Brundle et al [70]. Lad and Henrich [72] further report re-oxidation of the reduced surface when it is subjected to annealing after 500 eV argon ion bombardment. Brundle et al [70] report the most unambiguous case of this chemical reduction in their investigation on the sputter etching of an Fe_2O_3 single crystal crushed in an argon atmosphere. Freshly crushed Fe_2O_3 crystals in an inert environment are expected to contain only Fe_2O_3 on the surface as well as in the bulk. They found that within only 50 seconds of ion bombardment a substantial amount of Fe^{II} is produced by reduction of Fe^{III}, even though the etch rate is only a few Å per minute.

7.2.2: The Cobalt oxides

A non-linear background subtraction has been carried out prior to curve synthesis due to the same reasons as discussed for the iron oxides. All binding energy measurements for the cobalt oxides and hydroxides are in good agreement with those

due to McIntyre and Cook [44]. For the CoO sample, sputtering induced reduction to the metallic Co^0 is evident which is in accordance with the studies due to Chuang et al [71] and Langell [90]. However, Langell [90] reports congruent sputtering of CoO at room temperatures and the onset of sputter induced reduction at elevated temperatures around 500 K. The current density used in their study is 20 mA/m^2 compared to that of 56 mA/m^2 used here. The congruent sputtering of CoO then can be explained as being due to insufficient ion beam current density used, although the onset of sputter reduction at elevated temperatures can suggest that in addition to preferential sputtering radiation enhanced diffusion process is responsible for the surface chemical changes even at this low current density.

The intense broad satellite peaks at 7 eV, 5.8 eV and ~2.5 eV above the main photopeak of CoO are due to shake-up processes. The presence of the first two satellites are also confirmed by Frost et al [56] and the presence of the additional third satellite is in agreement with the study of McIntyre and Cook [44].

The Co_3O_4 sample shows a reduction to CoO and then to the metallic cobalt. In the chapter on results in section 5.5.5, two separate curve-fitting results for the unetched Co $2p_{3/2}$ lines are presented to demonstrate the possibility of existence of two extreme cases. For one case it is considered that all the intensity contributions in the peak at 780.0 eV are due to mainly Co^{III} and to a smaller degree due to Co^{II} ions of Co_3O_4. This is very likely since the Co^{II} ions in Co_3O_4 is well reported [56, 71] for showing weak shake-up satellites compared to those due to the Co^{II} ions in CoO. The weak shake-up satellites are measured at ~4.7% of the main photopeak intensity compared to those at 24% for the case with CoO sample. Thus existence of only Co_3O_4 state is confirmed. This is thought to be the case for the unbombarded surface especially since in addition to the weak satellites, the purity of bulk Co_3O_4 has been confirmed by XRD. However, to restrain any dispute that might arise, the other extreme case is also presented where there might be a very small possibility that a significant amount of CoO is present on the unbombarded Co_3O_4 surface (since the

Co^{II} ions in CoO and both Co^{II} and Co^{III} ions in Co_3O_4 cannot be resolved separately, according to their binding energies, in the XPS spectra). The second curve-fit then represents the situation when part of the 780.0 eV energy peak is due to Co^{II} ions in CoO (a contribution for this has been taken into account such that the the satellite intensity now represents ~24% of the Co^{II} peak of CoO, the remainder of the 780.0 eV peak intensity is attributed to the Co_3O_4 state) . Even if the latter was the actual situation for the unbombarded surface, ion bombardment induced reduction of Co^{III} to Co^{II} is undisputable from the evidence of the increase in satellite intensity to ~ 24% of the total intensity of the main peak at 780.0 eV within 10 minutes of exposure to the ion beam. This ion induced reduction behavior of Co_3O_4 is in agreement with the work due to Chuang et al [71].

7.2.3: The oxides TiO_2, ZrO_2, Nb_2O_5, WO_3 and Ta_2O_5

All these oxides reduce to lower oxidation states when subjected to ion bombardment and all except TiO_2 show reduction to the corresponding metallic state. For the TiO_2 and ZrO_2 samples the reduction behavior is in agreement with the investigations of Holm and Storp [52] and Hofmann et al [66]. However these investigations were carried out on thin anodic oxides grown on corresponding metals and hence it is not possible to distinguish whether the presence of the metallic ions are due to the substrate or a direct result of ion induced decomposition. For the ZrO_2 sample, the results found here are contradictory to those of Naguib and Kelly [186], who observed no reduction after bombardment with 35 keV kr^+ ions as detected by electron microscopy. Electron microscopy studies of such ion bombardment induced artifacts cannot be taken as a true representation since it can only detect a new phase when it is sufficiently thick and also the presence of more than one final phase at the steady state makes the interpretation of electron microscopy results unreliable.

The presence of all the states Nb_2O_5, NbO_2, NbO and metallic Nb are found at the steady state after ion bombardment of bulk Nb_2O_5 powder. Reduction down to the NbO state has been reported by Murti and Kelly [42] and whereas Hofmann and Sanz

[66] have reported that NbO is stable against ion bombardment if it is an ion induced reduction product of NbO but decompose as a pure material. Both these investigations however do not give information on the current densities employed. It is possible that the current densities used were too low for reduction to the metallic Nb to occur. In addition, in the study of Hofmann and Sanz [66] anodic oxide of NbO on Nb substrate has been used in the experiments which would mislead the interpretation of the spectra for the presence of the metallic Nb. The results found here for the bombardment induced compositional changes are in agreement with those due to Karulkar [74] and Brown et al [75] and the binding energy values agrees well with those due to Fontain et al [43].

The oxides Ta_2O_5 and WO_3 are probably the most investigated and the least investigated transition metal oxides respectively, in terms of ion bombardment induced compositional changes. Reports in current literature on the composition of the altered layer at steady state after ion bombardment for WO_3 is nearly non-existent. Both Ta_2O_5 and WO_3 show extensive surface compositional changes. The results for the existence of the Ta_2O_5 in addition to the reduced states TaO_2, TaO and Ta at the steady state are in good agreement with those of Hofmann and Sanz [66]. The results for the WO_3 sample agree with the qualitative reports of Kim et al [60] and Holm and Storp [52].

7.2.4: The oxides MgO and Al_2O_3

These oxides are expected to show less surface compositional changes than the oxides discussed above if the role of mass effects play an important part in the mechanism of preferential sputtering. The results here suggest that this is the case. The results for MgO showed a peak widening of ~0.2 eV, which can be interpreted to be due to one of the following two reasons. The first possibility is that the surface MgO has reduced to the metallic Mg due to beam induce reduction. The second is that the bombardment does not chemically reduce or decompose the oxide but the primary

action of ion bombardment is the destruction of Mg-O bonds and the generation of point defects; but due to radiation enhanced diffusion a very fast bond recovery takes place, so that almost all of the Mg-O bonds are re-established. However, the original MgO state has been sufficiently perturbed to give rise to a phase change which can account for the observed peak broadening. The results obtained for the Al_2O_3 sample can also be explained by the latter reasoning. Similar peak broadening behavior for insulating oxides such as SiO_2 has been reported by Hofmann and Thomas [78]; they also attribute this peak broadening to bombardment induced phase changes.

7.3: Dependency on the beam energy and the current density

Amongst the three iron oxides investigated for the effect of ion bombardment, Fe_2O_3 has been chosen for further investigations involving the ion beam parameters because of its surface purity (that is, the XPS investigation on the unbombarded surface of Fe_2O_3 showed no hydroxide contaminant and the surface represented the bulk). The other oxides TiO_2, ZrO_2, Nb_2O_5 and WO_3 are chosen (in addition to their surface purity) because of their narrow main photopeaks which give a higher possibility of detection of the lower oxidation states even at low intensities. Also, the choice of these oxides enabled investigations on a wide mass range of the transition metals.

All oxides except ZrO_2 show that the extent of the surface chemical changes do not depend on the energy in the energy range 1 to 5 keV. In accordance with this, ZrO_2 shows a linear dependence between the range 2 to 5 keV, but the extent of the chemical reduction is lower for the lower beam energy of 1 keV which is evident in figure (5.87). There are no experimental reports in the current literature on the effect of beam energy variation on the extent of the surface compositional changes comparable to this work, thus it is not possible to give a direct comparison with other workers. However, as mentioned in chapter 1, section 5.3.3, Sanz and Hofmann [25] conclude of a linear dependency on energy in the range 2 to 5 keV based on a very crude estimate of the metal concentrations detected by AES. Below the beam energy of 2 keV, an increase in

the total metal intensity has been detected. Since AES cannot give accurate information on the exact chemical state, it is not possible to distinguish whether this detected increase in the metal intensity is due to the metal in the bulk oxide state or due to the metal in the beam induced reduced states. Thus it is not possible to conclude from the works of Sanz and Hofmann [25], whether the 'true' extent of 'chemical damage' increases below 2 keV or decreases. The term 'chemical damage' is used here to mean the extent of surface compositional changes (i.e., the chemical reduction) induced by ion bombardment.

Karulkar [74] has suggested from observations of the Nb 3d photoelectron spectra after subjecting bulk Nb_2O_5 to 0.5 keV and 2 keV Ar^+ ions respectively that the use of lower ion energy for sputtering chemically reduces Nb_2O_5 more effectively. The spectra found is shown in figure (7.1). Whether a conclusion as suggested by Karulkar [74] can be made from observations of figure (7.1) is open to dispute. Since the spectra for 2 keV is very similar to that for 0.5 keV, apart from a slightly more intense shoulder at the binding energy for the original state, it can be equally claimed that the surface chemical damage is approximately the same for the beam energies. Although the presence of the slightly higher shoulder, at the original binding energy value, for the 0.5 keV can only indicate an opposite conclusion to that suggested by Karulker, that is the extent of chemical reduction is lower for the lower beam energy.

In the beam energy range of 1 to 5 keV considered here, the sputtering mechanism proceeds in the linear cascade regime. The beam energy change between 1 and 5 keV is small (compared to the range for which the linear cascade regime is applicable) which can account for the linear dependency of the extent of chemical damage on the energy. It is expected that as the beam energy is increased from 5 keV up to a few tens of keV a change in the surface chemical damage can be expected from the predictions of the linear cascade theory. The same behaviour can be expected for energies below 1 keV. The sputtering yield measurements carried out on oxides and presented as a function of the beam energy (see for example ref. [17] and chapter 1,

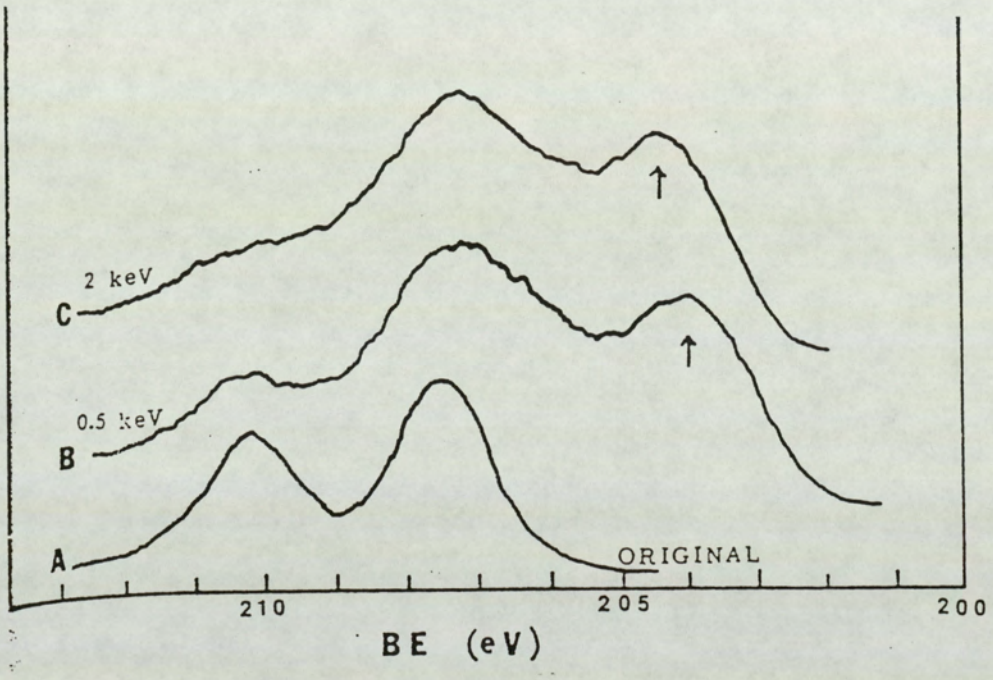

Figure 7.1.

Nb 3d spectra due to Karulkar [90].

section 1.5.3) showed for some oxides (e.g. SiO_2, Ta_2O_5, WO_3 and Nb_2O_5) two general types of behaviour. In the first, the sputtering yield increases with energy in the range ~0.1 keV to ~1 keV, then a linear dependency with energy is shown for the range ~1 keV to ~ a few keV and then decreases again. In the second behaviour, an increase in the sputtering yield is observed for energies up to 1 to 2 keV and then the sputtering yield stays approximately constant with further increase in the energy (see for example figures (1.12, 1.13). It should be pointed out that in these measurement of the sputtering yield as a function of the beam energy, the energy range in the 'plateau' region (i.e., the region in which the sputtering yield stays constant) depends very much on the species of the bombarding ion and on the target concerned [17]. The linear dependency of the extent of the surface chemical damage between 1 to 5 keV for the oxides of Fe_2O_3, Nb_2O_5, TiO_2 and WO_3 and that for ZrO_2 between 2 to 5 keV obtained here is in good agreement with the plateau region being in this energy range.

All oxides investigated for the current density variation show an initial rapid increase in the extent of the surface chemical damage with beam current density (between current densities of 8 and ~60 mA/m^2) and then increases rather slowly towards a steady state (note that this is the case when the extent of the chemical damage at a constant bombardment period of 120 minutes is considered for the different current densities). The oxides ZrO_2, TiO_2 and WO_3 show attainment of a steady state of the surface composition (as shown by the graphs of the (X_M/X_O) surface to bulk ratio plotted as a function of the current density) within a current density increase to ~111 mA/m^2. For the oxides Nb_2O_5 and Fe_2O_3 the indications are that at the maximum current density of 139 mA/m^2, a steady state is approached. The results do not show the existence of a threshold (minimum) current density for the establishment of a changed surface chemical composition under ion bombardment for current densities between 8 and 139 mA/m^2.

Next, it has been confirmed that the extent of the surface chemical damage is dose dependent rather that current density dependent, since plotting the (X_M/X_O) surface to bulk ratio as a function of the dose (in $A.sec/m^2$ units) yields a curve similar to the plot

showing dependency on current density for the 120 minutes of bombardment. However, additional undisputed evidence of dose dependency has also been shown for each of the oxides. As a typical example, these evidences for Nb_2O_5 are discussed below:

Considering the results for the Nb_2O_5 (figure (5.78)), it is seen that for the case of the lowest current density of 8 mA/m^2, reduction to the metallic Nb state is not detected. Results from each of the current density cases of 28, 56, 83 and 139 mA/m^2, show that a minimum dose of ~85 $A.sec/m^2$ (irrespective of the current density) is necessary before reduction to the metallic state can be achieved. This thus explains why the metallic state cannot be detected for the set of experiments at 8 mA/m^2, since at the maximum bombardment time of 120 minutes the dose attained is only 58 $A.sec/m^2$. Additionally, a dose of 101 $A.sec/m^2$ at the current densities of 28 and 56 mA/m^2 respectively gives a value of ~1.3 for the (X_M/X_O) surface to bulk ratio (this values are tabulated in Appendix 1, which gives the results used to plot the figures (5.80c), (5.83c), (5.86c), (5.89c) and (5.92c)); and a dose of ~17 $A.sec/m^2$, at the current densities of 28 and 139 mA/m^2 respectively, gives the (X_M/X_O) values to within 1% of each other.

In agreement with this work, Storp and Holm [89] report that a net rate of reduction of ion bombarded MoO_3 dependence on the current density, but contrary to this work the reduction effects are claimed to be less marked after application of the same dose with a lower ion current density. However, these reports are only qualitative compared with the extensive quantitative investigation carried out here over a large dose range (between ~1 to 1000 $A.sec/m^2$ which is equivalent to a range between $6x10^{18}$ and $6x10^{21}$ in units of $ions/m^2$). The conclusions of Storp and Holm [89] are based on qualitative observations of the Mo 3d spectra for two different ion current densities at the same dose. With only one such measurement the results have a much higher experimental error associated with it than when a large number of measurements are carried out.

In agreement with this work, Langell [90] reports a dose dependency for the oxygen to metal concentration ratio detected by AES. Since in this AES study the ratio of oxygen to the total metal content is considered, the results are not subject to errors which would have arisen if only the metal AES intensity signal is considered to give an indication of the surface chemical changes. The curves showing the dependency on dose (figures (1.8-1.10)) at elevated target temperatures show exactly same trend as found in this investigation (note that here effectively a metal to oxygen concentration is plotted compared with Langell's oxygen to metal concentration ratio, which explain the mirror image of the curves shown in these two studies). However Langell [90] report on a linear behaviour with dose at room temperature. In the room temperature studies carried out here, between 2 to 4 orders of magnitude higher doses than in the studies of Langell [90] have been used. Thus comparisons of the two studies indicate that there is possibly the existence of a threshold dose which is necessary for ion induced surface compositional changes to take place.

7.3.1: Quantification of the influence of dose

The overall influence of the dose on the extent of the surface chemical changes can be quantified by curve-fitting procedures employed on the graphs showing the $(X_M/X_O)^S/(X_M/X_O)^B$ ratios plotted as a function of dose. It is found that for low doses the best fits to the plots are given by power law equations such that the following equations for each of the oxides are obtained:

a) for WO_3: $y = 0.93\ (x^{0.074})$

b) for Nb_2O_5: $y = 0.94\ (x^{0.063})$

c) for ZrO_2: $y = 0.95\ (x^{0.049})$

d) for TiO_2: $y = 1.01\ (x^{0.044})$

e) for Fe_2O_3: $y = 1.07\ (x^{0.035})$

where 'y' is the $(X_M/X_O)^S/(X_M/X_O)^B$ ratio and 'x' is the dose. It should be realized here that the power law equations such as above increase without limit, and never reach

a steady state. Thus, although these equations give the best fit for the data for low doses up to the steady state, they cannot be applied for the steady state situation.

It can however be argued that, the shape of the plots are of an exponential type, given by a general equation as below:

$$y = \delta e^{-b/x^c} + 1 \qquad (b,c \text{ are constants} > 0) \qquad \ldots. (7.1)$$

where $(\delta + 1)$ is the value of y at the steady state. The limits for this equation are:

$$\lim_{x \to \infty} y = \delta e^{o} + 1 = \delta + 1 \qquad \lim_{x \to 0} y = (e^{-\infty}) + 1 = 1$$

So, a steady state is reached for high doses, contrary to the power law equations as above. Rearranging equation (7.1) and taking natural logarithm of both sides:

$\rightarrow \quad (y-1) = \delta e^{-b/x^c}$

$\rightarrow \quad \ln (y-1) = \ln (\delta e^{-b/x^c})$

$\rightarrow \quad \ln (y-1) = \ln \delta - (b/x^c)$

$\rightarrow \quad \ln \delta - \ln (y-1) = (b/x^c)$

taking the natural logarithm of both sides again:

$$\rightarrow \quad \ln \{\ln \delta - \ln (y-1)\} = \ln b - c \ln x \qquad \ldots. (7.2)$$

thus, plotting [ln {ln δ - ln (y-1)}] as a function of (ln x), a straight line should be obtained if an exponential function of the form of equation (7.1) gives the best fit to the $(X_M/X_O)^S/(X_M/X_O)^B$ versus dose plots. However, when the function [ln {ln δ - ln (y-1)}] is plotted against (ln x), the best fit to a straight line is obtained for ZrO_2. The other four oxides show a large deviations from the straight line; the worst deviation is found for WO_3. In figure (7.2) these fits for the best and the worst cases for ZrO_2 and WO_3 respectively together with the corresponding fits due to the power law functions, described above, are shown. From the exponential fits, the following relationships for the best fits to the data are found:

a) for WO_3: $y = 1.45\, e^{-(4.06/x^{0.20})} + 1$

b) for Nb_2O_5: $y = 1.55\, e^{-(5.54/x^{0.24})} + 1$

c) for ZrO_2: $y = 1.30\, e^{-(4.46/x^{0.18})} + 1$

d) for TiO_2: $y = 1.33\, e^{-(3.59/x^{0.15})} + 1$

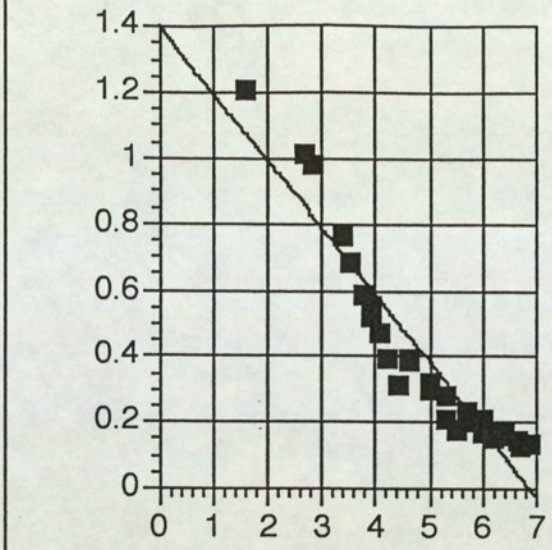

a1

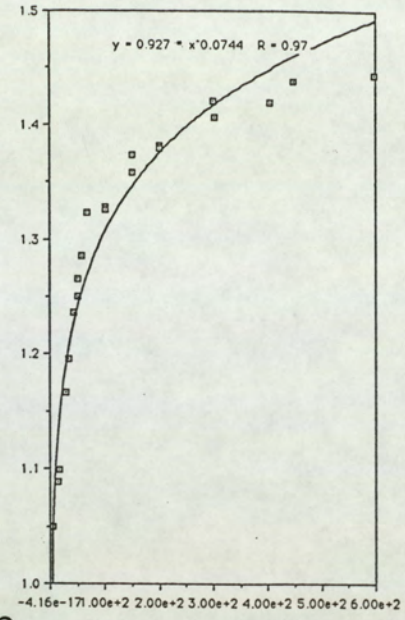

a2

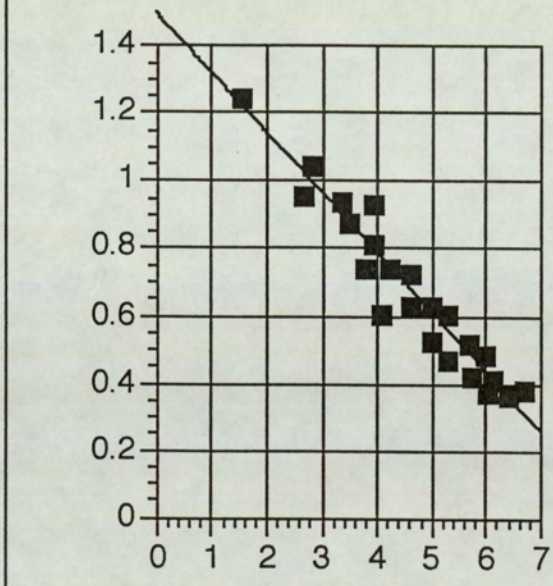

b1

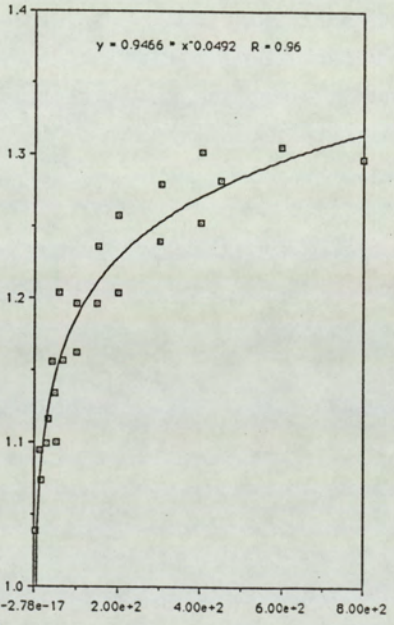

b2

Figure 7.2.

a1) Exponential curve-fit for the data from WO_3.
a2) A power-log curve-fit for the data from WO_3.

b1) Exponential curve-fit for the data from ZrO_2.
b2) A power-log curve-fit for the data from ZrO_2.

e) for Fe_2O_3: $y = 1.40\ e^{-(2.54/x^{0.09})} + 1$

However, from the evidence shown in figure (7.2), it is concluded that for low doses the power law equations give a far better relationship for describing the dose dependency of the extent of the surface chemical damage (up to the steady state). This has a very important implication as far as physics of the sputtering mechanism is concerned; there must be a physical process, at the approach of the steady state, responsible for the deviation from the power law relationship to a linear value. This will be further discussed in section 7.5.

7.4: Comparison of ion bombardment with atom bombardment

Investigations carried out on TiO_2 showed beam induced chemical reduction when subjected to both He and Ar atom bombardment respectively, but there is a significant difference in the degree of reduction between ion bombardment and fast atom bombardment with the latter producing effectively less chemical changes on the surface. This difference in the degree of reduction is particularly more pronounced for the lower mass projectile, i.e, He than for Ar. This investigation gives extensive evidence for a charge induced contribution to the extent of chemical damage. It is therefore not unexpected that this effect is more marked in the lighter projectile. For Ar, in the energy range employed, sputtering is accounted for in terms of the linear cascade theory, whereas the linear cascade regime is not applicable for very light projectiles such as He where the energy transfer is insufficient to generate a cascade. Hence, the sputtering yield will be smaller for the lighter species, but the effect of charge for both projectiles would be the same provided the same dose is applied. Thus if sputtering is due to electronic as well as cascade processes, the former will have a greater proportional effect for He. It is also expected that the extent of chemical damage is suppressed more effectively with a sufficient increase in sputtering yield since a larger fraction of the damaged layer is simultaneously removed and this effect may obscure the differences when Ar bombardment is used.

A combined mass effect and binding energy effect has been shown to be the best

model in the current literature for explaining the preferential sputtering of oxides. This can explain the differences in surface chemical damage created by ions and atoms. The mass effects are due to purely collisional energy transfer and hence cannot be influenced by the charge on the projectile, but binding energies would be considerable affected. Hence, the results obtained here show that the contribution due to binding effects play an important role in oxide sputtering.

A charged particle approaching a surface loses its charge within about 5 Å of the surface. This leads to an increase in the target of the local surface potential until some compensating mechanism establishes dynamic equilibrium. In the absence of an external source of electrons, the compensating mechanism is likely to be electrical breakdown within the oxide. The breakdown would result in an effective decrease in the mean binding energy and would hence produce an enhancement in the oxygen sputtering. The direction of the bombardment induced potential field is also likely to enhance the removal rate of the negatively charged oxygen component. With the neutral particles, although there will still be an increase in local surface potential due to emission of secondary electrons, the effect is significantly smaller. This hypothesis thus can account for the higher degree of surface chemical damage produced by ions than with atoms.

7.5: Comparisons with existing theories and model predictions

It has already been mentioned that for Ar ion bombardment in the energy range considered, a linear cascade regime of sputtering can be assumed. Thus the extent of the ion beam induced chemical damage is well expected to be related to both the mass effects and the binding effects. In chapter 5, figure (5.73), an increase of approximately 40% in the extent of the surface chemical damage is seen when the mass is increased from 24 a.m.u. to 181 a.m.u. (neglecting the scatter in the mass region for iron, reasons for this scatter is explained later). Thus it is seen that the effects due to mass difference are not negligible, contrary to the theoretical models due to Kelly and

co. workers [40,49,87] where the mass effects are neglected. In their model a thermal approach is favoured in attempting to explain specific stoichiometries, which cannot explain the existence of more than one final state in the altered layer at steady state. In addition, no account has been taken for parameters such as beam current density or the dose. Thus this model is grossly insufficient to account for the beam induced artifacts of oxides. This opinion has also been expressed by Kelly in a more recent review [88] in view of the published experimental evidence from this thesis [80] and experimental studies of other workers [52,66,90].

In chapter 6 on theoretical considerations, the model due to Malherbe et al [47] has been discussed. The results found here indicates some agreement with this theory since both the mass and binding energy dependency is observed. The model predictions giving a better agreement for the lower mass (i.e., the metal mass) oxides such as MgO, Al_2O_3, Fe_2O_3, Fe_3O_4, CoO, Co_3O_4 and TiO_2 (up to a mass of ~60 a.m.u.) than for the higher mass oxides such as Nb_2O_5, Ta_2O_5 and WO_3. Neglecting the scatter seen in figure (5.73), a correlation of less than ~7% is seen, for the low mass oxides, between the experimental values of (X_M/X_O) surface to bulk ratios found here with those calculated by Malherbe et al [47]. If the scatter in the iron mass region is taken into account then the correlation is within 22%. The scatter seen in figure (5.73) is due to the low (X_M/X_O) surface to bulk ratio of 1.18 found for FeO, this ratio is expected to be similar to that found for the other iron oxides i.e., ~1.35. The low value of the extent of surface chemical damage found for FeO compared to the other iron oxides is due to fact that the 2p spectra form FeO showed presence of a substantially high contaminant hydroxide species (FeOOH) containing the Fe^{III} ions which can give misleading results. A deviation of ~50% seen in the larger mass metal region (above ~60 a.m.u.) between the calculated values of Malherbe et al [47] and those measured here. This model also, can not account for the dose dependency of the degree of surface chemical damage and the effect of the projectile charge. In addition to the preferential sputtering effects, other mechanisms must also exist which would account

for these parameters.

From the discussions in section 7.4, it is seen that a beam induced surface potential contribution to the cascade sputtering can account for the influence of the projectile charge on the degree of surface chemical damage. The same hypothesis can also explain the dose dependency. This is explained as follows:

The metal oxides considered here are insulators at room temperatures. When these oxides are subjected to ion bombardment, a net positive charge is induced at the outermost atomic layers of the surface (due mostly to neutralization of the incoming ion within a distance of 5 Å of the surface and due to secondary electron emission and to some extent by the negative oxygen loss). A positive potential gradient towards the surface from the bulk is thus created, within the altered layer, which increases as the bombardment proceeds until a compensating mechanism causes dynamic equilibrium. At the dynamic equilibrium a constant value of the induced surface potential exists. It has been proposed in section 7.4 that this compensating mechanism is an electrical breakdown within the altered layer. This would implicate that the altered layer becomes gradually more conductive. No measurement on the conductivity of the bombarded surface has been carried out here. However, an extensive conductivity measurement of the transition metal oxides have been carried out by Kelly's group [40,87]. Their findings for TiO_2 are shown in figures (7.3). In figure (7.3a) a conductivity increase is seen with increment of the ion dose, the steady state value of the conductivity is reached at a dose of ~300 A.sec/m^2. This result is very important since it correlates very well with the value of the dose measured here needed to reach a steady state value of the (X_M/X_O) surface to bulk ratio (see for example figures (5.80c, 5.83c, 5.86c etc)). Thus evidence for electrical breakdown within the oxide due to ion bombardment is given. In addition, figure (7.3b) shows the conductivity measurements due to Kelly and co. workers [87] as a function of the ion energy for Nb_2O_5 bombarded with O^{2+} ions at a constant dose. A threshold value of 5 keV is given.

The quantification carried out in section 7.3.1 has shown that at the approach of the steady state a mechanism must exist which would cause the gradual deviation from

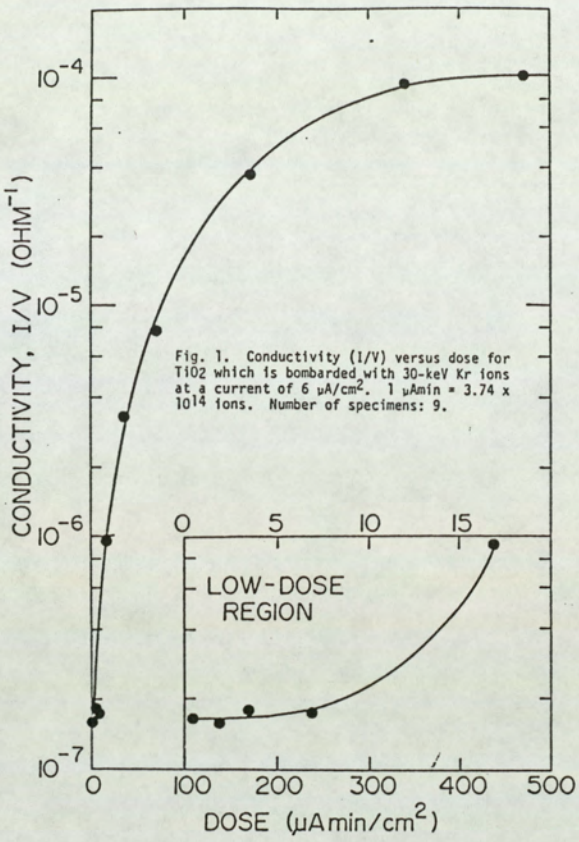

a

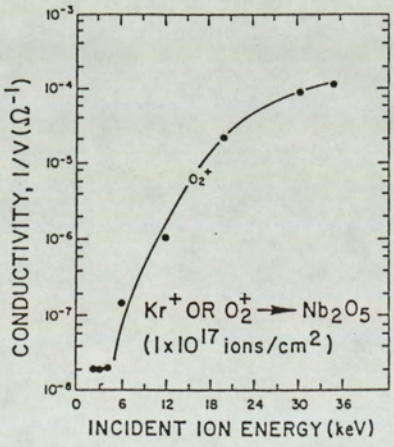

b

Figure 7.3.

a) Conductivity versus dose for TiO_2 bombarded with 30keV Kr^+ ions [186]
b) Conductivity versus ion energy at a dose of 10^{17} ions/cm^2, bombarded with O^{2+} ions.

the power law relationship towards a constant value. This thus gives additional evidence for the electrical breakdown within the altered layer.

In view of the above discussion, the evidence for the beam induced surface potential is profound. Hence an increase in the bombardment dose will increase the surface potential, until electrical breakdown occurs, which in turn results in an effective decrease in the mean binding energy; this thus explains the shape of the (X_M/X_O) surface to bulk ratio versus dose plots.

Thus the investigations carried out here show that the sputtering mechanism in oxides can not be explained by preferential sputtering alone. The existing theoretical models such as those due to Kim et al [60] and Kelly and co. workers [40,49,87], based on thermodynamic equilibrium, are inadequate to apply to the experimental findings. The model due to Malherbe et al [47] show some agreement but, in addition to the mass effects and the binding energy effects, a 'bombardment induced surface potential effect' also has to be incorporated.

Comparisons of the sputtering results given by Langell [90] indicate the possibility of the existence of a threshold dose required to cause preferential sputtering and that temperature dependent mechanisms such as bombardment induced diffusion may also play an active role. All these parameters are needed to be investigated before a general rule for quantifying the sputtering mechanism in oxides can be proposed. The following recommendation for further work is thus made:

1) In-situ temperature measurements of the surface during ion bombardment should be made. Also, XPS altered layer studies at different temperatures (similar to the AES Investigations of Langell [90]) to establish the influence of bombardment induced diffusion on the extent of surface compositional changes for a wide mass range of the metal oxides.

2) Simultaneous measurement of the sputtered flux should be made by collecting the sputtered material and analysing by RBS or SIMS and hence the partial sputtering yields can be found. This should be carried out for a range of different values of the

dose (at a constant beam energy) to establish the dose dependent partial sputtering yields.

3) Similar beam energy variation as carried out here should be performed for a range of energies below 1 keV down to a few hundred eV, and for energies above 5 keV. The partial sputtering yields needs to be determined for the entire energy range.

4) Investigations on the effect of dose dependency below the minimum value employed here to show whether there is a threshold value.

5) In addition to the XPS investigation of the surface, during sputtering SIMS measurements of the sputtered particles can yield a more accurate $(X_M/X_B)^S$ data.

6) In-situ conductivity measurements should be made of the sputtered surface before subjecting it to ion bombardment and after each bombardment period, together with an accurate incident dose measurement both a distance from the target surface and on the surface.

7) Transmission electron microscopy measurement of the altered layer should be made at the steady state. This will give information on the thickness of the altered layer, but more importantly it can show if the altered layer is made up of a number of layers composed of different component depletion regions.

Only from such experimental investigations as above, it will be possible to predict fully the sputtering process of oxides.

CHAPTER 8: Conclusion

X-ray photoelectron spectroscopic investigations on the effect of ion bombardment on transition metal oxides have been carried out. The oxides FeO, Fe_3O_4, Fe_2O_3, CoO, Co_3O_4, TiO_2, ZrO_2, Nb_2O_5, Ta_2O_5 and WO_3 have been investigated. It is shown that Ar^+ bombardment of these oxides lead to a build up of a steady state altered layer on the surface which has been quantitatively characterized by XPS. All oxides show a reduction to the metallic state provided that sufficient doses of the bombarding ions are applied. The reduction path taken by these oxides for 5 keV Ar^+ bombardment at a current density of 56 mA/m^2 are found to be as follows:

1) $FeO\,(Fe^{II}) \Rightarrow Fe^0$
2) $Fe_2O_3\,(Fe^{III}) \Rightarrow FeO\,(Fe^{II}) \Rightarrow Fe^0$
3) $Fe_3O_4\,(Fe^{III}, Fe^{II}) \Rightarrow FeO\,(Fe^{II}) \Rightarrow Fe^0$
4) $Co_3O_4\,(Co^{III}, Co^{II}) \Rightarrow CoO\,(Co^{II}) \Rightarrow Co^0$
5) $CoO\,(Co^{II}) \Rightarrow Co^0$
6) $TiO_2\,(Ti^{IV}) \Rightarrow Ti_2O_3\,(Ti^{III}) \Rightarrow TiO\,(Ti^{II}) \Rightarrow Ti^0$
7) $ZrO_2\,(Zr^{IV}) \Rightarrow ZrO\,(Zr^{II}) \Rightarrow Zr^0$
8) $Nb_2O_5\,(Nb^{V}) \Rightarrow NbO_2\,(Nb^{IV}) \Rightarrow NbO\,(Nb^{II}) \Rightarrow Nb^0$
9) $WO_3\,(W^{VI}) \Rightarrow W_2O_5\,(W^{V}) \Rightarrow WO_2\,(W^{IV}) \Rightarrow W^0$
10) $Ta_2O_5\,(Ta^{V}) \Rightarrow TaO_2\,(Ta^{IV}) \Rightarrow TaO\,(Ta^{II}) \Rightarrow Ta^0$

At the steady state all reduced states as well as the bulk state are present in the altered layer. Similar investigations carried out on the metal oxides MgO and Al_2O_3, showed negligible surface chemical reduction. A phase change rather than definite compositional change has been suggested for these two oxides.

The electron core binding energies of the metal and oxygen components of the various oxides and hydroxides are identified and tabulated. The extent of the surface chemical reduction is quantified in terms of the metal-to-oxygen surface to bulk concentration ratio, i.e. the $\{(X_M/X_O)^S/(X_M/X_O)^B\}$ ratio. Plotting this value against

the cation mass, a ~40% increase in the extent of the surface chemical damage is observed when the cation mass is increased from 24 a.m.u. to 184 a.m.u..

A comparison of fast atom bombardment with ion bombardment on TiO_2 with two different projectile species (i.e. He and Ar) respectively showed beam induced chemical reduction with fast atoms of both species. A significant difference in the degree of the chemical damage is detected between bombardment with fast atoms and ions. For helium, the percentage chemical reduction caused by ions is ~2.5 times that caused by atoms but for argon, this value is between 1 to 1.5. This influence of charge of the projectile on the degree of the surface chemical reduction suggest that oxide sputtering is due to electronic as well as linear cascade processes.

The influence of the ion beam energy on the extent of the surface chemical damage has been investigated for the energy range 1 to 5 keV. A linear dependency is found for the oxides studied except ZrO_2 which show linear dependency for the energy range 2 to 5 keV but a decrease in the extent of the chemical damage for 1 keV beam energy. A similar study carried out with a range of ion current densities between 8 mA/m^2 and 139 mA/m^2 (at a constant beam energy) showed after 120 minutes of bombardment an initial in increase of the surface chemical damage with current density and then flattening-off to a steady state. However, when all the bombardment periods are considered a dose dependency rather than current density dependency is observed. Thus when the same dose is used irrespective of the current density, the same extent of surface chemical damage is seen. The plot of $\{(X_M/X_O)^S/(X_M/X_O)^B\}$ as a function of the dose can be can be explained by a power law relationship for low doses up to the steady state situation.

The results found here support that the linear cascade theory of sputtering can be applied to oxides, since mass effects as well as the binding energy effects have been shown to be important. It has also been shown that oxide sputtering theories based on thermodynamic equilibrium are not applicable. The results for $\{(X_M/X_O)^S/(X_M/X_O)^B\}$ values found here have been compared with the theoretically predicted values of

Malherbe et al [47], in which in accordance with the linear cascade theory a combined mass and binding effects are considered. Some agreement has been found; between ~7 to ~20% agreement is seen for the cation mass of up to 60 a.m.u.. However, it has been shown that in addition to the preferential sputtering effects, an "induced surface potential effect" can also contribute to the overall sputtering mechanism applicable to oxides. Based on the experimental evidence, a hypothesis is given for the bombardment induced surface potential effect to explain the dose dependency and influence of the projectile charge.

For a quantitative model, fully describing the sputtering behaviour of oxides, further investigations are needed. It is recomended that quantitative work comparable to this thesis should be carried out on a dose range below and above those used here. Also required are crucial investigations such as temperature dependency, simultaneous measurements of the partial sputtering yields, in-situ measurement of the conductivity of the sputtered surface, altered layer thickness measurements with TEM etc.

In conclussion, this thesis presents an extensive quantitative determination of the effects of ion bombardment of oxides.

REFERENCES

1. Sigmund P , in "Sputtering by particle bombardment I, Topics in Appl. Phys.", vol. 47, ed: R Behrisch (Springer, Berlin, Heidelburg, New York 1981). Ch. 2, pg 9-67.
2. Sigmund P , Phys. Rev. **184** (1969) 383.
3. Sigmund P , J. Appl. Phys. **50** no 11 (1979) 7261.
4. Powell C J and Larson P E , Appl. Surface Sci. **1** (1978) 186.
5. Wild K, Vacuum **31** (1981) 183.
6. Hofmann S, Analusis **9** no.5 (1981) 181.
7. Andersen H H, Appl. Phys. **18** no. 2 (1979) 131.

8a. Auciello O, J. Vac. Sci. Tech. **19** no.4 (1981) 841

8b. Auciello O, Radiat. Eff. **60** (1982) 1.

9. Harper J M E, Cuomo J J and Kaufmann H R, J. Vac. Sci. Tech. **21** no.3 (1982) 737.
10. Dearnaley G, Radiat. Eff. **63** (1982) 1.
11. Benninghoven A, Rudenauer F G and Werner H. W. in "Secondary ion mass spectroscopy- Basic concepts, instrumental aspects, applications and trends" vol 86 ed: Elving and Winefordner (John Wiley & Sons) (1987).
12. Baun W L, Surf. Interface Anal. **3** no.6 (1981) 243.
13. Reuter W and Baglin J E E, J. Vac. Sci. Technol. **18** no.2 (1981) 282.
14. Patterson W L and Shirn G A, J. Vac. Sci. Tech. **4** (1967) 343.
15. Shimizu and Saeki , Surf. Sci. **62** (1977) 751.
16. Kirschner J and Etzkom H W, Appl. Surf. Sci. **3** (1979) 251.
17. Betz and Wehner, in "Sputtering by particle bombardment II, Topics in Appl. Phys.", vol. 52, ed: R. Behrish (Springer, Berlin, Heidelburg, New York, Tokyo), chapter 2.
18. Coburn J W, Thin Solid Films **64** (1979) 371.

19. Coburn J W, J. Vac. Sci. Technol. **13** (1976) 1037.

20. Andersen H H, J. Vac. Sci. Technol. **16** (1979) 770.

21. Hofmann S and Zalar A , Thin Solid Films **60** (1979) 201.

22. Pickering H W , J. Vac. Sci. Tech. **13** (1976) 618.

23. Ho P S , Surf. Sci. **72** (1978) 253.

24. Ho P S, Lewis J E, Wildman H S and Howard J K, Surf. Sci. **57** (1976) 393.

25. Sanz J M and Hofmann S, Surf. and Int. Anal., **5** no. 5 (1983) 210.

26. Sigmund P, J. Appl. Phys. **50** no. 11 (1979) 7261.

27. Kelly R, Nucl. Instrum. Methods, **149** (1978) 553.

28. Kelly R and Sanders J B, Nucl. Instrum. Methods, **132** (1976)335.

29. Asada T and Quasebarth K, Z. Phys. Chem. A **143** (1929) 435.

30. Gillam E, J. Phys. Chem. Sol. **11** (1959) 55.

31. Fisher T F and Weber C E, J. Appl. Phys. **23** (1952) 181.

32. Wolsky S P, Zdanuk E J and Shooter D, Surf. Sci. **1** (1964) 110.

33. Szymonski M, Bhattacharya R S, Overeijnder H and de Vries A E , J. Phys. D **11** (1978) 751.

34. Liau, Z L, Mayer J W, Homer R and Poate J M , Appl. Phys. letters **30** (1977) 626.

35. Li R S, Tu L X and Sun Y Z, Appl. Surf. Sci. **26** (1986) 77.

36. McIntyre N S and Stanchell F W, J. Vac. Sci. Technol. **16** (1979) 798.

37. Mathiew H J and Landolt D, Proc. 7th Intern. Vac. Congr. & 3rd Intern. Conf. Solid Surfaces (Vienna 1977) 2023.

38. Hofmann S and Sanz J M, Surf. and Int. Anal. **6** no.2 (1984) 78.

39. Paparazzo E, Appl. Surf. Sci. **25** (1986) 1.

40. Parker T E and Kelly R, J. Phys. Chem. Solids **36** (1975) 377.

41. Kelly R and Lam N Q, Radiation Effects **19** (1977) 39.

42. Murti D K and Kelly R, Surf. Sci. **47** (1975) 282.

43. Fontaine R, Caillat R, Feve L and Guittet M J, J. Elect. Spectros. and Rel. Phenom. **10** (1977) 349.

44. McIntyre N S and Cook M G, Anal. Chem. **47** no.13 (1975) 2208.

45. Bach H, Fresenius Z. Anal. Chem. **333** (1988) 373.

46. Bach H, J. Non-Crystalline Solids **102** (1988) 36.

47. Malherbe J B, Hofmann S and Sanz J M, Appl. Surf. Sci. **27** (1986) 355.

48. Kelly R, Radiation Effects **80** (1984) 273.

49. Kelly R, Surf. Sci. **100** (1980) 85.

50. Hofmann S and Sanz J M, Mikrochimica Acta [Wien], Suppl.10 (1988) 135.

51. Carter and Colligon " Ion bombardment of solids" (Heinemann Educational Books Ltd.) 1968.

52. Holm R and Storp S, Appl. Phys. **12** (1977) 101.

53. Mills P and Sullivan J L, J. Phys. D **16** (1983) 723.

54. Andersen C and Hinthorne J, Anal. Chem. **45** (1973) 1421.

55. Holm R and Storp S, Appl. Phys. **9** (1976) 217.

56. Frost D C, McDowell C A and Woolsey I S, Molecular Phys. **27** no.6 (1974)1473.

57. Allen G C, Curtis M T, Hooper A J and Tucker P M, J.C.S. Dalton **14** (1974) 1525.

58. Allen G C, Tucker P M and Wild R K, Philosophical Mag. B **46** no.5 (1982) 411.

59. Fahlman A, Hermin K. Hedman J Nordberg R, Nordling C and Siegbahn K, Nature **210** (1966) 4.

60. Kim K S, Battinger W E, Amy J W and Winograd N, J. Elect. Spectros. Rel. Phenom. **5** (1974) 351.

61. McIntyre N S and Zetaruk D G, J. Vac. Sci. Technol. **14** no.1 (1977) 181.

62. Oechsner H, Schoof H and Stumpe E, Surf. Sci. **76** (1978) 343.

63. Bispinck B, Ganschow O, Weidmann L and Benninghoven A, Appl. Phys. **18**

(1979) 113.

64. Holloway P H and Nelson G C, J. Vac. Sci. Technol. **16** (1979) 793.
65. Taglauer E and Heiland W, Appl. Phys. Lett. **33** (1978) 950.
66. Hofmann S and Sanz J M, J. Trace and Microprobe Techniques **1** no.3 (1982-1983) 213.
67. Murti D K, Kelly R, Lieu Z L and Poate J M, Surf. Sci. **81** (1979) 571.
68. McIntyre N S and Zetaruk D G, Anal. Chem. **49** (1977) 1521.
69 Mitchell D F, Sproule G L and Graham M J, J. Vac. Sci. Technol. **18** no 3 (1981)690.
70. Brundle C R Chuang T J and Wandelt K, Surf. Sci. **68** (1977) 459.
71. Chuang T J, Brundle C R and Wandelt K, Thin Solid Films **53** (1978) 19.
72. Lad R J and Henrich V E, Surf. Sci. **193** (1988) 81.
73. Murti K and Kelly R, Thin Solid Films **33** (1976) 149.
74. Karulkar P C, J. Vac. Sci. Technol. **18** (1981) 63.
75. Brown A, Van den Burg J A and Vickerman J C, J. Chem. Soc., Chem. Commun. (1984) 1684.
76. Thomas S, Surf. Sci. **55** (1976) 754.
77. McGuire G, Surf. Sci. **76** (1978) 130.
78. Hofmann S and Thomas J H, J. Vac. Sci. Technol. B1 no.1 (1983) 43.
79. Thomas J H and Hofmann S, J. Vac. Sci. Technol. A3 no.5 (1985) 1921.
80. Choudhury T, Saied S O, Sullivan J L and Abbot A M, J. Phys D **22** (1989) 1185.
81. Saied S O, Sullivan J L, Choudhury T and Pearce C G, Vacuum **38** no. 8-10 (1988).
82. Haff P K, Appl. Phys. Lett. 31 no. **4** (1977) 259.
83. Liau Z L, Mayer J W, Brown W L and Poate J M, J. Appl. Phys. **49** (1978) 5295.
84. Garrison B J, Surf. Sci. **114** (1982) 23.
85. Sigmund P, Oliva A and Falcon G, Nucl. Instrum. Methods **194** (1982) 541.

86. Taglauer E and Heiland W, In Proc. Symp. on Sputtering ed: Verga P, Betz G and Vienbock F P, Vienna (1980) 423.

87. Kelly R, in "Ion beam modification of insulators" vol. 2 ed: Mazzoldi P and Arnold G W (Elsevier) 1987.

88. Kelly R, Mat,. Sci. Eng. **A115** (1989) 11.

89. Storp S and Holm R, J. Elect. Spectros. Rel. Phenom. **16** (1979) 183.

90. Langell M A, Surf. Sci. **186** (1987) 323.

91. Ishitani T and Schimizu R, Phys. Lett. **46A** (1974) 487.

92. Robinson H R, Phil. Mag. S.6 **50** (1925) 241.

93. Nordling C, Sokolowsli E and Siegbahn K, Phys. Rev. **105** (1957) 1676.

94. Siegbahn K, "ESCA- atomic molecular and solid state structure studied by means of electron spectroscopy" Nova Acta Regiae Societatis Scientriarum Upsaliensis, vol. 20 ser.IV (1965).

95. Siegbahn K, "ESCA applied to free molecules" Pub. North Holland (Amsterdam) 1969.

96. Siegbahn K, Rev. Modern Phys. **54** no. 3 (1982) 709.

97. Brundle C R and Roberts M W, Proc. Roy. Soc. **A331** (1972) 383.

98. Seah M P, Surf. Sci. **32** (1972) 703.

99. Hagstrom S, Nordling C and Siegbahn K, Z. Physik **178** (1964) 439-444.

100. Fahlman A, Harmin K, Hedman J, Nordberg R, Nordling C and Siegbahn K, Nature **4** (1966) 210.

101. Gelius U, Basilier E, Svensson S, Bergmark T and Seigbahn K, J. Elect. Spectros. Rel. Phenom. **2** (1974) 405.

102. Brundle C R and Baker A D, "Electron Spectroscopy: Theory, Techniques and Application vol 1, ed: Brundle and Baker, (New York: Academic) 1977.

103. Carlson T A, Photoelectron and Auger Spectroscopy, (New York: Plenum) 1975.

104. Briggs and Seah (Ed), "Practical surface analysis: by Auger and X-ray Photoelectron Spectroscopy. John Wiley and Sons (Chicester, New York,

Brisbane, Toronto, Singapore) 1983.

105. Gosh P K, "Introduction to photoelectron spectroscopy" ed: Elving P J and Winefordner J D, John Wiley and Sons (Chicester, New York, Brisbane, Toronto, Singapore) vol 67 1983.

106. Williams R H, Contem. Phys. **19** no.5 (1978) 384-414.

107. Williams R H, Srivastava G P and McGovern I T, Rep. Prog. Phys. **43** (1980) 1357-1413.

108. Briggs D (Ed), "Handbook of X-ray and Ultra-violet Photoelectron Spectroscopy" Heyden (London) 1977.

109. Bahr J L, Contemp. Phys. **14** no.4 (1973) 329-355.

110. Jenkin J G, Leckey R C G and Liesegang J, J. Electr. Spectros. Rel. Phenom. **12** (1977) 1.

111. Jenkin J G, Liesegang J, Leckey R C G and Riley J D, J. Electr. Spectros. Rel. Phenom. **15** (1979) 307.

112. Weightman P, Rep. Prog. Phys. **45** (1982) 753.

113. Chang C C, "Characterization of Solid Surfaces" ed: Kane P F and Larrabee G B (Plenum New York) 1974 chapter 20.

114. Chang C C, J. Vac. Sci. Technol. **18** no.2 (1981) 276-281.

115. Hercules D M, Anal. Chem. 48 (1976) 294R.

116. Jenkin J G, J. Electr. Spectros. rel. phenom. **23** (1981) 187.

117. Albridge R G, in "Techniques of Chemistry vol-1: Physical Methods of Chemistry" ed: Weissoberger A and Rossiter B W, 1972, 308-308.

118. Fadley C, Geoffray J, Hagstrom S and Hollander , J. Nuclr. Instr. Methods **68** (1969) 177.

119. Koopman T, Physica **104** (1934) 1.

120. Briggs D and Riviera J C, in "Practical Surface Analysis by Auger and X-ray Photoelectron Spectroscopy." ed: Briggs D and Seah M P (John Wiley and Sons Ltd.) 1983.

121. Jolly W L, in "Electron Spectroscopy: Theory, Techniques and Applications" vol.1 ed: Brundle C R and Baker A D (New York: Academic) (1977) 119-149.

122. Fadley C S, in "Electron Spectroscopy: Theory, Techniques and Applications" vol.2 ed: Brundle C R and Baker A D (New York, Academic) (1978) 1-156.

123. Shirley D A, Adv. Chem. Phys. **23** (1973) 85.

124. Lindberg BJ, Hamrin K, Johansson G, Gelius U, Fahlman A, Nordling C and Siegbahn K, Phys. Scrip. **1** (1970) 286.

125. Gelius U, Roos B and K, Chem. Phys. Lett. **4** (1970) 471.

126. Carver J C, Gray R C and Hercules D M, J. Amer. Chem. Soc. **96** (1974) 6851.

127. Rosencwaig A, Wertheim G K and Guggenheim H J, Physical Rev. Letts. **27** no.8 (1971) 479.

128. Frost D C, McDowell C A and Ishitani A, Mol. Phys. **24** (1972) 861.

129. Yin L, Adler I, Tsang T, Matiezo L Z and Grim S O, Chem. Phys. Lett. **24** (1974) 81.

130. Carlson T A, Carver J C, Saethre L J, Santibanez F G and Vernon G A, J. Elect. Spectros. Rel. Phenom. 5 (1974) 247-258.

131. Briggs D and Gibson V A, Chem. Phys. Lett. **25** (1974) 493.

132. Fadley C S and Shirley D A, Freeman A J, Bagus P S and Mallow J F, Phys. Rev. Lett. **23** no.24 (1969) 1397.

133. Fadley C S and Shirley D A, Phys. Rev. **A2** (1970) 1109-1120.

134. Gupta R P and Sen K, Physical Rev. B 10 no. **1** (1974) 71.

135. Kittel C, "Introduction to solid state physics" (John Willey and Sons) 1976.

136. Ritchie R H, Phys. Rev. **106** (1957) 874.

137. Inglesfield J E, J. Phys. C: Solid State Phys. **16** (1983)403-416.

138. Seah M P and Dench W A, Surf. Interface Anal. **1**(1979)2.

139. Pijolat M and Hollinger G, Surf. Sci. **105** (1981) 114.

140. Ebel B, Surf. Interface Anal. **3** no.4 (1981) 149.

141. Seah M P, Surf. Interface Anal. **2** (1980) 222.

142. Heddle D W O, J. Phys **E4** (1971) 589.

143. Reilman R F, Msezane A and Manson S T, J. Electr. Spectros. REl. Phenom. **8** (1976) 389.

144. Schofield J H, J. Electr. Spectros. rel. phenom. **8** (1976) 129.

145. Shirley D A, Phys. ReV. **B5** (1972) 4709.

146. Bishop H E, Surf. Interface anal. **3** (1981) 272.

147. Proctor A and Sherwood P, Anal. Chem. **54** (1982) 13.

148. Wagner C D, Riggs W M, Davies L E, Moulder J F, and Muilenberg G E, "Handbook of X-ray Photoelectron Spectroscopy", Perkin-Elmer Corp., Minnesota (1979).

149. Evans S, Pritchard R G and Thomas, J. Phys. **C4** (1977) 2483.

150. Wagner C D, Anal. Chem. **49** (1977) 1282.

151. Penn D R, J. Electer. Spectros. Rel. Phenom. **9** (1976) 29.

152. Johansson G, Hedman J, Berndtsson A, Klasson M and Nilsson R, J. Electr. Spectros. Rel. Phenom. **2** (1973) 295-317.

153. Bird R J and Swift P, J. Electr. Spectros. Rel. Phenom. **21** (1980) 227-240.

154. Dianis W P and Lester J E, Anal. Chem. **45** (1973) 1416.

155. Hnatowich D J, Hudis J, Perlman M L and Ragnini R C, J. Appl. Phys. **42** (1971) 4883.

156. Swift P, Surf. Interface Anal. **4** (1982) 47.

157. Hunt C P, Stoddart C T H and Seah M P, Surf. Interface Anal. **3** (1981) 157.

158. Copperthwaite R G, Surf. Interface Anal. 2 no. **1** (1980) 17.

159. Marien J. and De Pauw E, Int. J. Mass Spect. Ion Phys. **43** (1982) 233.

160. American Standard For Testing of Materials.

161. Yates K, Barrie A and Street F J, J.Phys. E **6** (1973) 130.

162. Steckelmacher W, J> Phys. E **6** (1973) 1061.

163. Bishop H E, Coad J P and Rievera J C, J. Electr. Spectros. Rel. Phenom. **1** (1972/1973) 389.

164. XSAM 800 operating manual.

165. Purcell E M, Phys. ReV. **54** (1938) 818.

166. Kuyatt C E and Simpson J A, Rev. Sci. Instrum. **38** no.1 (1967)103.

167. Sherwood P, "Handbook of data analysis software" (1984).

168. Sherwood P, in "Practical surface analysis by Auger and X-ray photoelectron spectroscopy" ed: Briggs D and Seah M P, (John Willey & Sons) (1983) pg. 437.

169. Proctor A and Sherwood P M A, Anal, Chem. **54** (1982) 13.

170. Proctor A and Sherwood P M A, Anal, Chem. **52** (1980) 2315.

171. Handbook of KRATOS MACROBEAM ion source.

172. Saied S O, Sullivan J L and Pearce C G, Vacuum **38** no.6 (1988) 469.

173. Saied S O, Sullivan J L and Fitch R K, Vacuum **38** no.2 (1988) 111.

174. Franks J and Ghander A M, VAcuum **24** no.10 (1974) 489.

175. Fitch R K, Khorassany M and T Mawlood, Proc 7th Int Vacuum Congr 3rd Int conf, Vienna (1977).

176. Franks J, Int. J. Mass Spec. Ion Phys. **H6** (1983) 343.

177. Ansell R O, Dickinson T, Povey A F and Sherwood P M A, J. Electroanal. Chem. **98** (1979) 79.

178. Powell C J, Erickson N E and Madey T E, J. Elecrtr. Spectros. Rel. Phenom. **17** (1979) 361.

179. Asami K, J. Elect. Spectros. Rel. Phenom. **9** (1976) 469.

180. Pauling L, "The nature of the chemical bond" 3rd ed.(Cornell University Press, Ithaca NY) (1960).

181. Kerr J F and Trotman-Dickenson A F, CRC Handbook of Chemistry and Physics ed: Weast R C 53rd ed. (CRC Press, Cleveland OH) (1972) pg.F-183.

182. Lauder W F, "the electron repulsion theory of the chemical bond (Reinhold, New York) (1967) 33.

183. Pivin J C, J. Mat. Sci. **18** (1983) 1267.

184. McIntyre N S, in: "in "Practical Surface Analysis by Auger and X-ray

Photoelectron Spectroscopy. ed: Briggs D and Seah M P (John Wiley and Sons Ltd) (1983) chapter 10.

185. Kim K S and Davies R E, J. Electr. Spect. Rel. Phenom. **1** (1972/73) 251.

186. Naguib H M and Kelly R, J. Nucl. Mat. **35** (1970) 293.

187. Parker T E A and Kelly R, in: "ion implantation in semiconductors and other materials: ed: Croder B L (Plenum New York) (1973) 551.

Appendix 1.

Dose dependency results.

Dose (A.s./m^2)	5 keV	2 keV
4.80	1.05	1.05
14.40	1.09	1.09
28.80	1.17	1.17
43.20	1.24	1.24
57.60	1.29	1.29
16.80	1.10	1.10
50.40	1.25	1.25
100.80	1.33	1.33
151.20	1.36	1.36
201.60	1.38	1.38
33.60	1.20	1.20
100.80	1.33	1.33
201.60	1.38	1.38
302.40	1.41	1.41
403.20	1.42	1.42
49.80	1.27	1.26
149.40	1.37	1.38
298.80	1.42	1.42
448.20	1.44	1.44
597.60	1.44	1.44
66.60	1.32	
199.80	1.42	
399.60	1.44	
599.40	1.44	
799.20	1.46	
83.40	1.37	
250.20	1.43	
500.40	1.45	
750.60	1.45	
1000.80	1.46	

Table A.1.

(X_M/X_O) surface to bulk ratios at constant beam energy of 2keV and 5keV for WO_3, as a function of the dose.

Dose (A.s./m^2)	5 keV	2 keV
4.80	1.13	1.13
14.40	1.19	1.19
28.80	1.24	1.24
43.20	1.25	1.25
57.60	1.26	1.26
16.80	1.17	1.17
50.40	1.23	1.23
100.80	1.26	1.26
151.20	1.27	1.27
201.60	1.29	1.29
33.60	1.21	1.21
100.80	1.26	1.26
201.60	1.29	1.29
302.40	1.31	1.31
403.20	1.32	1.32
49.80	1.26	
149.40	1.28	
298.80	1.29	
448.20	1.32	
597.60	1.33	
66.60	1.27	
199.80	1.30	
399.60	1.31	
599.40	1.33	
799.20	1.34	
83.40	1.29	
250.20	1.31	
500.40	1.33	
750.60	1.35	
1000.80	1.36	

Table A.2.

(X_M/X_O) surface to bulk ratios at constant beam energy of 2keV and 5keV for Fe_2O_3, as a function of the dose.

Dose (A.s./m^2)	5 keV	2 keV
0.96	1.01	1.01
4.80	1.02	1.02
14.40	1.07	1.07
28.80	1.14	1.14
57.60	1.20	1.20
3.36	1.02	1.03
16.80	1.12	1.12
50.40	1.26	1.25
100.80	1.32	1.32
201.60	1.37	1.36
6.72	1.02	1.02
33.60	1.12	1.13
100.80	1.25	1.25
201.60	1.32	1.32
403.20	1.38	1.37
9.96	1.04	1.04
49.80	1.23	1.23
149.40	1.31	1.31
298.80	1.36	1.36
597.60	1.39	1.38
16.68	1.11	
83.40	1.30	
250.20	1.38	
500.40	1.44	
1000.80	1.49	

Table A.3.

(X_M/X_O) surface to bulk ratios at constant beam energy of 2keV and 5keV for Nb_2O_5, as a function of the dose.

Dose (A.s./m^2)	5 keV	2 keV
0.96	1.02	1.02
4.80	1.06	1.06
14.40	1.12	1.12
28.80	1.16	1.16
57.60	1.20	1.20
3.36	1.04	1.04
16.80	1.12	1.12
50.40	1.20	1.20
100.80	1.23	1.23
201.60	1.26	1.26
6.72	1.08	1.08
33.60	1.20	1.20
100.80	1.26	1.25
201.60	1.28	1.28
403.20	1.29	1.28
9.96	1.13	1.12
49.80	1.24	1.24
149.40	1.28	1.27
298.80	1.30	1.30
597.60	1.32	1.31
13.32	1.14	
66.60	1.25	
199.80	1.29	
399.60	1.31	
799.20	1.32	
16.68	1.15	
83.40	1.26	
250.20	1.29	
500.40	1.31	
1000.80	1.32	

Table A.4.

(X_M/X_O) surface to bulk ratios at constant beam energy of 2keV and 5keV for TiO_2 , as a function of the dose.

Dose (A.s./m^2)	5 keV	2 keV
4.80	1.04	1.04
14.40	1.09	1.05
28.80	1.10	1.06
43.20	1.16	1.08
57.60	1.20	1.09
16.80	1.07	1.08
50.40	1.10	1.10
100.80	1.20	1.17
151.20	1.24	
201.60	1.26	1.24
33.60	1.12	
100.80	1.16	
201.60		
302.40	1.28	
403.20	1.30	
49.80	1.13	
149.40	1.20	
298.80	1.24	
448.20	1.28	
597.60	1.31	
66.60	1.16	
199.80	1.20	
399.60	1.25	
799.20	1.30	

Table A.5.

(X_M/X_O) surface to bulk ratios at constant beam energy of 2keV and 5keV for ZrO_2 , as a function of the dose.

Appendix 2.

Publications.

J. Phys. D: Appl. Phys. **22** (1989) 1185–1195. Printed in the UK

Reduction of oxides of iron, cobalt, titanium and niobium by low-energy ion bombardment

T Choudhury, S O Saied, J L Sullivan and A M Abbot

Department of Electrical and Electronic Engineering and Applied Physics, Aston University, Birmingham B4 7ET, UK

Received 20 July 1988, in final form 20 March 1989

Abstract. Ion-beam bombardment of solid surfaces with rare gas ions is used extensively in conjunction with XPS and AES for surface cleaning and depth profiling. It is sometimes not appreciated that the process can give rise to extensive chemical changes in the surface to be examined.

The purpose of this investigation is to study this ion-induced chemical damage. As a vehicle for this, changes in the elemental chemical states associated with some transition metal oxides have been examined using XPS, when the oxides were subject to progressive periods of argon ion bombardment. Chemical reduction of all oxides investigated has been observed and the data have been compared with theoretical predictions from a current model for preferential oxygen removal.

Measurements of the core electron energy levels in oxides and some hydroxides of iron, cobalt, titanium and niobium have been made and the results are tabulated.

1. Introduction

Ion-beam bombardment of solid surfaces with rare gas ions is used extensively as a method of surface analysis in such techniques as secondary ion mass spectroscopy (SIMS) and ion scattering spectroscopy (ISS) and in conjunction with other techniques such as x-ray photoelectron spectroscopy (XPS) and Auger electron spectroscopy (AES) for surface cleaning and depth profiling. It is perhaps not always recognised that such ion-beam bombardment may change the chemical nature of the surface to be examined. For example, there have been various reports of changes in oxidation state of metal oxides due to ion bombardment (Kim *et al* 1977, Kelly and Lam 1973, McIntyre and Zetaruk 1977). These changes are usually manifested by reduction of the metal oxide. Mills and Sullivan (1983) in their investigation of core-level electron energy states in iron and its oxides reported rapid reduction of iron such that $Fe^{III} \rightarrow Fe^{II} \rightarrow Fe^{0}$.

This form of ion-induced chemical damage is almost certainly due to what is conventionally called preferential sputtering of the oxygen from the oxide matrix. Models have been proposed to account for the preferential removal of oxygen and ion-induced oxide reduction (Malherbe *et al* 1986, Kelly 1980) based on Sigmund's classification of sputtering events and sputtering yield equation (Sigmund 1969, 1981). The model due to Malherbe *et al* (1986) uses a collisional approach to explain the average composition in terms of the metal-to-oxygen concentration ratio, C_M/C_O, whereas in the model due to Kelly (1980) a thermal approach is favoured in attempting to explain specific stoichiometries.

It is the purpose of this investigation to study in detail the changes in oxidation state of the transition metal oxides FeO, Fe_3O_4, α-Fe_2O_3, CoO, TiO_2 and Nb_2O_5 brought about by the bombardment of 5 keV argon ions. X-ray photoelectron spectroscopy was chosen to monitor the changes through examination of core-level electron energies, when the oxides were subject to successive periods of ion bombardment. A secondary object of this investigation is a careful measurement of the energies associated with core-level lines of the various chemical states of the metal and oxygen in oxides and hydroxides and these measured values are tabulated in this work for future reference. In addition, the collisional model due to Malherbe *et al* (1986) is examined in terms of the data obtained in this investigation.

2. Experimental details

The analysis described in this work was carried out using a Kratos XSAM 800 electron spectrometer,

0022-3727/89/081185 + 11 $02.50

employing Mg Kα as the exciting radiation. The base pressure inside the experimental chamber was always better than 10^{-9} Torr.

A Kratos Macrobeam ion gun was used for the argon ion bombardment. All experiments were carried out at a beam energy of 5 keV, rastered area of 4 mm × 9 mm and current density of 2.6 μA cm^{-2}. Under these conditions the estimated rate of metal oxide surface removal was ~5 Å min^{-1}.

The oxides used were commercially obtained high-purity powders and all were first bulk characterised by means of powder x-ray diffraction. The oxide surfaces were prepared by intimately mixing oxide powder with gold powder and then pressing into high-purity lead sheet. All binding energy measurements were then made with reference to the Au $4f_{7/2}$ line at 84.0 eV unless otherwise stated.

Samples of the oxides FeO, Fe_3O_4, α-Fe_2O_3, CoO, TiO_2 and Nb_2O_5 were each studied in turn. Initial measurements were made on the oxides in their air-exposed form, before being successively etched by argon ions for periods of 1 min, 10 min, 30 min, 1 h, 2 h and 3 h duration. Spectra were recorded between each period of argon ion bombardment.

Each analysis was performed several times to ensure reproducibility of results.

The spectrometer was interfaced with an Apple IIe microcomputer system which was employed for instrumental control, data collection and processing. Spectral procesing and curve fitting was achieved using the methods described by Sherwood (1983).

3. Results and discussion

For each sample examined during this investigation, the metal component core lines (for example for iron the Fe $2p_{1/2}$, $2p_{3/2}$, 3p and 3s lines), O 1s, C 1s and Au $4f_{7/2}$ spectral lines were recorded. The C 1s line was used as a secondary reference, but also served to indicate the extent of hydrocarbons present on the sample surfaces. For all samples in the air-exposed unetched condition the carbon line was invariably the most intense spectral peak. The O 1s spectra gave valuable additional information on the sample surface oxidation states.

To distinguish quantitatively the contribution of different oxidation states curve synthesis was employed on the measured spectral peaks. The procedure employed was the Gauss–Newton least-squares method described by Sherwood (1983). Prior to curve fitting a Shirley non-linear background subtraction was employed on the majority of the spectra examined. There have been criticisms of background subtraction techniques in curve-fitting procedures, hence in this study comparisons of synthesised peak intensities taken from Nb_2O_5 data were made with and without non-linear background subtraction. No significant differences were found in the measured intensities of the synthetic peaks, the maximum variation being about 6%. However, it is noted that the background rise of the Nb 3d peak at the binding energy of approximately 210 eV is relatively modest compared to the metal oxides of iron, cobalt and titanium. Thus, it is possible that comparisons of the peak intensities obtained for these latter oxides with and without a non-linear background subtraction may not always give approximately the same result.

In this work the effect of argon ion bombardment on the oxides FeO, Fe_3O_4, α-Fe_2O_3, CoO, TiO_2 and Nb_2O_5 was studied. Before this was attempted, however, the binding energies of the components of the oxide were measured. These experimentally determined values are shown in table 1. Table 2 shows the relative concentration results of the O 1s spectra obtained for the different oxides investigated over the various periods of ion bombardment.

We now consider the oxides in turn.

3.1. FeO

As mentioned above the $2p_{1/2}$, $2p_{3/2}$, 3p and 3s spectral peaks for iron were recorded and curve-fitting techniques were applied to each peak. The results obtained over these peaks were found to be consistent, hence in the interest of brevity, only the results for the most intense Fe $2p_{3/2}$ lines and the O 1s lines will be reported here. Figure 1 shows a series of such spectra for the FeO powder surface for different periods of argon ion bombardment.

For the air-exposed unetched surface the curve-fitting procedure on the Fe $2p_{3/2}$ peak revealed two components, one at binding energy 711.8 eV and the other at 710.8 eV, both with FWHM of 3.3 eV. These values are in agreement with the binding energies of 711.9 and 711.0 eV reported by McIntyre and Zetaruk (1977) for the Fe^{III} components in FeOOH and α-Fe_2O_3 respectively. These authors quote FWHM values of about 3 eV, the broad peak being due to multiplet splitting. It thus appears that the surface of our FeO powder has oxidised to form α-Fe_2O_3 which has further reacted with atmospheric water vapour to form FeOOH.

The O 1s spectrum confirms this view. Two major peaks may be observed in this spectrum, figure 1(*a*), at binding energies of 530.4 and 531.9 eV (FWHM = 1.8 eV) with a third broader less intense peak centred at 533.2 eV binding energy with a FWHM of 2.1 eV.

The peak at 530.4 eV is due to the metal oxygen bond and the higher-binding-energy peak is due to the hydroxide bond (OH). This view is supported by the work of Mills and Sullivan (1983), Allen *et al* (1974) and Habier *et al* (1976), although Brundle *et al* (1977) suggest that the higher-energy peak could be due to non-stoichiometric surface oxidational states. It has been suggested (McIntyre 1983) that the broad O 1s peak centred at 533.2 eV is probably due to a multiplicity of chemically and physically bonded water on and within the surface.

Within 10 minutes of argon ion bombardment, the

Table 1. Measured binding energy values (±0.2 eV) and full width at half maximum (±0.2 eV). The iron, cobalt and niobium compounds were calibrated with the Au $4f_{7/2}$ peak at 84.0 eV; the titanium compounds were calibrated with the C 1s peak at 284.6 eV.

Identity			Binding energy (eV)	FWHM (eV)
Iron compounds (Fe $2p_{3/2}$)	α-Fe_2O_3	Fe^{III}	710.8	3.3
	Fe_3O_4	Fe^{III}	710.8	3.3
		Fe^{II}	709.4	3.3
	FeO	Fe^{II}	709.4	3.3
	FeOOH	Fe^{III}	711.8	3.3
	Fe^0		707.2	2.0
	O 1s	Metal bond	530.4	1.8
		Hydroxide bond	531.9	1.8
Cobalt compounds (Co $2p_{3/2}$)	CoO	Co^{II}	780.2	2.8
	$Co(OH)_2$	Co^{II}	781.3	3.2
	CoOOH	Co^{III}	780.2	1.8
	Co^0		778.5	1.7
	O 1s	Metal bond	530.2	1.8
		Hydroxide bond	531.6	1.8
Niobium compounds (Nb 3d)	Nb_2O_5	Nb^V (doublet)	210.3	1.9
			207.6	1.9
	NbO_2	Nb^{IV} (doublet)	208.6	1.9
			205.9	1.9
	NbO	Nb^{II} (doublet)	207.1	1.9
			204.4	1.9
	Nb^0	(doublet)	205.7	1.3
			202.9	1.3
	O 1s	Metal bond	531.0	1.8
Titanium compounds (Ti 2p)	TiO_2	Ti^{IV} (doublet)	458.7	1.5
			464.6	2.5
	Ti_2O_3	Ti^{III} (doublet)	457.2	2.0
			463.0	2.5
	TiO	Ti^{II} (doublet)	455.3	2.0
			461.0	2.3
	O 1s	Metal bond	530.5	1.6
		Hydroxide bond	531.9	1.6

Fe $2p_{3/2}$ spectra, figure 1(*c*), shows an intensity reduction for the FeOOH and α-Fe_2O_3 peaks. Also after this period, examination of the Fe $2p_{3/2}$ shows the appearance of a peak of binding energy 709.4 eV (FWHM = 3.2) with an associated satellite at 715.2 eV. The peak at 709.4 eV is the most intensive peak and is due to Fe^{II} in FeO. The Fe^{II} state is a high spin state and the associated satellite is expected to be due to a shake-up process.

Brundle *et al* (1977), McIntyre and Zetaruk (1977) and Mills and Sullivan (1983) quote binding energies of 709.7, 709.5 and 709.6 eV respectively and these authors suggest that the satellite appears at about 6 eV above the main peak.

The appearance of the 709.4 eV peak and the diminution of the hydroxyl component in the oxygen spectra (see table 2) indicates the removal of surface contaminants, but the most important feature is the appearance in the Fe $2p_{3/2}$ spectrum, figure 1(*c*), of a much narrower peak at binding energy 707.2 eV (FWHM = 2.0) which is due to Fe^0. This indicates that partial reduction of the oxide has taken place due to ion bombardment. This agrees well with binding energy values for Fe^0 determined by other workers, for example McIntyre and Zetaruk (1977) at 703.3 eV and Allen *et al* (1974) at 706.9 eV.

Further bombardment for periods of 1, 2 and 3 h produced changes in the intensity ratio of the components in the spectra. For example the Fe^{II}:Fe^0 ratio (satellite contribution for the Fe^{II} has not been taken into account) in the Fe $2p_{3/2}$ spectrum reduced from 8.3 at 10 min bombardment time to 2.4 after 2 h when this ratio stabilised. Figure 1(*d*) shows the spectrum after 2 h of ion bombardment. The retention of small amounts of α-Fe_2O_3 and FeOOH in the sample is most probably due to the nature of the powder sample used and the very low etching rates employed. However, it may also be noted that FeO is thermodynamically unstable below about 500 °C and that the beam may have brought about the appropriate change through the reaction

$$4\,FeO = Fe_3O_4 + Fe.$$

This reaction requires that a substantial amount of Fe^{III} (at binding energy 710.8 eV) should persist which was not observed in this case. Also, a higher concentration of Fe^0 than observed would be expected for the beam-initiated breakdown of FeO to Fe_3O_4 and Fe. Thus retention of α-Fe_2O_3, as mentioned before, is the most likely explanation of the results.

Table 2. Showing relative percentage concentration of oxygen components (i.e. total oxygen concentration = 100) in the metal oxides with bombardment time. The dash indicates that the O 1s spectrum is not recorded for this bombarding period. (M–O bond) indicates the O 1s peak due to a metal–oxygen bond. (OH bond) indicates the O 1s peak due to a hydroxide bond. (water bond) indicates the O 1s peak due to surface bound water.

Sample / Binding energy (eV)	Percent concentration at bombardment time (min) 0	10	30	60	120	180
FeO						
530.4 (M–O bond)	45	62	—	74	86	93
531.9 (OH bond)	30	19	—	12	7	5
533.2 (water bond)	25	19	—	14	7	2
Fe_3O_4						
530.4 (M–O bond)	80	81	84	88	90	90
532.5 (water bond)	12	11	11	10	10	10
533.4 (water bond)	8	8	5	2	0	0
Fe_2O_3						
530.2 (M–O bond)	72	77	85	92	93	—
532.2 (water bond)	28	13	9	8	7	—
533.2 (water bond)	0	10	6	0	0	—
CoO						
530.2 (M–O bond)	53	56	59	65	75	—
531.6 (OH bond)	34	30	28	23	18	—
533.5 (water bond)	13	14	13	12	7	—
TiO_2						
530.5 (M–O bond)	74	70	67	67	69	—
531.9 (OH bond)	12	13	13	13	13	—
533.4 (water bond)	14	17	20	20	18	—
Nb_2O_5						
531.0 (M–O bond)	81	78	—	72	70	—
533.3 (water bond)	19	22	—	28	30	—

Spectra for 3 h total bombardment time showed no changes, indicating that a stable equilibrium condition has been established after 2 h.

3.2. Fe_3O_4

Figure 2 shows selected Fe $2p_{3/2}$ and O 1s spectra. For the unetched sample, Figure 2(*a*), the O 1s spectrum consists of a major peak at binding energy 530.4 eV and two less intense peaks at 532.5 and 533.4 eV respectively. All these O 1s components have FWHM of 1.8 eV. The corresponding Fe $2p_{3/2}$ peak, figure 2(*b*), consists of a single component of binding energy 710.9 eV and FWHM of 3.3 eV. Fe_3O_4 contains both Fe^{III} and Fe^{II} ions in an inverse cubic spinel structure, with the Fe^{II} ions in octahedral sites and the Fe^{III} ions in octahedral and tetrahedral sites. Therefore, the absence of Fe^{II} contribution in the unbombarded Fe $2p_{3/2}$ spectrum indicates that oxidation of the surface of Fe_3O_4 has taken place to form α-Fe_2O_3. Unlike in the previous case for FeO no subsequent formation of FeOOH has occurred. This could be due to storage or production conditions of the oxide powder. The two minor O 1s peaks at binding energies of 532.5 and 533.4 eV indicate the presence of surface bound water or adsorbed oxygen (McIntrye 1983).

Figure 2(*c*) shows the Fe $2p_{3/2}$ spectrum after 10 minutes of ion bombardment. Two distinct peaks are visible, at binding energies of 710.9 and 709.4 eV both with FWHM of 3.3 eV. The latter of these components is due to the Fe^{II} ions from Fe_3O_4 and FeO and the former due to Fe^{III} from both Fe_3O_4 and the surface α-Fe_2O_3. The shake-up satellite due to the Fe^{II} ions is seen at 715.1 eV.

The peak intensity ratio of Fe^{III}:Fe^{II} is 0.71 (again satellite contribution neglected). For stoichiometric Fe_3O_4 one would expect this ratio to be 2.0 and the presence of significant amounts of α-Fe_2O_3 containing only Fe^{III} ions would be expected to increase the ratio further. Thus the only explanation for the value of 0.71 for the ratio measured here is that significant reduction of $Fe^{III} \rightarrow Fe^{II}$ has occurred.

Further ion bombardment for periods of 30 min, 1, 2 and 3 h resulted in the ratio Fe^{III}:Fe^{II} varying to values of 0.43, 0.36, 0.23 and 0.25 respectively, thus providing further evidence of ion-beam-induced reduction. This evidence is reinforced by the appearance of a narrow, small peak of binding energy 707.3 eV and FWHM of 2.0 eV in the Fe $2p_{3/2}$ spectra. This can be clearly seen in figure 2(*d*), showing the spectrum for 2 h of ion etching. This narrow peak is due to Fe^0 ions formed to a small extent from the reduction of $Fe^{III} \rightarrow Fe^{II} \rightarrow Fe^0$. The intensity ratio of Fe^{II}:Fe^0 ion reduces from 12.5 at 30 min of bombardment to 5.0 after 2 h. As in the previous case for FeO, equilibrium conditions were established after 2 h of ion bombardment.

3.3. α-Fe_2O_3

Stoichiometric α-Fe_2O_3 contains Fe^{III} ions in a rhombohedral lattice. Figure 3 shows selected photoelectron spectra for Fe $2p_{3/2}$ and O 1s. The O 1s is spectrum for the unbombarded case, figure 3(*a*), shows a major peak due to the oxygen–metal bond at binding energy of 530.2 eV and a less intense peak at 532.2 eV which may be attributed to surface bound water. Allen *et al* (1974), however, reported an O 1s peak at 532.2 eV and speculated that this might be due to adsorbed oxygen rather than water. The unbombarded spectrum of Fe $2p_{3/2}$, figure 3(*b*), shows just one component at 710.8 eV binding energy and 3.3 eV FWHM, this being due to the Fe^{III} ions from α-Fe_2O_3.

Within 10 min of ion bombardment a peak at 709.3 eV (FWHM of 3.3 eV appeared in the iron spectrum, figure 3(*c*), with an associated satellite at 715.2 eV, showing the presence of Fe^{II} due to beam-induced reduction. The O 1s spectrum shows a significant decrease in the relative intensity of the component at 532.2 eV, exposing another peak at 533.2 eV due to underlying surface bound water. All the relative concentration measurements for the O 1s spectra are included in table 2.

After 30 min of bombardment a further peak at a binding energy of 707.2 eV appears in the iron spectrum showing the presence of Fe^0, metallic iron. Thus

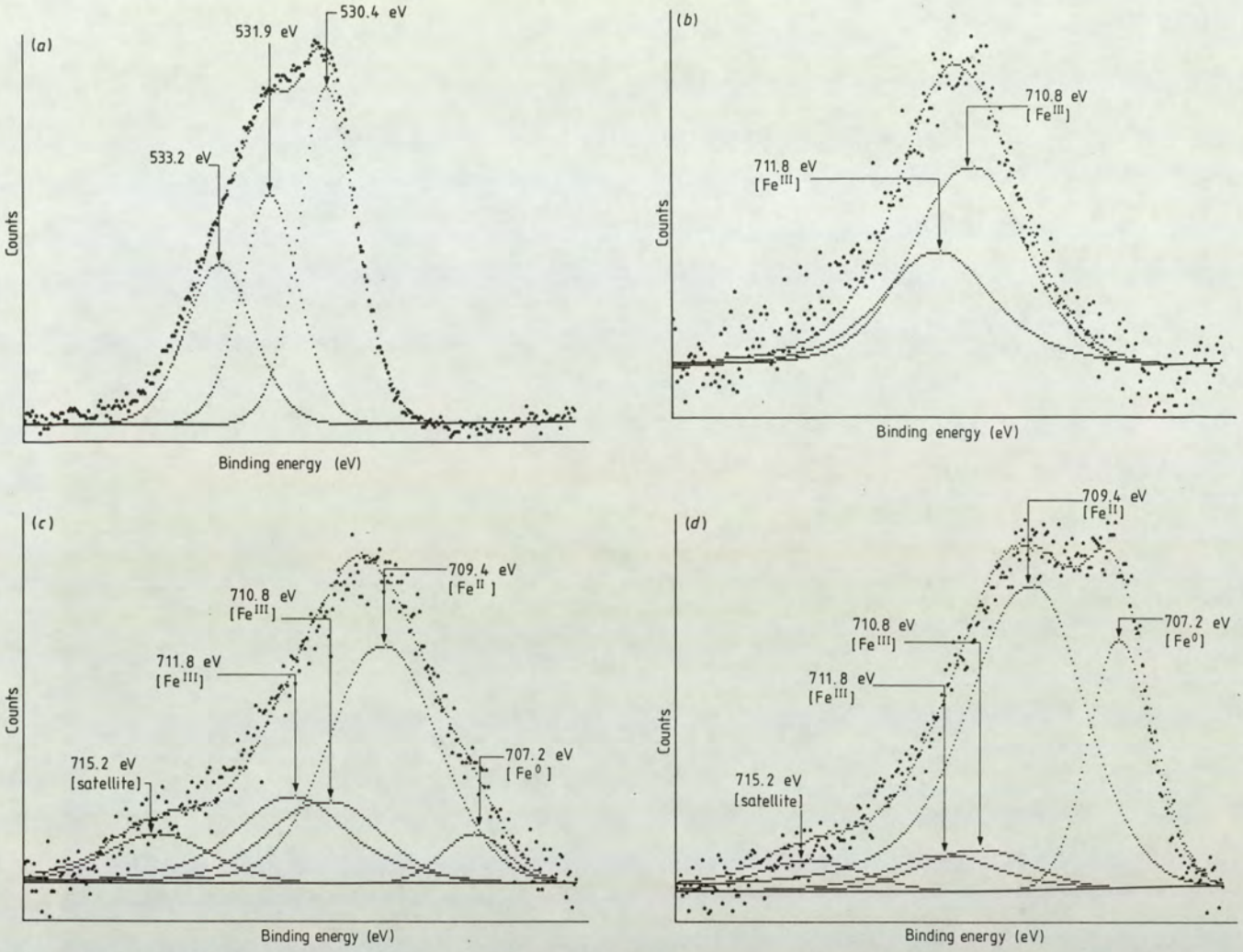

Figure 1. O 1s and Fe $2p_{3/2}$ spectra showing the effect of Ar^+ ion bombardment of FeO powder. (*a*) O 1s spectrum from unetched air-exposed sample. (*b*) Fe $2p_{3/2}$ spectrum from unetched air-exposed sample. (*c*) Fe $2p_{3/2}$ spectrum after 10 min of ion bombardment. (*d*) Fe $2p_{3/2}$ spectrum after 2 h of ion bombardment.

full reduction $Fe^{III} \rightarrow Fe^{II} \rightarrow Fe^0$ has occurred. This form of reduction behaviour of α-Fe_2O_3 is also reported by Lad and Henrich (1988) after 500 eV argon ion bombardment. They also reported reoxidation of the reduced surface when it is subjected to annealing after ion bombardment.

The intensity ratio of Fe^{III}:Fe^{II} (satellite contributions not taken into account) decreases from 1.1 for 10 min bombardment to 0.33, 0.18 and 0.15 for 30 min, 1 and 2 h of bombardment respectively. Similarly the intensity ratio of Fe^{II}:Fe^0 decreases from 12.33 for 30 min bombardment to 10.70 and 9.60 respectively for 1 and 2 h of bombardment. After 1 h the oxygen spectrum shows complete removal of contaminants at 533.2 eV (see table 2).

3.4. CoO

Figure 4 shows selected Co $2p_{3/2}$ spectra for different periods of argon ion bombardment. As for the case of oxides of iron other cobalt spectral lines were recorded and the curve-fitting procedure undertaken. The results for the other lines were, however, entirely consistent and hence will not be included in detail here.

For the unbombarded sample, the O 1s spectrum is very similar to those obtained from the FeO surface (for example see figure 1(*a*)). The O 1s peak may be resolved into three components at binding energies of 530.2, 531.6 and 533.5 eV, all with FWHM of 1.8 eV. The first of these components is due to the metal–oxygen bond and the second due to the oxygen in an OH group (this strongly suggests the presence of a hydroxyl species of the form CoOOH on the CoO powder). The third peak at 533.5 eV corresponds to some form of surface bound water. All relative concentration measurements of the O 1s spectrum for the unbombarded case and also for different durations of ion bombardment are included in table 2.

Considering the Co $2p_{3/2}$ spectrum for the unbombarded surface, figure 4(*a*), three major peaks could be resolved; two peaks at 780.2 eV and the third peak at 781.3 eV. The peak at 781.3 eV (FWHM = 3.2 eV) is considered to be due to the Co^{II} ions in $Co(OH)_2$. The component at 780.2 eV cannot be due to a single species owing to its extreme width. It is thus interpreted as a double peak, one with a FWHM of 1.8 eV corresponding to the Co^{III} ions in CoOOH and the other with FWHM of 2.8 eV being due to Co^{II} ions CoO.

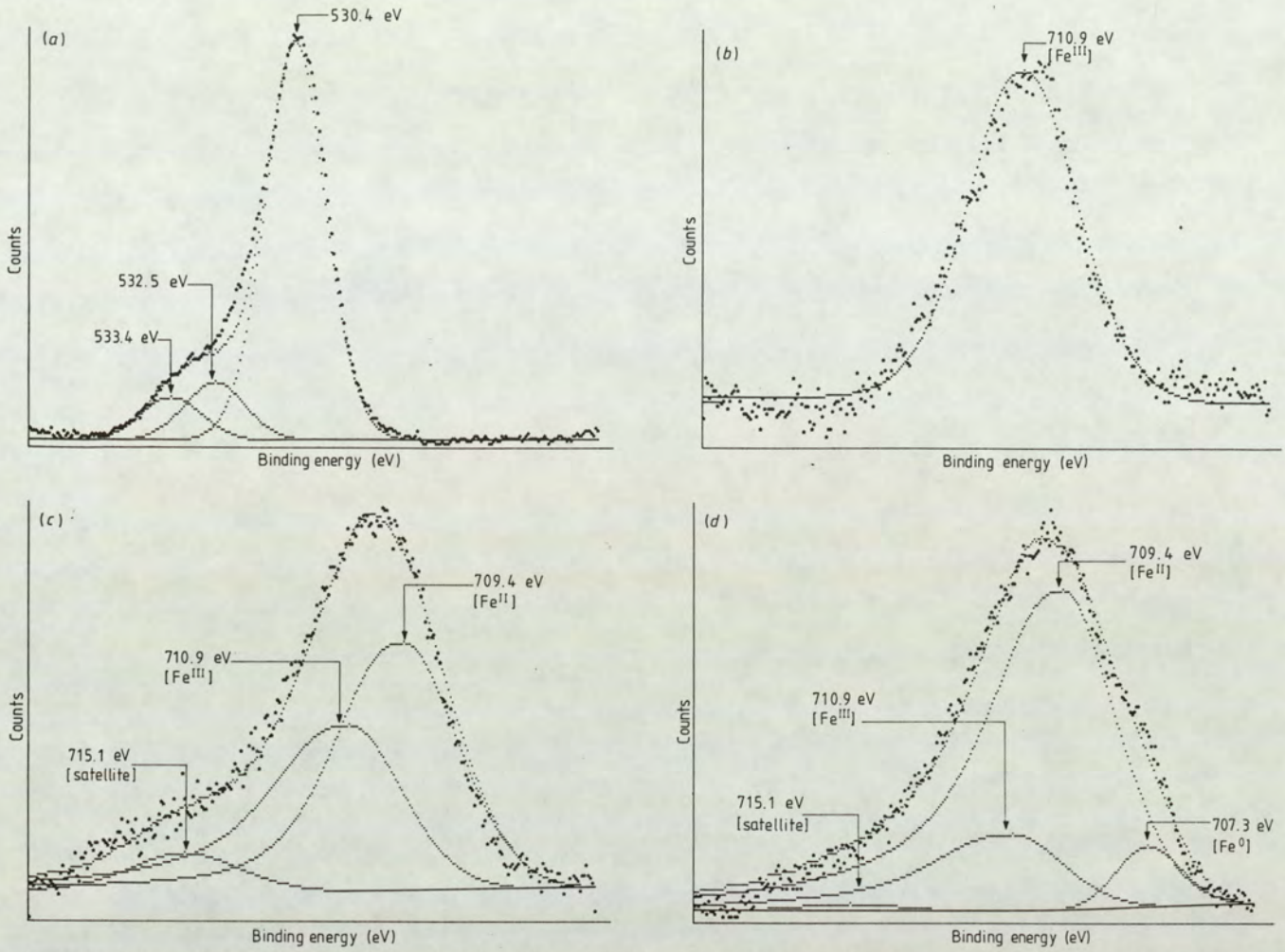

Figure 2. O 1s and Fe $2p_{3/2}$ spectra showing the effect of Ar^+ ion bombardment of Fe_3O_4 powder. (*a*) O 1s spectrum from unetched air-exposed sample. (*b*) Fe $2p_{3/2}$ spectrum from unetched air-exposed sample. (*c*) Fe $2p_{3/2}$ spectrum after 10 min of ion bombardment. (*d*) Fe $2p_{3/2}$ spectrum after 2 h of ion bombardment.

The presence of two broad satellites at 6.8 and 5.6 eV above the main CoO photopeak also confirms the existence of CoO. These satellites due to the high-spin Co^{II} were ascribed by Frost *et al* (1974) to be caused by shake-up processes. The curve-fitting procedure also suggests a third satellite peak due to Co^{II} in CoO at 2.3 eV above the main peak, i.e. at 782.5 eV.

All the measured binding energies and FWHM values are in good agreement with McIntyre and Cook (1975), who also suggest the presence of a third satellite at an energy of 2.1 eV above the Co^{II} peak from CoO.

After 10 min of ion bombardment, figure 4(*b*), the Co $2p_{3/2}$ spectrum is broadened and the peak synthesis procedure reveals near removal of the thin layer of surface CoOOH. This is suggested by the presence of only one peak at 780.2 eV (FWHM = 2.8 eV), due to the Co^{II} ions in CoO; however, there may be negligible contribution from Co^{III} ions in CoOOH. The presence of predominantly CoO is also indicated by the prominence of its satellite peaks.

After 30 min of ion bombardment an additional peak at a binding energy of 778.5 eV, FWHM = 1.7 eV, is apparent in the Co $2p_{3/2}$ spectrum. This is due to metallic cobalt, Co^0. McIntyre and Cook (1975) ascribed a value of 778.0 eV, FWHM = 1.7 eV, to this line, but that was measured from pure metallic cobalt. The oxide matrix environment of the Co^0 component measured in our experiments could give rise to the higher binding energy.

Further bombardment reduces the relative intensity ratio of Co^{II} in CoO to Co^0 from 20.5 at 30 min of bombardment to 4.4 and 3.7 respectively after 1 and 2 h. This ratio was calculated using the area under the main Co^{II} peak only, satellite contribution was not taken into account. Thus again, as for the case of oxides of iron, there is a clear evidence of ion-beam reduction to a lower oxidation state. Equilibrium conditions were established after 2 h of bombardment.

However, congruent sputtering of CoO is observed at room temperature by Langell (1987) in his investigation of preferential sputtering of CoO(100) single crystals for the substrate temperature range 300–900 K. He reported the onset of sputter reduction of CoO at about 500 K. Temperature measurements during bombardment had not been carried out in this investigation.

3.5. TiO_2

Figure 5 shows selected Ti 2p spectra for different durations of argon ion bombardment. TiO_2 powder

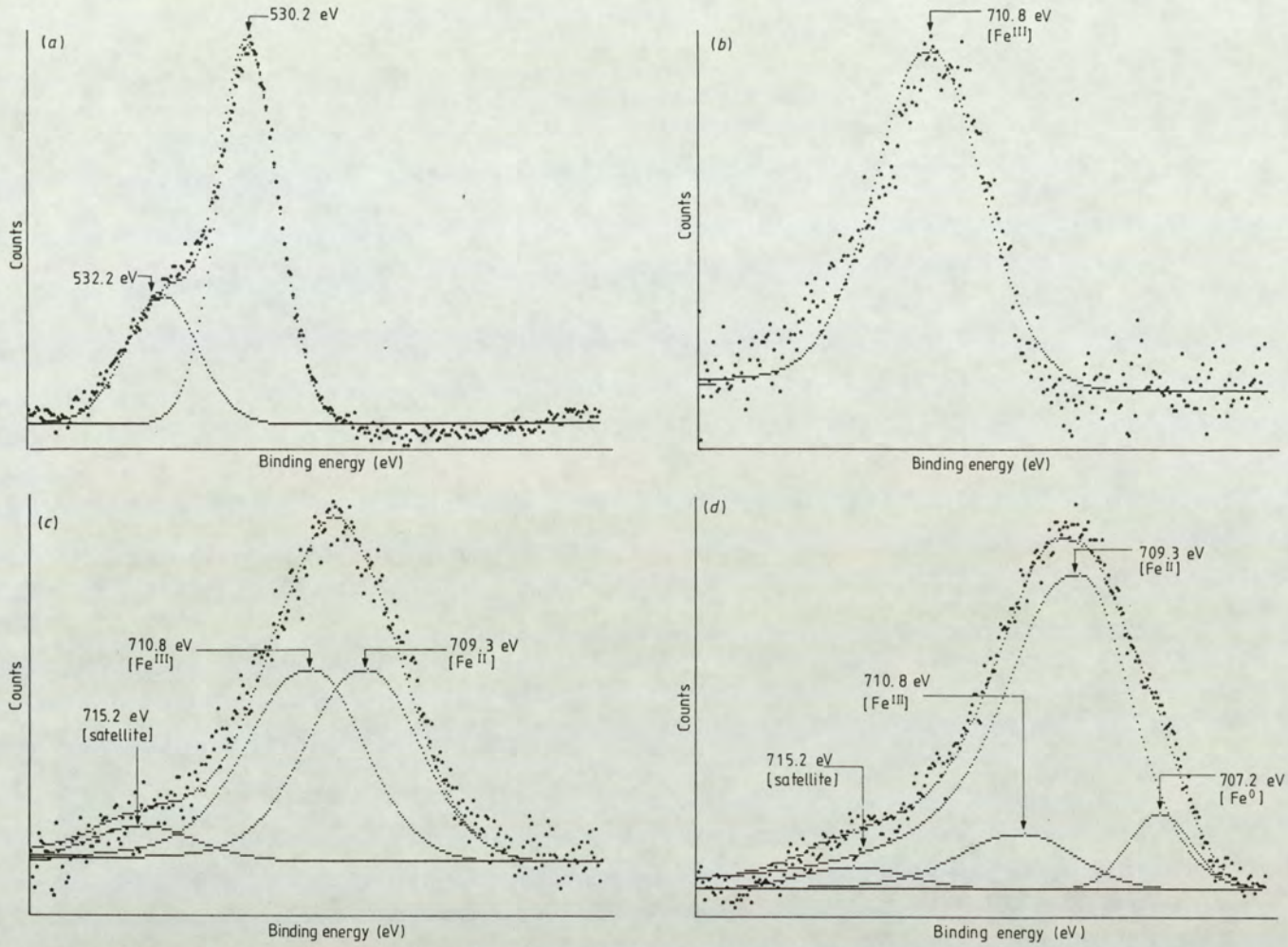

Figure 3. O 1s and Fe $2p_{3/2}$ spectra showing the effect of Ar^+ ion bombardment of α-Fe_2O_3 powder. (*a*) O 1s spectrum from unetched air-exposed sample. (*b*) Fe $2p_{3/2}$ spectrum from unetched air-exposed sample. (*c*) Fe $2p_{3/2}$ spectrum after 10 min of ion bombardment. (*d*) Fe $2p_{3/2}$ spectrum after 2 h of ion bombardment.

was obtained by firmly grinding commercially obtained high-purity TiO_2 chunks. The unbombarded O 1s spectrum shows the appearance of three peaks at 530.5, 531.9 and 533.4 eV binding energy with FWHM values 1.6, 1.6 and 1.7 eV respectively (table 2). The O 1s peak at 533.4 eV, as previously stated, is attributed to bound water and the peak at 531.9 eV is due to some form of hydroxide bond. The peak at 530.5 eV is due to the oxide metal–oxygen bond. The corresponding Ti 2p spectra, figure 5(*a*), show two peaks at binding energies of 458.7 eV (FWHM = 1.5 eV) and 464.6 eV (FWHM = 2.5 eV) correspond to Ti $2p_{3/2}$ and $2p_{1/2}$ respectively and are due to the Ti^{IV} ions in TiO_2.

X-ray photoelectron spectroscopy carried out after ion bombardment shows widening of the Ti 2p peak caused by the appearance of four more peaks. Two, at 457.2 eV (FWHM = 2.0 eV) and at 463.0 eV (FWHM = 2.5 eV), are due to the $2p_{3/2}$ and $2p_{1/2}$ lines respectively of Ti^{III} in Ti_2O_3. The other two peaks, at 455.3 eV (FWHM = 2.0 eV) and at 461.0 eV (FWHM = 2.3 eV), correspond to the $2p_{3/2}$ and $2p_{1/2}$ lines of Ti^{II} ions in TiO. All the binding energies are measured with respect to the C 1s line as differential charging was observed with gold.

The reduction of TiO_2 to Ti_2O_3 and eventually to TiO is accompanied by a reduction in the relative intensity of the O 1s peak due to the metal–oxygen bond. All the O 1s relative intensities for different bombardment times are also included in table 2. The O 1s peak binding energy due to the metal–oxygen bond of each suboxide Ti_2O_3 and TiO cannot be resolved from that due to TiO_2. The relative intensity of the O 1s peak, at binding energy of 531.9 eV (hydroxide bond) seems to increase initially and then decrease. This is most probably due to the powder nature of the sample and it is possible that sputtering exposes a surface containing more hydroxide than on the initial surface.

The binding energy values found for Ti 2p are in good agreement with the data of Hofmann and Sanz (1982–3); they have also shown a similar reduction behaviour for TiO_2. However, in a reflected electron diffraction investigation, undertaken by Parker and Kelly (1975), only one final product, Ti_2O_3, is reported on the surface of TiO_2 after Kr ion bombardment. They conclude that the stoichiometry change to Ti_2O_3 is in part collisional and in part thermally activated, and occurs to a depth which is similar to the mean ion range.

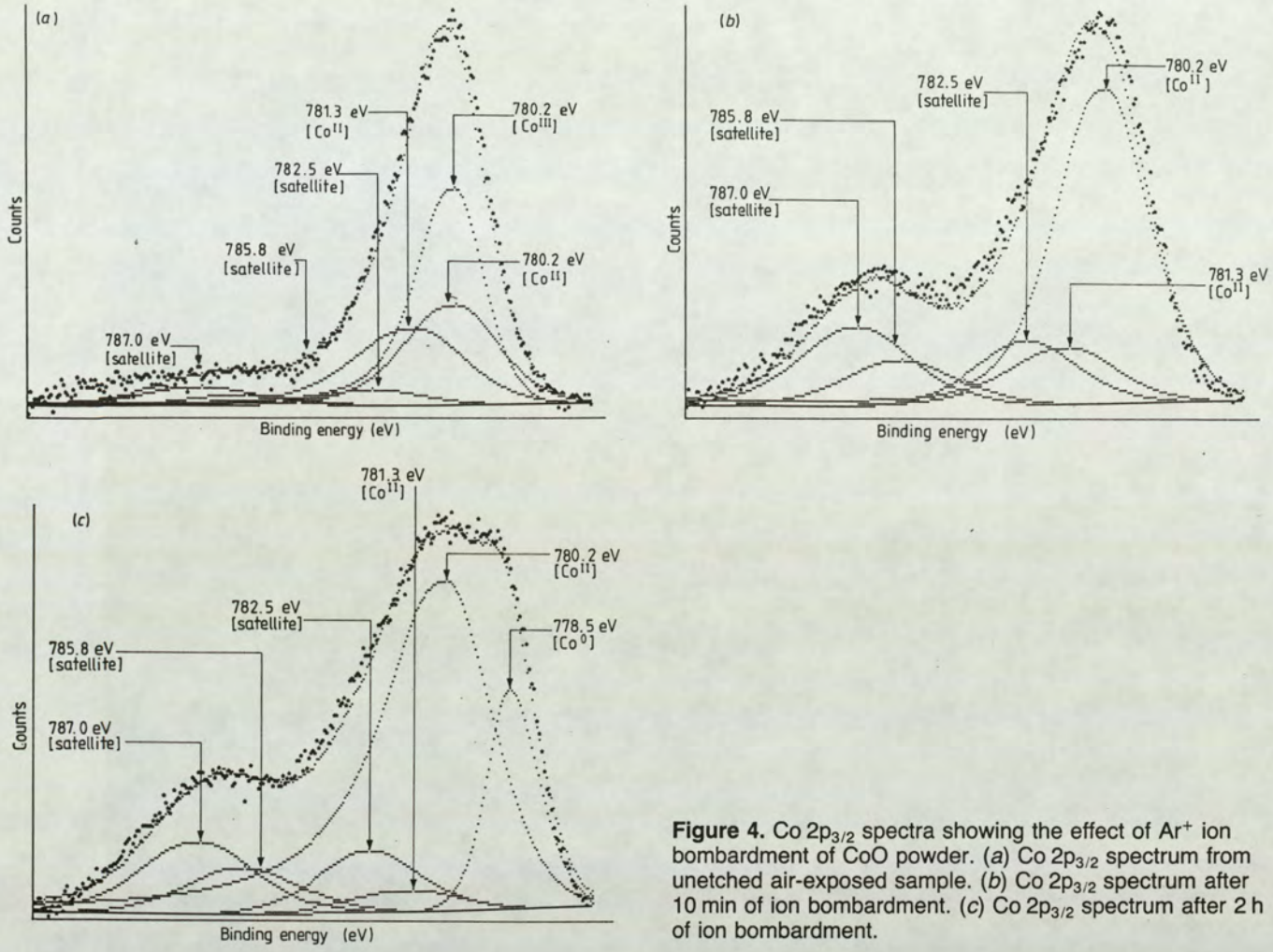

Figure 4. Co $2p_{3/2}$ spectra showing the effect of Ar^+ ion bombardment of CoO powder. (*a*) Co $2p_{3/2}$ spectrum from unetched air-exposed sample. (*b*) Co $2p_{3/2}$ spectrum after 10 min of ion bombardment. (*c*) Co $2p_{3/2}$ spectrum after 2 h of ion bombardment.

3.6. Nb_2O_5

Selected Nb 3d spectra from Nb_2O_5 samples are shown in figure 6 for different periods of argon ion bombardment. The reduction from higher to lower oxidation states is most evident in this oxide.

For the unetched sample, the O 1s spectrum shows a major peak at a binding energy of 531.0 eV (FWHM = 1.8 eV) with a further less intensive peak at 533.3 eV, with FWHM of 1.9 eV. The Nb $3d_{3/2}$ and $3d_{5/2}$ spectra, figure 6(*a*), consist of single peaks at binding energies of 210.3 and 207.6 eV respectively with FWHM of 1.9 eV. These values are in agreement with those proposed by Fontaine *et al* (1977) for Nb^V in Nb_2O_5 and also those due to Hofmann and Sanz (1982–3). The results indicate that no hydroxides are present on the surface, although there is some evidence of water inclusion (table 2 shows the O 1s relative intensities).

After 10 min of ion bombardment, figure 6(*b*), the Nb 3d spectra show additional peaks at binding energies of 208.6 and 205.9 eV. These are due to the $3d_{3/2}$ and $3d_{5/2}$ lines for the Nb^{IV} ions in NbO_2. The peak intensity ratio for Nb^V:Nb^{IV} is 4.4 for both the $3d_{3/2}$ and $3d_{5/2}$ peaks.

After 1 h of bombardment the Nb^V:Nb^{IV} ratio is reduced to 1.6 for both the 3d peaks. In addition to this figure 6(*c*) shows that two further peaks appear in the Nb 3d spectrum at binding energies of 207.1 and 204.4 eV both with FWHM of 1.9 eV. These binding energy values correspond to Nb^{II} due to NbO. The binding energy values for both NbO_2 and NbO are again in good agreement with those due to Fontaine *et al* (1977) and also Hofmann and Sanz (1982–3).

After 2 h of ion-beam bombardment, two further narrow peaks at 205.7 and 202.9 eV binding energy (FWHM = 1.3 eV) may be observed (figure 6(*d*)). These are due to Nb^0. Fontaine *et al* (1977) measured the latter value for a Nb metal matrix as 202.4 eV but again following the arguments advanced in previous sections one might expect that Nb^0 would have higher associated binding energies when the metal is present in an oxide environment.

As with iron, cobalt and titanium, this work has clearly demonstrated that ion-beam reduction of this oxide has occurred through the reaction:

$$Nb^V \rightarrow Nb^{VI} \rightarrow Nb^{II} \rightarrow Nb^0.$$

Similar reductions of Nb_2O_5 have been reported by Hofmann and Sanz (1982, 1982–3) and by Brown *et al* (1984). Murti and Kelly (1976) have observed preferential sputtering of Nb_2O_5 with Kr^+ ions and a surface layer of only NbO have been detected with reflection electron diffraction.

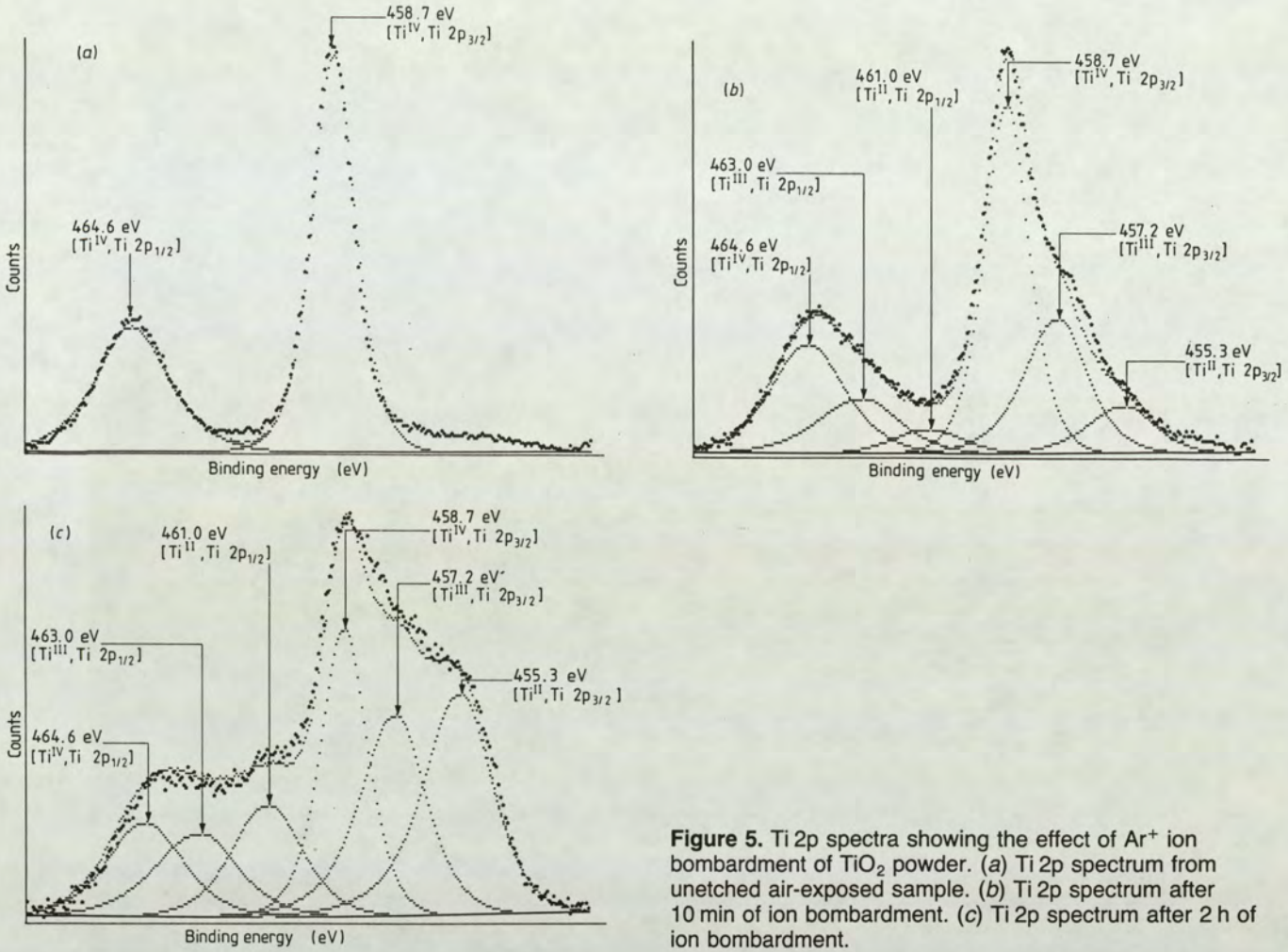

Figure 5. Ti 2p spectra showing the effect of Ar^+ ion bombardment of TiO_2 powder. (*a*) Ti 2p spectrum from unetched air-exposed sample. (*b*) Ti 2p spectrum after 10 min of ion bombardment. (*c*) Ti 2p spectrum after 2 h of ion bombardment.

4. Summary

In summary, the work has shown that ion-beam induced chemical reduction takes place in all the oxides examined in this investigation. The agreement between the measured values of binding energy for the ions in this ion-beam induced reduction system and published values for the ions in pure lower oxides, supports the view that the reduction is due to the preferential removal of oxygen and atomic rearrangement to form lower oxides and metallic species.

Recent theory by Malherbe *et al* (1986) proposes a mechanism for preferential sputtering of oxides in which both mass and bonding effects of the binary components are incorporated. In this model, when the steady state is reached, the ratio of the surface fractional composition $(X_i)^s$ to the bulk fractional composition $(X_i)^b$ of a metallic oxide, M_cO_d, is given by

$$(X_m/X_0)^s/(X_m/X_0)^b = (A_m/A_0)^{2m}(U_m/U_0)^{1-2m}. \quad (1)$$

A_i and U_i are the atomic mass and surface binding energy respectively. It should be pointed out here that equation (1) is valid only for alloys and even then only if appropriate use of U is made. However, Malherbe *et al* (1986) has applied this equation to binary oxides taking the value of the constant m to be 0.165 and defining U_0 in terms of the metal–oxygen bond energies, the dissociation energy of the oxygen molecule and the metal and oxygen electronegativity values; U_m is given in terms of the electronegativity values and the sublimation energy of the metal. They have found a reasonable correlation between their predicted and the experimental values.

It should also be noted that Kelly (1980) has also proposed a different model for the ion-induced compositional changes of oxides in which chemical bonding is presumed to be the dominant factor and mass effects are negligible. He has suggested that the predominant sputtering process of the oxides may be a thermal spike mechanism rather than collisional cascade sputtering and hence the preferential sputtering of oxides is explained in terms of the stability and decomposition of the various oxides at the spike temperature. This model thus also differs by putting emphasis on the particular state (e.g. NbO) rather than on averages (e.g. (X_m/X_0)) of all the reduced states at steady state. The experimental results found here are in disagreement with this model as more than one final state is detected at the surface of the bombarded sample at steady state. It is reasonable to expect that Kelly (1980) could have overlooked the existence of NbO_2, the first reduced state from bombardment of Nb_2O_5, as a result of the detection method used. Electron diffraction technique was used which may not detect NbO_2 owing to the likelihood that this reduced state was amorphous.

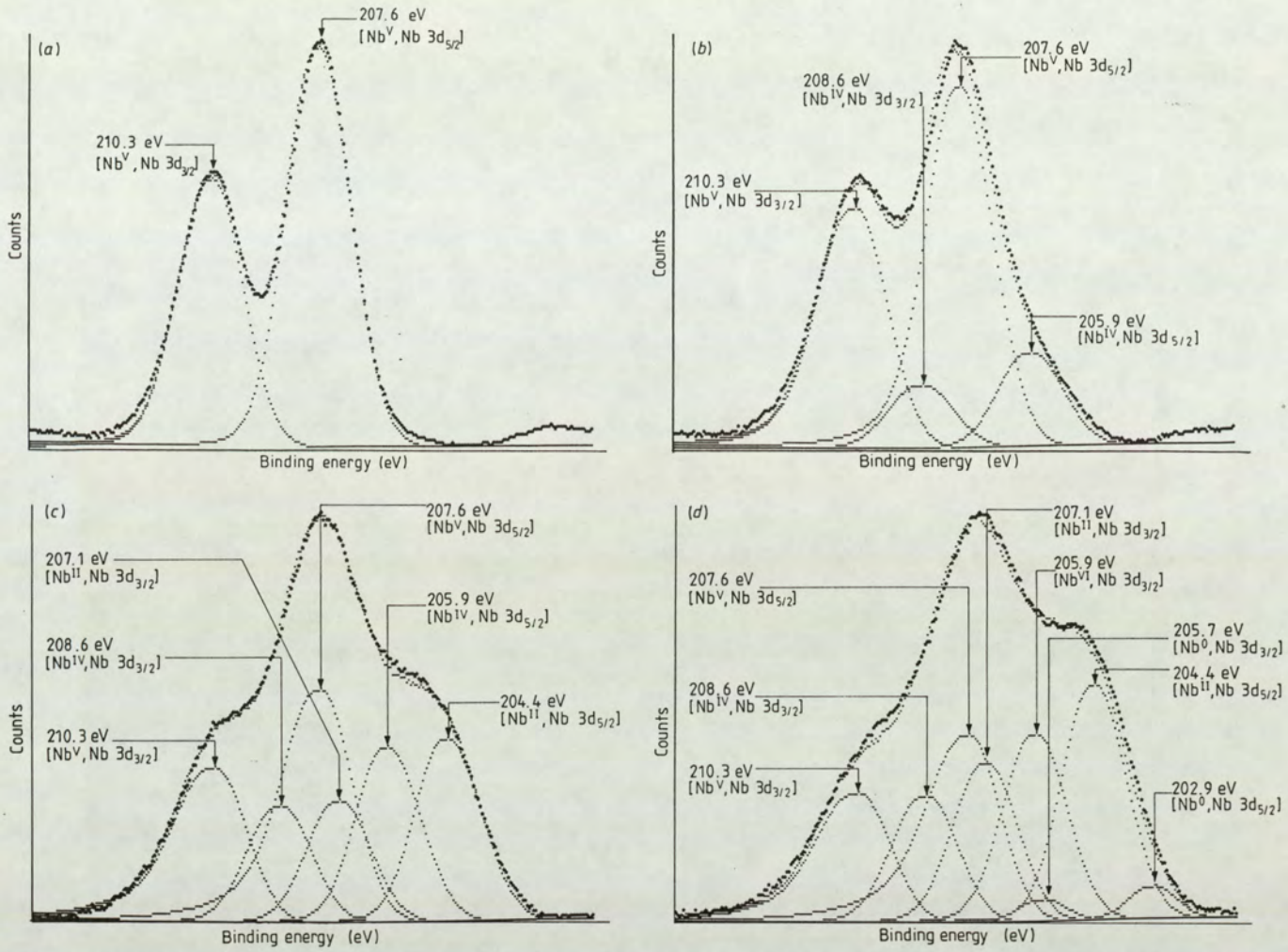

Figure 6. Nb 3d spectra showing the effect of Ar^+ ion bombardment of Nb_2O_5 powder. (*a*) Nb 3d spectrum from unetched air-exposed sample. (*b*) Nb 3d spectrum after 10 min of ion bombardment. (*c*) Nb 3d spectrum after 1 h of ion bombardment. (*d*) Nb 3d spectrum after 2 h of ion bombardment.

Table 3. A comparison of the results obtained for (X_m/X_0) surface-to-bulk ratio in this analysis with those due to Malherbe *et al* (1986).

Molecule	Results for (X_m/X_0) surface-to-bulk ratio due to Malherbe *et al* (1986)		(X_m/X_0) surface-to-bulk ratio obtained in this analysis
	Calc.	Expt.	
FeO	1.45	1.05	1.31
Fe_3O_4	1.44	1.05	1.39
Fe_2O_3	1.44	1.05	1.59
CoO	1.51†	1.33†	1.20
TiO_2	1.32	1.50	1.36
Nb_2O_5	2.04	2.22	1.56

† These are the results for Co_3O_4 due to Malherbe *et al* (1986).

Considering Sigmund's (1969) classification of sputtering events and assuming the linear cascade regime, a model based on both mass and bonding effects could be expected to give better agreement with experimental results. Hence for the experimental results obtained here, the ratio $\{(X_m/X_0)^s/(X_m/X_0)^b\}$ was calculated for each of the oxides used. Table 3 shows these values compared with the theoretically calculated and experimentally obtained results due to Malherbe *et al* (1986).

As an example, the steps undertaken in calculating the (X_m/X_0) surface to bulk ratio, using the experimental data obtained for Nb_2O_5, are now outlined.

(1) Under steady state conditions the curve-fitting procedure carried out on the Nb 3d peak yields areas under each of the Nb components for Nb_2O_5, NbO_2, NbO and metallic Nb to be 4884.07, 3928.47, 4965.00 and 477.79 respectively. Considering that each molecule of Nb_2O_5 contains two atoms of niobium, the constituents are calculated to be 20.7% Nb_2O_5, 33.3% NbO_2, 42.0% NbO and 4% metallic Nb. Hence the intensity ratio is

$$Nb^V : Nb^{IV} : Nb^{II} : Nb^0 = 20.7 : 33.3 : 42.0 : 4.0.$$

(2) Letting the total number of niobium ions and/or atoms = 1, namely

0.207 part due to Nb_2O_5

0.333 part due to NbO_2

0.42 part due to NbO

0.04 part due to metallic Nb.

The associated total number of oxygen ions and/or atoms can be found by considering that

each Nb in Nb_2O_5 has 5/2 associated oxygen atoms

each Nb in NbO_2 has 2 associated oxygen atoms

each Nb in NbO has 1 associated oxygen atom

each Nb in Nb^0 has no associated oxygen atom.

(3) Hence the total number of associated oxygen atoms is

$$(5/2 \times 0.207) + (2 \times 0.333) + 0.42 = 1.60.$$

This yields a value for $(X_m/X_0)^s$ to be (1/1.6) and the (X_m/X_0) surface-to-bulk ratio to be 1.56. The ratios for the other oxides are calculated in a similar manner.

(4) Calculation of the (X_m/X_0) surface-to-bulk ratio using the above method eliminates the need for the various atomic sensitivity factors. This possibly gives a more accurate result as the atomic sensitivity factors for the Kratos hemispherical sector analyser are not accurately known.

The experimental values obtained here are in fairly good agreement with those obtained by Malherbe *et al* (1986). However, it is important to note that their proposed theory does not account for the effect of variation of beam energy or beam current density on the extent of chemical damage. It is hence suggested that more experimental work, to establish the effect of variation of the beam energy and the beam current density, is required before a full theoretical model for the ion-induced reduction of oxides can be formed.

5. Conclusion

Electron core level lines for the oxides of iron, cobalt, titanium and niobium have been examined using XPS during successive periods of Ar^+ ion bombardment.

In all cases after the removal of initial contaminant layers of oxide and/or hydroxides the Ar^+ ion bombardment leads to a rapid chemical reduction.

Data for reduction, after equilibrium conditions have been established, are in good agreement with the theoretical predictions of Malherbe *et al* (1986). This result indicates that both mass difference and surface binding energy effects are important in explaining the preferential removal of oxygen from the oxide and hence the oxide reduction.

The electron core binding energies of metal and oxygen components of the various oxides and hydroxides are identified and tabulated.

References

Allen G C, Curtis M T, Hooper A J and Tucker P M 1974 *J. Chem. Soc.* 1525–30

Brown A, Van den Berg J A and Vickerman J C 1984 *J. Chem. Soc. Chem. Commun.* 1684–6

Brundle C R, Chung T F and Wandelt K 1977 *Surf. Sci.* **68** 459–68

Fontaine R, Caillat R, Feve L and Guillet M J 1977 *J. Electron Spectrosc. Relat. Phenom.* **10** 349–57

Frost D C, McDowell C A and Woolsey I S 1974 *Mol. Phys.* **27** 1473–89

Habier J, Stock J and Ungier L 1976 *J. Electron. Spectrosc. Relat. Phenom.* **9** 459–67

Hofmann S and Sanz J M 1982 *Microchim. Acta Suppl.* **10** 213–23

—— 1982–3 *J. Trace and Microprobe Tech.* **1** 213–64

Kelly R 1980 *Surf. Sci.* **100** 85–107

Kelly R and Lam N Q 1973 *Radiat. Eff.* **19** 34–47

Kim K S, Baitinger W E, Amy J W and Winograd N 1974 *J. Electron. Spectrosc. Relat. Phenom.* **5** 351–67

Lad R J and Henrich V E 1988 *Surf. Sci.* **193** 81–93

Langell M A 1987 *Surf. Sci.* **186** 323–38

McIntyre N S 1983 in *Practical Surface Analysis by Auger and X-Ray Photoelectron Spectroscopy* ed. D Briggs and M P Seah (New York: Wiley)

McIntyre N S and Cook M G 1975 *Anal. Chem.* **47** 2208–13

McIntyre N S and Zetaruk D G 1977 *Anal. Chem.* **49** 1521–9

Malherbe J B, Hofmann S and Sanz J M 1986 *Appl. Surf. Sci.* **27** 355–65

Mills P and Sullivan J L 1983 *J. Phys. D: Appl. Phys.* **16** 723–32

Murti M and Kelly R 1976 *Thin Solid Films* **33** 149–63

Parker T E and Kelly R 1975 *J. Phys. Chem. Solids* **36** 377–85

Sherwood P 1983 in *Practical Surface Analysis by Auger and X-Ray Photoelectron Spectroscopy* ed. D Briggs and M P Seah (New York: Wiley)

Sigmund P 1969 *Phys. Rev.* **184** 383–416

—— 1981 in *Sputtering by Particle Bombardment I* (Topics in Applied Physics, vol. 47) ed. R Behrish (Berlin: Springer)

Vacuum/volume 38/numbers 8–10/pages 917 to 922/1988
Printed in Great Britain

0042–207X/88$3.00+.00
Pergamon Press plc

A comparison of ion and fast atom beam reduction in TiO_2

S O Saied, J L Sullivan, T Choudhury and C G Pearce, *Department of Electrical and Electronic Engineering and Applied Physics, University of Aston, Aston Triangle, Birmingham B4 7ET, UK*

Ion beam bombardment of solid surfaces has been used extensively for surface conditioning, surface cleaning and in various aspects of surface and interface analysis. The process can give rise to extensive physical and chemical changes in the bombarded surface. It has recently been suggested that bombardment by means of fast atoms, rather than ions of the same mass and energy, produces less surface damage. This investigation was therefore initiated to study the relative damage produced by ion and fast atom bombardment. To do this, changes in elemental chemical states associated with TiO_2 have been examined using XPS, when the oxide was subject to progressive periods of argon and helium ion and fast atom bombardment. Chemical reduction of the oxide, according to the interaction $TiO_2 \rightarrow Ti_2O_3 \rightarrow TiO \rightarrow Ti$ was obtained for both Ar and He bombardment. The degree of reduction was compared and it was found that in all cases ions produced significantly more reduction than fast atoms. This difference was greatest in the case of He bombardment. The difference between atom and ion surface damage may be explained in terms of a high local surface potential produced in the case of ions leading to electrical breakdown and effective reduction in the mean metal–oxygen binding energy.

1. Introduction

When low energy noble gas ion beams are used for surface cleaning, surface modification or as an analytical tool in surface analysis, it is well known that the beams produce both physical and chemical damage. For example, large increases in surface roughness and extensive chemical and compositional changes due to ion bombardment have been reported by a number of authors[1–5].

In the case of metal oxides the damage is manifested by a change in oxidational state of the metal from high to low valency with eventual full reduction to the metallic state. This reduction has been observed by various authors for a wide range of metal oxides[6–11]. There is general agreement that this form of ion-induced chemical damage is due to preferential sputtering of oxygen from the oxide matrix. Preferential sputtering might be expected since elemental sputtering yields vary considerably[12] and are very matrix dependent.

Models have been proposed to account for this ion-induced oxide reduction[13,14] based mainly on Sigmund's classification of sputtering events and sputtering yield equation[15,16]. Although there is some disagreement on the relative importance of surface binding energy and mass difference effects, the models give plausible explanations of the observed oxide reduction. The models, however, take no account of the charge on the bombarding particle and any subsequent effect of charge induced damage is ignored.

The fact that charge has an effect has been reported by Franks[1] who claimed less physical damage in terms of surface roughness increases when fast atoms were used for surface cleaning rather than ions; and by Brown *et al*[17] who showed that Nb_2O_5 suffered less chemical reduction when bombarded with fast atoms rather than ions of the same energy and species.

If one considers ion surface bombardment of insulators, it is not surprising that charge should have an effect on sputtering yield. Ions approaching a surface are neutralized within about 5 Å of the surface by a process involving electronic excitation of the surface atoms[18]. This results in bombardment induced charge injection[19] and in the case of insulators an increase in local surface potential and the production of a high field surface region. Zalm[18] has shown that local surface potentials due to ion bombardment will be present for all materials and that the magnitude will increase with increased resistivity. This effect is likely, then, to have a profound effect on sputtering processes. Also with ionic solids, there is the possibility of Coulomb explosion[20] which will also contribute to the yield. Atom bombardment will also result in increased local surface potential due to secondary electron emission, but the magnitudes in this case will be substantially lower.

It is the purpose of this work to investigate relative chemical reduction for fast atoms and ions in one particular metal oxide, that is TiO_2. The object is firstly to determine whether a significant difference in chemical damage exists when fast atoms and ions are employed in surface bombardment and secondly to isolate the important factors. Argon is the most common rare gas used in surface bombardment and hence this gas was used in the investigation. It is likely that the contribution to surface damage will be similar whatever the rare gas used, hence in order to produce a more pronounced relative effect due to the charge (if such an effect exists) the very light particle, helium, was used where the low mass and hence low energy transfer will give physical yields of about an order of magnitude lower than those

for argon[21]. X-ray photoelectron spectroscopy was used to monitor reduction of the oxides by careful measurement of photoelectron chemical shifts and intensities of metal and oxygen spectral lines between successive periods of ion and atom bombardment.

2. Experimental details

The XPS analysis described in the work was carried out in a Kratos XSAM 800 electron spectrometer. The instrument employs a hemispherical electrostatic electron energy analyser with aberration compensated input lens and a dual anode (Al/Mg) X-ray source, which in the case of this instrument was non-monochromated. For these present studies Mg K_α radiation was used (at energy 1253.6 eV) and the source was operated at 15 kV and 10 mA applied voltage and emission current, respectively. The analysed area of the sample was approximately 15 mm^2.

Spectra were collected with the analyser operated in fixed retarding ratio (FRR) mode. Slit widths of 4 mm at both entrance and exit of the analyser were used to provide adequate resolution and maintain good sensitivity. Under these conditions the measured full width at half maximum of the Au $4f_{7/2}$ photoelectron line was 1.6 eV. All measured binding energies were calibrated by reference to the Au $4f_{7/2}$ line at 84 eV and the C ls line at 284.6 eV.

The spectrometer was interfaced with an Apple IIe microcomputer system which was employed for instrumental control, data collection and data processing. Spectral processing and curve fitting was achieved by the method described by Sherwood[22].

Analyses were performed in an UHV environment with a base pressure better than 10^{-9} mbar. During operation of the fast atom and ion source, however, chamber pressures reached 5×10^{-6} mbar due to leakage of the noble gas employed for bombardment from the source into the chamber. The noble gases, argon and helium, were research grade gases used without further purification.

The transition metal oxide used in the investigation was TiO_2 and was in the form of a commercially available high purity powder. All samples were first bulk characterized by means of power X-ray diffraction prior to XPS analysis. Samples were prepared by gently mixing the oxide with gold powder and then pressing into a high purity lead sheet immediately prior to insertion into the experimental chamber. Prior to examination the oxide powder was stored under argon.

The fast atom/ion source used for surface bombardment in this study was an Ion Tech FAB 11 saddle field source. This source is a cold cathode device which operates at about the same pressure as other conventional cold cathode sources. To investigate the manufacturer's claim that this FAB 11 source produces a beam which is 'truly neutral and does not contain a mixture of ions, atoms and electrons', Saied *et al*[23,24] have completely characterized this source. They reported that, in their system, the neutral content of the beam was only 40% when the source was operated in its most efficient mode at low chamber pressures. Similar measurements have been made on the neutral content of the beam in the present system with the FAB 11 source attached to the Kratos XSAM 800 experimental chamber. Here the measurements were extended to lower chamber and hence lower source pressures and the results for argon are shown in Figure 1. Very similar results were obtained for a helium beam. From Figure 1 it can be seen that at the lowest pressures

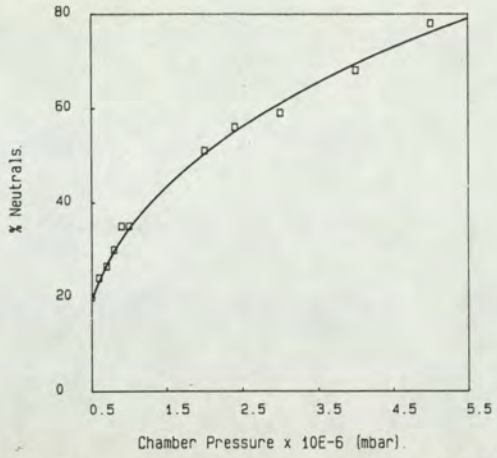

Figure 1. Neutral content of the argon beam from the saddle field source vs chamber pressure.

employed, that is 5×10^{-7} mbar, the beam contained less than 20% neutrals. In the chamber pressure range used in these experiments, from 5×10^{-7} to 5×10^{-6} mbar, the source was capable of supplying total beam currents of up to 20 μA.

It is the variable mixture of fast atoms and ions in the beam from this source which allows direct comparison between neutral and ion damage to surfaces under very similar conditions of beam profile, beam energy spread, etc. If different sources of fast atoms and ions had been used there would have been far less confidence in the results.

Beam currents were measured at the start of an experiment and periodically throughout an experiment by monitoring the current flowing in a detector plate attached to the underside of the specimen holder and exposed by rotating the holder through 180°. To ensure that all secondary electrons produced by bombardment at the plate were repelled and hence that true secondary electron current was measured, a voltage of −12 V was applied during current measurements.

When a pure neutral fast atom beam was required, ions were removed from the beam by deflection in an electrostatic field. To achieve this a plate was placed parallel to the beam at a distance of about 50 mm from the screened exit aperture of the source and a high voltage applied. For this condition chamber pressures of about 3×10^{-6} mbar were chosen to correspond to a neutral content of about 60%.

The current measured at the detector plate, I'_A, was then wholly due to secondary electron emission and is given by:

$$I'_A = \gamma I_A$$

where γ is the secondary yield and I_A the fast atom beam current.

For ion bombardment the source was operated at a chamber pressure of 5×10^{-7} mbar where the measured neutral content of the beam was 20%. Under these conditions the current measured at the detector plate, I'_T, due to the total beam (measured without energizing the deflection plate) was

$$I'_T = I_I + \gamma(I_I + I_A)$$

where I_I is the ion current in the beam and where it is assumed that the secondary electron yield is the same for both atoms and ions. At these low pressures doubly charged species represented less than 5% of the beam and were neglected.

Since under the conditions of these experiments, $I_I = 0.8\ I_T$ and $I_A = 0.2\ I_T$ where I_T is the total beam current (both atom and neutral), then for atom current I_A and total current I_T to be equal

$$I'_T = \frac{0.8+\gamma}{\gamma} I'_A.$$

Hence to give a total beam current equivalent to the atom current, the source output was adjusted until the detector plate current was $(0.8+\gamma)/\gamma$ times that measured for the pure neutral beam. Secondary electron yields were measured by Saied *et al* in a different system.

All sample bombardment was carried out at a mean beam energy of 5 keV. In the experiments, XPS spectra were recorded for the TiO_2 samples initially in their air exposed state and then after periods of 2, 10, 30, 60 and 120 min of energetic beam bombardment. It was found that the more reliable and consistent results were obtained for the shorter periods of bombardment. For the longer periods it was difficult to maintain the source current at constant levels.

Series of spectra were recorded for both He and Ar noble gas atoms and total (80% ion, 20% neutral) beams at high and low beam currents. High currents were chosen to be 10 μA and low currents 1 μA, respectively. He and Ar were chosen because of their large mass difference, in the hope that charge and mass effects might be effectively separated. For example, if charge is important, one would expect it to have a greater proportionate effect with the low mass particle. Each analysis was performed several times in order to check the reproducibility of the results.

3. Experimental results and discussion

For this investigation on the effect of fast atom and ion bombardment on TiO_2, photoelectron core line spectra were recorded for the metal 2p, 3p, and 3s lines, O 1s, C 1s and Au $4f_{7/2}$. The C 1s line was used as a secondary reference, but also served to indicate the extent of hydrocarbon species present on the sample. For all the powder surfaces examined in the air exposed unetched condition, the carbon line was invariably the most intense spectral peak, but the intensity rapidly diminished after short periods of bombardment. The Ti 3p and 3s lines are not shown in this paper, but confirmed that particle-induced reduction of the oxide samples had occurred. Similarly the oxygen 1s lines are not included since apart from showing the presence of oxygen adsorbed species, the spectra gave little additional information on the oxidational state of the Ti. The effects of fast atom and ion bombardments on the reduction of the oxide are therefore illustrated in this work by reference to the distinct alteration and shift of the metal 2p peaks.

The overall effect of particle bombardment on the Ti $2p_{3/2}$ and $2p_{1/2}$ spectral lines with increased time of bombardment may be seen in Figures 2 and 3. These figures represent the most mild and most severe conditions of bombardment employed in this investigation. Figure 2 shows the spectra recorded for He atom bombardment at low current (current density of 1.3×10^{-2} Am^{-2}). The spectra shown are for 0, 2, 10, 30, 60 and 120 min of bombardment. It may be seen from the spectra that there is little change in peak shape even after long periods of fast atom bombardment. This indicates that the degree of particle-induced reduction of the oxide is low for these conditions. It should be noted, however, that for small amounts of reduction, the relatively subtle peak shape changes are not immediately obvious from a cursory examination of the spectra.

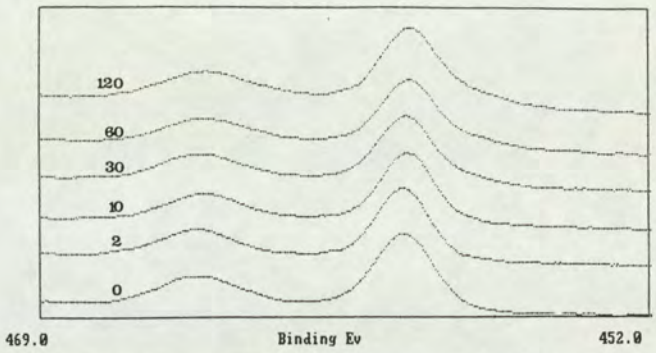

Figure 2. Series of X-ray photoelectron Ti 2p spectra recorded for different periods of helium atom bombardment at a current density of 1.3×10^{-2} A m^{-2}. The time of bombardment in minutes is shown on each spectrum.

Figure 2 may be contrasted with Figure 3 which shows a similar series of Ti 2p spectra, but for Ar ion bombardment at high current (current density of 1.3×10^{-1} A m^{-2}). It may be seen from this latter series that there are large changes in peak shape after very short periods of etching. A reduction in the oxidational state of the Ti produces a shift of core level photoelectron lines to lower binding energies. This results in a broadening of the spectral peaks on the low binding energy side and this may be clearly observed from the spectra in Figure 3. Thus under these conditions of bombardment, by a relatively massive ion at high current, a considerable degree of oxide reduction occurs. As mentioned above the two series of spectra shown here represent the extremes of the conditions applied, all other conditions produced spectral changes somewhere between these two.

It is the purpose of this work to examine the differences in chemical damage produced in surfaces by charged and uncharged particles and to achieve this we have chosen to study bombardment induced oxide reduction. To do this, very careful comparison must be made of the spectra generated from surfaces bombarded by atoms and those bombarded by ions. It is not immediately obvious from even the most careful comparison of the complete composite spectral peaks, whether there is a difference or how to quantify any which exists. Hence, in order to compare spectra and distinguish quantitatively the con-

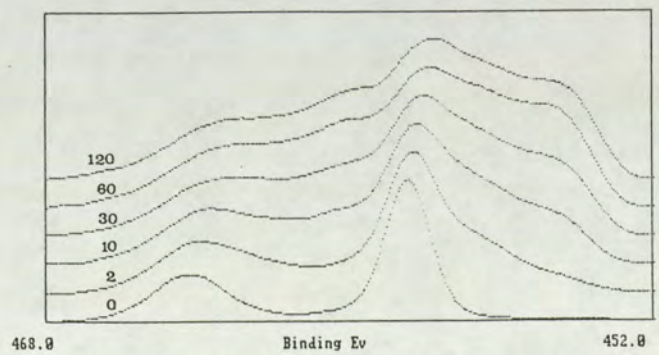

Figure 3. Series of X-ray photoelectron Ti 2p spectra recorded for different periods of argon ion bombardment at a current density of 1.3×10^{-1} A m^{-2}. The time of bombardment in minutes is shown on each spectrum.

tribution of different oxidational states, curve synthesis must be employed on the measured spectral peaks. The procedure employed was, as stated in a previous section, similar to that described by Sherwood[22]. For fitting in this series of experiments a linear background subtraction routine was employed and Gaussian peak shapes were assumed for each single component. Full width half maxima (FWHM) were taken to be constant and equal to that of the Ti^{4+} peak in the original oxide spectra, that is 1.8 eV for the $2p_{3/2}$ and 2.5 eV for the $2p_{1/2}$ components. In common with Hofman[25], we found it necessary to employ fitting parameters in order that the relative peak intensities of the individual $2p_{3/2}$ and $2p_{1/2}$ components were in the expected ratio of 2:1. These relative intensities are given by the ratio of the occupation number of the subshell state $(2j+1)$. The final correctness of fit was estimated by comparing the composite fitted sum of components with original data smoothed using the method of Savitsky and Golay[26].

Figures 4–7 show original measured Ti 2p spectra with corresponding synthesised peaks. From the synthesised spectra, the reduction $TiO_2 \rightarrow Ti_2O_3 \rightarrow TiO$ was observed through the corresponding Ti^{4+}, Ti^{3+} and Ti^{2+} components. For some spectra recorded after long periods of bombardment, full reduction to Ti metal had occurred. The peak position of the various components were at the following binding energies. For the $2p_{3/2}$ peaks, Ti^{4+} at 458.8 eV, Ti^{3+} at 457.1 eV, Ti^{2+} at 455.3 eV and Ti^{0} at 453.9 eV with corresponding energies for the $2p_{3/2}$ peaks at 464.5 eV, 462.8 eV, 460.9 eV and 460.0 eV, respectively. The synthesised peak position for all spectra examined were all within ± 0.1 eV binding energy. All the spectra shown in Figures 4–7 were for a 10 min bombardment period. Considering each of the figures in turn, Figure 4(a) shows the Ti 2p peaks for He bombardment at

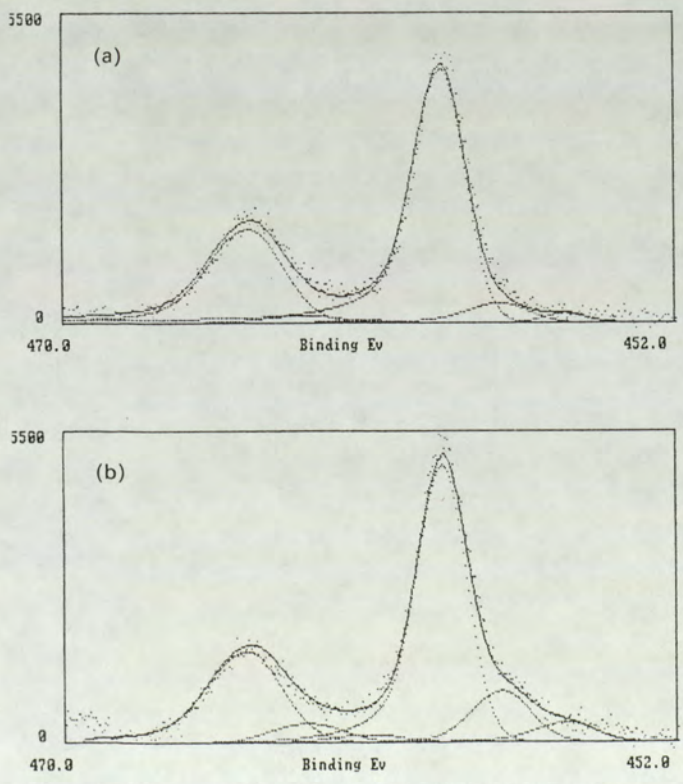

Figure 4. Ti 2p spectra recorded after 10 min helium bombardment at a current density of 1.3×10^{-2} A m^{-2}; (a) for atoms, (b) for ions.

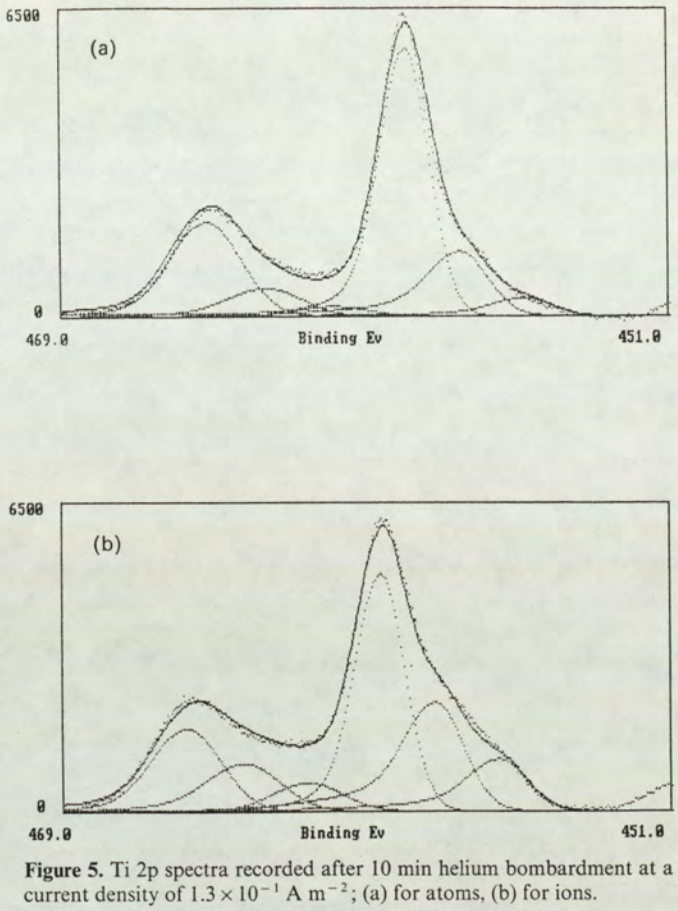

Figure 5. Ti 2p spectra recorded after 10 min helium bombardment at a current density of 1.3×10^{-1} A m^{-2}; (a) for atoms, (b) for ions.

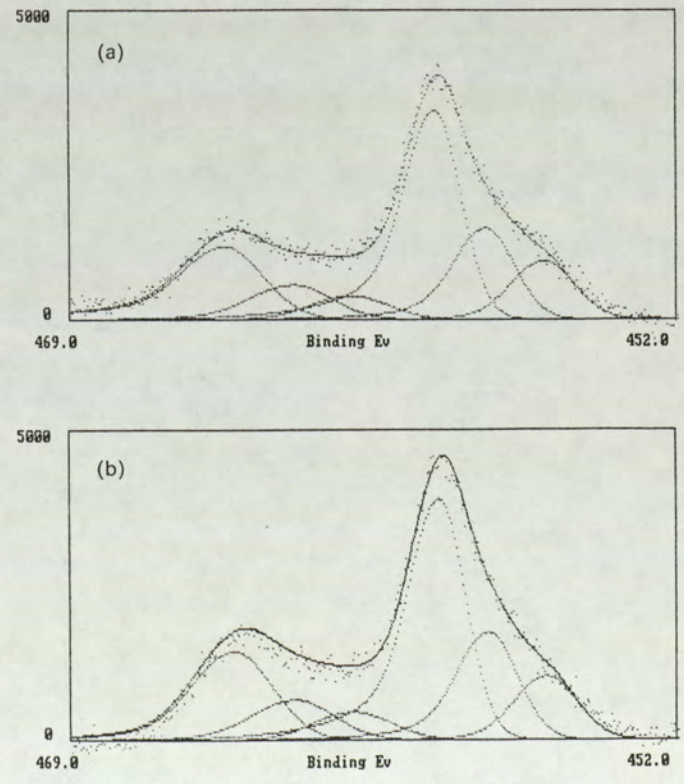

Figure 6. Ti 2p spectra recorded after 10 min argon bombardment at a current density of 1.3×10^{-2} A m^{-2}; (a) for atoms, (b) for ions.

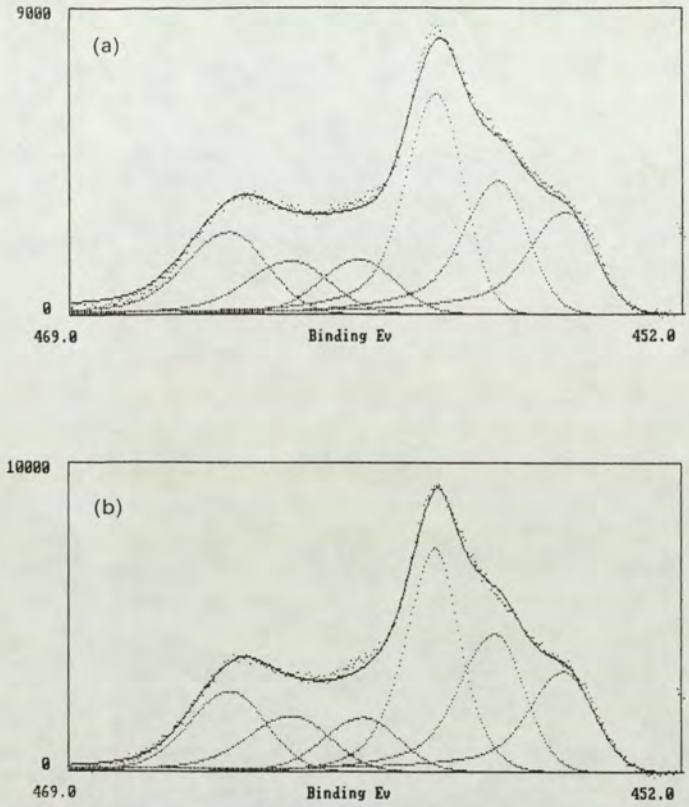

Figure 7. Ti 2p spectra recorded after 10 min argon bombardment at a current density of 1.3×10^{-1} A m^{-2}; (a) for atoms, (b) for ions.

low current. Curve synthesis of the spectrum reveals two peaks. Considering the $2p_{3/2}$ peak, the major component at a binding energy of 458.8 eV is due to Ti^{4+} from the original TiO_2 and there is a smaller component at 457.1 eV due to Ti^{3+} from Ti_2O_3. It is possible that there is a peak due to Ti^{2+} at 445.3 eV due to TiO, but this must be of low concentration. Corresponding $2p_{1/2}$ components are also apparent.

Figure 4(b) shows the corresponding spectrum for He ion bombardment with similar beam current. In this figure there are three obvious components due to Ti^{4+}, Ti^{3+} and Ti^{2+} and the relative magnitude of the latter two components when compared to the Ti^{4+} signal from the original oxide, shows that substantially more reduction has occurred in this case than in the case of the atom bombardment under the same conditions.

In order to quantify the degree of reduction in each case, the ratio of the sum of the intensities of the product oxide lines to the intensity associated with the original oxide, $(I^3+I^{2+})/I^{4+}$, is calculated. This value expressed as a percentage is shown in Table 1. Also shown in that table is the ratio of ion to atom reduction.

Figure 5(a) shows the Ti 2p spectra for the atom bombardment at high current, together with synthesised peaks. This figure again shows components due to Ti^{4+}, Ti^{3+} and Ti^{2+}. It can be seen from comparison with Figure 4(a) that the increased current leads to greater reduction.

The spectrum shown in Figure 5(b) is the corresponding spectrum for He ion bombardment at high current. Again this shows that the higher current produces a greater degree of reduction. In both cases of atom and ion bombardment an order of magnitude difference in current produces about four times the degree of reduction. Comparison of Figures 5(a) and (b) shows that, in common with the results for He bombardment at low current, the charged ions produce substantially more reduction in the oxide than do the neutral fast atoms. Thus in the case of these light projectiles the charge has a profound effect on the differential sputtering process. The calculated percentage reductions and ratios of ion to atom reduction are shown in Table 1.

Figures 6(a) and (b) show the Ti 2p spectra with synthesised components for Ar bombardment at low current. As for the previously described spectra, components due to Ti^{4+}, Ti^{3+} and Ti^{2+} are apparent. In contrast to the He derived spectra, however, there is little difference in reduction between atom and ion bombardment, although ion bombardment does produce the greater change. The more massive Ar particles do, of course, produce the greater overall degree of reduction.

The spectra shown in Figures 7(a) and (b) for Ar bombardment at high current also indicate that the difference between atom-induced and ion-induced reduction in the case of Ar is not nearly as pronounced as in the case of He. Figures 6 and 7 also show the effect of current on reduction, similarly not so pronounced in the case of argon as it is in the case of helium. For argon an order of magnitude increase in current approximately doubled the degree of reduction compared with twice this amount for helium.

Table 1 shows the calculated percentage reduction and the ratio of ion to atom reduction for both high and low Ar currents.

We have shown in this paper the spectra recorded after 10 min total bombardment time, but even for the shortest bombardment periods measured, that is, 2 min, significant reduction was observed. For longer periods of bombardment the degree of reduction increased with time. In general, however, the ratio of ion-induced reduction to atom-induced reduction remained fairly constant with time of bombardment. The scatter of results increased significantly with increasing time and this was due principally to instability of the source current after prolonged periods of operation. This resulted in the shorter period experiments giving more consistent and more reliable information.

In summary, the work has shown that ion-beam-induced and fast atom-beam-induced chemical reduction of TiO_2 takes place for both He and Ar bombardment. It has further shown that there is a significant difference in the degree of reduction between ion bombardment and fast atom bombardment with the latter producing less chemical change. The difference in reduction is particularly obvious when He bombardment was employed where fast atoms produced about 2.5 times less reduction than did ions of the same energy. For Ar the difference in reduction was not nearly so pronounced, with fast atom beams producing

Table 1. The percentage reduction and ratio of ion to atom reduction for the various bombarding species after 10 min exposure to bombardment

Bombarding species	Current density A m^{-2}	Percentage reduction	Ratio ion to atom reduction
He^0	1.3×10^{-2}	11	2.5 : 1
He^+		28	
He^0	1.3×10^{-1}	43	2.3 : 1
He^+		98	
Ar^0	1.3×10^{-2}	73	1.5 : 1
Ar^+		77	
Ar^0	1.3×10^{-1}	127	1.12 : 1
Ar^+		142	

about 1.05–1.12 times less damage for the spectra shown, although differences of up to 1.5 times were measured for longer periods of bombardment. It should be remembered that the 'ion' beam in fact contained about 20% atoms, hence one would expect the difference to be less pronounced than if the beam was comprised wholly of charged particles.

This work has demonstrated that there is a difference in chemical damage produced in an insulating surface due to charge on the bombarding particle. It is not, therefore, surprising that this effect should be more pronounced in the lighter species. For Ar, in the energy range employed in these experiments, sputtering may be accounted for in terms of the linear cascade theory, whereas this theory breaks down for very light species such as He where the energy transfer is insufficient to generate a proper cascade. Hence, the sputtering yield, will be far less for the lighter species, but the absolute effect of charge for the same input current will be similar. Thus if sputtering is due to electronic as well as linear cascade processes the former will have a greater proportional effect for He. It is also a fact that damage will be suppressed more effectively with increase in sputtering yield since a high fraction of the damaged layer is simultaneously removed and this effect may obscure the differences when Ar bombardment is employed.

We should now speculate on why there should be a difference in surface damage created by atom and ion bombardment. It is now accepted that bombardment-induced reduction of metal oxide is due to preferential sputtering of the lower mass component, i.e. the oxygen, followed by atomic re-arrangement to form a lower oxide. The rate of preferential sputtering is then determined by surface binding effects (related to binding energies) and to mass difference effects. It is unlikely that the latter will be influenced by charge, but binding energies could be considerably affected.

A charged particle approaching a surface loses its charge within about 5 Å of that surface due to an electric excitation process of the target atom. This leads to an increase in local surface potential until some compensating mechanism establishes dynamic equilibrium. In the absence of an external source of electrons, the compensating mechanism is likely to be electrical breakdown within the oxide. The breakdown would result in an effective decrease in the mean binding energy and would hence produce enhancement of sputtering yield of the oxygen. The direction of the induced field is also likely to enhance the removal rate of the negatively charged oxygen component.

With uncharged particles, although there will still be an increase in local surface potential due to emission of secondary electrons, the effect is likely to be far less pronounced. Hence one would expect on this hypothesis that ions would produce greater sputtering yield and a greater differential sputtering effect.

4. Conclusions

Ion-beam-induced and fast atom-beam-induced chemical reduction of TiO_2 occurs for both He and Ar bombardment, producing the reaction $TiO_2 \rightarrow Ti_2O_3 \rightarrow TiO \rightarrow Ti$.

There is a significant difference in the degree of reduction between ion bombardment and fast atom bombardment with fast atoms producing less chemical change. The lighter bombarding particle produced the greatest difference in reduction. For bombardment with He, fast atoms produced about two and a half times less reduction than ions of the same energy and for Ar the difference in reduction was about 1.0–1.5 times.

References

[1] J Franks, *Vacuum*, **34,** 259 (1984).
[2] P J Holloway and R S Bhattacharaya, *J Vac Sci Technol*, **20,** 444 (1982).
[3] H J Stein, *J appl Phys*, **47,** 3421 (1976).
[4] R Kelly, *Nucl Instrum Meth*, **182/183,** 351 (1981).
[5] J Fine, T D Andreadis and F Davarya, *J Vac Sci Technol*, **A1,** 507 (1983).
[6] K S Kim, W E Baitinger, J N Amy and J Winograd, *J Elect Spec Rel Phemon*, **5,** 351 (1974).
[7] R Kelly and N Q Lam, *Radiat Effects*, **19,** 39 (1973).
[8] N S McIntyre and D G Zetaruk, *Anal Chem*, **49,** 1521 (1977).
[9] G C Allen, M T Curtis, A J Hooper and P M Tucker, *J Chem Soc Dalton*, 1525 (1974).
[10] R Holm and S Storp, *Appl Phys*, **12,** 101 (1977).
[11] P Mills and J L Sullivan, *J Phys D*, **16,** 723 (1983).
[12] M P Seah, *Thin Solid Films*, **81,** 279 (1981).
[13] R Kelly, *Surface* Sci, **100,** 85 (1980).
[14] J B Malherbe, S Hofman and J M Sanz, *Appl Surface Sci*, **27,** 355 (1986).
[15] P Sigmund, *Sputtering by Particle Bombardment* (Edited by R Behrish. Springer, Berlin (1981).
[16] P Sigmund, *Phys Rev*, **184,** 383 (1969).
[17] A Brown, J A van den Berg and J C Vickerman, *J Chem Soc, Chem Com*, **24,** 1684 (1984).
[18] P C Zalm, *Surf Int Anal*, **11,** 1 (1988).
[19] U Bangert, J Belson and I H Wilson, *Nucl Instrum Meth Phys Res*, **B1,** 370 (1984).
[20] R Kelly, *Radiat Effects*, **80,** 273 (1984).
[21] P C Zalm, *J appl Phys*, **54,** 2660 (1983).
[22] P M Sherwood, *Practical Surface Analysis* (Edited by D Briggs and M P Seah). Wiley, New York (1983).
[23] S O Saied, J L Sullivan and R K Fitch, *Vacuum*, **38,** 111 (1988).
[24] S O Saied, J L Sullivan and C G Pearce, *Vacuum*, **38,** 469 (1988).
[25] S Hofman, *J Vac Sci Technol*, **A4,** 2789 (1986).
[26] A Savitsky and M J E Golay, *Anal Chem*, **36,** 1627 (1964).